UNIVERSITE PARIS-SUD

ÉCOLE DOCTORALE DE PHYSIQUE DE LA REGION PARISIENNE

Laboratoire de Physique des Solides

***DISCIPLINE :*** *Physique*

**THÈSE DE DOCTORAT**

soutenue le 25/10/2013

par

**Arthur Losquin**

# Surface Plasmon modes revealed by fast electron based spectroscopies : from simple model to complex systems

**Directeur de thèse :** Mathieu Kociak

**Composition du jury :**

| | |
|---|---|
| *Président :* | Jean-Pierre Hermier |
| *Rapporteurs :* | Michel Bosman |
| | Rémi Carminati |
| *Examinateurs :* | Luc Henrard |
| | Carsten Rockstuhl |
| *Membre invité :* | Odile Stéphan |

**Abstract**

**Surface Plasmon modes revealed by fast electron based spectroscopies: from simple model to complex systems**

Surface Plasmons (SP) are elementary excitations mixing electrons and photons at metal surfaces, which can be seen in a classical electrodynamics framework as electromagnetic surface eigenmodes of a metal-dielectric system. The present work bases on the ability of mapping SP eigenmodes with nanometric spatial resolution over a broad spectral range using spatially resolved fast electron based spectroscopies in a Scanning Transmission Electron Microscope (STEM). Such an ability has been separately demonstrated during the last few years by many spatially resolved experiments of Electron Energy Loss Spectroscopy (EELS), which measures the energy lost by fast electrons interacting with the sample, and CathodoLuminescence (CL), which measures the energy released by subsequently emitted photons. In the case of EELS, the experimental results are today well accounted for by strong theory elements which tend to show that the quantity measured in an experiment can be safely interpreted in terms of the surface eigenmodes of the sample. In order to broaden this interpretation to fast electron based spectroscopies in general, I have performed combined spatially resolved EELS and CL experiments on a simple single nanoparticle (a gold triangular nanoprism). I have shown that EELS and CL results bear strong similarities but also slight differences, which is confirmed by numerical simulations. I have extended the theoretical analysis of EELS to CL to show that CL maps equally well than EELS the radiative surface eigenmodes, yet with slightly different spectral features. This work is a proof of principle clarifiying the quantities measured in EELS and CL, which are shown to be respectively some nanometric equivalent of extinction and scattering spectroscopies when applied to metal-dielectric systems. Based on this interpretation, I have applied EELS to reveal the SP eigenmodes of random metallic media (in our case, semicontinuous metal films before the percolation threshold). These SP eigenmodes constitute a long standing issue in nanooptics. I have directly identified the eigenmodes from measurements and data processing. I have fully characterized these eigenmodes experimentally through an electric field intensity pattern, a resonance energy and a spectral width inherent to the eigenmodes. Doing so, I have shown that the fractal geometry of the medium, which grows towards the percolation, induces random-like eigenmodes in the system at low energies.

Keywords: Surface plasmons, fast electron based spectroscopies, scanning transmission electron microscopy, disordered media

**Modes propres plasmon de surface révélés par spectroscopies d'électrons rapides: de systèmes modèles simples vers des systèmes complexes**

Les plasmons de surface (SP) sont des excitations mêlant électrons et photons localisées aux surfaces et interfaces métalliques. On peut les voir classiquement comme les modes électromagnétiques propres d'un ensemble constitué d'un métal et d'un diélectrique. Cette thèse se base sur la capacité offerte par les techniques de spectroscopie utilisant des électrons rapides disponibles dans un microscope électronique à balayage en transmission (STEM), de cartographier, dans une large

gamme spectrale et avec une résolution spatiale nanométrique, les modes propres SP. Une telle capacité a été démontrée séparément, durant ces dernières années, par des expériences de spectroscopie de pertes d'énergie d'électrons (EELS), qui mesurent l'énergie perdue par des électrons rapides intéragissant avec un échantillon, et de cathodoluminescence (CL), qui mesurent l'énergie réémise par l'échantillon par l'intermédiaire de photons, toutes deux résolues spatialement. Dans le cas de l'EELS, ces résultats expérimentaux sont aujourd'hui interprétables à l'aide d'analyses théoriques convaincantes tendant à prouver que la quantité mesurée dans une telle expérience peut être interprétée de façon sûre en terme de modes propres de surface de l'échantillon. Afin d'élargir une telle interprétation aux techniques de spectroscopies utilisant des électrons rapides en général, j'ai effectué des expériences combinées d'EELS et de CL résolues spatialement sur une nanoparticle unique simple (un nanoprisme triangulaire d'or). J'ai montré que les résultats offerts par ces deux techniques présentent de fortes similitudes mais également de légères différences, ce qui est confirmé par des simulations numériques. J'ai étendu l'analyse théorique du signal EELS au signal CL, et ai montré que la CL cartographie, tout comme l'EELS, les modes de surface radiatifs du sytème, mais avec des propriétés spectrales légèrement différentes. Ce travail constitue une preuve de principe clarifiant les quantités mesurées en EELS et CL sur des systèmes métal-dielectriques. Ces dernières sont démontrées être respectivement des équivalents nanométriques des spectroscopies d'extinction et de diffusion de la lumière. Basé sur cette interprétation, j'ai utilisé l'EELS pour dévoiler les modes propres SP de milieux métalliques aléatoires (dans notre cas, des films semicontinus métalliques avant le seuil de percolation). Ces modes propres constituent une problématique de longue date dans le domaine de la nanooptique. J'ai directement identifié ces modes par des mesures et le traitement de leurs résultats. J'ai complètement caractérisé ces modes propres via les variations spatiales de l'intensité liée à leur champ électrique, une énergie de résonance et une largeur spectrale caractéristiques du mode. Ce faisant, j'ai montré que la géométrie fractale du milieu, dont la prédominance croit au fur et à mesure que l'on s'approche de la percolation, est responsable de l'existence de modes propres de type aléatoire à basse énergie.

Mots clés: Plasmons de surface, spectroscopies d'électrons rapides, microscopie électronique à balayage en transmission, milieux désordonnés

# Remerciements

J'aimerais ici remercier un certain nombre de personnes qui ont contribué, de près ou de loin, aux travaux exposés dans le présent manuscrit.

Evidemment, mes premiers remerciements vont à Mathieu Kociak, et ce pour de multiples raisons. Quand j'ai accepté mon sujet de thèse, qui parlait d'injecter de la lumière dans un microscope électronique pour aider des plasmons à interagir avec des électrons (?!), je ne connaissais absolument rien à la microscopie électronique, ni même aux plasmons. La seule spectroscopie que je connaissais était la spectroscipe d'absorption UV-vis, pas vraiment résolue spatialement donc, que j'utilisais à l'Imperial College simplement pour vérifier la "qualité" de mes échantillons. Je remercie donc Mathieu, d'un côté pour m'avoir convaincu, par un savant mélange de cordialité et de cartes colorées de triangles, de jeter mon dévolu sur la spectroscopie d'électrons rapides, de l'autre pour m'avoir fait confiance sans même m'avoir vu à l'oeuvre en stage. Durant ces trois ans, Mathieu s'est révélé être un directeur de thèse exemplaire, humain, extrêmement sympathique, compréhensif[1], ouvert, toujours de bon conseil, et, au risque de paraphraser ses anciens thésards, une source d'informations proprement intarissable, que ce soit à propos des monochromateurs ou des fonctions de Green. Je ne cache pas ma profonde admiration pour la qualité de sa recherche, qui restera probablement pour moi comme un modèle[2].

Je remercie ensuite Dominique Chandesris pour m'avoir permis de rejoindre le Laboratoire de Physique des Solides, ainsi qu'Odile Stéphan, pour m'avoir accueilli au sein du groupe STEM, mais également pour ses encouragements, sa gentillesse et ses précieuses suggestions lors des longs processus de rédaction d'articles. Je la remercie aussi pour m'avoir permis de prendre part de façon active aux diverses conférences et autres événements scientifiques ayant jalonné cette thèse, et de me rendre à l'université de Mc Master pour des manipes monochromatées. Je remercie enfin Christian Colliex pour son soutien et ses recommandations, et pour avoir diffusé mes travaux lors de ses communications orales.

Parmi les membres de groupe STEM, je remercie tout particulièrement nos super-ingénieurs pro-VG, Marcel Tencé et Jean-Denis Blazit, sans qui les résultats de manipes présentés dans cette thèse n'auraient probablement jamais vu le jour. Je remercie également toutes les personnes ayant oeuvré à la conception du détecteur de lumière permettant des manipes CL, en particulier Luiz Fernando Zagonel, Michaël Pelloux et Stefano Mazzucco. J'en profite par ailleurs pour remercier Luiz pour les conseils dont il m'a fait profiter, mais également pour sa bienveillance et son écoute. Merci à Guillaume Boudarham pour nos discussions et sa décomposition modale qui a probablement changé le cours de ma ~~vie~~ thèse. Merci à mon frère de thèse, Zackaria Mahfoud, pour sa sympathie et nos

[1] Et perspicace, aussi: il a vite compris que la conception de ressorts n'était pas franchement mon truc.

[2] S'il fallait lui trouver un défaut, cela serait probablement son manque de rigueur, étonnant de sa part, dans la prononciation de mon nom.

échanges toujours riches d'enseignement[3]. Merci à mes cobureaux successives, Farah Attouchi et Laura Bocher, de m'avoir supporté au quotidien. Un grand merci à Farah pour ne pas m'avoir mis dehors à l'arrivée de Nadia, un autre à Laura pour sa bretonnerie (on se comprend), ses répètes, mais aussi pour ses anecdotes, conseils et autres trucs intéressants à connaitre lorsqu'on vise une carrière académique. Enfin, un très grand merci à Nadine Mehl et Marie-France Cozic pour leur disponibilité et leur aide administrative inestimables.

Je remercie toutes les autres personnes du groupe STEM que j'ai pu côtoyer durant ma thèse et qui ont également contribué à rendre ces trois années particulièrement plaisantes. Côté permanents, merci à Nathalie Brun, Katia March et Claudie Mory pour leur gentillesse toute féminine, Alexandre Gloter et Alberto Zobelli pour la partie de baby foot des journées labo (si si!), Mike Walls pour sa descente de pintes[4]. Coté non-permanents, merci aux post-docs: Santhana Eswara-Moorthy, Nadia Haneche, Maya Marinova, Sounderya Nagarajan, Luiz Tizei et Almudena Torres Pardo, et spéciale dédicace aux thésards que je n'aurais pas encore cité: Vincent Badjeck, Romain Bourrellier[5], Xiaoyan Li et Sophie Meuret. Enfin, merci à Yannick Dappe, Anna Tararan et Justin Demory. Tous ont contribué d'une façon ou d'une autre à l'ambiance plus ou moins studieuse qui règne au 2e étage aile est du bâtiment 510, et qui me manquera très probablement[6].

Je remercie la DGA et le CNRS pour leur attribution d'une bourse cofinancée, ainsi que l'Université Paris Sud pour la rallonge de financement qu'elle m'a accordée. De plus, je remercie toutes les sources de financement dont j'ai pu occasionnellement profiter durant ma thèse, notamment le réseau de microscopie METSA, la Société Française des microscopies, le projet européen Esteem 2 et l'Agence Nationale de la Recherche.

Merci à tous mes collaborateurs ayant contribué à ces travaux: Luiz Fernando Zagonel, Sophie Camelio, David Babonneau et Frédéric Pailloux, David Rossouw et Gianluigi A. Botton, Mondher Besbes et Jean-Jacques Greffet, Viktor Myroshnychenko et Javier Garcia de Abajo, et Benito Rodriguez-Gonzalez et Luis M. Liz-Marzan. Je remercie tout particulièrement David Rossouw et Gianluigi A. Botton pour m'avoir accueilli de la plus belle des manières à l'université de Mc Master. Merci également à Pierre-Eugène Coulon et Giancarlo Rizza pour leur confiance sur des manipes non-présentées dans ce manuscrit, et leur indulgence face à ma capacité non-contrôlée à détruire ou perdre leurs échantillons.

Merci à Santhana Eswara Moorthy et Pascale Auban-Senzier pour leur aide et leur patience sur la préparation de films métalliques semicontinus malheureusement non-reproductibles. Ces essais m'ont permis de conclure que finalement, on n'est pas si bien servi que ça par soi-même (merci Poitiers!).

Je tiens ensuite à remercier tous mes potes qui m'ont vu mûrir (ou pas) durant ces trois ans et m'ont offert la détente nécessaire à la survie du thésard[7]. Merci aux grenoblois (en particulier Manue, Dav, Alex et Coco), aux colloques-pour-la-vie (Mathieu et Tom) et aux vieux de la vieille (Alissia, Camille, Gallou, Fi et Marianne (Le Gall)). Merci à tous ceux que j'ai pu côtoyer sur Paris, notamment certaines des personnes pré-nommées, mais aussi Léa, Marianne (Le Roy),Yannou et Pierre. Merci à toutes les autres personnes que j'ai pu croiser de façon plus occasionnelle. Merci à Fanch pour nos discussions enflammées sur la recherche, la physique, l'avenir, la vie, David Lynch et la Guiness ((double) pléonasme). Enfin, merci au Pantalon et à Vic pour nous avoir vendu sans

[3]Par respect pour Zackaria, je m'en tiendrai ici à un aspect purement scientifique en préférant passer sous silence ses blagues plus que discutables.

[4]Mike, il faut que je te l'avoue, tu es mon héros.

[5]Non, les gars, je ne citerai pas Ryan Gosling dans ces remerciements!

[6]Vous avez de la chance, la place me manque pour balancer du gros dossier sur chacun d'entre vous!

[7]A ne pas confondre avec la survie de son foie.

faillir du rêve en pinte.

Merci à Michel Bosman, Rémi Carminati, Luc Henrard, Jean-Pierre Hermier, Carsten Rockstuhl, Mathieu et Odile pour avoir accepté de faire partie du jury de soutenance. Merci à toutes celles et ceux ayant été là durant la soutenance et le week end mémorable qui suivit.

Merci à toute ma famille, cousins, cousines, oncles, tantes, mais aussi et surtout mes parents, Math et ma grand-mère pour leur soutien durant ces années. C'est promis, après ça, fini les études (ça va être difficile d'aller plus loin)! Enfin, un grand merci à Amélie pour m'avoir suivi à Paris, m'avoir offert une oreille attentive et m'avoir épaulé jour après jour.

# Résumé

Les plasmons de surface (SP) sont des excitations mêlant électrons et photons localisées à la surface d'un matériau ou aux interfaces entre matériaux. On peut les voir classiquement comme les modes électromagnétiques propres d'un ensemble constitué d'un métal et d'un diélectrique. Ceux-ci ont la caractéristique première d'être évanescents des deux côtés de l'interface entre les deux milieux. Dans le cas où le métal prend la forme d'une nanoparticule, les modes SP soutenus par la structure acquièrent des propriétés résonantes, et dictent les propriétés optiques de l'objet. En particulier, les caractéristiques spectrales de ces modes dépendent, pour des nanoobjets uniques à géométrie simple, des dimensions et matériaux constitutifs du système. Ces modes forment en outre des ondes stationnaires localisées à des échelles nanometriques, et permettent, une fois l'objet soumis à une excitation lumineuse, de localiser et amplifier l'énergie électromagnétique à de très petites échelles.

La caractérisation complète et, in fine, la compréhension des modes SP de nanoparticules ne peut donc se faire que via un accès très local à leur réponse spectrale entière, bien souvent inaccessible aux techniques d'optique en champ proche. D'un autre côté, les techniques de spectroscopies se basant sur l'interaction entre un électron rapide et un échantillon se sont révélées être, ces dernières années, un outil précieux pour l'étude des modes SP. En particulier, la spectroscopie de pertes d'énergie d'électrons (EELS), qui sonde l'énergie perdue localement par un électron rapide par un phénomène de diffusion inélastique quelconque, et la cathodoluminescence (CL), qui détecte la lumière émise par la désexcitation radiative de ce phénomène de diffusion, ont séparément permis, par l'utilisation d'un microscope électronique à balayage en transmission (STEM), de "cartographier" les modes SP d'objets métalliques simples, avec une résolution spatiale nanométrique et dans une large gamme spectrale.

L'intérêt d'utiliser un STEM réside en effet dans la possibilité d'obtenir, simultanément et en chaque point de l'échantillon, un spectre complet ainsi qu'une information morphologique sur le matériau sondé localement, permettant la mise en place d'expériences d'EELS ou CL résolues spatialement. A la fin d'une acquisition, on obtient une image de l'échantillon (une image champ sombre annulaire à grand angle HAADF, dans laquelle un matériau lourd apparaitra clair) ainsi qu'un jeu complet de données spectroscopiques (un spectre image) incluant la totalité des spectres acquis localement sur toute la surface de l'échantillon. En manipulant un spectre image, on peut non seulement examiner et éventuellement traiter un spectre complet local, mais aussi observer les variations spatiales du signal spectroscopique filtré à une énergie donnée.

Dans la suite, nous allons détailler les résultats principaux de la thèse, qui se décomposent en deux grandes parties. Le but de ces deux parties est d'illustrer la capacité propre aux techniques de spectroscopies à base d'électrons rapides de révéler les modes SP de nanosystèmes composés de métal et de diélectrique. Nous adresserons pour ce faire deux systèmes de complexité croissante. Tout d'abord, nous aborderons le cas relativement simple d'un nanoprisme triangulaire d'or unique,

une nanoparticule dont les modes SP sont à ce jour relativement bien compris. Par des résultats d'expérience et des éléments de théorie, nous allons clarifier les quantités mesurées lors d'expériences d'EELS et CL résolues spatialement. Nous étudierons ensuite un système métal-diélectrique dit aléatoire ou désordonné, dont les modes SP sont au contraire fortement problématiques. Nous montrerons quelles informations nouvelles concernant les modes de tels systèmes peuvent être obtenues grâce à l'utilisation des techniques de spectroscopies à base d'électrons rapides (dans notre cas, de l'EELS uniquement) résolues spatialement. Nous nous concentrons ici sur l'essentiel des résultats, les bases théoriques et expérimentales ainsi que l'essentiel de la bibliographie pouvant être trouvées dans le manuscrit en lui-même.

# EELS et CL, équivalents nanométriques d'extinction et diffusion

## Introduction

Aujourd'hui, il est bien établi d'un point de vue expérimental que des expériences d'EELS et CL résolues spatialement permettent d'obtenir des "cartographies de plasmons". De plus, les nombreuses observations rapportées sur des nanoobjets métalliques de formes et tailles diverses sont étayées par des formalismes théoriques à la portée plus ou moins générale. D'un autre côté, les spectroscopies à base d'électrons rapides sont couramment comparées à des techniques de spectroscopie optique. De façon tout à fait intuitive, on peut tout à fait voir l'EELS et la CL comme des équivalents nanométriques respectifs de spectroscopies d'extinction et de diffusion de la lumière. Le but de cette partie sera de valider et d'établir, tant d'un point de vue expérimental que théorique, un lien entre ces deux approches. Le point de départ de cette démonstration consiste en une expérience combinée d'EELS et CL résolues spatialement sur un objet modèle, dans notre cas, un nanoprisme d'or de faibles dimensions.

## Expériences

La figure 1a montre l'image HAADF du nanoprisme triangulaire d'or, obtenue avant des expériences d'EELS et CL résolues spatialement effectuées successivement sur le meme objet. A gauche de la figure 1b, nous présentons des spectres EEL obtenus pour une sonde électronique localisée à la pointe (spectre T EELS) et dans le vide (spectre V EELS). Une franche résonance apparait dans le spectre T EELS à l'énergie de résonance de 2.27 eV. En comparaison, le spectre V EELS ne montre aucune caractéristique particulière. La carte filtrée montrée à droite de la figure 1b représente les variations spatiales du signal EELS filtré à l'énergie de résonance apparaissant dans le spectre T EELS. Cette carte montre des maximas locaux situés sur les pointes du nanoprisme, indiquant que les électrons rapides sont plus largement susceptibles de perdre une énergie de 2.27 eV lorsqu'ils sont dirigés sur les pointes du nanoprisme. Une telle carte est aujourd'hui familière pour la communauté. La figure 1c (gauche) montre les spectres CL obtenus pour une sonde électronique localisée à la pointe (spectre T CL) et dans le vide (spectre V CL). A nouveau, une résonance apparait dans le spectre T CL, mais à une énergie très légèrement inférieure à l'énergie de résonance du spectre T EELS, très précisemment de 2.22 eV. Cette légère variation spectrale mise de côté, la carte filtrée à l'énergie de resonance de T CL, donnée en figure 1c (droite), montre elle-aussi des maximas locaux situés sur les pointes du nanoprisme, indiquant que des photons d'énergie 2.22 eV sont sont

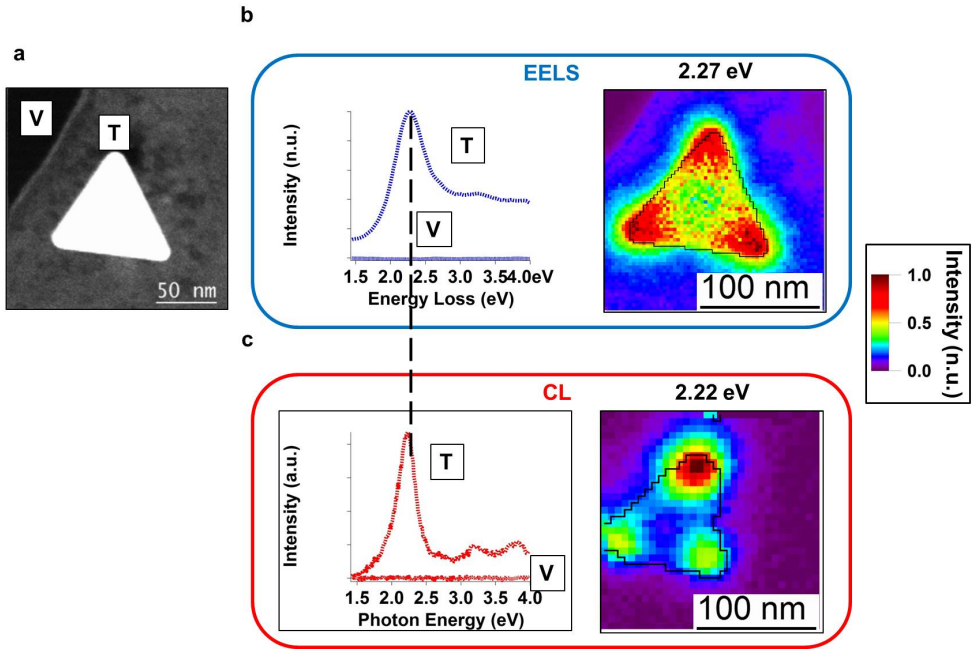


Figure 1: Expériences combinées d'EELS et CL résolues spatialement sur un nanorésonateur modèle. a) Image HAADF du nanoprisme d'or étudié. b) et c) A gauche: spectres EEL (b) et CL (c) obtenus pour une sonde électronique incidente focalisée à la pointe du nanoprisme (position T) et dans le vide (position V). A droite: variations spatiales des signaux EELS (b) et CL (c) filtrés à l'énergie de résonance apparaissant dans le spectre obtenu à la position T.

plus largement susceptibles d'être émis lorsque les électrons rapides sont dirigés sur les pointes du nanoprisme. De nouveau, ces observations sont en accord avec des travaux précédemment publiés.

Ces observations ont été confirmées par des simulations numériques effectuées par nos collaborateurs, qui peuvent être consultées dans la suite du manuscrit. Nous nous contenterons ici de donner une justification théorique à de tels résultats.

## Interprétation

Dans une approche heuristique basée sur les principes de l'électrodynamique classique, les mécanismes de base de perte d'énergie d'un électron rapide intéragissant avec un système composé de milieux diélectriques, ainsi que d'émission de photons en résultant, sont relativement bien compris. Un électron rapide voyageant dans le vide peut en effet être vu, soit dans l'espace réel comme une source de champ électromagnétique évanescent, soit dans l'espace de Fourier comme une source lumineuse blanche. A l'approche d'un milieu diélectrique, ce champ extérieur crée une polarisation, elle-même associée à un champ électromagnétique induit, ou diffusé. La composante parallèle à la trajectoire de l'électron du champ électrique associé à ce champ électromagnétique induit est susceptible d'agir contre l'électron en le freinant. En parallèle, cette polarisation peut rayonner en champ lointain via les composantes transverses du champ électrique associé. L'énergie perdue par

un électron rapide peut donc être décrite par la somme des travaux élémentaires dûs aux champs électriques associés au champs électromagnétiques induits tout le long de sa trajectoire, tandis que l'énergie des photons émis est donnée par l'énergie électromagnétique elle-aussi associée à ces champs électromagnétiques induits. Il va donc sans dire que l'énergie perdue par les électrons d'une part, l'énergie des photons émis d'autre part, sont reliées à la fréquence du processus de polarisation, et que la probabilité pour l'électron de perdre (ou d'induire des photons) d'une certaine énergie est directement reliée à l'intensité du champ électrique induit par cette polarisation.

Cette approche heuristique peut être très bien formalisée mathématiquement dans l'approximation quasistatique à partir de la théorie des éléments finis de frontière (BEM, Boundary Element Method). On peut en effet montrer que les probabilités qu'a un électron de perdre une certaine quantité d'énergie (probabilité EEL) et d'émettre un photon d'une certaine énergie (probabilité CL) peuvent s'écrire, pour un électron se déplaçant à une vitesse $v$ selon une trajectoire droite non pénétrante dirigée suivant $z$ située à une distance $\vec{R}$ de l'origine [8]:

$$\Gamma_{EEL}(\vec{R},\omega) = \frac{e^2}{\pi\hbar\omega^2}\sum_i \Im\left\{f_i(\omega)\right\}\left|E_i^z(\vec{R},\frac{\omega}{v})\right|^2 \tag{0.0.1}$$

$$\Gamma_{CL}(\vec{R},\omega) = \frac{e^2\omega}{64\pi^4\hbar c^2}\sum_{i=d}\left|f_i(\omega)\right|^2\left|\int \vec{p}_{i\perp}d\Omega_{\vec{e}_r}\right|^2\left|E_i^z(\vec{R},\frac{\omega}{v})\right|^2 \tag{0.0.2}$$

où $\Im$ désigne la partie imaginaire d'un complexe et $d\Omega_{\vec{e}_r}$ l'angle solide correspondant à une sphère de rayon $|\vec{r}|$ dirigée selon une direction $\vec{e}_r$. Dans les expressions ci-dessus, les sommes font intervenir les modes de surface du système $i$. La somme apparaissant dans la première expression comprend tous les modes, tandis que la somme apparaissant dans la deuxième expression n'inclut que les modes dipolaires (c'est à dire de moment dipolaire transverse non nul) du système. Pour chaque mode, $f_i(\omega)$ est une polarisabilité généralisée faisant intervenir les fonctions diélectriques des milieux composant le sytème, $\vec{p}_{i\perp}$ est le moment dipolaire transverse du mode et $E_i^z(\vec{R},\frac{\omega}{v})$ est la transformée de Fourier suivant z $E_i^z(\vec{R},q_z)$ de la composante suivant $z$ du champ électrique du mode évaluée en $q_z=\frac{\omega}{v}$.

Dans ces expressions, qui découpent les probabilités EEL et CL en modes de surface uniques, les variations spatiales et spectrales sont généralement découplées les une des autres. Ces variations spectrales sont respectivement dictées, pour les probabilités EEL et CL, par les dépendances en énergie de la partie imaginaire et du module au carré d'une même fonction de réponse: $f_i(\omega)$. Le pôle de cette fonction de réponse donne la condition d'existence, autrement dit l'énergie propre, du mode de surface $i$. D'un autre côté, les variations spatiales sont données par la même quantité: la norme au carré de la transformée de Fourier suivant z du champ électrique du mode de surface $i$.

Considérons pour commencer un cas très simple: celui d'un système composé de deux milieux non-dissipatifs. Dans ce cas, on peut montrer que tout mode de surface a une énergie propre réelle $\omega_i$, et que $\Im\left\{f_i(\omega)\right\} = \left|f_i(\omega)\right|^2 = \delta(\omega-\omega_i)$ . Les probabilités EEL et CL piquent aux mêmes énergies: les énergie propres des modes de surface. Cependant, si l'on considère le caractère dissipatif des matériaux, tout mode de surface à une énergie propre complexe. Dans ce cas, les partie imaginaire et module au carré de $f_i(\omega)$, bien que toujours résonants, ne sont pas forcément maximals à la même énergie. Ceci est dû à des formes fonctionnelles légèrement différentes autour

[8] La première formule a été dérivée par Boudarham et Kociak dans Phys. Rev. B **85**, 245447 (2012).

du pôle de $f_i(\omega)$. Si l'on considère un système composé de vide et d'un milieu diélectrique décrit par un modèle de Drude non-dissipatif, on peut par exemple montrer que les énergies de résonance de la probabilité EEL sont légèrement inférieures aux énergie de résonance de la proabilité CL.

Examinons à présent le cas d'un mode de surface dipolaire d'un nanoprisme d'or. La figure 2a montre les charges de surface associées à un tel mode. Ces charges sont maximales à une pointe et minimales à une autre pointe. La figure 2b montre la contribution spatiale du mode dipolaire aux probabilités EELS et CL, obtenues en calculant la grandeur $\left|E_i^z(\vec{R},\frac{\omega}{v})\right|^2$ pour différents paramètres d'impact $\vec{R}$ en prenant $\omega$=2.3 eV et pour $v$=c/2. Cette carte montre que l'intensité du mode s'accroit localement autour des pointes du nanoprisme, dû à un confinement local du champ électrique associé au mode dipolaire. De plus, la figure 2c montre la contribution spectrale du mode dipolaire aux probabilités EELS et CL, obtenues en calculant les grandeurs $\frac{1}{\omega^2}\Im\{f_i(\omega)\}\left|E_i^z(\vec{R},\frac{\omega}{v})\right|^2$ (pour l'EELS) et $\omega\left|f_i(\omega)\right|^2\left|E_i^z(\vec{R},\frac{\omega}{v})\right|^2$ (pour la CL) pour différentes énergies $\omega$ en prenant $\vec{R}$ situé à la pointe du nanoprisme. A cause des variations spectrales légèrement différentes de $\Im\{f_i(\omega)\}$ et $\left|f_i(\omega)\right|^2$, la résonance EELS caractéristique du mode est située à une énergie relativement plus haute que la résonance CL. Il est à noter que ce comportement est l'extrême inverse que celui prédit pour un oscillateur harmonique classique, pour lequel l'absorption maximale (l'EELS) a lieu à une énergie plus faible que l'amplitude d'oscillation maximale (la CL). Ceci démontre le caractère singulier des modes plasmons de surface de nanoparticules d'or résonants dans le domaine du visible.

Ce modèle explique donc de façon satisfaisante les résultats expérimentaux présentés précédemment. La CL se distingue de l'EELS par des énergie de résonance caractéristiques d'un mode donné légèrement différentes, ce qui était effectivement observé expérimentalement. Néanmoins, en EELS comme en CL, si l'on se place à la résonance d'un mode donné, on observe une somme incohérente des carrés des transformées de Fourier suivant z des composantes suivant z des champs électriques associés aux modes SP du système. Dans notre cas, le motif obtenu dans chaque carte filtrée est la somme de trois modes dipolaires dégénérés en énergie, dont les transformées de Fourier sont très proches des composantes suivant z des champs électriques associés évalués à distance finie de l'échantillon. Cette somme de modes induit des confinements locaux de champ autour des trois pointes du nanoprisme, similaires aux maxima locaux observés sur les cartes de la figure 1.

Ces deux expressions valident donc l'interprétation de telles cartes comme étant des "cartographies de plasmon", à condition de garder en tête le fait que seule la grandeur à laquelle l'électron est sensible est le carré de la transformée de Fourier suivant z de la composante suivant z des champs électriques des modes, et que l'on observe en général une somme incohérente de modes.

## Spectroscopies à bases d'électrons rapides et spectroscopies optiques

Des simulations ont montré que des spectres EELS et CL obtenus pour une sonde électronique localisée à la pointe du nanoprisme correspondaient parfaitement à des spectres d'extinction et de diffusion de la lumière obtenus sur le même objet. En particulier, le léger décallage en énergie entre EELS et CL se retrouve entre spectroscopies d'extinction et de diffusion. Ceci conforte le lien intuitif entre EELS et spectroscopie d'extinction d'une part, CL et spectroscopie de diffusion d'autre part.

Pour aller plus loin, on peut montrer, toujours dans la même approche que celle exposée ci-dessus, que les sections efficaces d'extinction et de diffusion de la lumière, s'écrivent:

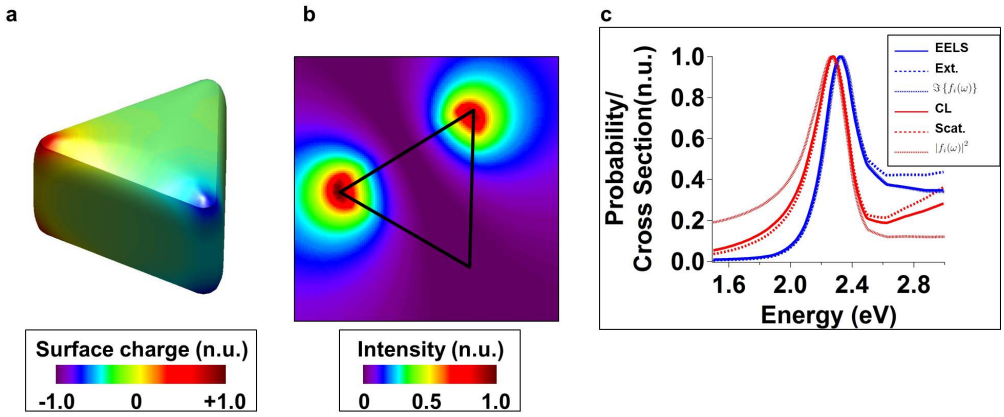


Figure 2: EELS et CL: théorie quasistatique. a) Charge de surface d'un mode SP dipolaire. b) Contribution spatiale du mode à l'EELS et à la CL. c) Contribution spectrale du mode à l'EELS, CL, extinction et scattering.

$$C_{ext}(\omega) \propto \sum_{i=d} A_{i,ext}\omega\Im\{f_i(\omega)\} \tag{0.0.3}$$

$$C_{sca}(\omega) \propto \sum_{i=d} A_{i,sca}\omega^4 |f_i(\omega)|^2 \tag{0.0.4}$$

où $A_{i,ext}$ et $A_{i,sca}$ sont des préfacteurs indépendants de l'énergie et les sommes ne comprennent que les modes de surface dipolaires de la structure. On retrouve à nouveau la partie imaginaire et la norme au carré de $f_i(\omega)$, qui apparaissaient dans les décompositions modales de l'EELS et de la CL données précédemment. La contribution spectrale du mode dipolaire aux sections efficaces d'extinction et de diffusion est tracée en figure 2c. Il est clair que, d'un côté, la résonance en EELS correspond à la résonance en extinction, et que d'un autre côté la résonance en CL correspond à la résonance en diffusion. Ceci est encore une fois dû aux variations spectrales légèrement différentes de la partie imaginaire et la norme au carré de $f_i(\omega)$. Ces expressions établissent donc un lien fort entre EELS et extinction d'un côté, CL et diffusion de l'autre. Précisemment, pour un même mode dipolaire, on trouve que les probabilités EEL et CL sont respectivement des sections efficaces d'extinction et de diffusion de la lumière convoluées par la norme au carré de la transformée de Fourier suivant z du champ électrique du mode.

## Conclusion

Dans cette partie, nous avons interprété des résultats d'EELS et CL résolues, d'une part sur la base des modes électromagnétiques propres de la structure (des modes SP dans le cas d'une structure métal-diélectrique), d'autre part sur la base de ses propriétés optiques. Nous avons de plus lié par notre formalisme ces deux interprétations. Ces résultats imposent l'EELS et la CL comme des équivalents nanométriques respectifs des spectroscopies d'extinction et de diffusion de la lumière, à la nuance près que l'EELS, contrairement à l'extinction, est sensible à tous les modes, y compris les modes "sombres" ou "non-radiatifs".

Comme nous l'avons vu, il est difficile de définir une caractéristique spectrale propre réelle unique pour un mode SP, dû au caractère dissipatif d'une structure composée de métal et de diélectrique. Malgré cela, nous assumerons que pour un mode SP $i$, l'énergie de résonance et la demi-largeur à mi-hauteur de $\Im\{f_i(\omega)\}$ ou $|f_i(\omega)|^2$ donnent respectivement une énergie propre et un taux de relaxation du mode.

Les expressions proposées ci-dessus ont été dérivées en utilisant une approximation quasistatique, et doivent donc être généralisées avec prudence. Cependant, on peut intuitivement penser que, dans le cas le plus général incluant des effets relativistes, l'EELS et la CL devraient être reliées à des phénomènes d'extinction et de diffusion, et que les variations spatiales des signaux EELS et CL donneraient les variations spatiales des composantes projetées suivant l'axe de l'électron des champs électriques associés aux modes électromagnétiques propres de la structure. Nous assumerons par la suite une telle généralisation.

# Application à un système complexe: un milieu désordonné

## Introduction

Dans la partie précédente, nous avons posé les bases, tant expérimentales que théoriques, permettant d'interpréter des résultats EELS et CL obtenus sur des systèmes composés de métaux et diélectriques sur la base de modes SP. Nous allons à présent montrer quel type d'informations nouvelles ces techniques permettent d'obtenir sur les modes SP, lorsqu'elles sont appliquées à des systèmes complexes. Précisemment, nous allons nous intéresser à un cas typique de milieu métal-diélectrique désordonné, appelé film métallique semicontinu. Un film semicontinu consiste en une assemblée de nanoparticules de tailles, formes et positions aléatoires, obtenue par dépôt de métal sur un milieu diélectrique. Un tel système a attiré une forte attention de la part de la communauté de l'optique, liée à de fortes propriétés d'absorption large bande autour du seuil de percolation. Des modèles théoriques simples ont relié ces propriétés optiques inhabituelles à l'existence de nombreux renforcements locaux de champ électromagnétique appelés "Hot Spots" (HS). Entre autres particularités, il a été prédit que les HS auraient des dimensions réellement nanométriques, une position sur le substrat aléatoire et fortement dépendente de l'énergie d'excitation, et qu'ils se manifesteraient tout particulièrement dans l'IR. Ces caractéristiques, malgré un nombre d'études conséquent, n'ont a l'heure actuel pas été démontrées. De plus, un tel comportement électromagnétique suggère l'existence de modes SP complexes. Cependant, le caractère exceptionnel de ces modes n'a jamais été directement identifié expérimentalement. Dans la suite, nous allons démontrer, par des résultats d'EELS résolus spatialement, que ces HS sont la conséquence de modes SP de type aléatoire, que nous avons pu entièrement caractériser grâce à notre technique. Les échantillons que nous considérerons seront des films semicontinus d'argent encapsulés dans une couche de nitrure de silicium.

## Expériences d'EELS résolue spatialement sur un film semicontinu autour de la percolation

La figure 3b montre des spectres EEL obtenus sur un film semicontinu situé autour de la percolation, dont les images HAADF sont données en figure 3a. Chaque spectre se compose d'un nombre important de résonances, indiquant la présence de nombreux modes SP. De plus, un léger déplacement de la sonde électronique induit des modifications radicales dans la structure des pics. Cette complexité spectrale se retrouve lorsque l'on observe les variations du signal EELS à une énergie

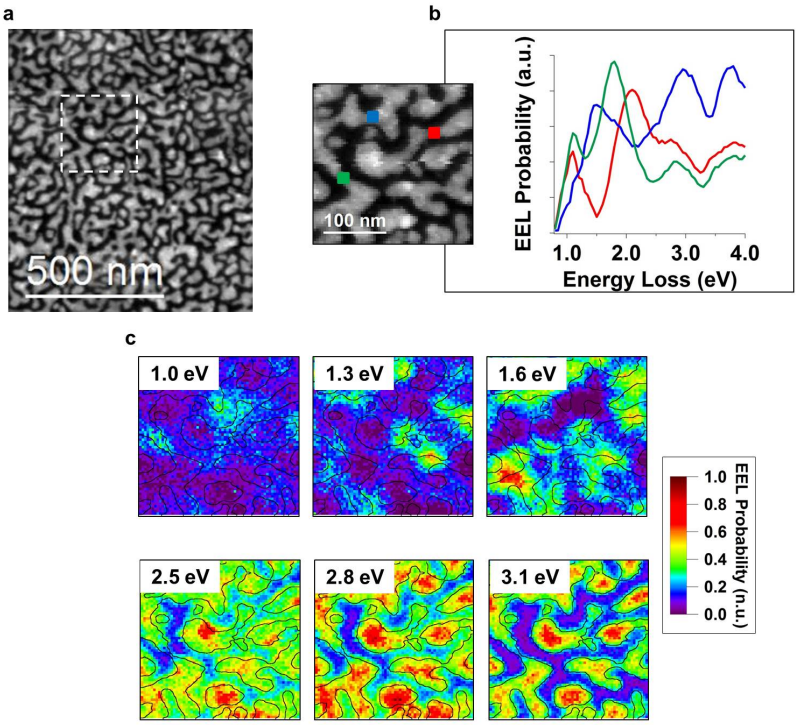


Figure 3: Expériences d'EELS résolues spatialement sur un film semicontinu d'argent situé autour du seuil de percolation. a) Images HAADF du système considéré à différentes magnifications. b) Spectres EEL obtenus pour une sonde électronique incidente focalisée sur des positions aléatoires séparées de 100 nm. c) Variations spatiales du signal EELS à six valeurs d'énergie différentes.

quelconque, comme le montrent les cartes filtrées données en figure 3c. Nous avons sélectionné six valeurs d'énergie, les trois premières étant plutôt situées à basse énergie, les dernières se rapprochant des hautes énergies. A basse énergie, on aperçoit de nombreux maxima locaux situés de façon aléatoire à des positions très dépendantes de l'énergie. Ce comportement singulier à basse énergie rappelle les prédictions théoriques concernant les HS. Cependant, à haute énergie, tous les maxima locaux sont localisés sur les particules métalliques quelle que soit l'énergie à laquelle on les observe. Ceci démontre que les HS, tels que prédits initialement, n'existeraient qu'à basse énergie. Nous allons par la suite nous attacher à décrire les modes SP responsables de telles observations.

## Modes SP de type aléatoire à basse énergie

Avant de discuter les modes SP à proprement parler, il faut souligner qu'une interprétation en terme de modes nécessite une procédure de fits multipics propres à démêler les modes les uns les autres s'ajoutant de façon incohérente sur une carte filtrée à énergie fixée. Si l'on étend la théorie donnée dans la partie précédente à une structure quelconque, on peut voir l'énergie centrale, la demi largeur à mi hauteur (FWHM) et l'amplitude de chaque pic apparaissant dans un spectre EEL

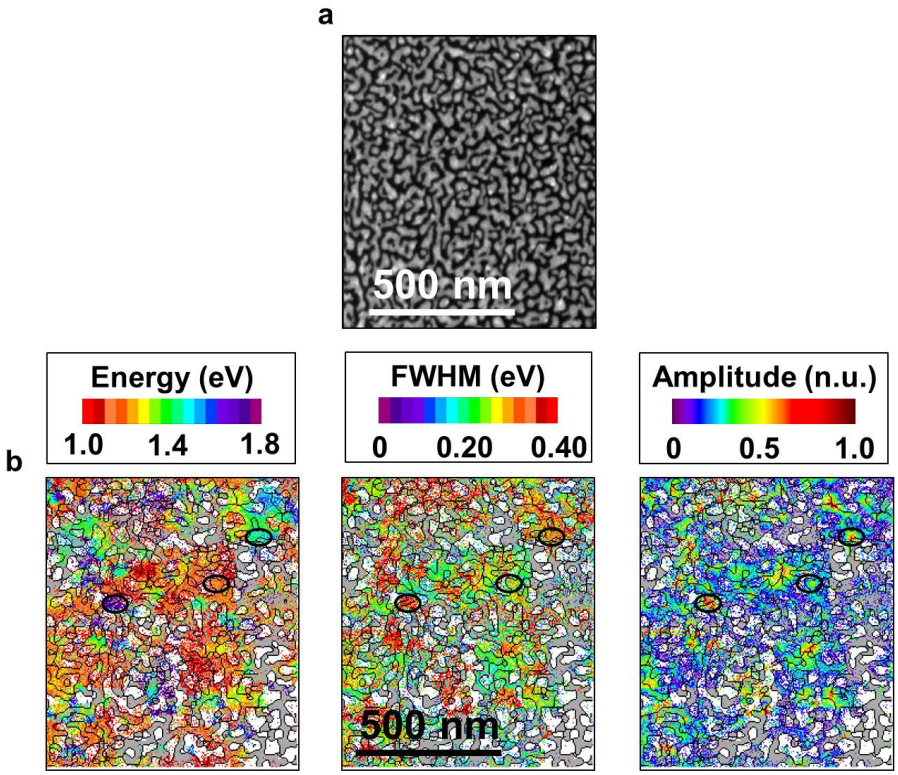


Figure 4: Cartographie des modes SP d'un milieu semicontinu autour du seuil de percolation. De gauche à droite: cartes d'énergie, FWHM et amplitude des pics trouvés à basse énergie dans chaque spectre acquis dans la zone introduite précédemment. Les cercles noirs soulignent trois modes SP différents. Dans le cas où aucun pic n'a été trouvé dans cette gamme d'énergie dans un spectre, son pixel correspondant est colorié soit en blanc si le matériau sondé localement est métallique, soit en gris si le matériau sondé localement est diélectrique.

donné comme une énergie propre, un taux de le relaxation (convolué par la résolution spectrale finie de la technique) et une intensité associée à la composante du champ électrique parallèle à la trajectoire des électrons d'un mode SP excité localement à la position de sonde correspondante. La figure 4 montre des cartes d'énergie, FWHM et amplitude des pics trouvés dans chaque spectre à basse énergie, obtenues en réassignant chaque valeur correspondant à un pic à sa position de sonde correspondante. De nombreux maxima locaux sont visibles sur la carte d'amplitude (par exemple, ceux soulignés par des cercles noirs). Si l'on compare les trois cartes, on peut voir que chacun de ces maxima locaux peut s'associer à une énergie et FWHM de pic constante sur les cartes d'énergie et FWHM. Cette observation valide bien l'interprétation proposée ci-dessus: chaque maximal local peut être vu comme un renforcement local du champ électrique d'un mode SP, d'énergie propre et de taux de relaxation (élargi) donnés par les énergies et FWHM de pic constantes. En distinguant ces modes les uns les autres selon cette énergie propre et ce taux de relaxation, on en conclut donc (voir par exemple les trois modes mis en évidence sur la figure) que le spectre d'excitations se compose d'un fort nombre de modes ayant la particularité d'avoir des énergie propres très proches, d'être

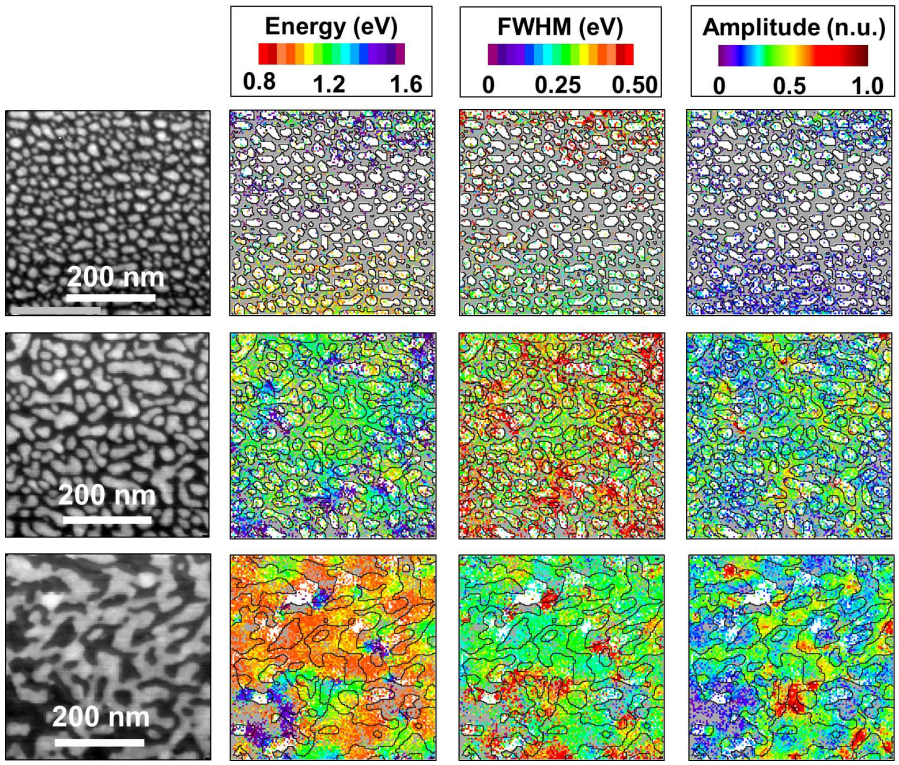


Figure 5: Modes SP de films semicontinus de fraction métallique croissante vers le seuil de percolation. A gauche: images HAADF des trois systèmes considérés. A droite: cartes d'énergie, FWHM et amplitude des pics trouvés à basse énergie dans chaque spectre acquis dans chaque zone. Dans le cas où aucun pic n'a été trouvé dans cette gamme d'énergie dans un spectre, son pixel correspondant est colorié soit en blanc si le matériau sondé localement est métallique, soit en gris si le matériau sondé localement est diélectrique.

fortement confinés spatialement et de ne montrer aucune corrélation triviale avec la géométrie du milieu. La coexistence de ces nombreux modes induirait non seulement la présence de HS, une fois le milieu soumis à une onde lumineuse, mais également des propriétés d'aborption de lumière large bande dans l'IR.

Des études supplémentaires menées avec un STEM monochromaté offrant une résolution spectrale supérieure ont permis de conclure que les modes étaient localement confinés sur des aires typiques inférieures à 100 $nm^2$, ce qui les font s'éloigner des modes SP classiques de nanoparticules métalliques. Cependant, une étude de leur taux de relaxation a permis de montrer que leur temps de vie était relativement court, comme on le retrouve également pour des nanoparticules uniques de formes simples. Hormis cette similarité et vu leur caractère autrement singulier, nous nous référerons à eux en tant que "modes de type aléatoire". Nous allons dans la suite démontrer que ces modes de type aléatoire sont en réalité liés à la géométrie fractale du milieu.

## Modes SP de type aléatoire et géométrie du milieu

Nous présentons ici le résultat principal d'une étude systématique de l'effet de la géométrie du système sur les modes SP de basse énergie. La figure 5 montre les images HAADF (à gauche) de plusieurs films semicontinus de fraction métallique croissante, ainsi que les cartes d'énergie, FWHM et amplitude des pics trouvés à basse énergie dans chaque spectre enregistré durant des expériences d'EELS résolue spatialement effectuées au sein de chaque zone. Il est bien connu (et a dans notre cas été vérifié) que les trois systèmes considérés se distinguent par une progressive complexité géométrique, le premier système étant composé d'un ensemble de nanoparticules isolées Euclidiennes, et le dernier consistant en un cluster de type percolant fractal. Les cartes issues des expériences d'EELS résolues spatialement démontrent une complexité du spectre d'excitations croissante, synonyme d'apparation progressive de modes SP de type aléatoire. Non seulement les modes s'étendent dans l'IR, mais leurs champs électriques associés ont des intensités locales de plus en plus fortes. Nous en déduisons donc que les modes SP de type aléatoire sont liés à la géométrie fractale du milieu qui les soutient, comme initialement proposé lors de la prédiction théorique des HS.

## Conclusion

Grâce à des expériences d'EELS résolues spatialement, nous avons observé de fortes variations spatiales et spectrales du signal EELS, à basse énergie et autour du seuil de percolation. Nous avons relié ce comportement singulier à un spectre d'excitations complexe composé de nombreux modes SP fortement confinés, d'énergies propres très proches et ne montrant aucune apparente corrélation avec la géométrie du substrat. Contrairement à un temps de vie très court, ces caractéristiques les font différer par nature des modes SP soutenus par des nanoobjets métalliques de forme simple. La comparaison de différents systèmes a permis de conclure que ces modes de type aléaoire étaient en outre induits par le caractère fractal d'un film semicontinu autour du seuil de percolation.

En conclusion, nous avons tout d'abord adressé la problématique de l'interprétation d'un signal EELS ou CL obtenu lors d'une expérience de spectroscopie d'électrons rapides résolue spatialement. Une fois celle-ci établie, aussi bien de façon expérimentale que théorique, nous avons fait appel à elle pour interpréter des résultats expérimentaux obtenus sur des systèmes célèbres dans la communauté de la nanooptique de par leur complexité. Nous avons ainsi pu obtenir de nouvelles connaissances sur les modes SP des systèmes en eux- mêmes, inaccessibles aux techniques d'optique en champ proche usuelles. Il est clair que les techniques de spectroscopie d'électrons rapides résolues spatialement constituent un atout pour l'étude des modes SP de nanosytèmes composé de métal et de diélectrique. D'autres exemples, ainsi que les références adéquates, peuvent être trouvées dans le manuscrit.

# Contents

# Introduction

Various light phenomena at the nanoscale studied in nano-optics rely on the elementary optical excitations of nanostructures [1]. In particular, plasmonics and all its related phenomena [2,3] bases on Surface Plasmon (SP) modes. In a fully retarded classical electrodynamics approach, SP modes can be seen as electromagnetic surface eigenmodes related to collective oscillations of the conduction electrons at the surface of a metal [4,5]. Similar to plane waves in infinite media, the number of SP modes sustained by an infinite boundary is limitless. However, in confined[9] systems or, otherwise speaking, metallic resonators, SP modes acquire some resonant properties [6]. In particular, a metallic nanoparticle sustains a finite set of modes, each one having its own eigenfrequency. These modes do not have infinite lifetimes. On the contrary, they remain highly damped due to multiple radiative or non-radiative decay channels. A relaxation, or dephasing rate, can thus be attributed to each mode. These spectral characterics depend on the geometry, dimensions and constitutive material of the system [7,8]. The simplest example would be a metallic sphere, whose SP modes are the so-called normal modes introduced by Mie [9]. It is, for instance, well known that, for a given mode, the eigenfrequency decreases and relaxation rate increases when the radius of the sphere increases [10]. For a gold or silver sphere whose size is on the order of 100 nm, the eigenfrequencies fall within the visible range. In this case, the optical properties of the nanoparticle, governed by the SP modes, are resonant in the visible range. Characterizing a mode spectrally can thus be done by measuring some center frequency [11] and spectral width [12] of the SP mediated resonances measured through absorption, extinction or scattering spectroscopy techniques, which can today probe a single particle with no inhomogeneous broadening [13].

SP modes of confined systems are well known to provide an efficient way of concentrating electromagnetic energy at very small scales, well beyond the diffraction limit. The strong field enhancement at the immediate vicinity of a metallic nanoobject induced by the scattering of a plane wave by the object is the basic principle of an optical nanoantenna [14], which introduces numerous potential applications in nanophotonics [15]. It turns out that this field enhancement is mediated by the SP modes of the object, most particularly by their strongly confined electric fields. Therefore, characterizing a mode spatially should be done by observing its electric field at the nanoscale [16]. Despite the spectral information they bring, optical techniques cannot offer such required spatial resolution, because of the diffraction limit. Scanning Near Field Optical Microscopy (SNOM) [17] paved the way for a subwavelength investigation of the optical properties of metal nanoparticles [18]. However, the spatial resolution was at that time limited to almost 100 nm. Moreover, most of the SNOM studies which followed focussed on near-field imaging using monochromatic laser excitation rather than subwavelength spectroscopy using a broadband source

[9] Here, "confined" should not be understood as "quantum confined". All the systems we will be concerned have minimum dimensions on the order of an optical wavelength, and are thus governed by electromagnetic effects.

[19]. However, valuable alternatives rely on the use of fast electrons as a source of excitation [20]. In particular, the electron beam of a Scanning Transmission Electron Microscope (STEM) acts both as a wave packet of picometric wavelength and a white light source to locally excite a sample [21]. It thus acts as a local probe for the numerous SP modes of a metal-dielectric system, with a spatial resolution only limited by the aberrations of the electron optics, and which can now reach the atomic scale. Over the past few years, Electron Energy Loss Spectroscopy (EELS), which probes the energy lost locally by the fast electrons by some inelastic scattering event, and Cathodoluminescence (CL), which detects the light emitted subsequently, have been shown, when performed in a STEM (STEM EELS, STEM CL), to "map" the SP modes of simple metallic nanoparticles with nanometric spatial resolution over a broad spectral range [22]. Such experimental evidence have required new theoretical developments to explain the underlying physical processes.

Even before considering the interaction processes between the fast electrons and the sample, which can be well accounted for by a classical electrodynamics theory [20], a great conceptual difficulty arises when trying to define a SP mode in an arbitrary system. Indeed, a SP mode is an electromagnetic eigenmode[10], or, otherwise speaking, a fundamental solution of the Maxwell equations with zero external source term. For a generic system, the Maxwell equations cannot be developped into an universal eigenvalue equation involving Hermitian operators. Therefore, the SP modes are only known in highly symmetric systems, such as nanospheres or nanowires [23]. On the other hand, a SP mode can be defined in a generic metal-dielectric system when using the quasistatic approximation, which neglects retardation effects within the Maxwell equations, and can be calculated numerically for an arbitrary structure [24–26]. The quasistatic approximation is known to be strictly valid only for systems whose dimensions are much smaller than the wavelength of light [27]. It thus often has the reputation for greatly underestimating the complexity of the problem for systems of dimensions on the order of hundreds of nanometers [28]. However, in the absence of any universal definition of a SP mode in a complete relativistic and dissipative approach, the quasistatic approximation is very welcome to intuit physical phenomena, yet it should be used with care. As an (extreme) example, the quasistatic approximation has been used on random metal-dielectric systems to interpret well-known singular optical properties [29]. Such systems are most probably one of the (if not the) most complicated systems involving SP modes. Their great complexity makes any intuitive picture of the modes difficult. Precisely, any prediction about the eigenfrequency, relaxation rate and electric field pattern of a mode, all of these features being now well understood for simple nanoobjects [30], is delicate to infer. As an example, their localized character, a typical disorder induced effect, has been questionned even in the absence of retardation [31–34].

The Electromagnetic Local Density of States (EMLDOS) [35] has been proposed as a first step towards a universal interpretation of STEM EELS in terms of electromagnetic eigenmodes of the sample and their intrinsic features [36]. A quasistatic SP modal decomposition of the EMLDOS in a generic metal dielectric provided further understanding on the experimental results obtained with STEM EELS on metallic nanoparticles [37]. These findings synthesized and generalized previous experimental observations made on "ideal", i.e., highly symmetric [38], or more complex [39] nanoobjects. Moreover, they offered a strong theoretical justification that STEM EELS is a much relevant technique to properly identify the SP modes of some arbitrary metal-dielectric system through some intrinsic features [40–42]. Yet it has been shown to provide very similar results on simple systems [43], such an interpretation has not been extended so far to STEM CL for nanoparticles. Nevertheless, STEM CL was mentioned, although no theoretical derivation was proposed,

[10] An equally valuable denomination would be, to draw a parallel with quantum mechanics, an eigenstate.

to measure a radiative EMLDOS (rEMLDOS) in extended systems [44].

This manuscript illustrates this ability of fast electron based spectroscopies to reveal the SP modes in metallic nanosystems. We will adress two different systems of gradual complexity. The first system will be a model system, namely, a metallic triangular nanoprism, whose SP modes have been extensively studied in the litterature, including with fast electron based spectroscopies [38,40,45–52]. The second system will be a random metal-dielectric system, whose SP modes are, on the contrary, highly problematical [31–34]. On the first system, we will propose a link between fast electron based spectroscopies and optical spectroscopies that make use of the concept of quasistatic SP modes. Precisely, we will show that EELS and CL can be seen as some respective nanometric equivalent of extinction and scattering spectroscopies. On the second system, we will show what insight can be gained on rather unknown SP modes by using STEM EELS. In particular, disorder effects on SP modes will be studied.

In chapter 1, we will briefly expose basic principles of STEM EELS and STEM CL. In chapter 2, we will recall the theoretical foundations necessary to adress the key results of this thesis. In chapter 3, the experimental techniques will be presented in more details. Finally, chapters 4 and 5 are devoted to present the significant original results obtained on the metallic triangular nanoprisms and random metal-dielectric media. Finally, chapter 6 presents some additional preliminary results related to these topics, which may lead to complete studies in a more or less close future.

The most significant results presented in this manuscript and due to the author himself can be listed as follows. On the experimental side:

1. The first combined STEM EELS and CL measurement on a single metallic nanoparticle is reported. It is evidenced that EELS and CL probes the SP modes of a metal-dielectric system through slightly shifted resonances.

2. The first STEM EELS measurements on semicontinuous metallic films with varying metallic filling fractions are reported, leading to the evidence of extraordinary random-type SP modes induced by the fractal geometry in percolating metal films at low energies.

On the theoretical side, modal decompositions of CL, extinction and scattering are derived in the quasistatic approximation using a Boundary Element Method (BEM) framework. When compared to their well-known EELS counterpart, this formalism provides a convenient way to:

1. explain the experimental observations of combined STEM EELS and CL experiments.

2. establish a parallel between fast electron based and optical spectroscopies, most particulary between EELS and extinction spectroscopy on the one hand, CL and scattering spectroscopy on the other hand.

Other "secondary" yet important implications of these results are:

1. the distinction evidenced between extinction and scattering cross section resonances.

2. the proof of a deviation of SP modes in gold nanoparticles from the highly used damped oscillator models.

3. the prediction of the appearance of singular "Hot Spots" (HS) in semicontinuous metal films only at low energies around the percolation threshold.

4. a theoretical background to directly interpret CL, extinction and scattering spectroscopies through the SP modes of a system.

The original character of this work mostly relies on the following points:

1. A parallel is drawn between EELS and extinction spectroscopy on the one hand, CL and scattering spectroscopy on the other hand.
2. Experimental data on semicontinuous films is directly and precisely interpreted in terms of the SP modes of the system.

All the theoretical expressions derived from the Maxwell equations use the CGS gaussian unit system.

# Chapter 1

# Fast electron based spectroscopies

## 1.1 Basic principles

Fast electron based spectroscopies rely on the interaction of relativistic electrons with a sample. To be more specific, their velocity is on the order of a fraction of the speed of light. This interaction results in a number of useful signals that can be recorded using various detectors. These signals inform on the material exposed to the electrons. Precisely, the latter act like a probe for studying the optical and electronic properties of the sample. The crucial advantage of using fast electrons to investigate matter relies on their small de Broglie wavelength, allowing restricting the size of this probe to very small dimensions. The Scanning Transmission Electron Microscope (STEM), which will be described bellow, directly makes use of this capability to extract very local information about the sample. Its basic principle of operation is shown on figure 1.1. A STEM is a very versatile tool which allows various studies in multiple science domains using numerous techniques. Without pretending to make a complete list of the capabilities of a STEM, this section emphasizes its use for performing spatially resolved spectroscopies. A more complete review can however be found for example in [21].

The interaction of relativistic electrons with a sample implies some scattering process. Fast electron based spectroscopies aim at interpreting this scattering process by collecting some useful information. A given scattering process affects the incoming electrons that transfer a corresponding amount of momentum and energy to the sample. As a consequence, the transmitted electrons are generally deflected from their initial trajectory and slowed down. In parallel, the excited sample tends to return to equilibrium by losing its freshly gained energy and momentum. The useful information is thus inscribed either in the transmitted electrons or, possibly, in some detectable signal resulting from some decay channel as, for example, the emission of photons.

We make conveniently a distinction between elastic and inelastic scattering processes. Elastic scattering only involves transfers of momentum to the sample. The elastically transmitted electrons are used to gain insight about the local morphology of the sample. On the other hand, inelastic scattering involves some transfer of momentum and energy to the sample. The inelastically transmitted electrons and possibly emitted electromagnetic radiation inform about the electronic or optical properties of the sample. As the incoming electrons are relativistic, a broad range of excitations, from core level excitations to valence excitations, can be studied. All along this thesis we will deal with valence excitations, which dominate the optical response of the sample. They

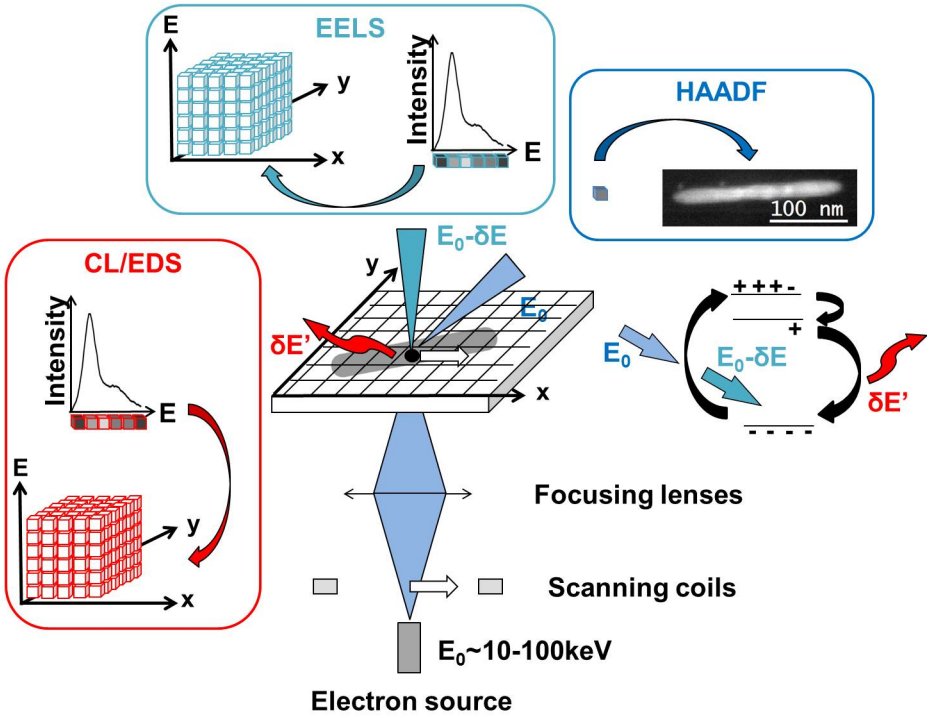


Figure 1.1: Scanning Transmission Electron Microscopy. A fast electron beam extracted from an electron source is focussed by a set of magnetic lenses onto a tiny area of a thin sample. The transmitted electrons elastically scattered at high angles are collected for HAADF imaging. The transmitted electrons inelastically scattered are collected for EELS. The light coming from the sample is collected for CL or EDS. Spatially resolved spectroscopies can be performed by deflecting the incoming electron beam using magnetic coils, allowing the acquisition of very local information over a large area by scanning the probe over the sample.

are hence commonly referred to as "optical excitations". The optical excitations include collective charge oscillations (plasmons, surface plasmons), collective lattice oscillations (optical phonons, surface phonons), single electron excitations (intraband transitions, interband transitions), excitons... For a complete theoretical review on optical excitations in the framework of fast electron based spectroscopies, we refer the reader to [20]. On the other hand, fast electrons can also be used to study core excitations, which dominate the electronic structure of the material constituting the sample. We refer the reader to the review given, for instance, in [53].

In a STEM, the energetic electron beam extracted from an electron source is focussed by a set of magnetic lenses onto a tiny area on a thin sample (see figure 1.1). The transmitted electrons elastically scattered at high angle are collected for High Angle Annular Dark Field (HAADF) imaging. The collected intensity is a monotonic function of the local material density projected along the electron beam, which includes the mass and atomic number of the illuminated constutive atoms. The information gained from such quantity thus informs directly about the local morphology of the sample. In parallel, the electrons inelastically scattered contribute to multiple spectroscopy techniques. Electron Energy Loss Spectroscopy (EELS) can be performed by analyzing the energy

lost by the transmitted electrons inelastically scattered at low angle. A thorough review of EELS can be found in [53]. Moreover, Cathodoluminescence (CL) [54] or Energy Dispersive Xray Spectroscopy (EDS) [55] can be achieved by analyzing the electromagnetic radiation coming from the sample. In the absence of any restriction on the energy lost by the electrons to the sample, an EEL spectrum extends from the InfraRed (IR) to the X-Ray range, thus allowing the study of optical excitations as well as core-level excitations. This is, however, not the case for CL and EDS spectra, which require the use of dedicated detectors and are respectively restricted to the optical and X-Ray ranges. Very often, EELS is devided into two "sub-spectroscopies", each one being devoted to the study of a given type (ie. optical or core-level) of excitations. Valence (also commonly referred to as "low-loss") EELS covers the so-called low-loss spectral range which extends from the IR to the UltraViolet (UV) while core-loss EELS covers the core-loss spectral range extending in the X-rays.

Importantly, spatially resolved spectroscopies can be performed by deflecting the incoming electron beam using magnetic coils. It thus allows the acquisition of very local information over a large area by scanning the probe over the sample. All the signals are collected simultaneously so that they may be safely compared for a given probe position. After a complete scan, the HAADF intensity recorded locally is assembled into an HAADF image of the scanned area. The HAADF image allows safe and direct access to the whole sample morphology. On the other hand, each spectrum is stored, probe position per probe position, into the rows of a three dimensional datacube that contains the full spectroscopic local information of the scanned area [56]. EELS and CL/EDS datacubes are shown on figure 1.1. Each row corresponds to a given spatial coordinate of the probe over the sample (x,y). Processing the datacube allows accessing, probe position per probe position, to the recorded signal within the whole spectrum. This is the basis of hyperspectral imaging, whose principle is sketched on figure 1.2. In this illustrative case, the datacube, commonly referred to as "Spectrum Image" (SI) [57], and the HAADF image are obtained from spatially resolved valence EELS (STEM EELS) measurements performed on a gold nanowire. The HAADF image of the scanned area is shown at the top right of the figure. In such an image, the nanowire appears bright over a dark background. The SI is three dimensional and can be manipulated in multiple ways. Two directions are the spatial coordinates of the probe over the sample (x and y) and the third direction is the energy lost by the electrons of the probe (E). Local EEL spectra are obtained by filtering the SI in the (x,y) direction. For example, the local spectra A and B correspond to the spectra recorded at the probe locations A and B indicated on the HAADF image. On the other hand, the local variations of the spectral intensity can be mapped at a given energy loss value by filtering the SI in the E direction. The maps displayed at the bottom of the figure, often called "energy filtered maps", show the spatial variations of the intensity at the energy loss values E1 and E2 corresponding to the resonances appearing within the local spectra A and B. The interpretation of such maps in the case of valence excitations will be the topic of the next chapter. For a general review of the broad capabilities of STEM EELS, see [56]. The spatial resolution of the technique is dictated by the probe size, which may ultimately reach the diffraction limit, that is, 1 pm for the range of energy we will consider. However, this size is in practice much limited by the aberrations of the probe forming lens system. Nowadays, they can be partially compensated by the use of aberration correctors which allow reaching atomic resolution. With no such optional component, the probe size is on the order of a few angstroms. The main strength of the technique is that, thanks to such a small spatial resolution, local spectra can be acquired at very small scales with no inhomogeneous broadening. Therefore, spatially resolved fast-electron based spectroscopies allow good spectral resolutions that take advantage of very high spatial resolutions.

Valence EELS and CL profit from the advantageous spatial resolution offered by the STEM for

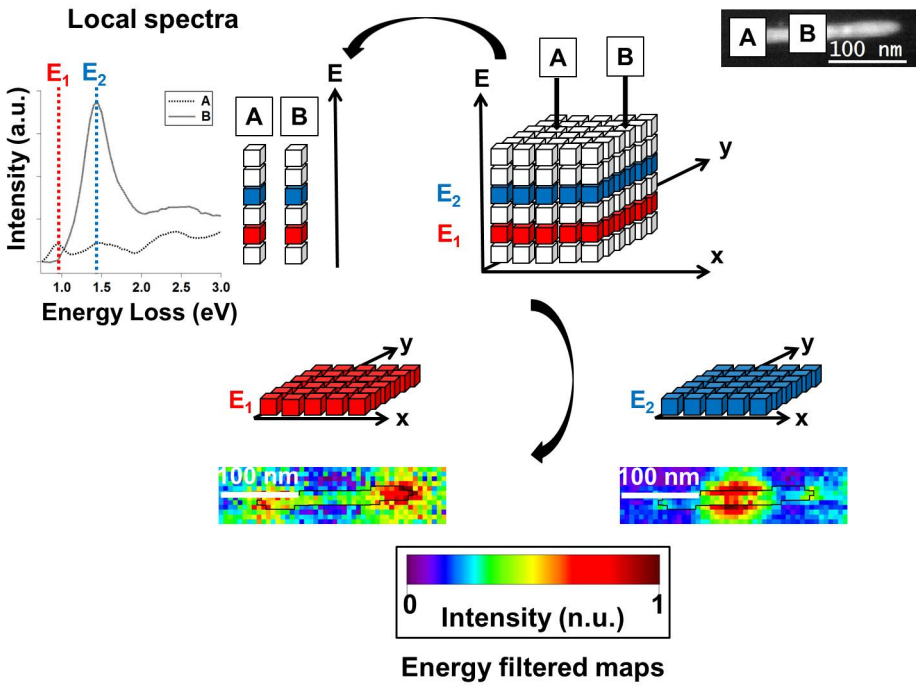


Figure 1.2: Hyperspectral imaging principle. Top right: HAADF image of a gold nanowire. Local EEL spectra are obtained by filtering the SI in the (x,y) direction. On the other hand, the local variations of the spectral intensity can be mapped at a given energy loss value by filtering the SI in the E direction to build energy filtered maps.

studying the optical response of samples requiring nanometric spatial resolutions, such as metal nanoparticles, quantum emitters, layered structures, photonic crystals or dielectric microcavities. A tutorial review can be found in [22]. Valence EELS and CL will be the topic on the next sections. On the other hand, core-level excitations are now routinely studied at the atomic scale using electron microscopes equipped with aberration correctors. The results obtained in core-loss EELS or EDS thus provide information on the local chemistry, bonding and electronic structures at the scale of the probed atoms. As this thesis focuses on valence excitations, core-loss EELS and EDS will not be adressed anymore. However, the reader can find additional information on this topic in the devoted chapters of [21].

## 1.2 Valence EELS

Valence EELS aims at studying the optical response of a specimen at the nanometer scale by, as already pointed out, analyzing the energy lost by the electrons inelastically scattered. The basic physical principle is simple (see figure 1.1): the incoming electrons which contribute locally to an excitation of energy $\delta E$ lose the corresponding amount of kinetic energy $\delta E$. Accessing the

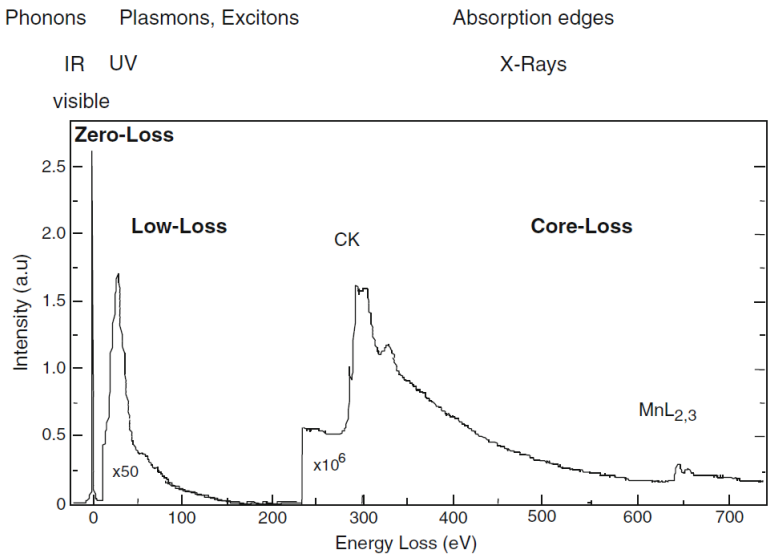


Figure 1.3: Typical EEL spectrum, extracted from [56]. The ZLP dominates the spectrum at zero energy loss. At higher values of the energy loss in the low-loss region, resonances appear due to valence excitations. At much higher energies in the core-loss region, resonances from core level excitations emerge to a much lesser extent.

energy lost by the electrons after they go through the sample, as is done in valence EELS, thus allows recovering the energy characteristics of the excitation. Very intuitively, valence EELS can hence be regarded as the nanometric equivalent of Raman spectroscopy, which permits studying low energy excitations of solids such as phonons or magnons, except that $\delta E$ extends from the near-IR to the UV range. Valence EELS has been extensively used to study the bulk optical properties of materials by measuring their dielectric functions or surface effects through the excitation of surface modes [58]. Nowadays, it is more largely applied to the study of metal nanoparticles, for which the combined nanometric spatial resolution and broad spectral range have proven to be strong advantages with respect to common optical techniques, such as extinction spectroscopy or Scanning Near Field Optical Microscopy (SNOM) [59]. Valence EELS is not only performed in STEM but also in Transmission Electron Microscopes (TEM), whose operation mode can noticeably differ from the STEM mode depicted on figure 1.1. We redirect the interested reader to a comparative study of surface plasmons using TEM and STEM EELS [48].

With regards to the broad possibilities of EELS, the spectral range of valence EELS is very limited. A typical EEL spectrum is shown on figure 1.3. As clear from this example, a very intense peak dominates the spectrum at zero energy loss. This is the so-called "Zero Loss Peak" (ZLP), which accounts for all the electrons which have not been inelastically scattered. By saying this, we embrace the electrons that have not been scattered, those which have been scattered elastically as well as those that have been scattered quasi-elastically. The latter are electrons that have induced very low energy excitations, such as phonons, and whose energy is too small to be resolved when compared to the spectral resolution of the experiment. All these electrons contribute to the spectral width of the ZLP which turns out to spread quite far towards the visible range. At higher values of

the energy loss, resonances appear within the tail of the ZLP due to some inelastic scattering with optical excitations. Finally, at much higher energies, resonances from core-level excitations emerge to a much lesser extent. The low-loss and core-loss regions are traditionnally separated by a loss value of around 50 eV, which thus constitues an upper value for valence EELS.

In a quantitative way, valence EELS should measure the probability for an electron to lose a given amount of energy, often called "EEL probability". As a consequence, a spectrum has to be normalized with the number of electrons reaching the detector and the contribution of the electrons that have have not been inellastically scattered has to be removed. EEL probability spectra obtained in this way exhibit resonance peaks which, as compared to the physical widths induced by the finite lifetime of the valence excitations, are broadened by the finite spectral resolution of the technique.

## 1.3 CL

In relation to EELS, CL also aims at studying the optical response of a specimen at the nanometer scale by analyzing the light induced by the electrons inelastically scattered, and not directly the electrons inelastically scattered. The physical principle is thus a bit more complex (see figure 1.1): after the electron has induced some excitation of energy $\delta E$ within the sample, the sample releases some energy $\delta E'$ in the form of photons to return to equilibrium via a radiative decay channel. Accessing the energy of the emitted photons, as is done in CL, thus allows recovering the energy characteristics of the radiative decay channel, which can be different from the energy of the excitation if fast non-radiative decay channels are available. CL can hence be regarded as the nanometric equivalent of photoluminescence spectroscopy, often used for studying the band structure of semiconductors or insulators. The light emission processes can be distinguished from each other with their degree of coherence. Coherence implies conservation of energy and momentum between the excitation and the released photons. A typical example of incoherent emission is the indirect transition of an excited electron from the conduction band to the valence band in a semiconductor with indirect band gap. To take place, such a transition requires the involvement of phonons or some elastic scattering process to supply the momentum required, while the emitted photons only supply the necessary energy. On the contrary, collective charge excitations are insensible to the phonon bath, thus induce coherent emission. Coherent light emission induced by fast electrons is sometimes called "Electron-Induced Radiation Emission" (EIRE) [20]. Most of the time, CL is performed in Scanning Electron Microscopes (SEM), while it also extends to STEM. CL is widely used either in mineralogy or for studying the electronic band structures of insulators and semiconductors [54]. In this last domain, CL benefits from the large kinetic energy of the incoming electrons to induce high energy excitations difficult to probe in photoluminescence.

As compared to EELS, a CL spectrum has no ZLP, thus consists of free-from-background resonances resulting from the sample excitations. It typically only extends from the IR to the UV range. Quantitatively, CL should measure the probability for an electron to emit a photon of given energy following an interaction process with the sample. If the scattering process is elastic, this probability is thus commonly called "EIRE probability".

# Chapter 2

# Theoretical foundations

## 2.1 Introduction

SP modes and EELS share a long history. Indeed, SP modes were first introduced by Ritchie, who studied theoretically the energy lost by fast electrons passing through thin metal foils [60]. He predicted that the boundaries of the film would induce, in addition to the recently discovered bulk plasmon loss peak occuring at the bulk plasmon energy, an anomalous loss peak at a lower energy. He also intuited that the thickness of the film would strongly affect the energy of this low-lying loss event, which was later observed in the EEL spectra of aluminium films [61]. This brought conclusive evidence of the strong effect of the boundaries of the medium on this new solid-state excitation. The interpretation of the latter as a new mode of oscillation of the conduction electrons of the metal that has the peculiarity of being located at the surface of the metal was expressed by Stern and Ferrell [62], who introduced the term "SP". In so doing, they considered them as pure charge density waves confined at the surface of the metal and travelling parallel to it.

Later on, it was felt that STEM EELS could be used as a nanometric probe for revealing the SP modes of metal nanoparticles. On the experimental side, Achèche et al. [63], then Batson [64], observed loss peaks resulting from the interaction of the fast electrons with metallic spheres. The spectral shifts of the resonance energies they evidenced were also observed later on small semiconducting spheres by Ugarte et al. [65]. Such findings were successfully accounted for by the quasistatic dielectric theory of Ferrell and Echenique [66], which was later extended to retarded regimes by García de Abajo [67]. These works helped at interpreting the resonances in EELS as the result of the excitation of the classical surface modes of the sphere, introduced by Mie in the case of metals [9] before being extended to dielectrics by Fuchs and Kliewer [68]. At that time, however, low energy surface modes, such as SP modes of silver or gold spheres, could not be observed experimentally due to the combined high spectral and spatial resolutions required.

More recently, soon after the experimental evidence by Khan et al. of 1 eV energy loss peaks in silver particles with a 10 nm spatial resolution [69] and simultaneously to a similar work performed by Bosman et al. [70], Nelayah et al. took profit of new instrumental and methodology advances to perform spatially resolved EELS on silver equilateral triangular flat nanoprisms [38]. Their main observations are summarized on figure 2.1. The HAADF image of the sample is shown on figure 2.1a. In such an image, the silver nanoprim appears bright over a dark background. Notice that the nanoprism has very small dimensions, namely an edge side of 78 nm and a thickness of 10 nm. The

EEL spectra recorded at different probe locations are shown on figure 2.1b. As obvious from these spectra, the recorded spectroscopic signal strongly depends on the position of the electron probe. Precisely, well defined resonances, absent in vacuum (spectrum D), appear in the EEL spectra when the probe is located at various points on the nanoprism. Three single yet different resonances dominate the spectra for an excitation probe located at the tip (spectrum A, resonance energy 1.75 eV), at the edge (spectrum B, resonance energy 2.70 eV) and at the centre (spectrum C, resonance energy 3.20 eV) of the nanoprism. Thanks to the STEM EELS technique, the authors were able to map spatially the EEL probability at given energy. The energy filtered maps shown on figure 2.1c display the spatial variations of the EEL probability at the three resonance energies. Strikingly, the EEL probability spatial variations form very peculiar standing wave patterns depending on the energy. Precisely, local maxima in the EEL probability are found at the three tips (1.75 eV), at the three edges (2.70 eV) and at the center (3.20 eV) of the nanoprism. Such results mean that fast electrons are most likely to lose some precise amounts of energy when they are directed to particular nanometric locations around the nanoparticle. These three maps were also interpreted as maps of SP modes.

The aim of this chapter is to precise and justify, step by step, this last statement by introducing the required theoretical notions and formalism. We will adopt this silver nanoprism as an illustrative example of a metal-dielectric system supporting SP modes. Although this example might appear very particular, much of what will be said, and, in particular, many of the theoretical derivations, can in principle be extended to any arbitrary finite system. We will clearly mention at specific points how much some notions can be understood as very general features. In particular, we are going to introduce very general concepts related to the excitation of SP modes by an electron beam and the induced loss of energy. In section 2.3, we will introduce the SP modes of confined metal-dielectric systems. In section 2.4, we will introduce the concept of EMLDOS and show how it can be precisely related to the SP modes of the system. In section 2.5, we will use these concepts to interpret the observations of figure 2.1. We summarize and generalize the main points in section 2.6. Finally, notice that although the starting point of this demonstration is the description of the interaction of fast electrons with matter using the framework of classical electrodynamics [20], an approach dating back to the work of Fermi [71], this chapter involves multiple recent theoretical developments which are still in progress at this time. In particular, we will rely on the close relationship between the EEL probability and the EMLDOS that was developped by García de Abajo and Kociak to explain the spatial modulations observed in STEM EELS measurements performed on arbitrary nanostructures, such as those shown on figure 2.1c [36]. The link between the EMLDOS and the SP modes of a small object was then established recently by Boudarham and Kociak [37], based on the BEM theory developped by García de Abajo and Aizpurua [72]. We thus use the EMLDOS, but recall that the work of Ouyang and Isaacson [73] already interpreted the energy loss between a fast electron and an arbitrarily shaped small particle as being the result of the excitation of the SP modes of the particle, yet with no use of such concept.

## 2.2 Methods

This whole chapter bases on the framework of classical electrodynamics, which requires as a first step to model the optical properties of a system similar to ours, namely, a finite system consisting in a nanoobject embedded in some matrix.

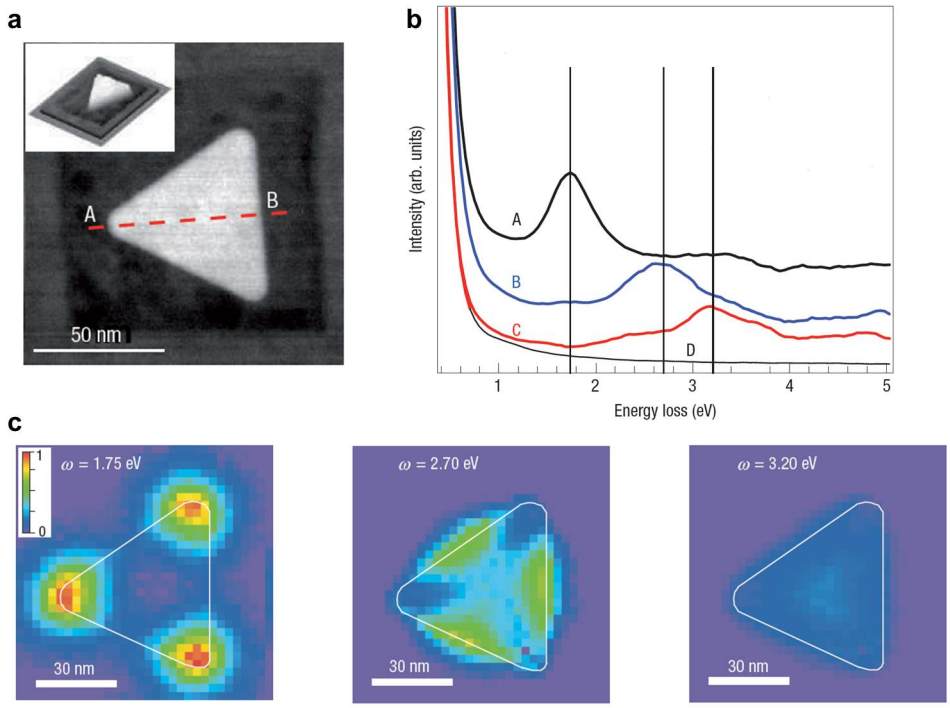


Figure 2.1: STEM EELS on a silver triangular flat nanoprism, extracted from [38]. a) HAADF image of the nanoprism. b) EEL spectra recorded for an electron probe located at the tip (spectrum A), at the edge (spectrum B), at the centre (spectrum C) and outside (spectrum D) the nanoprism. c) Energy filtered maps of the EEL probability for the energy loss values of 1.75 eV, 2.70 eV and 3.20 eV.

In the case of non-magnetic materials, the most accurate description of the optical properties of a solid relies in the use of a dielectric function $\varepsilon(\vec{k},\omega)$ in order to model its band structure [75]. In the linear response theory, the dielectric function links the Fourier transform of the displacement fields $\vec{D}(\vec{k},\omega)$ and the Fourier transform of the electric fields $\vec{E}(\vec{k},\omega)$ generated by a given external source through the expression:

$$\vec{D}(\vec{k},\omega) = \varepsilon(\vec{k},\omega)\vec{E}(\vec{k},\omega) \tag{2.2.1}$$

Such an expression implies that, in real space, the displacement field at a given point $\vec{r}$ and time $t$ depends on the value of the electric field at each time $t'$ preceeding $t$ and each point $\vec{r}'$ surrounding $\vec{r}$. Therefore, solving the Maxwell equations in this way generally turns out to be extremely complex, requiring the use of strong approximations. Significant simplication is achieved by using a local dielectric function $\varepsilon(\omega)$ verifying[1]:

$$\varepsilon(\omega) = lim_{\vec{k}\to 0}\varepsilon(\vec{k},\omega) \tag{2.2.2}$$

[1]This relation is the so-called local approximation, which reads in real space: $\varepsilon(\vec{r},\vec{r}',t,t') = \delta(\vec{r}-\vec{r}')\varepsilon(t,t')$ where $\varepsilon(\vec{r},\vec{r}',t,t')$ and$\varepsilon(t,t')$ are the inverse Fourier transforms of $\varepsilon(\vec{k},\omega)$ and $\varepsilon(\omega)$ .

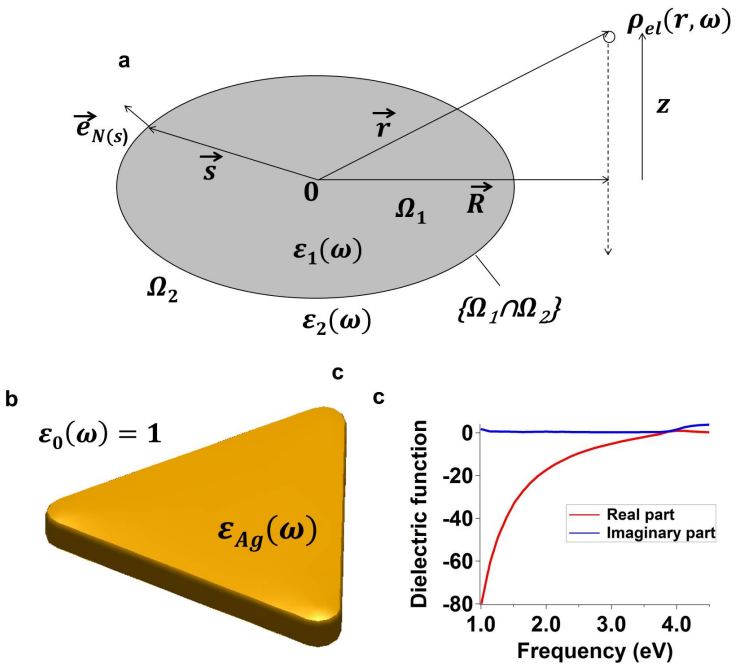


Figure 2.2: a) Schematic representation of a generic 3D system consisting in some object $\Omega_1$ of local dielectric function $\varepsilon_1(\omega)$ embedded in a matrix $\Omega_2$ of local dielectric function $\varepsilon_2(\omega)$. In this sketch, O denotes the origin of the vector space, $\vec{r}$ an arbitrary vector, $\vec{s}$ a vector pointing to the interface $\{\Omega_1 \cap \Omega_2\}$ and $\vec{e}_{N(\vec{s})}$ a normal unit vector located at position $\vec{s}$ on the boundary pointing outside the object. The fast electron whose trajectory along the z axis writes $\vec{r}_e(t) = \vec{R} + \vec{v}t = R\vec{e}_\perp + z\vec{e}_z$ enters the Maxwell equations through an external charge density current $\rho_{el}(\vec{r},t)$ in real space, or $\rho_{el}(\vec{r},\omega)$ in Fourier space. b) System modelled numerically: a silver nanoprism embedded in vacuum. c) Real and imaginary part of the local dielectric function of silver. Obtained from [74].

We can also consider our system as an heterogeneous system composed of homogeneous piecewise media separated by abrupt interfaces. The optical properties of the system can thus be described through a global frequency and space dependent dielectric function $\tilde{\varepsilon}(\vec{r},\omega)$, where:

$$\tilde{\varepsilon}(\vec{r},\omega) = \begin{cases} \varepsilon(\vec{r},\omega) & \vec{r} \in medium \\ \frac{1}{2}\left[\varepsilon(\vec{s} \to \vec{r}^{-},\omega) + \varepsilon(\vec{s} \to \vec{r}^{+},\omega)\right] & \vec{s} \in boundary \end{cases} \tag{2.2.3}$$

Such a model appears to be sufficient if the homogeneous piecewise media have dimensions much greater than the mean free path of the conduction electrons and the Fermi wave vector, in practice, if the typical dimensions of the media are superior to 10 nm. The systems we are considering here thus plainly justify the use of the above approximations. Otherwise, non-local effects must be included through the use of specific dielectric functions [76].

In order to give a global impact to the following derivations, we will consider a generic 3D finite system consisting in some object $\Omega_1$ of surface $\{\Omega_1 \cap \Omega_2\}$ embedded in a matrix $\Omega_2$, whose global frequency and space dependent dielectric function writes (see figure 2.2a):

$$\tilde{\varepsilon}(\vec{r},\omega) = \begin{cases} \varepsilon_1(\omega) & \vec{r} \in \Omega_1 \\ \varepsilon_2(\omega) & \vec{r} \in \Omega_2 \\ \frac{1}{2}\left[\varepsilon_1(\omega) + \varepsilon_2(\omega)\right] & \vec{r} \in \{\Omega_1 \cap \Omega_2\} \end{cases} \tag{2.2.4}$$

where $\varepsilon_1(\omega)$ and $\varepsilon_2(\omega)$ are some local dielectric functions. The media we will consider mostly are noble metals and dielectrics. The dielectric function of a noble metal can be obtained from reference measurements [74, 77]. For illustration, figure 2.2c shows the real and imaginary part of the dielectric function of silver, extracted from [74]. The non zero imaginary part of the dielectric function results in dissipation or absorption of electromagnetic radiation. In the case of noble metals, this dissipative character is due to various fundamental absorption processes, including intraband transitions, dominant in the IR range, to which interband transitions add in the visible range [78]. Such dissipative character will have important implications further. Ideally, noble metals can be described with the help of a simple Drude model. See appendix A for further information.

In the following, we will consider the mechanism of energy loss of a fast electron interacting with the system by considering the electron as a point-like external source, entering the Maxwell equations and moving along a time dependent trajectory $\vec{r}_e(t)$. If we assume that the loss of energy and momentum of the electron is small as compared to its initial energy and momentum, we may consider that the electron has a straight line trajectory with constant velocity $\vec{v}$[2]. Conveniently, we will define its direction as along a z axis, so that we can decompose its trajectory as: $\vec{r}_e(t) = \vec{R} + \vec{v}t = R\vec{e}_\perp + z\vec{e}_z$, where $\vec{v} = v\vec{e}_z$ is the velocity and $\vec{R} = R\vec{e}_\perp$ is the impact parameter of the electron.

The illustrations shown in this chapter have been performed from BEM numerical simulations performed with Ulrich Hohenester and Andreas Trugler's MNPBEM toolbox[3] [79]. Such a method allows solving numerically the Maxwell equations in frequency space in an inhomogeneous system similar to the system we described hereabove. To model the situation of figure 2.1, the calculations were performed for a nanoprism geometry. The dielectric function inside the nanoprism was taken from [74] to correspond to silver. The dielectric function outside the nanoprism was set to 1 to model vacuum (see figure 2.2b). See appendix A for further details.

## 2.3 Surface Plasmon (SP) modes

### 2.3.1 A complex problem

When introducing SP modes, a distinction is often made between a mode of a thin film, often called propagating SP, and a mode of particle, usually referred to as localized SP. The former is often adressed by deriving the electromagnetic surface eigenmodes of an infinite interface problem [4]. On the contrary, the latter is often adressed by deriving the fields scattered by a small sphere illuminated by a plane wave, which appear to be a superposition of the modes of the sphere[4] [6]. We can however draw a parallel between these two visions by noting that, in both cases, the modes are surface solutions[5] of the Maxwell equations with no external sources, expressed at each point

[2] This is the so-called "non-recoil approximation" [20].

[3] This Matlab toolbox is freely available at http://physik.uni-graz.at/~uxh/mnpbem/mnpbem.html. The (not yet open) version allowing EELS calculations has been used.

[4] The reason why only these two examples are examined is that they are part of the few highly symmetrical geometries for which analytical expressions exist.

[5] By "surface solutions", we mean that the electromagnetic fields are evanescent at both sides of the boundaries.

and time. Otherwise speaking, they are electromagnetic surface eigenmodes. It should be noticed that such surface electromagnetic eigenmodes are not found only in metal-dielectric systems. They can be sustained by any system presenting boundaries, at the condition that the media at both sides have appropriate dielectric functions[6]. In the case of metal-dielectric systems, these surface eigenmodes are associated to the collective oscillations of the conduction electrons at the surface of the metal, hence their definition as SP modes.

Ideally, one would like to extend this definition to a generic system, because it is clear that a continuum exists between these two types of modes. However, it turns out that determining the surface electromagnetic eigenmodes without neglecting retardation is extremely complicated and has been reported so far only for highly symmetric systems [23]. Therefore, the SP modes are often determined numerically when exciting the system with an external perturbation. A typical approach relies, for instance, on interpreting the resonance frequency of a calculated extinction spectra as the resonance frequency of a mode, and the electric field calculated at resonance as its electric field [7]. However, such a method eludes the fundamental, intrinsic character of the SP mode as an elementary excitation of the system.

On the other hand, surface eigenmode solutions of an eigenvalue equation can be calculated numerically in the quasistatic approximation. The quasistatic approximation thus allows to define a generic SP mode of a metal-dielectric system, an approach that has been previously used, among others, by Stockman [24,34], Mayergoyz [25] and Hohenester and Krenn [26], in the two latter cases based on the works by Ouyang and Isaacson [73] and García de Abajo and Aizpurua [72].

Even in the case of a simple nanoprism, retarded electromagnetic surface eigenmodes are delicate to obtain. A simple picture, however, can be drawn from the well known surface eigenmodes of infinite boundaries, only by noticing that the nanoprism is a flat film with some geometrical out-of-plane boundary conditions. We will present this simple, intuitive and very informative model first. We will then rely on the quasistatic approximation to extend our conclusions to an arbitrary small system. An extension to a true arbitrary system will then be assumed.

### 2.3.2 A simple picture

It is well known that the SP modes of simple nanoparticles follow clear trends with the size, constitutive metal and dielectric environment of the nanoparticle. As a matter of fact, a nanoprism, as a flat nanoparticle, is a perfect textbook case for explaining such statement. Well-defined trends with the edge length ad thickness of a nanoprism in the extinction spectrum resonances have been observed from calculations [80, 81], before being evidenced experimentally with optical spectroscopies [82, 83]. Associated to these resonances, calculations [7, 84] and SNOM experiments [85] resolved very characteristic electric field intensity standing-wave like patterns. Nelayah et al. synthesized these findings into a simple picture, that we reproduce here in order to give a simple, comprehensive definition of a SP mode of a finite system[7]. Notice that this definition is purely empirical and bases on the flat character of the nanoprism. It has been considered in flat systems in [49] and [86]. Such an approach is also very common for interpreting experimental results obained on 1 dimensional nanorods with optical spectroscopy [11], STEM EELS [87, 88], STEM CL [43] or other near-field techniques [89, 90].

[6] This is the case of, for instance, dielectric-vacuum systems, which support surface phonon modes [23].

[7] Precisely, they supported their assertion with the dependences of the EELS resonance energies with the size of the nanoprism. This last remark should be more understandable at the end of this chapter, when it will be shown that the EEL probability is resonant very close to the eigenfrequency of a mode. This interpretation was later extended to other modes in [49].

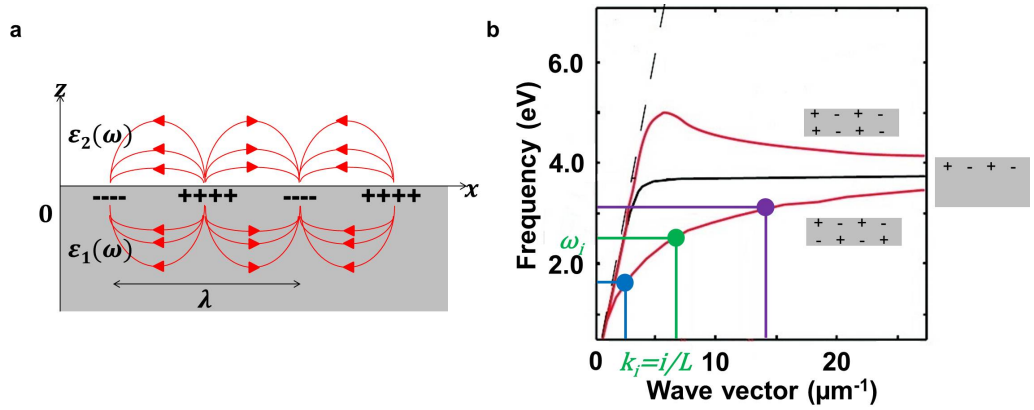


Figure 2.3: a) Surface eigenmode of a single interface. The interface separates two media of local dielectric functions $\varepsilon_1(\omega)$ (z<0) and $\varepsilon_2(\omega)$ (z>0) at the plane z=0. The electric field of the surface mode of frequency $\omega$ and wave vector $\vec{k} = k\vec{e}_x$ is plotted in red at time $t = n\frac{2\pi}{\omega}$, where $n$ is an integer. $\lambda = 2\pi/k$ is the wavelength of the eigenmode. The sign of the associated charge density is also added. b) Dispersion relation of SP modes (adapted from [40]). Red curves: SP modes of an infinite thin silver film with thickness 5 nm surrounded by vacuum. Black curve: surface eigenmodes of an infinite silver-vacuum interface. Black dotted line: transverse photonic modes in vacuum ("light line").

When introducing electromagnetic surface eigenmodes, the simplest example to be considered is a mode of an infinite plane interface. To begin with, we can thus consider an interface located at the plane z=0 separating two media of dielectric functions $\varepsilon_1(\omega)$ and $\varepsilon_2(\omega)$ (see figure 2.3a). The electric and magnetic fields of the surface electromagnetic eigenmode of wave vector $\vec{k} = k\vec{e}_x$ and frequency $\omega$ propagating along the interface towards the x direction write [5]:

$$\begin{cases} \vec{E}(\vec{r},t) = (1,0,-\frac{k}{\gamma_j})e^{-\gamma_j z}e^{i(kx-\omega t)} & z>0 \\ \vec{E}(\vec{r},t) = (1,0,\frac{k}{\gamma_j})e^{\gamma_j z}e^{i(kx-\omega t)} & z<0 \end{cases} \tag{2.3.1}$$

and:

$$\begin{cases} \vec{H}(\vec{r},t) = (0,-i\frac{\omega}{c}\frac{\varepsilon_j(\omega)}{\gamma_j},0)e^{-\gamma_j z}e^{i(kx-\omega t)} & z>0 \\ \vec{H}(\vec{r},t) = (0,i\frac{\omega}{c}\frac{\varepsilon_j(\omega)}{\gamma_j},0)e^{\gamma_j z}e^{i(kx-\omega t)} & z<0 \end{cases} \tag{2.3.2}$$

where $\gamma_j = \sqrt{k_i^2 - \varepsilon_j(\omega)\frac{\omega^2}{c^2}}$ and $Im(\gamma_j) > 0$ for $j \in \{1,2\}$. This second condition ensures that the electric and magnetic fields are evanescent at both sides of the interface, which is the main characteristics of a surface eigenmode.

As clear from these expressions, the fields are not continuous at the interface. There are thus a non-zero surface charge density and surface current density, respectively associated to the discontinuities of the normal electric displacement field and of the tangential component of the magnetic field:

$$\sigma(\vec{r},t) = -k(\frac{\varepsilon_1(\omega)}{\gamma_1}+\frac{\varepsilon_2(\omega)}{\gamma_2})e^{i(kx-\omega t)} \quad (2.3.3)$$

$$\vec{J}_s(\vec{r},t) = -i\frac{\omega}{c}\left(\frac{\varepsilon_1(\omega)}{\gamma_1}+\frac{\varepsilon_2(\omega)}{\gamma_2}\right)e^{i(kx-\omega t)}\vec{e}_x \quad (2.3.4)$$

As a consequence, a surface eigenmode can be equivalently viewed as an evanescent electromagnetic field or a surface charge density wave and surface current density field propagating along the interface. The electric field of a given surface eigenmode is shown on figure 2.3a, together with its associated surface charge density.

In the most general case, the electric and magnetic fields, or the surface charge and surface current, of a surface eigenmode are coupled through the Maxwell equations. However, if its wave vector and frequency verify:

$$k \gg \frac{\omega}{c} \quad (2.3.5)$$

the electric field of the eigenmode satisfies the relation:

$$\vec{\nabla} \times \vec{E}(\vec{r},t) \approx \vec{0} \quad (2.3.6)$$

which means that the magnetic field or surface current of the eigenmode is zero. Condition 2.3.6 is the quasistatic condition, which ensures that the fields are roughly electrostatic and can be determined from the Maxwell equations when neglecting the time derivatives of the fields. Condition 2.3.5 then delimits the so-called non-retarded region in ($\omega$,$\vec{k}$) space, where the eigenmodes can be known by solving the Poisson equation with no external source term. This constitutes the quasistatic approximation. In the non-retarded region the surface eigenmodes can be seen as pure electric fields or surface charge density waves. However, in the most general case, a surface eigenmode is a polariton, which is a mixed excitation between a surface charge density wave and a light wave.

The continuities of the tangential component of the electric field and of the normal component of the magnetic induction impose the dispersion relation:

$$k^2 = \frac{\varepsilon_1(\omega)\varepsilon_2(\omega)}{\varepsilon_1(\omega)+\varepsilon_2(\omega)}\frac{\omega^2}{c^2} \quad (2.3.7)$$

where $\omega$ can take any real value. We thus have a continuum of modes, resulting from the infinite dimensions of the system, which can be represented in ($\omega$,$\vec{k}$) space through some dispersion curves.

Let us now move closer to the situation corresponding to figure 2.1. We thus have to consider a metal-dielectric interface, whose surface eigenmodes are SP modes[8]. Figure 2.3b (black curve) shows the real part of $\omega$ as a function of real $k$ when $\varepsilon_1(\omega)$ is taken as the dielectric function of silver and $\varepsilon_2(\omega) = 1$. The complex character of $\omega$ results from the non zero imaginary part of the dielectric function of silver [91]. Therefore, a SP mode has a finite lifetime and is said either "pseudonormal" or "virtual" [23]. The real and imaginary parts of $\omega$ are respectively the eigenfrequency and relaxation rate of the SP mode. The relaxation rate is inversely proportional to the lifetime of the mode. At

[8] As already pointed out, SP modes were initially defined as pure charge density waves confined at the surface of the metal and travelling parallel to it [62]. The SP modes we define here are thus in accordance with this seminal description only in the non-retarded region. However, we here follow an extended definition very common in the literature [5].

low frequencies, the dispersion curve is close to the light line. In this region, the SP modes have a strong polaritonic character and are SP polaritons (SPP). On the contrary, the dispersion curve flattens at high frequencies until it follows an horizontal asymptote[9]. At high frequencies, the SP modes satisfy the quasistatic condition and are often called quasistatic SP.

In thin infinite films, the surface eigenmodes of both sides can couple if the thickness of the film is not too high. The resulting eigenmodes are of two types, and can be differentiated by the relative signs of their surface charges at both sides of the film, and have dispersion relations which deviate from the dispersion relation of a single interface. In the case of SP modes, the low frequency and high frequency modes are respectively antisymmetric and symmetric in charge with respect to the plane of the film. The relation dispersion of the SP modes of an infinite silver film of thickness 5 nm surrounded by vacuum are plotted in red on figure 2.3b.

We now have all the elements at hand to define very intuitively the SP modes of a finite flat metallic system similar to a triangular silver nanoprism. Based on its confined character, the nanoprism may naturally be viewed as a resonant cavity. As a consequence, we may easily assume, yet without any demonstration, that the SP modes of the nanoprism should be some of the SP modes of an infinite silver thin film of similar thickness, the selection of which being imposed by the out-of-plane geometrical boundary conditions. Precisely, it seems natural to quantify the wave vectors of these SP modes of the nanoprism as:

$$k_n \sim \frac{n}{L} \tag{2.3.8}$$

where $n$ is an integer and $L$ is the edge length of the nanoprism. The above expression is a quantization condition, which can be properly demonstrated for light waves in ideal (ie, non dissipative and with perfectly reflecting boundaries) cavities. As a consequence, the SP modes of the nanoprism have thus eigenfrequencies which follow the dispersion curve of the infinite film and electric fields characterized by a given number of nodes and antinodes (see figure 2.3a).

### 2.3.3 Geometric modes

The previous subsection aimed at defining a SP mode of a finite metal-dielectric system in a simple picture. This picture is very intuitive but relies on some flat character of the metallic medium, which works quite well in the case of a flat nanoprism, but cannot be extended to any truly arbitrary system. There is thus a need for a more generic definition of a mode. If we consider our situation where the nanoprism has very small dimensions, a reliable alternative definition can be adopted. Indeed, for small objects, the modes have large wave vectors and satisfy the quasistatic condition 2.3.6. The quasistatic approximation can thus be used, leading to considerable simplification to define the SP modes.

Let us first consider our generic 3D system (see figure 2.2a and annotations therein). In the quasistatic approximation, the surface eigenmodes can be deduced from some geometric modes [37] which can be obtained from the BEM theory developped by García de Abajo and Aizpurua [72]. Precisely, the surface eigenmodes can be known by solving the Poisson equation with no external source, expressed in frequency space as [25]:

$$\vec{\nabla}.\left[\tilde{\varepsilon}(\vec{r},\omega)\vec{\nabla}\phi(\vec{r},\omega)\right] = 0 \tag{2.3.9}$$

[9] In a Drude model, the equation of this asymptote is $\omega = \omega_s = \frac{\omega_p}{\sqrt{2}}$.

where the Fourier transform of the potential is defined as a function of the Fourier transform of the electric field through the relation:

$$\vec{E}(\vec{r},\omega) = -\vec{\nabla}\phi(\vec{r},\omega) \tag{2.3.10}$$

The surface eigenmodes can be obtained by expressing the electric potential as an electric potential created by a single layer of electric charges encompassing the whole boundary of the object, which reads:

$$\phi(\vec{r},\omega) = \oint_{\Omega_1\cap\Omega_2} \frac{\sigma(\vec{s},\omega)}{|\vec{r}-\vec{s}|} d\vec{s} \tag{2.3.11}$$

Expressing the discontinuity of the normal component of the electric field at the boundary as well as the continuity of the normal component of the electric displacement at the boundary, one obtains that the surface charge $\sigma(\vec{s},\omega)$ has to fullfil the Fredholm integral equation given by [37, 72]:

$$2\pi\lambda(\omega)\sigma(\vec{s},\omega) = PP\left\{\oint_{\Omega_1\cap\Omega_2} F(\vec{s},\vec{s}\,')\sigma(\vec{s}\,',\omega)d\vec{s}\,'\right\} \tag{2.3.12}$$

where $PP$ denotes the principal value, $\lambda(\omega)$ is given by the relation:

$$\lambda(\omega) = \frac{\varepsilon_1(\omega)+\varepsilon_2(\omega)}{\varepsilon_2(\omega)-\varepsilon_1(\omega)} \tag{2.3.13}$$

and $F(\vec{s},\vec{s}\,')$ is defined if $\vec{s}\neq\vec{s}\,'$ as:

$$F(\vec{s},\vec{s}\,') = -\frac{\vec{e}_{N(\vec{s})}.(\vec{s}-\vec{s}\,')}{|\vec{s}-\vec{s}\,'|} \tag{2.3.14}$$

where $\vec{e}_{N(\vec{s})}$ is defined as the normal unit vector located at position $\vec{s}$ on the boundary pointing from medium 1 to medium 2 (see figure 2.2a). The non-zero solutions of equation are given by the association of a complex number $\lambda_i$ and a complex charge density $\sigma_i(\vec{s})$ satisfying the relation:

$$2\pi\lambda_i\sigma_i(\vec{s}) = PP\left\{\oint_{\Omega_1\cap\Omega_2} F(\vec{s},\vec{s}\,')\sigma_i(\vec{s}\,')d\vec{s}\,'\right\} \tag{2.3.15}$$

The above equation only depends on the geometry of the system and is independent on the dielectric properties of the composites. The solutions can thus be viewed as geometric modes of the system [37], with eigenvalue $\lambda_i$ and eigenvector $\sigma_i(\vec{s})$. It can be shown that their eigenvalues are actually real and verify the inequality:

$$-1 \leq \lambda_i \leq +1 \tag{2.3.16}$$

Although the above eigenvalue equation cannot be solved analytically, numerical tools, and most particularly the BEM [72], can provide solutions for an arbitrary system.

For illustration, a mode (eigenvector) of the triangular nanoprism of eigenvalue -0.84, calculated with the MNPBEM toolbox, is shown on figure 2.4a. The eigenvector shows a characteristic pattern composed of a local maximum located at one tip and a local minimum at another tip.

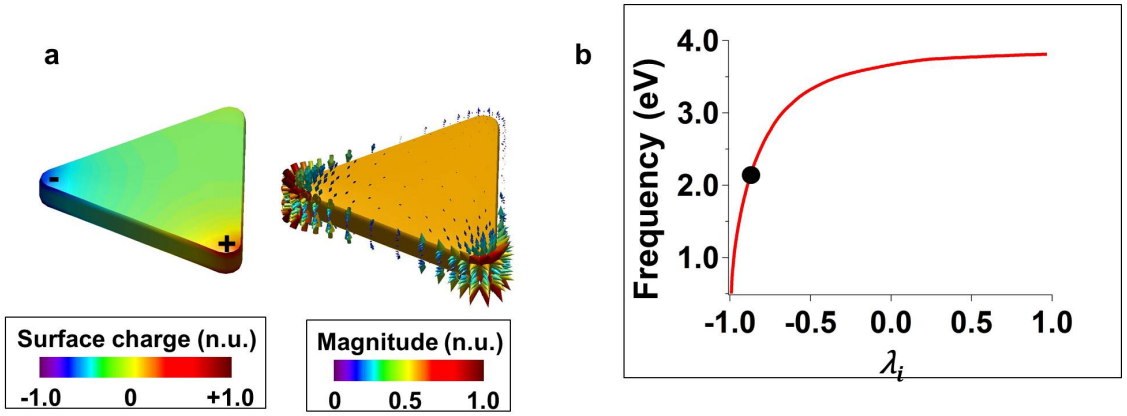


Figure 2.4: Geometric mode/surface eigenmode of the triangular nanoprism. a) Eigenvector of the geometric mode/surface charge wave of the eigenmode at time $t = n\frac{2\pi}{\omega_i}$. The relative signs of the surface charge maxima are added for clarity. Electic field of the eigenmode at the boundaries of the particle at time $t = n\frac{2\pi}{\omega_i}$. b) Dispersion relation of the SP modes likely to be supported by a silver object surrounded by vacuum. The shape of the object determines the allowed eigenvalue, and, in turn, the eigenfrequency of the eigenmode. In particular, the black dot corresponds to the eigenmode of a).

### 2.3.4 Quasistatic SP modes

Following equations 2.3.12 and 2.3.15, the surface eigenmodes of our generic 3D system [24, 25] are defined as the geometric modes $i$ such as there exists some frequency $\omega_i$ verifying:

$$\lambda(\omega_i) = \lambda_i \tag{2.3.17}$$

where $\lambda(\omega)$ was given by equation 2.3.13. The above equation is the existence condition of a surface eigenmode within the system, which defines the spectral features of the eigenmode. Moreover, $\sigma_i(\vec{s},t) = \sigma_i(\vec{s})e^{i\omega_i t}$ and $\vec{E}_i(\vec{r},t) = \vec{E}_i(\vec{r})\,e^{i\omega_i t}$, where $\vec{E}_i(\vec{r})$ is defined as:

$$\vec{E}_i(\vec{r}) = -\vec{\nabla}\phi_i(\vec{r}) \tag{2.3.18}$$

with $\phi_i(\vec{r})$:

$$\phi_i(\vec{r}) = \oint_{\Omega_1\cap\Omega_2} \frac{\sigma_i(\vec{s})}{|\vec{r}-\vec{s}|}d\vec{s} \tag{2.3.19}$$

, are respectively the non-propagating (ie. standing) surface charge wave and electric field of the surface eigenmode $i$[10]. The surface charge wave of a surface eigenmode of the triangular nanoprism thus corresponds at time $t = n\frac{2\pi}{\omega_i}$, where $n$ is an integer, to the eigenvector shown on figure 2.4a.

[10]Notice that, because we are using the quasistatic approximation, $\sigma_i(\vec{s},t)$ and $\vec{E}_i(\vec{r},t)$ equivalently describe the eigenmode $i$. However, the equivalence between a distribution of surface charges and an electric field does not hold anymore in a retarded approach, because a surface current enters as an additional contribution to the electric field [92].

The electric field associated to this surface eigenmode at the same time is shown at the surface of the nanoprism on figure 2.4a. The pattern agrees with the empirical definition of a mode we gave on subsection 2.3.2. As implied by the spatial distribution of the surface charge wave, this surface eigenmode can be referred to as a dipolar surface eigenmode.

As associated to the notion of eigenmode is the notion of coherence, and, in particular, of spatial coherence[11]. The spatial coherence of an eigenmode implies that, when excited locally by some point-like perturbation, the mode is excited as a whole. For instance, locally exciting the dipolar eigenmode at the left tip of the nanoprism induces electric fields not only at the left tip, but also, although far away from the perturbation, at the bottom tip[12].

We can now consider the case of a metal-dielectric system. In this case, the eigenfrequency and relaxation rate[13] of the SP modes can be deduced from the the complex frequency solving equation 2.3.17, when appropriate dielectric functions are introduced in equation 2.3.13. Precisely, for weak relaxation rates, the eigenfrequency of a mode $\omega_{i_0}^{SP}$ is defined as [24]:

$$\Re\left\{\lambda(\omega_{i_0}^{SP})\right\} = \lambda_i \tag{2.3.20}$$

while the relaxation rate $\Gamma_i^{SP}$ is found from[14]:

$$\Gamma_i^{SP} = \frac{1}{\left[\dfrac{d\left(\Re\left\{\lambda(\omega)\right\}\right)}{d\omega}\right]_{\omega=\omega_{i_0}^{SP}}} \Im\left\{\lambda(\omega_{i_0}^{SP})\right\} \tag{2.3.21}$$

For illustration, figure 2.4b shows the eigenfrequencies of the SP modes likely to be supported by a silver object surrounded by vacuum, plotted for a continuum of eigenvalues $\lambda_i \in [-1, 1]$ by taking $\varepsilon_1(\omega)$ as the silver dielectric function and $\varepsilon_2(\omega) = 1$ within equation 2.3.17. This graph can be seen as a dispersion curve, very similar to the dispersion curve given in subsection 2.3.2, except that this time it includes any object shape. The shape of the object determines the allowed eigenvalues, thus the spectral chararacteristics of the SP modes[15]. In the case of our triangular silver nanoprism, the dipolar SP mode, symbolized by the black dot on the dispersion curve, has an eigenfrequency of 2.25 eVand a relaxation rate of around 12.5 meV.

The spectral features of a mode can be expressed simply using a Drude model (see appendix A), which allows to demonstrate that the lifetime of the modes are dictated by the dissipative character of the metal (see also [96]). As the dissipation is mediated by intraband and interband transitions, the relaxation rates thus globally tend to increase when leaving the IR to the visible, due to the appearance of interband transitions[16].

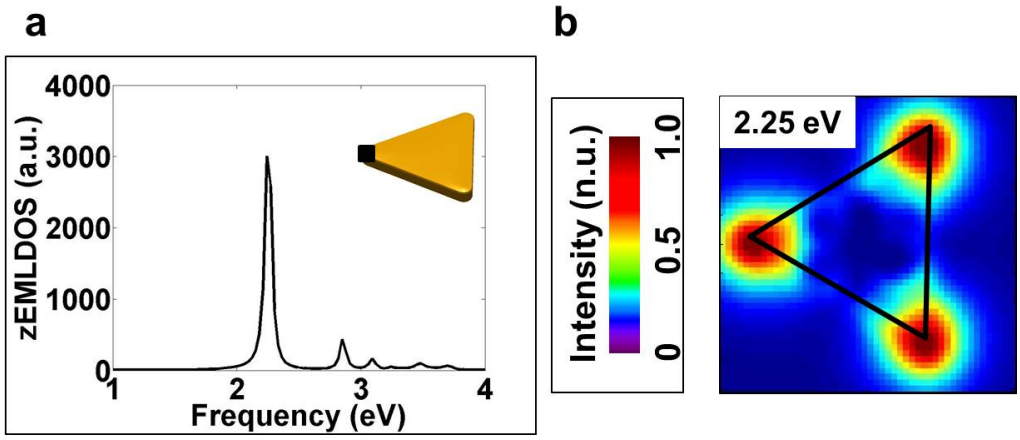


Figure 2.5: EMLDOS for the silver nanoprism. a) Electric part of the zEMLDOS as a function of frequency at fixed position located 15 nm above the tip of the nanoprism. b) Spatial variations of the electric part of the zEMLDOS in a plane located 15 nm above the nanoprism at 2.25 eV.

### 2.3.5 Extension to an arbitrary system

Our definitions of a SP mode as an electromagnetic surface eigenmode of a metal-dielectric finite system relied on either the flat character of the system or the quasistatic approximation, and should thus be extended with care to some system of any size and shape. However, we can intuitively extend both the phenomenological picture we gave first and the more mathematical approach we then followed to a truly arbitrary system. Namely, the SP modes are some resonant surface eigenmodes that are defined spectrally through an eigenfrequency and a relaxation rate that result from some boundary conditions. Due to retardation effects, the relaxation rate of a mode is not necessarily dictated by the dissipative character of the metal only. A mode might also decay via radiative channels by radiating electromagnetic energy, inducing additional, radiative damping to the relaxation rate [12, 18, 42, 98]. Such a mode would be a radiative mode, contrary to a non-radiative mode whose relaxation rate is limited by non-radiative damping only[17]. Despite this subtelty, all these features can be well understood, if not guessed [30], for simple systems, only from their size, geometry and constitutive media. However, these intuitions may not hold in complex systems (see

[11] If not specified, the word "coherence" will denote the spatial coherence of a mode all along its thesis, and not its temporal coherence [93, 94].

[12] A simple analogue would be the vibrations of a string.

[13] Following our definition, the dephasing time of a mode as defined in [12, 18, 42] is equal to the inverse of its relaxation rate.

[14] An equivalent alternative would be to consider simply the real and imaginary part of the complex frequency solving equation 2.3.17 as the resonance frequency and relaxation rate of the mode [95].

[15] Contrary to the retarded approach followed previously, the eigenfrequencies of the quasistatic SP modes do not explicitely depend on the length of the object but rather on the shape through the aspect ratio of the object [40].

[16] More precisely, the frequency dependence of the relaxation rate of the modes is mediated by different intraband and interband electron scattering processes [97], which leads to the fine peak structure shown in [24] (figure 2).

[17] A simple example of a radiative mode would be a low frequency mode of a flat particle (for instance, the dipolar and, if the particle is large enough, the higher order modes of a prism [49]). Indeed, such a mode would be a SPP located close to the light line in $(\omega,\vec{k})$ space (see the dispersion relation of figure 2.3).

chapter 5).

## 2.4 Electromagnetic Local Density of States (EMLDOS)

### 2.4.1 EMLDOS: an introduction

The Electromagnetic Local Density of States (EMLDOS) is an essential quantity that is often met in nanooptics [1]. Initially, the EMLDOS has been introduced in analogy with the Local Density of States (LDOS) of quantum physics, defined as:

$$\rho(\vec{r},\mathcal{E}) = \sum_i \delta(\mathcal{E}-\mathcal{E}_i)\left|\psi_i(\vec{r})\right|^2 \tag{2.4.1}$$

where $\psi_i(\vec{r})$ and $\mathcal{E}_i$ are the wave function and eigenenergy of the solutions of the time-independent Schrodinger equation, the so-called stationnary states $i$. By extension, $\rho(\vec{r},\mathcal{E})dEd\vec{r}$ is the probability of finding the particle in a stationnary state of eigen energy $\mathcal{E}_i$ between $\mathcal{E}$ and $\mathcal{E}+d\mathcal{E}$ within the infinitesimal volume $d\vec{r}$ located at point $\vec{r}$.

Over the last few years, the EMLDOS has been introduced for various purposes. In the context of equilibrium thermodynamics, the EMLDOS is known to provide the basis from which various macroscopic quantities can be derived, such as heat capacities or forces [35]. It thus constitutes a tool of choice for discussing a rich set of effects involving surface eigenmodes, from the Casimir force to heat transfers phenomena or some anomalous coherence properties of thermal emission near interfaces (for a review, see [99]). In the context of cavity quantum electrodynamics, the EMLDOS is known to enter the expression of the spontaneous decay rate of a quantum emitter. It thus accuretely describe the modification of spontaneous emission occuring, for instance, near interfaces [100] or nanoparticles. The EMLDOS was also early felt to be one of the most faithful quantities to describe the SP modes of metallic systems [101]. Finally, the EMLDOS was introduced to interpret the experimental results obtained in various near-field techniques, including SNOM [102–104], EELS [36], CL [36, 44] or Two Photon Luminescence (TPL) [105].

Following [35], the Electromagnetic Local Density of states (EMLDOS) $\rho(\vec{r},\omega)$ of a system should be defined such as $\rho(\vec{r},\omega)d\omega d\vec{r}$ is the number of electromagnetic eigenmodes[18] with a frequency between $\omega$ and $\omega+d\omega$ located within the infinitesimal volume $d\vec{r}$ located at point $\vec{r}$. Although any extension to a truly arbitrary dissipative system is very delicate to derive [106, 107], we will assume that the EMLDOS, in its most general form, is given by its expression for $\vec{r}$ belonging to vacuum [35], namely:

$$\rho(\vec{r},\omega) \quad = \quad -\frac{2\omega}{\pi}\mathcal{T}\left[\Im\left\{\overleftrightarrow{G}(\vec{r},\vec{r},\omega)\right\}\right] \tag{2.4.2}$$

where $\mathcal{T}\left[\overleftrightarrow{M}\right]$ denotes the trace of the matrix $\overleftrightarrow{M}$ and $\overleftrightarrow{G}(\vec{r},\vec{r},\omega) = \overleftrightarrow{G}^E(\vec{r},\vec{r},\omega) + \overleftrightarrow{G}^H(\vec{r},\vec{r},\omega)$ is the sum of the Fourier transforms of the electric and the magnetic Green functions $\overleftrightarrow{G}^E(\vec{r},\vec{r}',\omega)$ and $\overleftrightarrow{G}^H(\vec{r},\vec{r}',\omega)$, that we will simply call in the following "dyadic Green function of the system". The EMLDOS can thus be decomposed into a sum of an Electric LDOS (eLDOS) $\rho^E(\vec{r},\omega)$ and a

[18] This definition includes the electromagnetic surface eigenmodes, but not exclusively. Another examples of electromagnetic eigenmodes are, for instance, plane waves in vacuum or photonic modes in dielectrics.

Magnetic LDOS (mLDOS) $\rho^H(\vec{r},\omega)$, respectively dictated by the Fourier transforms of the electric and the magnetic Green functions.

For a non-magnetic system similar to the system we have defined in section 2.2, the electric and magnetic Green functions are defined as the solutions of the equations[19] [108]:

$$\vec{\nabla}\times\vec{\nabla}\times\overleftrightarrow{G}^E(\vec{r},\vec{r}',\omega)-\frac{\omega^2}{c^2}\tilde{\varepsilon}(\vec{r},\omega)\overleftrightarrow{G}^E(\vec{r},\vec{r}',\omega) = -\frac{1}{c^2}\delta(\vec{r}-\vec{r}')\overleftrightarrow{I} \tag{2.4.4}$$

$$\vec{\nabla}\times\frac{1}{\tilde{\varepsilon}(\vec{r},\omega)}\vec{\nabla}\times\overleftrightarrow{G}^H(\vec{r},\vec{r}',\omega)-\frac{\omega^2}{c^2}\overleftrightarrow{G}^H(\vec{r},\vec{r}',\omega) = \delta(\vec{r}-\vec{r}')\overleftrightarrow{I} \tag{2.4.5}$$

with the appropriate boundary conditions. The use of the Green functions allows expressing the electric and magnetic fields created by an arbitrary external current source $\vec{J}_{ext}(\vec{r},\omega)$ through the expressions[20]:

$$\vec{E}(\vec{r},\omega) = -4\pi i\omega\int\vec{J}_{ext}(\vec{r}',\omega)\overleftrightarrow{G}^E(\vec{r},\vec{r}',\omega)d\vec{r}' \tag{2.4.6}$$

$$\vec{H}(\vec{r},\omega) = -4\pi i\omega\int-\frac{i}{\omega}\vec{\nabla}\times\frac{1}{\tilde{\varepsilon}(\vec{r}',\omega)}\vec{J}_{ext}(\vec{r}',\omega)\overleftrightarrow{G}^H(\vec{r},\vec{r}',\omega)d\vec{r}' \tag{2.4.7}$$

In a similar way, a n-projected EMLDOS (simply called nEMLDOS) can be defined from the relation:

$$\rho_n(\vec{r},\omega) = -\frac{2\omega}{\pi}\Im\left\{\vec{e}_n.\overleftrightarrow{G}(\vec{r},\vec{r},\omega).\vec{e}_n\right\} \tag{2.4.8}$$

where $\vec{e}_n$ refers to a unit vector pointing along some direction. Similarly to the EMLDOS, the nEMLDOS can thus be decomposed into electric and magnetic contributions.

The link between the EMLDOS and the LDOS defined by equation 2.4.1 can be made clear when considering an ideal cavity surrounded by vacuum. In this case, neglecting the magnetic Green function with respect to the electric Green function, an orthonormal basis of eigenmodes $i$, also called "cavity modes", with eigenvalues $\omega_i$ and eigenvectors $\vec{E}_i(\vec{r})$ can be defined. The dyadic Green function of the system thus verifies a so-called modal decomposition which reads, for $\vec{r}$ and $\vec{r}'$ belonging to the cavity [112]:

[19] In such case, the magnetic and electric Green functions satisfy the equation [35, 108]:

$$\frac{\omega^2}{c^2}\overleftrightarrow{G}^H(\vec{r},\vec{r}',\omega)=\left[\vec{\nabla}\times\right].\overleftrightarrow{G}^E(\vec{r},\vec{r}',\omega).\left[\vec{\nabla}'\times\right] \tag{2.4.3}$$

As a consequence, the magnetic and electric Green functions are not independent and clearly do not show similar weights, leading to different contributions for the eLDOS and the mLDOS to the EMLDOS. In the case of a metal-vacuum interface, the mLDOS is negligible with respect to the eLDOS at frequencies larger than the IR [35]. However, in a general situation, the mLDOS cannot be eluded. Typical examples where the mLDOS is large in the visible spectral range are high refractive index dielectric nanoparticles [109] or U-shaped metallic nanostructures [110], also called Split Ring Resonators, an ensemble of which being commonly referred to as metamaterials [111].

[20] The physical meaning of the term $-\frac{i}{\omega}\vec{\nabla}\times\frac{1}{\tilde{\varepsilon}(\vec{r},\omega)}\vec{J}_{ext}(\vec{r},\omega)$ appearing within the expression for the magnetic field is that it can be viewed as a *magnetic* current density pretty much in the same way $\vec{J}_{ext}(\vec{r},\omega)$ is an *electric* current density for the system.

$$\overleftrightarrow{G}(\vec{r},\vec{r}\,',\omega) = \sum_i c^2 \frac{\vec{E}_i(\vec{r}) \bigotimes \vec{E}_i^*(\vec{r}\,')}{\omega^2-\omega_i^2} \tag{2.4.9}$$

Using the identity $\Im\left\{\frac{1}{x-x_0+i\varepsilon}\right\} \to_{\varepsilon\to 0} -\pi\delta(x-x_0)$, the EMLDOS and nEMLDOS can thus be expressed, for $\vec{r}$ and $\vec{r}\,'$ belonging to the cavity, as [1, 112]:

$$\rho(\vec{r},\omega) = \sum_i \delta(\omega^2-\omega_i^2)\left|\vec{E}_i(\vec{r})\right|^2 \tag{2.4.10}$$

$$\rho_n(\vec{r},\omega) = \sum_i \delta(\omega^2-\omega_i^2)\left|E_i^n(\vec{r})\right|^2 \tag{2.4.11}$$

We thus revover the classical general definition of a LDOS given by equation 2.4.1 if we replace the quantum state $i$, wave function $\psi_i(\vec{r})$ and eigenenergy $\mathcal{E}_i$ by a mode $i$, electric field $\vec{E}_i(\vec{r})$ (or $E_i^n(\vec{r})$) and eigenvalue $\omega_i$.

Figure 2.5 shows calculations of the EMLDOS for the silver nanoprism, determined from equation 2.4.2. Precisely, if we refer as $\vec{e}_z$ as a unit vector pointing parallel to the thickness direction of the nanoprism, figure 2.5a displays the electric part of the zEMLDOS as a function of frequency at fixed position located 15 nm above the left tip of the nanoprism. Some resonances appear at certain frequencies, the main one being located at 2.25 eV. Furthermore, figure 2.5b shows the spatial variations of the electric part of the zEMLDOS in a plane located 15 nm above the nanoprism at this resonance frequency. This map shows local spots where the EMLDOS increases located around the three tips of the nanoprism. The aim of the following is to give a physical interpretation of these figures, based on the previous section.

### 2.4.2 A synthetic quantity to describe a set of SP modes

In this subsection, we are going to clarify the spatial and spectral dependences of the EMLDOS in a generic 3D system, and show how they can be related to the surface eigenmodes. The basic idea is to obtain an equivalent of equations 2.4.10 and 2.4.11. When starting from scratch, it turns out that such a derivation is not an easy task. The reason why the modal decomposition holds for an ideal cavity is that the operator entering the Helmoltz equation whose cavity modes are solutions is Hermitian. The cavity modes thus form a complete orthonormal basis with respect to the scalar product $\left\langle \vec{f}(\vec{r}),\vec{g}(\vec{r})\right\rangle = \int \vec{f}(\vec{r})\vec{g}^*(\vec{r})d\vec{r}$, within which the Dyadic Green function can be expanded. In a full relativistic approach, our problem is unfortunately not Hermitian. However, in the quasistatic approximation, the geometric modes introduced in section 2.3.3 form a orthonormal basis with respect to the scalar product $\langle f(\vec{s}),g(\vec{s}\,')\rangle = \oint_{\Omega_1\cap\Omega_2} \frac{f(\vec{s})g^*(\vec{s}\,')}{|\vec{s}-\vec{s}\,'|}d\vec{s}d\vec{s}\,'$ [73]. The modal decomposition of the dyadic Green function of the system within this basis reads [37]:

$$\overleftrightarrow{G}(\vec{r},\vec{r}\,',\omega) = \frac{1}{4\pi\omega^2}\sum_i \left[g_i(\omega) - \frac{1}{\tilde{\varepsilon}(\vec{r}\,',\omega)}\right]\vec{E}_i(\vec{r})\otimes\vec{E}_i^*(\vec{r}\,') \tag{2.4.12}$$

where $\vec{E}_i(\vec{r})$ has been defined in equation 2.3.18 and:

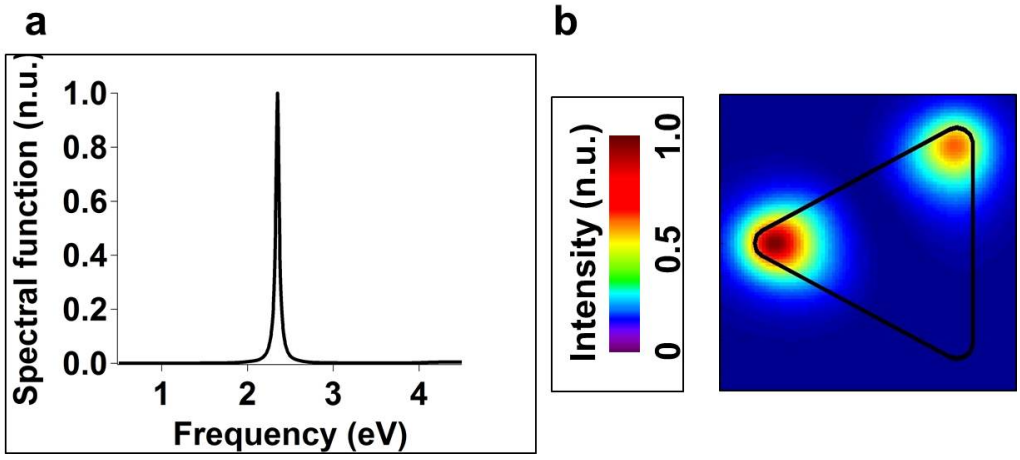


Figure 2.6: Spectral and spatial contributions of the dipolar mode of the nanoprism to the EMLDOS. a) Spectral function $\frac{1}{\omega}\Im\{f_i(\omega)\}$. b) Spatial variations of $\left|E_i^z(\vec{r})\right|^2$ calculated in a plane located 15 nm above the nanoprism.

$$g_i(\omega) = \frac{2}{\varepsilon_1(\omega)\left[1+\lambda_i\right] + \varepsilon_2(\omega)\left[1-\lambda_i\right]} \tag{2.4.13}$$

Notice that, if $\vec{r}\,'$ is outside the object:

$$g_i(\omega) - \frac{1}{\tilde{\varepsilon}(\vec{r}\,',\omega)} = f_i(\omega) \tag{2.4.14}$$

where:

$$f_i(\omega) = \frac{1}{\varepsilon_2(\omega)}\frac{1+\lambda_i}{\lambda(\omega)-\lambda_i} \tag{2.4.15}$$

and $\lambda(\omega)$ has been defined in equation 2.3.13. Introducing the above modal decomposition inside the definition of the EMLDOS (equation 2.4.2), we find the new modal decomposition [37]:

$$\rho(\vec{r},\omega) \quad = \quad \frac{1}{2\pi^2\omega}\sum_i \Im\left\{-g_i(\omega) + \frac{1}{\tilde{\varepsilon}(\vec{r},\omega)}\right\}\left|\vec{E}_i(\vec{r})\right|^2 \tag{2.4.16}$$

Similarly, the nEMLDOS expresses as:

$$\rho_n(\vec{r},\omega) = \frac{1}{2\pi^2\omega}\sum_i \Im\left\{-g_i(\omega) + \frac{1}{\tilde{\varepsilon}(\vec{r},\omega)}\right\}\left|E_i^n(\vec{r})\right|^2 \tag{2.4.17}$$

where $E_i^n(\vec{r}) = \vec{e}_n.\vec{E}_i(\vec{r})$. In the special case where $\vec{r}$ is outside the object, these expressions become:

$$\rho(\vec{r},\omega) = \frac{1}{2\pi^2\omega}\sum_i \Im\{f_i(\omega)\}\left|\vec{E}_i(\vec{r})\right|^2 \quad (2.4.18)$$

$$\rho_n(\vec{r},\omega) = \frac{1}{2\pi^2\omega}\sum_i \Im\{f_i(\omega)\}\left|E_i^n(\vec{r})\right|^2 \quad (2.4.19)$$

We will consider these last two expressions for simplicity. These expressions are equivalent to the modal decompositions proposed in equations 2.4.10 and 2.4.11. In comparison, the modes $i$ are geometric modes, not cavity modes, and the delta function of equations 2.4.10 and 2.4.11 is replaced by the quantity $\frac{1}{\omega}\Im\{f_i(\omega)\}$, whose frequency dependence dictates the spectral behaviour of the EMLDOS for a given mode $i$. This frequency dependence depends both on the dielectric functions of the media and the eigenvalue of the geometric mode through equation 2.4.13. Furthermore, the spatial variations of $\left|\vec{E}_i(\vec{r})\right|^2$ or $\left|E_i^n(\vec{r})\right|^2$ dictate the spatial variations of the EMLDOS and nEMLDOS for a given mode $i$.

Let us now consider back our silver nanoprism to examine the spatial and spectral dependences of the EMLDOS. Figure 2.6a shows a plot of $\frac{1}{\omega}\Im\{f_i(\omega)\}$ as a function of frequency for an eigenvalue corresponding to the geometric mode of the nanoprism introduced in subsection 2.3.3 when taking $\varepsilon_1(\omega)$ as the dielectric function of silver and $\varepsilon_2(\omega) = 1$. This frequency dependent function is resonant yet broadened. Moreover, figure 2.6b shows the spatial variations of $\left|E_i^z(\vec{r})\right|^2$ of the geometric mode when taken in a constant plane located 15 nm above the upper side of the nanoprism. This map displays a number of spots of high intensity located at the tips which are due to local strengthenings of $\left|E_i^z(\vec{r})\right|^2$.

From the above expressions, we can draw a clear link between the EMLDOS of a metal-dielectric system and its SP modes. Indeed, as seen in the denominator of $f_i(\omega)$, the poles of the EMLDOS are the complex frequencies solutions of the SP mode condition given by equation 2.3.17. The poles of the EMLDOS thus give the spectral characteristics (eigenfrequency and relaxation rate) of the SP modes. As a consequence, for each mode, $\frac{1}{\omega}\Im\{f_i(\omega)\}$ is resonant and maximum at about the eigenfrequency of the SP mode with a FWHM approximately equal to twice its relaxation rate (compare figure 2.6a with the spectral characteristics of the dipolar SP mode given in subsection 2.3.4). Furthermore, because $\vec{E}_i(\vec{r})$ is the electric field of the SP mode $i$ at time $t = n\frac{2\pi}{\omega_i}$, where $n$ is an integer, $\left|E_i(\vec{r})\right|^2$ and $\left|E_i^n(\vec{r})\right|^2$ are the square electric field and projection of the electric field of the same SP mode. The spots seen at the tips of the nanoprism in the map of figure 2.6b are due to some local strengthening in the magnitude of the z-projection of the electric field of the dipolar SP mode of the nanoprism. As a consequence, the EMLDOS and nEMLDOS well describe, through is spectral and spatial variations, the spectral and spatial features of the SP modes[21]. Notice, however, that the EMLDOS is only sensitive to the absolute magnitude of the field. Therefore, the phase of the field cannot be recovered from some knowledge of the EMLDOS.

[21] This can be also illustrated directly for a model SP mode described with a Drude model, as shown in appendix A.

### 2.4.3 In-plane spatial variations of the EMLDOS at constant frequency: spatial coherence issues

We can now come back to figure 2.5. The local zEMLDOS spectrum of figure 2.5a is akin to a sum of peaks of fixed central frequency and FWHM with varying amplitudes. This confirms equation 2.4.17. In particular, the dominant resonance at 2.25 eV is due to the high z electric field of the dipolar SP mode at the left tip of the nanoprism. Some local strenghtenings are identified in the in-plane spatial variations of the zEMLDOS at 2.25 eV shown on figure 2.5b. However, notice that this map does not strictly display the square projected electric field of the dipolar SP mode but rather a superposition of modes. Indeed, the map shows intensity local maxima located at the three tips, which is contrary to the dipolar mode defined previously. This can be well understood from equation 2.4.16: at the resonance frequency of a mode, the EMLDOS does not give a single mode but a sum of modes. In particular, the map at 2.25 eV shows a superposition of three degenerate dipolar SP modes of eigenfrequencies 2.25 eV which correspond to charge oscillations between two of the three tips of the nanoprism. This degeneracy of the dipolar modes results from the symmetry of the object. Therefore, in these maps, a single dipolar mode cannot be identified directly, because the spatial coherence of the modes is lost [37].

In the most general case, because the spectral contribution of a mode to the EMLDOS is broadened by its non-infinite lifetime, an energy filtered maps shows a complex weighted sum of the square z projected electric fields of the modes[22]. Therefore, two SP modes with close yet different resonant frequencies may mix when observing the spatial variations of the EMLDOS at one of these two frequencies. Such effect is negligible only if the SP modes have resonant frequencies separated by a spectral amount much larger than their relaxation rate. As a consequence, safely identifying a single mode from an energy filtered map is often difficult[23].

### 2.4.4 Extension to an arbitrary system

The above modal decomposition relies on the geometric modes we defined in section 2.3.3. It is thus, strictly speaking, incorrect for a system whose dimensions exceed about 100 nm. However, in the absence of universal definition of a surface electromagnetic eigenmode in a retarded approach, such a modal decomposition may unfortunately be unthinkable without invoking the quasistatic approximation. An alternative phenomenological approach was proposed in [112], consisting in introducing virtual modes by broadening the cavity modes of equation 2.4.10 using a given linewidth. A similar modal decomposition was derived in this way. Therefore, it is most probably quite realistic to intuitively extend these findings to an arbitrary metal-dielectric system of any size. Namely, the EMLDOS or nEMLDOS, at a given point, should be resonant at about the eigenfrequency the mode, with a spectral width related to the relaxation rate of the mode and an amplitude given by some local intensity characteristic of the mode. However, because an arbitrary mode would have a non-zero magnetic field, such local intensity of the mode should include this magnetic field as well. Precisely, we can expect that the eLDOS should probe the square of the electric field of the mode, while the mLDOS should probe the square of the magnetic field of the mode. By extension, the EMLDOS should probe a sum of the square of the electric field and the square of the magnetic field of the mode. Because relaxation rates of SP modes are non-zero, the spatial variations of the EMLDOS at a given frequency is very likely to reflect a mixing of modes with close eigenfrequencies

[22] This can be shown simply with a Drude model (see appendix A).

[23] Such loss of spatial coherence is typical of the EMLDOS of dissipative systems. However, the spatial coherence may be recovered by measuring the Cross Density Of States (CDOS) [112].

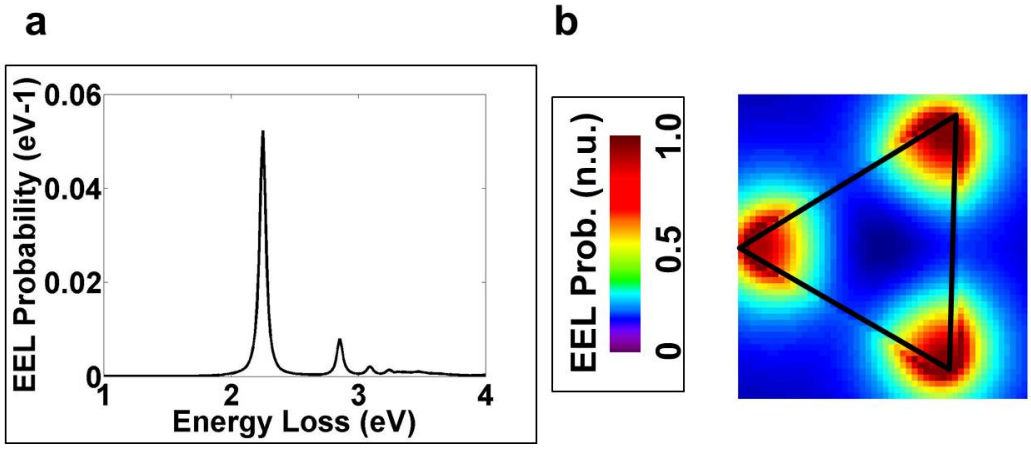


Figure 2.7: STEM EELS from classical electrodynamics. a) EEL probability spectra calculated for an electron impact parameter located at the tip of the nanoprism. b) Calculated energy filtered map of the EEL probability for the energy loss value of 2.25 eV.

rather than a single mode whose eigenfrequency would be equal to this frequency. This is especially true as radiation damping might add to interband and intraband damping to reduce the lifetime of the modes.

## 2.5 Valence EELS, EMLDOS and SP modes

### 2.5.1 Valence EELS and classical electrodynamics

As previously stated, valence EELS can be well accounted for in the framework of electrodynamics. Indeed, keeping the notations of section 2.2, a fast electron enters the Maxwell equation through either an external charge density:

$$\rho_{el}(\vec{r},t) = -e\delta\left(\vec{r} - \vec{r}_e\left(t\right)\right) \tag{2.5.1}$$

or an external curent density current:

$$\vec{J}_{el}(\vec{r},t) = -e\delta\left(\vec{r} - \vec{r}_e\left(t\right)\right)\vec{v} \tag{2.5.2}$$

For a given impact parameter $\vec{R}$, the electron gives rise at each time of its trajectory to an electromagnetic field at each point of space $\vec{E}_{el}(\vec{r},t)$ and $\vec{B}_{el}(\vec{r},t)$. For example, the electric field induced in an infinite homogeneous medium of dielectric function $\varepsilon(\omega)$ writes [20]:

$$\vec{E}_{el}(\vec{r},t) = \frac{2e}{v^2}\int \frac{\omega}{\gamma(\omega)\varepsilon(\omega)}\left[\frac{i}{\gamma(\omega)}K_0\left(\frac{\omega R}{v\gamma(\omega)}\right)\vec{e}_z - K_1\left(\frac{\omega R}{v\gamma(\omega)}\right)\vec{e}_\rho\right]e^{i\omega z/v}d\omega \tag{2.5.3}$$

$$\vec{B}_{el}(\vec{r},t) = -\frac{4e^2}{v^3 c}\int \frac{\omega^2}{\gamma(\omega)^2\varepsilon(\omega)}K_1\left(\frac{\omega R}{v\gamma(\omega)}\right)\vec{e}_\varphi e^{i\omega z/v}d\omega \tag{2.5.4}$$

where $\gamma(\omega) = \dfrac{1}{\sqrt{1-\varepsilon(\omega)v^2/c^2}}$, $K_n$ is the Bessel function of second kind of order n, and $(\vec{e}_\rho, \vec{e}_\varphi)$ are unit vectors in cylindrical coordinates. The fast electron can thus be viewed as a broad source of evanescent monochromatic electromagnetic fields (a "white-light" source). Its Fourier spectrum can be further analyzed from the expression of the electric field in $(\omega, \vec{k})$ space, namely [20]:

$$\vec{E}_{el}(\vec{r},t) = \frac{ie}{2\pi^2}\int\int \frac{\vec{k}-\dfrac{\omega v}{c^2}}{\left|\vec{k}\right|^2-\dfrac{\omega^2}{c^2}}\delta\left(\omega-\vec{k}.\vec{v}\right)e^{i(\vec{k}.\vec{r}-\omega t)}d^3\vec{k}d\omega \tag{2.5.5}$$

We here well see that the Fourier spectrum of the electron contains all real frequencies $\omega$ and wave vectors $\vec{k}$ verifying the relation $\omega = \vec{k}.\vec{v}$.

When the charge enters or comes close to the nanoparticle, this electromagnetic field is modified due to charge polarization phenomena occuring inside the nanoparticle and resulting in some scattering of the field accompanying the electron. The total electromagnetic field can thus be decomposed into a sum of a field due to the electron itself (a "bare field") and an induced electromagnetic field, resulting from the scattering of this bare field by the nanoparticle. If we denote this induced field $\vec{E}_{el}^{ind}(\vec{r},t)$ and $\vec{B}_{el}^{ind}(\vec{r},t)$, the fast electron thus experiences the Lorentz force $-e\left[\vec{E}_{el}^{ind}\left(\vec{r}_e\left(t\right),t\right)+\vec{v}\times\vec{B}_{el}^{ind}\left(\vec{r}_e\left(t\right),t\right)\right]$. In the case where the induced electric field has a non zero component antiparallel to the electron trajectory at the position of the electron, the contribution of the Lorentz force due to the induced electric field works against the electron[24], which is thus slowed down. Precisely, the fast electron loses, during the corresponding infinitesimal time $dt$, the kinetic energy given by the elementary work of the electric force, that is $e\vec{v}.\vec{E}_{el}^{ind}\left(\vec{r}_e\left(t\right),t\right)dt$. The total energy lost by the electron during its trajectory is nothing but the sum of these elementary works, which reads:

$$\Delta W(\vec{R}) = e\int_{-\infty}^{+\infty}\vec{v}.\vec{E}_{el}^{ind}\left(\vec{r}_e\left(t\right),t\right)dt \tag{2.5.6}$$

The total loss can be decomposed in spectral components by introducing the EEL probability (defined in chapter 1)$\Gamma_{EEL}(\vec{R},\omega)$:

$$\Delta W(\vec{R}) = \int_0^{+\infty}\hbar\omega\Gamma_{EEL}(\vec{R},\omega)d\omega \tag{2.5.7}$$

Introducing the Fourier transform $\vec{E}_{el}\left(\vec{r}_e\left(t\right),\omega\right)$ of $\vec{E}_{el}\left(\vec{r}_e\left(t\right),t\right)$, the EEL probability is thus given by the following formula [20]:

$$\Gamma_{EEL}(\vec{R},\omega) = \frac{e}{\pi\hbar\omega}\int\Re\left\{e^{-i\omega t}\vec{v}.\vec{E}_{el}^{ind}\left(\vec{r}_e\left(t\right),\omega\right)\right\}dt \tag{2.5.8}$$

The EEL probability is thus known from the electric field induced by the electron at each time of its trajectory, which can in turn be determined by solving the Maxwell equations in Fourier space once the relevant dielectric functions of the system are specified[25]. Because the Fourier spectrum

[24] The magnetic contribution does not contribute to work.

[25] For an arbitrary inhomogenous sample, this cannot be done analytically. However, it can be achieved from standard computational methods, such as the Boundary Element Method (BEM) [92, 113], the Finite Difference Time Domain (FDTD) method [51], the Discontinuous Galerkin Time-Domain (DGTD) method [114] or the Discrete Dipole Approximation (DDA) method [115] (for a review, see [116]).

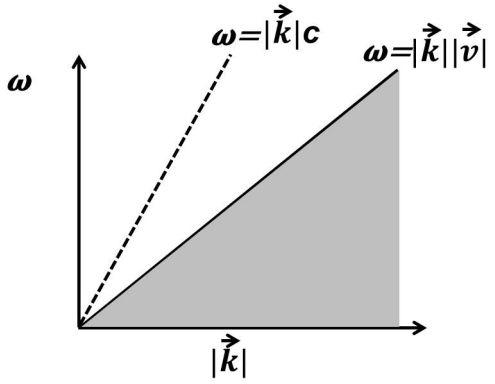


Figure 2.8: $(\omega, \vec{k})$ space. The gray area represents the Fourier spectrum of the electron or, equivalently, the regions where the modes are accessible to the electron. The dotted line shows, for comparison, the dispersion relation of a light wave in vacuum.

of the electron is broad, the probability for an electron to lose a given energy is non zero in a wide range of energies. The probability is larger as the projection along z of the induced electric field at the position of the electron is large.

Figure 2.7a shows an EEL probability local spectrum, calculated in our system from equation 2.5.8, for an electron impact parameter corresponding to the left tip of the nanoprism. Again, some resonances appear, the main one appearing at 2.25 eV. Figure 2.5b shows the spatial variations of the EEL probability at this resonance energy. Similarly to the EMLDOS, this map shows local spots where the EEL probability increases located around the three tips of the nanoprism. In the following, we are going to justify this point and comment the consequences.

### 2.5.2 EEL probability and EMLDOS

We have reached a central point of this chapter, namely, the close relationship between the EEL probability and the EMLDOS [36]. From equation 2.5.8, the EEL probability is known from the electric field induced by the electron at each time of its trajectory. This electric field can in turn be expressed using the electric Green function by using the relation (see equation 2.4.6) :

$$\vec{E}_{el}(\vec{r},\omega) = -4\pi i\omega \int \overleftrightarrow{G}^{E}(\vec{r},\vec{r}\,',\omega)\vec{J}_{el}(\vec{r}\,',\omega)d\vec{r}' \tag{2.5.9}$$

The EEL probability can thus be expressed, after introduction of equations 2.5.9 and 2.5.2 into equation 2.5.8, as:

$$\Gamma_{EEL}(\vec{R},\omega) = -\frac{4e^2}{\hbar}\int\int \Im\left\{e^{i\frac{\omega}{v}(z'-z)}\vec{e}_z.\overleftrightarrow{G}^{E}(\vec{R}+z\vec{e}_z,\vec{R}\,'+z'\vec{e}_z,\omega).\vec{e}_z\right\}dzdz' \tag{2.5.10}$$

We may here recognized the Fourier transform of the zz component of the electric Green function with respect to z and z'

$\vec{e}_z.\overleftrightarrow{G}^E(\vec{R},\vec{R}\,',k_z,k'_z,\omega).\vec{e}_z = \int\int \vec{e}_z.\overleftrightarrow{G}^E(\vec{R}+z\vec{e}_z,\vec{R}\,'+z'\vec{e}_z,\omega).\vec{e}_z e^{i(k_z z+k'_z z')}dzdz'$. At this point, we can introduce a quantity expressed in the combination of real and Fourier spaces as:

$$\tilde{\rho}_n(\vec{R},k_z,\omega) = -\frac{2\omega}{\pi}\Im\left\{\vec{e}_n.\overleftrightarrow{G}^E(\vec{R},\vec{R},k_z,-k'_z,\omega).\vec{e}_n\right\} \tag{2.5.11}$$

so that the EEL probability expresses as [36]:

$$\Gamma_{EEL}(\vec{R},\omega) = \frac{2\pi e^2}{\hbar\omega}\tilde{\rho}_z(\vec{R},\frac{\omega}{v},\omega) \tag{2.5.12}$$

Notice that $\tilde{\rho}_n(\vec{R},k_n,\omega)$ is not strictly speaking a Fourier transform of the nEMLDOS given by equation 2.4.8. Precisely, only in the case of a 2D system whose magnetic Green function is negligible with respect to its electric Green function and possessing translational invariance along the z axis, the EEL probability is directly proportional to the partial Fourier transform of the zEMLDOS $\rho_z(\vec{R}_0,k_z,\omega)$ taken at $k_z = \frac{\omega}{v}$. In the most general case, the EEL probability is proportional to a generalized LDOS that is local in real space along the $\vec{R}$ direction, and local in Fourier space along the z direction. The differences between this generalized LDOS and the EMLDOS of the system can be understood quite easily. First, the electric nature of this LDOS (the magnetic Green function being absent from equation 2.5.11) comes from the fact that only the electric fields couple to the fast electron. Second, its z-projected nature can be inferred from the the simple fact that the electron is only affected by the electric field components parallel to its trajectory. Finally, the locality in Fourier space can be presumed as resulting from the finite Fourier spectrum of the electron, which contains all real frequencies $\omega$ and wave vectors $\vec{k}$ verifying the relation $\omega = \vec{k}.\vec{v}$[26]. Such a relation covers a continuous area in $(\omega,\vec{k})$ space, which however does not fill the whole space, and is shown in grey on figure 2.8. The fast electron is thus able to couple to some modes belonging to this area only.

### 2.5.3 EEL probability and SP modes

Based on the previous subsections, we can now completely understand the link between EELS and the SP modes of an arbitrary small object, which was established recently by Boudarham and Kociak [37]. Introducing equation 2.4.12 into equation 2.5.12, the EEL probability reads, in the simplified case of a non-penetrating trajectory [37]:

$$\Gamma_{EEL}(\vec{R},\omega) = \frac{e^2}{\pi\hbar\omega^2}\sum_i \Im\left\{f_i(\omega)\right\}\left|E_i^z(\vec{R},\frac{\omega}{v})\right|^2 \tag{2.5.13}$$

$$= \frac{e^2}{\pi\hbar}\sum_i \Im\left\{f_i(\omega)\right\}\left|\phi_i(\vec{R},\frac{\omega}{v})\right|^2 \tag{2.5.14}$$

where $f_i(\omega)$ has been defined in equation 2.4.15, and $E_i^z(\vec{R},k_z) = \int E_i^z(\vec{R}+z\vec{e}_z,\omega)e^{ik_z z}dz$ and $\phi_i(\vec{R},k_z) = \int \phi_i(\vec{R}+z\vec{e}_z,\omega)e^{ik_z z}dz$ are the Fourier transform along z of $E_i^z(\vec{r}) = \vec{e}_z.\vec{E}_i(\vec{r})$ and

[26] Such a relation expresses conservation of energy and momentum involved from a transfer of energy and momentum from the electron to the sample in a kinematical approach [20].

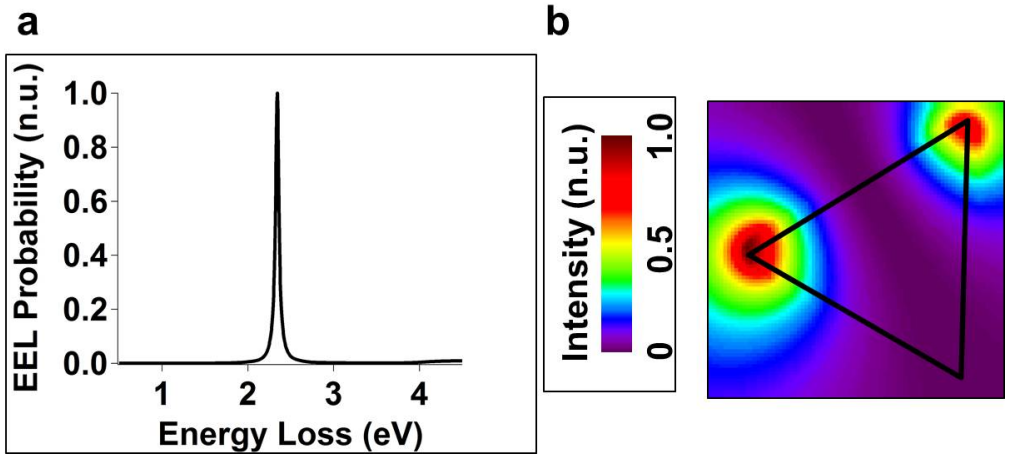


Figure 2.9: Spectral and spatial contributions from the dipolar mode of the nanoprism to EELS. a) $\Im\{f_i(\omega)\}\left|\phi_i(\vec{R},\frac{\omega}{v})\right|^2$ as a function of $\omega$ for an electron impact parameter located at the tip of the nanoprism. b) $\left|\phi_i(\vec{R},\frac{\omega}{v})\right|^2$ as a function of $\vec{R}$ for $\omega$=2.25 eV and $v$=c/2.

$\phi_i(\vec{r})$, each one being related to the other through: $E_i^z(\vec{R},k_z) = -ik_z\phi_i(\vec{R},k_z)$. $\phi_i(\vec{R},k_z)$ can be directly expressed as a function of the geometric mode as:

$$\phi_i(\vec{R},k_z) = 2\oint_{\Omega_1\cap\Omega_2} \sigma_i(\vec{s})\, e^{-ik_z s_z} K_0\left(k_z\left|\vec{R}-s_\perp\vec{e}_\perp\right|\right) d\vec{s} \tag{2.5.15}$$

where $\vec{s} = s_\perp\vec{e}_\perp + s_z\vec{e}_z$ .

Notice the close similarity between the above expression of the EEL probability and the modal decomposition of the zEMLDOS given by expression 2.4.17, despite the fact that EELS does measure only a generalized LDOS. In particular, yet $|E_i^z(\vec{r})|^2$ is changed into the quantity $\left|E_i^z(\vec{R},\frac{\omega}{v})\right|^2$ (or $\left|\phi_i(\vec{R},\frac{\omega}{v})\right|^2$), we well recover the term $\Im\{f_i(\omega)\}$. The physical meaning of $\left|E_i^z(\vec{R},\frac{\omega}{v})\right|^2$ (or $\left|\phi_i(\vec{R},\frac{\omega}{v})\right|^2$) can be well understood from equation 2.5.15 for a thin nanoparticle whose symmetry plane is perpendicular to z. In this case, these last quantities are readily understandable as the square of the eigenvector of the geometric mode convolved by a Coulombic kernel.

Figures 2.9a and 2.9b show the spectral and spatial contributions from the dipolar mode of the triangular nanoprism to the EEL probability. Because the nanoparticle is thin and plane, $\left|E_i^z(\vec{R},\frac{\omega}{v})\right|^2$ is very close to $|E_i^z(\vec{r})|^2$ when evaluated in a plane located a distance above the particle [36, 37] (compare the map of figure 2.9b with the map of figure 2.6b). Furthermore, the spectral contribution from the mode to EELS is equivalent to its spectral contribution to the EMLDOS, due to the dominant term $\Im\{f_i(\omega)\}$ appearing in both expressions (compare figure 2.9a with figure 2.6a). Therefore, the EEL probability and the EMLDOS are very close from each other.

As a consequence, EELS, similarly to the EMLDOS, can be readily understood through the SP modes of the system. For a given resonance within an EELS spectrum, the center energy, half

FWHM and amplitude of the peak are related to the eigenfrequency, relaxation rate and local value of the z-electric field intensity when evaluated in a plane located a distance above the particle, of the SP mode locally excited. On the other hand, an energy filtered map gives a weighted sum of the z-electric field intensities of the SP modes.

### 2.5.4 Extension to an arbitrary system

Once again, the quasistatic approximation has been evoked to explain the spatial and spectral variations of the EEL probability. Notice, however, that the link between the EEL probability and the electric Green function of the system given by equations 2.5.11 and 2.5.12 makes no use of this approximation. Furthermore, it turns out that the spatial variations of the EEL probability in a complete arbitrary planar geometry actually closely resemble the spatial variations of the electric part of the zEMLDOS calculated in a plane located a distance away from the surface [36], and is thus not a consequence of the quasistatic approximation. We have intuitively generalized the interpretation of the spatial and spectral variations of the EMLDOS in an arbitrary metal-dielectric finite system through the features of the SP modes in subsection 2.4.4. We can thus transpose such statement to the spatial and spectral variations of the EEL probability, at least in a flat system, but most probably to a true arbitray system. We however stress two key points. First, the fast electron does not couple to the magnetic fields of the mode. EELS thus only probes the square of the electric field of a mode at a given point. Second, the EMLDOS is a universal quantity that does not depend on the measuring technique. This is obviously not the case of the generalized LDOS the EEL probability is proportional to. Precisely, STEM EELS may be blind to some modes (precisely, some modes standing at the left of the $\omega = \vec{k}.\vec{v}$ line and some modes with no electric field component parallel to the electron trajectory) in particular systems [113].

## 2.6 Conclusion

We are now able to completely interpret the experimental observations of figure 2.1 in terms of the spatial and spectral characterics of the SP modes of the nanoprism. A resonance occurs in the EEL spectra (figure 2.1b) at specific electron locations where the electron can excite a given SP mode and be slowed down by its electric field. This resonance occurs at a resonance energy related to the eigenfrequency of the mode, has a typical spectral width related to the relaxation rate of the mode and an amplitude related to the local value of the z projected electric field intensity of the mode[27]. Yet demonstrated in the quasistatic approximation, we will assume that such statements are basically true for a generic metal-dielectric system of arbitrary size and shape.

In our case, because the modes have well separated eigenfrequencies when compared to their relaxation rate, the maps of figure 2.1c show the z electric field intensities spatial variation of some dipolar (at 1.75 eV), quadrupolar (2.70 eV) and higher order (3.20 eV) modes[28]. Notice, however, that the situation could be less ideal. Indeed, when the EEL probability is mapped spatially at a given energy, we may face spatial coherence issues if different modes with close resonance energies

[27] We will qualify this last statement in chapter 5, where we will show that resonance energies can slightly deviate from the eigenfrequencies of the modes in gold. In such case, the resonance energies depend on the technique (EELS, CL, extinction, scattering spectroscopy...).

[28] The deviation from our numerical simulations can be explained by the presence of a carbon foil and the fact that the simulations are done on the quasistatic approximation, which is well-known to blueshift the resonances [27] with respect to real situations.

coexist in the system. As mentioned in section 1.2, the finite resolution of a STEM EELS experiment induces a broadening of the peaks in the EEL spectra. This broadening thus induces a degradation of the spatial coherence in an experimental energy filtered map, which adds to the mode mixing already resulting from the intrinsic virtual character of a SP mode.

However, the characterics of a mode to which STEM EELS is sensitive to (namely, the eigenfrequency, relaxation rate and z-electric field intensity) are plainly sufficient to faithfully characterize the mode. Therefore, if one is able to disentangle the contribution of each mode in a STEM EELS dataset, as will be done in the studies presented in chapters 4 and 5, much information can be gained on a mode. We thus conclude that STEM EELS proves particularly useful for studying the SP modes of finite metal-dielectric systems, which has been demonstrated in many studies, from nanoparticles with simplest shapes [87,88] to complex systems [39,41]. Such studies can bring useful information for photonics applications [117]. They may also reveal modes that cannot be probed by optical tools, the so-called "dark modes" [52, 86, 118]. With the help of monochromators, very low frequency modes can today be probed [119], and their relaxation rate accessed with precision [42]. Furthermore, the magnetic field of a mode, that a simple EELS experiment cannot probe, can be simply accessed by performing EELS on complementary structures [120], and may be available in the future by using fast electrons carrying angular momentum [108, 121].

Moreover, an important point is the clear safe relation between the EEL probability and the EMLDOS. SP modes can be probed at the nanoscale with numerous techniques (for a review, see [16]), including SNOM [85], or Photo-Emission Electron Microscopy (PEEM) [122]. If the EMLDOS has been evoked to interpret SNOM maps [102–104], it turns out that such a relationship only holds in perfect, idealized situations [103]. In practice, the experimental results are strongly affected by the optical setup[29] [123–125]. As for PEEM, it relies on non-linear 2 photon emission processes taking place in metals only. Therefore, it is delicate to compare experimental results obtained with such techniques to the EMLDOS. By extension, they cannot be safely interpreted on the basis of the SP modes. As we have shown in this chapter, this is not the case of STEM EELS measurements.

[29] A SNOM tip does not probe the intrinsic mode of the sample, but a mode of the system encompassing the sample and the tip. Otherwise speaking, the probe is invasive.

# Chapter 3

# A closer view on the experimental techniques

## 3.1 STEM for fast electron based spectroscopies

Figure 3.1 shows a detailed scheme of a STEM dedicated to fast electron based spectroscopies. Before the specimen, a set of magnetic lenses (at least one condenser lens and an objective lens) focuses the electron beam produced by an electron gun onto the sample. These lenses set the illumination conditions (probe size, convergence angle, current). In particular, the objective lens is the strongest lens and aims at demagnifying as much as possible the electron source. An objective aperture introduced in the electron path at the focal plane of the objective lens allows adjusting the illumination (or incident) angle, which in turn affects both the total current to which the sample is exposed and, by minimizing the effect of the spherical aberrations, the probe size. The position of the electron beam over the specimen is changed by deflecting the incoming electron beam with the help of scanning coils. The transmitted electrons elastically scattered at high angles (typically more than 25 mrad) are directly collected, with no intermediate optical elements, by an HAADF detector. An HAADF image is obtained by integrating the signal collected all over this annular detector. On the other hand, the transmitted electrons inelastically scattered at small angles (less than 15 mrad) enter a magnetic spectrometer after having possibly crossed a collector aperture. The size of this aperture fixes the EELS collection angle, which affects both the number of electrons analyzed in EELS and, again, the aberrations. The spectrometer both disperses the electrons at different angles with respect to their kinetic energy and brings the divergent beam back towards the electron axis. The outcoming electrons are then focused onto a scintillator with the help of quadrupoles. The resulting signal is finally imaged on a Charge Coupled Device (CCD) camera, which has a dispersive and non-dispersive direction. The pixels in the non-dispersive direction are binned in order to achieve a spectrum with reduced dwell time and readout noise. CL requires the use of a mirror located very close to the sample, which directs the beam onto a light spectrometer via some light collection system[1]. The geometry of the mirror, which is located around the incoming electron path, defines the CL collection angle. The light is finally focused onto a CCD camera.

[1]This light collection system is crucial for obtaining a satisfactory signal to noise ratio with both high spatial and spectral resolution. The light detection system used in this thesis will be detailed further.

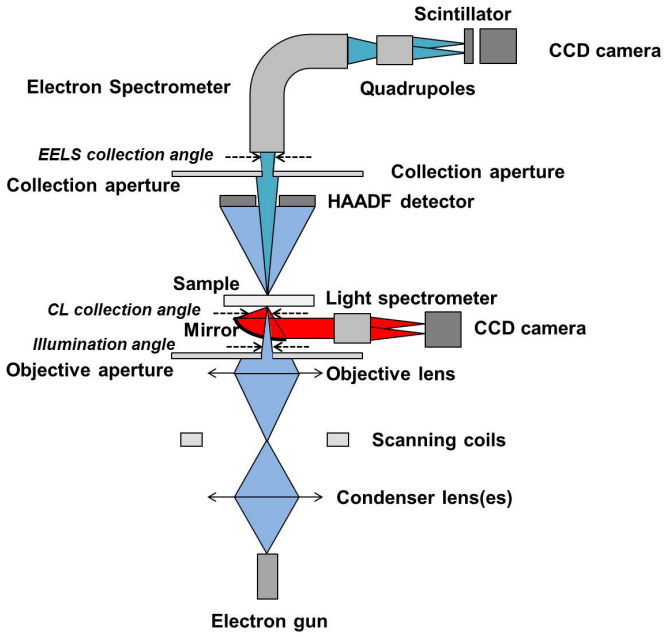


Figure 3.1: Scheme of a STEM dedicated to fast electron based spectroscopies.

The capabilities of a STEM to perform fast electron based spectroscopies can be estimated from various parameters. In particular, valence EELS is strongly affected by the presence of the ZLP as most of the low-energy resonances are masked by the background resulting from its tail [126]. The ability of the technique to study low energy excitations can be estimated from its instrumental impulse response function (also called Point Spread Function (PSF)), which can be safely modelled by an EEL spectrum acquired in vacuum. This EEL spectrum (the so-called "vacuum ZLP") consists of a ZLP whose spectral width is only due to the intrinsic characteristics of the setup. These characteristics include the energy spread of the incoming electrons, the aberrations of the spectrometer and the various instabilities. The natural energetic width of the electrons is inherent to the emission process, which characterizes the electron gun, and thus cannot be avoided. Neverthess, it can be partly limited at the expense of high current by introducing a monochromator within the electron path [127]. An alternative which does not involve the setup of the STEM is the use of deconvolution techniques to process the measured spectra [128]. Furthermore, the instrumental instabilities can be reduced by acquiring spectra with a dwell-time well below half a period corresponding to the mains frequency[2], a capability allowed nowadays by fast acquisition techniques [56]. An additionnal advantage is that, in this case, the direct beam does not saturate the CCD camera, which is a sine qua non to avoid any damaging of the camera. Over the past few years, significant advances have been achieved in extracting a signal of interest in the near IR or visible

[2]In Europe, whose mains standards is 50 Hz, such a condition would correspond to a dwell time being much less than 10 ms.

range with a good signal to noise ratio in the near-IR and visible ranges by using high brightness electron sources, in particular, cold Field Emission Guns (cFEG) or novel acquisition modes [129]. Among these new acquisition modes, the so-called Chrono-SI mode, which permits acquiring several spectra at each probe position [56], has been used in the framework of this thesis. The FWHM of an EELS instrumental impulse response function can today reach 50 meV. Unfortunately, such a value is still insufficient to resolve the low energy excitations, such as phonons and, to a lesser extent, IR SP modes, which remain invariably masked within the tail of the ZLP. Today's state of the art experiment is due to Rossouw and Botton, who observed SP modes down to 0.17 eV [119]. In comparison to EELS, the only limitation for probing low energy excitations in CL resides in the quantum efficiency of the CCD camera used to collect the light. Unfortunately, typical quantum efficiencies tend to strongly degrade in the IR, which also sets a limitation for studying low energy excitations. The main challenge for CL is the optimization of the light transfer efficiency by the light collection setup, as the light emission may be very weak. The signal to noise ratio can also be partly improved by the use of mathematical procedures, such as Principal Component Analysis (PCA) [130]. Moreover, innovative experiments can be performed by introducing optical devices within the light path. These include resolving the polarization [131] or [132]/and [133] the angular pattern, or the quantum character of light [134].

## 3.2 The instruments

The majority of the results presented in this thesis have been obtained using the Vacuum Generators (VG) HB-501 STEM set-up in Orsay, whose picture is shown on figure 3.2a. The VG STEM is equipped with a cold Field Emission Gun (cFEG) and can be operated from 20 to 100 kV. To avoid contamination, ie., deposition of carbonaceous material over the sample surface caused by electron bombardment, the measurements are performed in cold atmosphere, the sample being liquid nitrogen cooled down by a home-made cooling system. The use of a cFEG ensures a high brightness (ie current per unit area per solid angle), on the order of $2x10^9 A.srd^{-1}.cm^2$ at 100 keV, unfortunately rather at the expense of a current stability[3]. The illumination angle can be chosen to be either 7.5 and 15 mrad, depending on the objective aperture used during the measurement. At low illumination angle, the fast electrons can be focussed onto a probe of size down to 0.5 nm. The use of two condenser lenses also allow working in two different modes which notably differ from their convergence angles, thus from the value of the probe current and size.

The peculiarity of the VG STEM is that both its electronics and components are highly customized. In particular, STEM EELS measurements can be achieved in the ChronoSI mode, allowing the acquisition of low-loss spectra with good signal to noise ratio. Beyond all the factors that affect the impulse response of EELS we previously listed in section 3.1, the analysis of low loss spectra is essentially limited by the energy spread of the incoming electrons. The FWHM of the energy distribution of the electrons emitted by the cFEG is of about 300 meV. The collection angles can be set from 7.5 to 15 mrad, depending on the aperture and the condenser mode chosen. Moreover, the VG STEM is fitted with an home made light detection system, which was built up to perform CL with the combined fine spatial resolution and high brightness inherent to a STEM. It has proved to provide unprecedented spatially resolved information on the emission of quantum confined nanostructures [135]. The light detection system is detailed on figure 3.2b. As already noticed, the

[3]The inevitable decrease of current can however be bypassed by "flashing the tip", ie., quickly heating the emitting tip to a high temperature to remove the contamination by gas particles.

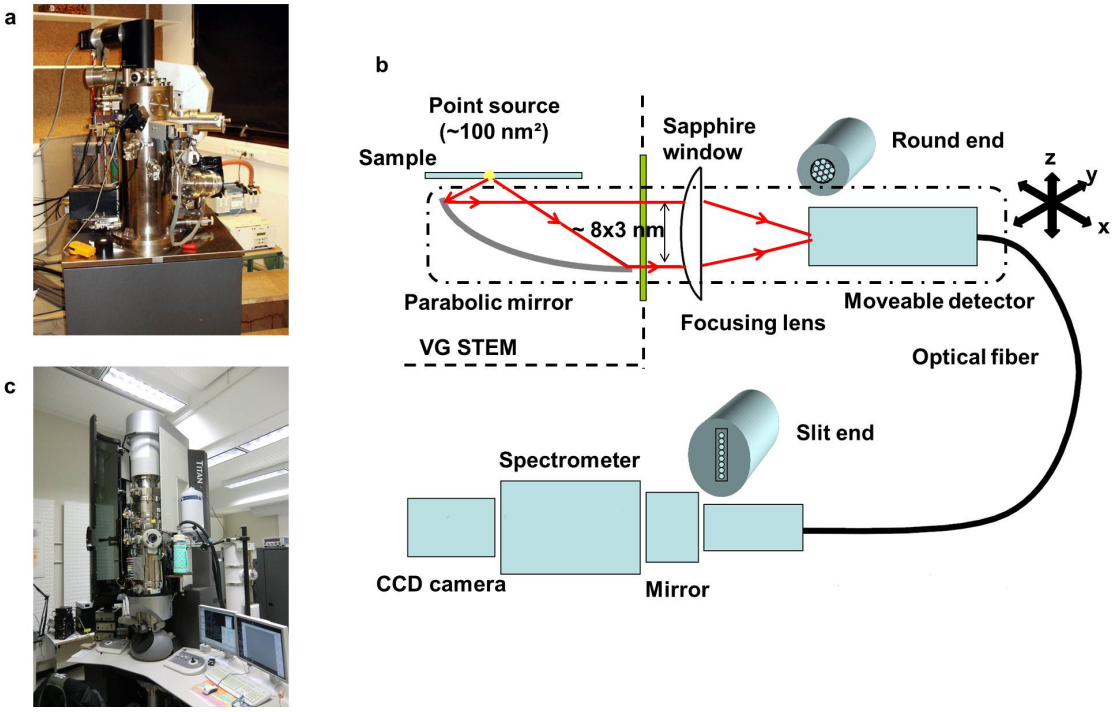


Figure 3.2: a) Photograph of the VG STEM set up in Orsay. b) Sketch of the light detection system fitted to the VG STEM (adapted from an original scheme drawn by Luiz Fernando Zagonel, see text for details). c) Photograph of the FEI TEM set up at Mc Master University.

optimization of the light collection efficiency is the critical point in such light detection system. Here, the use of a parabolic mirror with an high collection angle allows maximizing the redirection of light outside the STEM from a point source located on the sample. This point source has a size ultimately dictated by the diffraction limit and is positionned around the position of the electron beam on the sample. When the focal point of the mirror is set to correspond to the emitting point source, the light exits the STEM through a saphirre window as a parallel beam of size 3 x 8 $mm^2$. The corresponding collection angle is 1.2 srd. This parallel beam reaches a condenser lens. The lens focuses light onto an optical fibre bundle through a round end located at focal distance in order to maximize the collection and guide the optical beam with minimum losses towards the spectrometer. Both the low numerical aperture (NA) of the fibres[4] and their exit slit end ensure a good spectral resolution. A mirror guarantees optimum coupling between the fibre bundle and the spectrometer. Finally, the fixed ensemble {mirror+lens+round end of the optical fiber} is moveable manually in the 3 directions through an home made detector, allowing perfect alignement of the mirror with respect to the light emitting point source, thus maximum light detection. Contrary to EELS, CL spectra are recorded in a simple SI mode, because the absence of the ZLP avoids risking exposing too much the CCD camera.

Some additional experiments were performed at Mc Master University using a FEI Titan TEM

[4]Typical NA is 0.12.

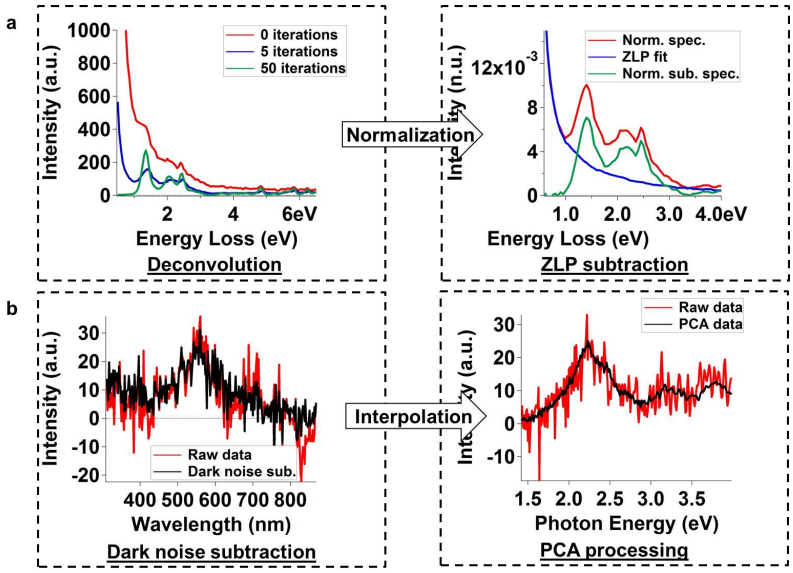


Figure 3.3: Preliminary processing. a) EELS. Each spectrum is deconvolved with an iterative Richardson-Lucy algorithm by a vacuum ZLP. Each deconvolved spectrum is then normalized with respect to the signal integrated over all the energy channels, which is roughly proportional to the incoming current. The tail of the ZLP is finally fitted over a given energy range, and subtracted. b) CL. The CCD dark noise is removed by subtracting to each spectrum a mean spectrum recorded in vacuum with similar acquisition conditions. Each spectrum is then interpolated to obtain a constant dispersion step in eV, and finally processed using PCA analysis in order to improve the signal to noise ratio.

working in STEM mode (figure 3.2c). The FEI TEM can be operated from 80 kV to 300 kV. With regards to the VG STEM, the FEI TEM is equipped with a Wien-filter type monochromator located directly behind a Field Emission Gun (FEG) [136], allowing the acquisition of EELS spectra with narrow ZLP. With the monochromator on, the probe size is around 2 nm, and the FWHM of a vacuum ZLP is on the order of 100 meV. Yet equipped with a light injection system [137], the FEI TEM does not allow at the moment STEM CL experiments. The STEM EELS measurements can be achieved in a SI mode only.

## 3.3 Data processing

### 3.3.1 Preliminary processing

#### EELS

In the case where the dataset was acquired in the ChronoSI mode, the spectra of the ChronoSI are first all aligned with respect to each other using Digital Micrograph homemade scripts. The spectra corresponding to a given probe position are then summed to obtain a simple SI. The

situation is basically the same if the dataset was not acquired in the ChronoSI mode, except that the spectra directly belong to a SI, and are possibly summed with their close neighboors to increase the signal to noise ratio. The spectra are calibrated with respect to the maximum amplitude of the spectrum, occuring at 0 eV energy loss, using the CCD dispersion of the experiment. The following steps are illustrated on figure 3.3a. Each spectrum of the obtained SI is deconvolved with an iterative Richardson-Lucy algorithm by a spectrum recorded in vacuum (a vacuum ZLP) [128]. The deconvolution process decreases the tail of the ZLP, thus increases the signal to background ratio, and improves the spectral resolution (see section 3.4). In principle, the more the iterations, the better the result. However, care has to be taken as a large number of iterations (typically 5 to 10) induces ring effects[5] which may blur the physical signals. The ZLP is also deconvolved with itself with the same number of iterations, thus giving a deconvolved vacuum ZLP, which sets the PSF of the experiment. Following data processing is performed with routines previously programmed and implemented in IGOR Pro 6.2 software (WaveMetrics$^{TM}$) by Stefano Mazzucco [41]. Each deconvolved EEL spectrum is first normalized with respect to the signal integrated over all the energy channels, which is roughly proportional to the incoming current. The tail of the ZLP is then fitted over a given energy range based on the deconvolved vacuum ZLP. The fitted ZLP is then subtracted in the whole energy range. The obtained normalized and subtracted spectra are EEL probability spectra and are stored in a new SI.

**CL**

Each CL dataset was recorded in a SI mode. Using Digital Micrograph, the spectra are properly calibrated from a reference spectrum, recorded from a UV lamp with similar acquisition conditions, before being transferred to IGOR Pro. The following steps are illustrated on figure 3.3b. The CCD dark noise is removed by subtracting to each spectrum of the SI a mean spectrum recorded in vacuum with similar acquisition conditions. The dispersion has a constant step in wavelength. The spectra are thus interpolated to have a constant dispersion step in eV, which is a necessary condition to process the data using previously written routines. The resulting SI is finally processed using PCA in order to improve the signal to noise ratio (see the spectra on figure 3.3b) [130][6]. It should be noticed that, because no normalization of the CL intensity is achieved, the spectra are not EIRE probability spectra. We will thus refer to them as CL spectra.

### 3.3.2 Data manipulation/multipeak fitting

A SI is easily manipulated using Stefano Mazzucco's IGOR Pro EELSLL toolbox. Filtering a SI at a given (x,y) pixel allows access to a local spectrum[7], while filtering the SI at a given energy value results in an energy filtered map (see section 1.1). The sample morphology during acquisition is indicated on an energy filtered map by superimposing the contour of the metallic objects obtained after thresholding and binarizing the HAADF image recorded during the measurement (see figure 1.2). Multipeak fitting is eventually performed in a SI, as illustrated on figure 3.4). Precisely, for all the results shown in this thesis, a sum of Gaussian functions and a sigmoid background is fitted

[5]Ring effects are due to some noise amplification of noisy data by the deconvolution algorithm (see the peaks appearing below 4eV in the 50 iterations deconvolved spectrum of figure 3.3a)

[6]Care is taken to retain a rather large number of components to avoid distorting the data.

[7]All along this thesis, the presented "local" spectra are actually spectra averaged over a few pixels in order to display a better signal to noise ratio.

in each spectrum[8]. Conditions on minimum noise level, number of binomial smoothing operations and maximum number of peaks are imposed. The amplitude, center and FWHM of each Gaussian function, qualified in the following as the amplitude, (central) energy and FWHM of the peaks, are stored within new SI, in the raw corresponding to the spectrum (or probe position) they belong to. Only a part of these parameters corresponding to the Gaussian functions whose center is found in a given energy range and whose FWHM is between two given values can possibly be retained. Maps of the amplitude, central energy and FWHM of the corresponding peaks can thus be obtained by attributing to a given pixel of these maps the amplitude, central energy and FWHM of the peak which was fitted in the spectrum corresponding to the same (x,y) position of the datacube. In this case, care is taken that only one fitted Gaussian function has its center in the retained energy range. If no peak has been found in this energy energy range, the pixel is either blanked if the material at the corresponding probe position is metallic, greyed if the material at the corresponding probe position is dielectric. The nature of the locally probed material is known from the binarized HAADF image. The sample boundary profile is also superimposed for clarity.

## 3.4 Spectral resolution

In a measured spectrum, the peaks are broadened by the finite energy resolution of the experimen. This spectral resolution can be estimated from the PSF of the measurement. Therefore, for a non-deconvolved STEM EELS dataset, this spectral resolution is limited, as previously said, by the energy spread of the incoming electrons, the aberrations of the spectrometer and the various instabilities. However, for a STEM CL measurement, the spectral resolutions is only affected by the aberrations of the spectrometer and the alignment of the light detector. In particular, the spectral resolution does not depend on the energy spread of the incoming electrons and is thus much better than a typical EELS spectral resolution. Precisely, STEM CL reaches spectral resolutions on the order of a fracion of meV, thus induces a negligible peak broadening when studying SP modes. Bosman et al. proposed a precise scheme to obtain quantitatively the real FWHM from the measured peaks in monochromated STEM EELS measurements [42]. However, in this thesis, a much simplified procedure, which aims by no means of being quantitative, will be used.

Mathematically, the peaks obtained in a spectrum are the result of the convolution product between some intrinsic, physical peaks and the instrumental impulse response function. We will simply assume that the spectrum one would ideally measure with an infinite resolution is a sum of Gaussian functions, and that the impulse response of the technique is also a Gaussian function centered at 0 eV. In this case, a measured spectrum is also a sum of Gaussian functions. As compared to the ideal spectrum, each function has an unchanged center energy but a FWHM equal to the square root of the sum of the squared FWHM of the ideal Gaussian function and the squared FWHM of the impulse Gaussian function. On the contrary, assuming that the spectrum one actually measures is approximately a sum of Gaussian functions, the FWHM of each physical peaks can be estimated from the square root of the subtraction of the square of the FWHM of the measured peaks and the square of the FWHM of the impulse response[9].

[8]Notice that such a fitting operation allows detecting not only frank peaks, but also shoulders (see the spectra on figure 1.2). It is thus able to identify peaks separated by energies lower than the spectral resolution of the experiment.

[9]Importantly, such an estimation can only be trusted if the deconvolved FWHM obtained is less than the spectral resolution of the measurement [42].

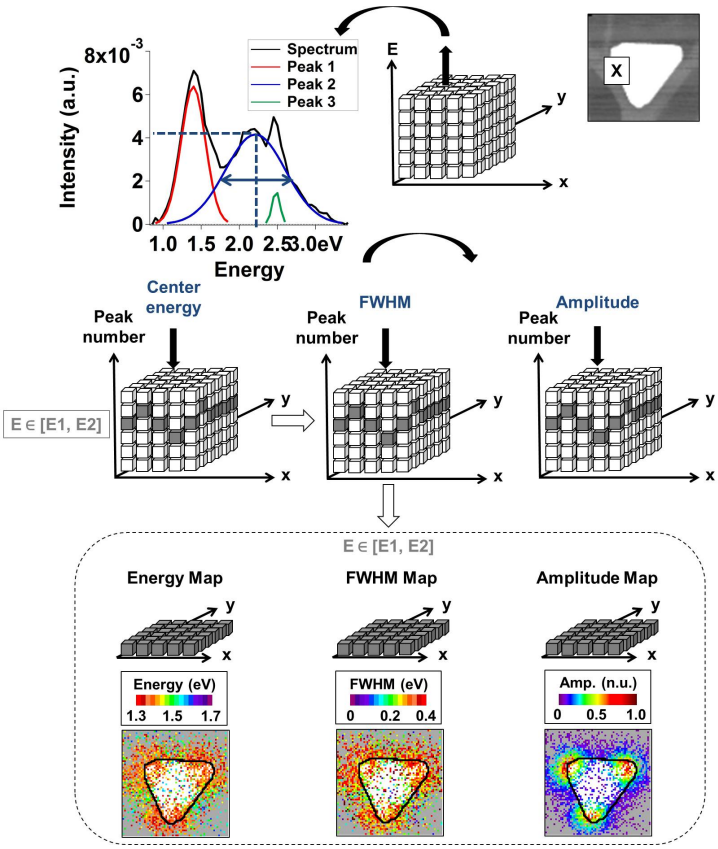


Figure 3.4: Multipeak fitting. A sum of Gaussian functions and a sigmoid background is fitted in each spectrum. The amplitude, center and FWHM of each Gaussian function, are stored within new SI, in the raw which corresponds to the spectrum (or probe position) they belong to. Maps of the amplitude, central energy and FWHM of the corresponding peaks can thus be obtained by attributing to a given pixel of these maps the amplitude, central energy and FWHM of the peak which was fitted in the spectrum corresponding to the same (x,y) position of the datacube.

In EELS, the PSF is the deconvolved vacuum ZLP, (see section 3.3), whose FWHM thus gives the spectral resolution of the dataset. It should be noticed that, because the deconvolution induces a slimming of the ZLP which depends on the number of iterations, the FWHM and amplitude of the peaks in a deconvolved EELS dataset also depend on the number of iterations. Precisely, the FWHM decreases and the amplitude increases when the number of iterations increases. However, the slimming of the PSF clearly partly compensates these changes. The extraction of quantitative physical amplitudes and FWHM from deconvolved datasets remains an open question, that we will move away by stressing, again, the qualitive character of the results presented in this manuscript.

In CL, the response function can be known from a spectrum recorded from a UV lamp. Assuming that the emission lines are in principle infinitely thin, the spectral resolution can be simply estimated as the measured FWHM of the emission lines.

# Chapter 4

# Fast electron based spectroscopies: nanometric optical spectroscopies for mapping SP modes

## 4.1 Introduction

### 4.1.1 Positioning of this study

Chapter 2 aimed at developping how STEM EELS probes the SP modes of a metal-dielectric system, which is now pretty much understood in the light of the theory elements presented. Precisely, the spectral and spatial variations of the EEL probability directly reflect the spatial and spectral properties of the SP modes of a system. Such an interpretation was based on a modal decomposition of EELS in terms of quasistatic SP modes that has has not been extended to other techniques so far.

However, a similar modal decomposition would also be very handy to interpret experimental results obtained with STEM CL. Indeed, well before STEM EELS was demonstrated to map SP modes, Yamamoto et al. observed light emission resulting from the interaction between fast electrons and a silver nanosphere [131]. Very similarly to STEM EELS, they demonstrated the appearance of peaks in the light spectra whose respective intensities vary with the electron probe position. The position of these peaks were also found to depend on the sphere size. Furthermore, they could also resolve very characteristic patterns when observing the spatial variations of the light intensity at the resonance wavelengths of those peaks. These results were in accordance with the relativistic theory of electron mediated emission of light by a dielectric sphere proposed by García de Abajo [67], Fuchs and Kliewer's theory of the normal modes of a dielectric sphere [68] as well as the Mie theory for absorption and scattering of light [9, 10]. As a consequence, the light emission was well understood as being the result of the coupling between the electrons and the SP modes of the nanosphere, and the wavelength filtered maps as being the maps of the dipolar and quadrupolar SP modes of the sphere. Several years after these pioneering findings, Vesseur et al. made very similar observations on gold nanowires [43]. These works were then followed by a number of studies involving single nanoparticles of various shapes and sizes using STEM CL [51, 130, 138–141].

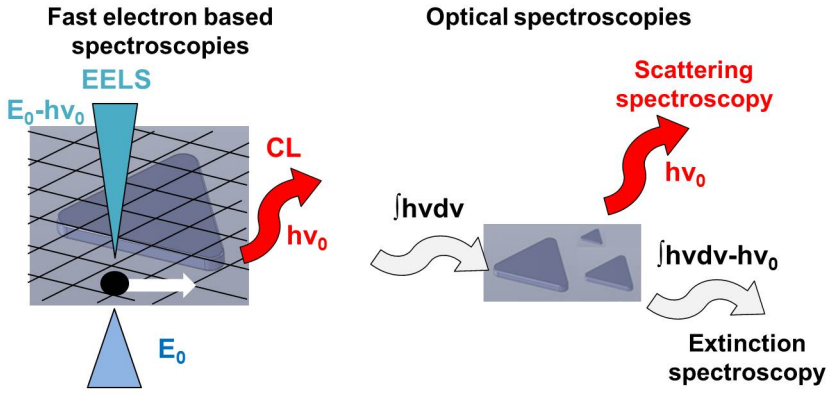


Figure 4.1: Fast electron based spectroscopies and optical spectroscopies. STEM EELS and CL can be intuitively thought of as being the nanometric equivalent of extinction and scattering spectroscopies.

As a first step towards a universal interpretation of CL in terms of modes, a connection between the probability of emitting a photon through a coherent process (see section 1.3), that we will refer to as the EIRE probability, and a radiative EMLDOS (rEMLDOS) was proposed in [44]. The rEMLDOS is a notion one can find trace of sporadically in the litterature [142], involving the radiative decay rate of quantum emitters [143–145]. However, no generic definition of the rEMLDOS involving the Dyadic Green function of the system has been proposed so far. At this time, it seems well established that CL would measure the rEMLDOS of the sample [146,147], yet no general proof of this statement has been established theoretically for an arbitrary system. Despite such lack, CL experiments are commonly compared to EMLDOS calculations [148, 149], often with success.

On the other hand, fast electron based spectroscopies are often compared to optical spectroscopies, whether experimentally [150–152], numerically [115, 118, 138] or theoretically [153]. Calculated EELS or CL and optical cross section spectra often show similar resonances for a light propagation direction parallel to the electron trajectory direction. Therefore, fast electron based spectroscopies should probe the optical properties at the nanometer scale, except that fast electron based spectroscopies may detect some modes that cannot be probed by optical tools [118, 138].

To go further, we can make a distinction between EELS, CL, extinction spectroscopy and scattering spectroscopy. Intuitively, following the sketch shown on figure 4.1, EELS should be related to extinction spectroscopy, while CL should be related to scattering spectroscopy. However, a demonstration would first of all require a comparison of EELS and CL results obtained on the very same object. Such comparison has been already adressed in the past by pure numerical simulations [59] and combined experiments and simulations [154]. Precisely, common points and differences between both techniques have been pointed out. However, no theoretical framework suitable for interpreting such observations has been given so far. Furthermore, the measurements reported in [154] were performed on slightly dissimilar nanoparticles, while it is known that small changes in the dimensions and dielectric environment of a nanoparticle may affect its SP modes [155] (see also chapter 6). Broadly speaking, no combined STEM EELS and CL experiment on the same system has been performed yet.

In this chapter, we will show that fast electron based spectroscopies can be viewed as nanometric equivalent of optical spectroscopies for mapping SP modes. More precisely, we will show that EELS

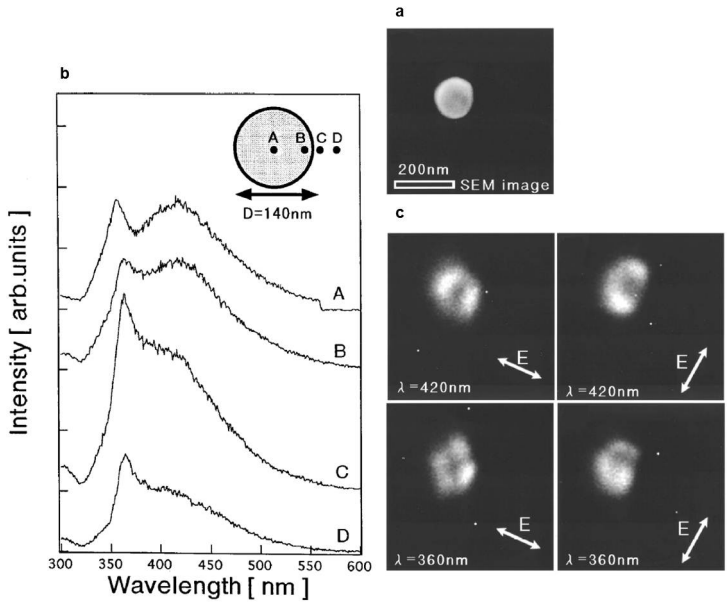


Figure 4.2: STEM CL on a silver nanosphere, extracted from [131]. a) Secondary Electron Emission (SEE) image of the nanosphere. b) CL spectra corresponding to electron probe positions located at various locations with respect to the sphere. c) Energy filtered maps of the CL Intensity at different polarizations for photon wavelengths of 420 nm and 360 nm.

is some nanometric equivalent of extinction spectroscopy, and that CL is some nanometric equivalent of scattering spectroscopy. In order to do so, we will present, justify and analyze the results of the first combined EELS and CL experiment on the very same object, that we will then relate to extinction and scattering. To do so, we will base on experiments, numerical simulations and theory. Our experimental work bases on the unique possibility of performing STEM EELS and CL using the same STEM. The numerical simulations and theory rely on the Boundary Element Methods (BEM) framework, in the framework of which EELS and CL [20], but also optical spectroscopies [116], can be directly expressed.

### 4.1.2 CL, EMLDOS and radiative SP modes

The results obtained by Yamamoto et al. are reproduced on figure 4.2. Figure 4.2a shows the Secondary Electron Emission (SEE) image[1] of a gold nanosphere. The light spectra acquired for different probe locations with respect to the sphere are shown on figure 4.2b. Finally, the wavelength filtered maps of figure 4.2c display the spatial variations of the light intensity whose polarization is filtered with a polarizer at the wavelengths of these peaks. These maps mean that the fast electrons are most likely to induce photons of precise energies when they are directed to particular nanometric locations around the nanoparticle. The underlying characteristic patterns are a good reminder of the dipolar and quadrupolar normal modes of a sphere [68].

[1] In such an image, the sphere appears bright over a dark background.

Based on this ability of STEM CL to reflect the spatial and spectral properties of the SP modes very similarly to STEM EELS, it is very tempting to extend the link STEM EELS and EMLDOS share to STEM CL. The relation between STEM EELS, STEM CL and EMLDOS is straightforward in the case of a non-dissipative dielectric nanoparticle. In this case, the EIRE probability equals the EEL probability [36, 67, 156, 157], and is thus proportional to the generalized projected LDOS given by equation 2.5.11. Furthermore, the non-dissipative modal decomposition of the electric Green function given by equation 2.4.11 holds. As a consequence, forgetting the Fourier transform, the EIRE probability at the energy corresponding to the eigen frequency of a mode gives the z projected electric field intensity of the mode.

However, as previously demonstrated in the last section, dissipation brings significant difficulties which have to be included in the case of SP modes. In dissipative systems, the only remaining certainty is that each process responsible for photon emission is also responsible for electron energy loss, yet the reverse is not true anymore. If we base on the extended yet intuitive definition of a SP mode in a relativistic approach we gave on subsection 2.3.5, a very intuitive difference between EELS and CL is that CL should detect only the radiative modes[2] [12]. This last remark has been confirmed in a particular case by Myroshnychenko et al, who performed STEM EELS and STEM CL simulations on a gold nanodecahedron, and evidenced a mode probed in STEM EELS yet absent in STEM CL [154]. Interestingly, they could also evidence a slight shift in the resonances of the EEL and EIRE probabilities apparently associated to a same radiative mode. This point will be examined and clarified in this chapter, which relies on the study of a simple model system, namely, a gold triangular nanoprism relying on a thin carbon foil.

Such system has been chosen because metallic triangular nanoprisms of various sizes and shapes have been studied extensively in the literature, most particularly using fast electron based spectroscopies, which demonstrated clear resonances [38, 40, 45–52] associated to some SP modes which at present have been well discussed. Nevertheless, it should be noticed that, as compared to the nanoprism tackled as an example in chapter 2, the studied nanoprism is made up of different metal (gold instead of silver) and has completely different dimensions. If we take back our approach exposed in subsection 2.3.2, we have to change in consequence the dispersion curve of an infinite film. The SP modes of the gold thick nanoprism that we will adress in this chapter thus have completely different eigenfrequencies as compared to the silver thin nanoprism of chapter 2. Despite such a difference, this simple object will also constitute, as part of this thesis, an illustrative and comprehensive example of how the SP modes can be directly accessed from a dataset.

Preliminary combined EELS and CL measurements were achieved using the VG STEM by Luiz Fernando Zagonel, who is currently at the Instituto de Física "Gleb Wataghin", Universidade Estadual in Campinas. These first observations were confirmed by following experiments performed with the author, who took care of the data processing and worked out on the theoretical elements with Mathieu Kociak, following some suggestions from Javier García de Abajo. The nanoprisms were synthesized chemically by Benito Rodriguez-Gonzalez and Luis M. Liz-Marzan the Departamento de Quimica Fisica at the Universidade de Vigo. Details can be found in [154]. Finally, numerical simulations of STEM EELS, STEM CL and optical properties were performed by Viktor Myroshnychenko and Javier García de Abajo at the Instituto de Química-Física Rocasolano of the Consejo Superior de Investigaciones Científicas in Madrid.

In section 4.3, results of experiments and numerical simulations of STEM EELS and CL on the

[2]Such radiative and non-radiative modes may also be called "bright" and "dark" modes. Nevertheless, we will keep these denominations to some modes which respectively can and cannot be excited by a plane wave with a given direction and polarization.

gold triangular nanoprism will be exposed. Common points and differences between both datasets will be noticed. Numerical simulations of the extinction and scattering cross sections calculated for a similar object will be compared to EELS and CL. Some differences evidenced between the extinction and scattering cross sections will be found to match the differences existing between EELS and CL. These observations will be explained in section 4.4. A theoretical justification will be given based on a comparison between the modal decomposition of EELS given in chapter 2 and original modal decompositions of CL, extinction and scattering. The whole chapter will set EELS and CL as nanometric equivalents of bulk optical spectroscopies for mapping SP modes.

## 4.2 Methods

### 4.2.1 Access to the nanoprism dimensions

The dimensions of the nanoprism were deduced from some HAADF images of the nanoprism (see section 4.3). A top-down view of the nanoprism was accessible directly from the nanoprism relying completely on the carbon foil. Well after the measurements, the carbon foil was deliberately damaged by extreme illumination conditions. This led to the destruction of the carbon foil and the subsequent tilt of the nanoprism, allowing access to a side view of the nanoprism

### 4.2.2 Experiments

STEM EELS and CL were performed successively on this nanoprism. Importantly, the nanoprism was lying completely on the whole carbon foil during both measurements. Furthermore, care was taken that the exact shape of the nanoprism and the direct dielectric environment was not affected by the measurements, which were checked for not having induced any contamination [155]. The incidence angle and acquisition time have been taken much higher for the CL measurement than for the EELS measurement to ensure obtaining a sufficient signal in CL. This suggests that the SP modes of the particle induce very weak light emission. As the complete scanned area was taken roughly equal during both measurements (EELS: 150x150 nm, CL: 180x180 nm), the sampling step had to be taken larger during the CL measurement to keep both the sample spatial drift and decrease in the incoming current acceptable. However, as the spatial resolution in CL is degraded by the high incidence angle, the sampling step is probably not too much different from the actual spatial resolution for both measurements. The sampling step is equal to 2.4 nm for the EELS dataset, 5.6 nm for the CL dataset. Finally, the spectral resolution is 180 meV for EELS, 30 meV for CL.

### 4.2.3 Numerical simulations

Numerical simulations were performed by our collaborators using a full relativistic 3D BEM [158], by modelling a gold nanoprism embedded in vacuum[3]. The dielectric function of gold was taken from [74]. Due to the large angles in the shape of the side, the nanoobject was approximated as being invariant along the z axis. Except from this deviation from the real geometry of the

[3]Although amorphous carbon shows some optical response around the visible range, the thickness of the foil on which the triangular nanoprism stands is no more than 5 to 10 nm. Some substrate effect, which tends to redshift the resonance associated to a given mode [115], can thus be considered to be negligible in our case. The carbon foil was indeed neglected in the numerical simulations for simplicity.

nanoprism, the thickness and in-plane dimensions were taken equal to the dimensions indicated on figure 4.3. STEM EELS and CL experiments were modelled by computing a complete set of EEL and EIRE probability spectra, each one corresponding to a given electron impact parameter. Simulated SI were thus built, then processed similarly to an experimental SI (see section 3.3.2). The optical properties of the system were also simulated by calculating extinction, scattering and absorption cross sections, as well as the electric fields induced by a monochromatic plane wave excitation. Details can be found in appendix B.

### 4.2.4 Theory

The theory will be based on a BEM framework in the quasistatic approximation [72]. In such framework, the electric field induced by a given external source can be determined from the Poisson equation, which reads in Fourier space:

$$\vec{\nabla}.\left[\tilde{\varepsilon}(\vec{r},\omega)\vec{\nabla}\phi(\vec{r},\omega)\right] = -4\pi\rho_{ext}(\vec{r},\omega) \tag{4.2.1}$$

where $\tilde{\varepsilon}(\vec{r},\omega)$ is the global dielectric function given by equation 2.2.4 and $\rho_{ext}(\vec{r},\omega)$ is the external source term. The Fourier transform of the electric potential $\phi(\vec{r},\omega)$ is related to the Fourier transform of the electric field $\vec{E}(\vec{r},\omega)$ through the relation:

$$\vec{E}(\vec{r},\omega) = -\vec{\nabla}\phi(\vec{r},\omega) \tag{4.2.2}$$

We justify the use of the quasistatic approximation for explaining our experimental observations from the fact that the object we consider is small. It also shows the strong advantage that it allows the use of modal decompositions [37].

## 4.3 EELS and CL on a single gold nanoprism: experiments and simulations

### 4.3.1 Introduction

In the following, some results from STEM EELS and STEM CL measurements performed on a single triangular gold nanoprism will be presented in subsections 4.3.2 and 4.3.3, before being compared to some numerical simulations of EELS and CL in subsection 4.3.4 as well as of extinction and scattering in subsection 4.3.5. In subsection 4.3.2, we will also show how to precisely access the modes within an EELS dataset, based on the theory elements presented in chapter 2. We will show that such approach, which can be intuitively extended, holds to CL, despite slight differences.

Yet several nanoprisms have been studied experimentally to check the validity of the results, only one nanoprism will be considered. We leave a few other examples to appendix B. Two HAADF images of the nanoprism are shown on figure 4.3a, together with some characteristic dimensions. For clarity, the nanoprism standing on a thin carbon foil is sketched in 3 dimensions on figure 4.3b.

### 4.3.2 EELS measurements

Figure 4.4a shows an HAADF image of the nanoprism acquired just before the STEM EELS measurement. EEL probability local spectra corresponding to probe positions located at the tip (red,

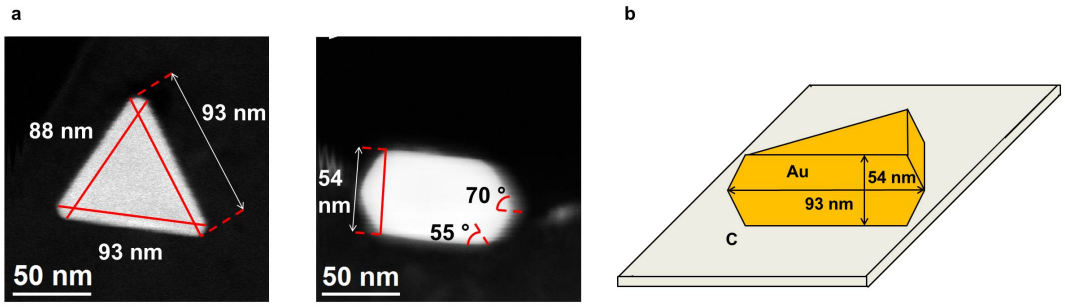


Figure 4.3: Geometry of the gold triangular nanoprism. a) HAADF images showing the top view (left) and the side view (right) of the gold triangular nanoprism. Some characteristic dimensions are added. b) Sketch of the nanoprism in 3 dimensions.

tip EEL spectrum), at the edge (blue, edge EEL spectrum) and at the centre (green, centre EEL spectrum) of the nanoprism are shown on figure 4.4b. A single resonant peak clearly appears at each probe position. The spectral characteristics of the peak depends on the electron probe location. In particular, the peak clearly blueshifts from the tip spectrum to the edge spectrum, then to the centre spectrum. The additionnal shoulders possibly appearing in the spectra are due to some imperfections in the subtraction of the ZLP. This is most particularly true for the case of the centre spectrum, which is by far the noisiest of the three spectra, because the high thickness of the nanoprism resulted in a large number of electrons diffracted at large angles, that did not reach the spectrometer. The precise spectral characteristics of each peak shown on the spectra have been obtained by performing multipeak fitting. They indicate three distinct resonances, each one having its own center energy and FWHM.

The energy filtered maps of figure 4.4c display the spatial variations of the EEL probability when filtered at the three center energies of these resonances. The first map clearly shows local spots where the EEL probability is high located at the tips, suggesting that the resonance is due to some dipolar SP mode[4]. In our case, the equilateral geometry of the nanoprism induces a degeneracy of three of such dipolar modes, the superposition of which will be referred to as a Tip mode for simplicity. The EEL probability increases around the edges of the nanoprism on the second map, despite the fact that local maxima at the tips are still dominant, in accordance with the observations of [51]. Notice that the peaks in the tip spectrum and in the edge spectrum have close resonance energies and quite broad spectral widths. As a consequence, as the maximum amplitude of the tip peak is almost two times higher than the maximum amplitude of the edge peak, the tail of the tip peak outbalances the edge peak. This is a typical example of loss of spatial coherence induced by both the intrinsic dissipative character of a SP mode and the finite spectral resolution of the experiment that we discussed in section 2.4: the center map gives a mix of the intensities of the electric fields induced by the Tip mode and a SP mode most probably located at the edges of the nanoprism. We will thus call this mode Edge mode[5]. Finally, the third map displays a rather

[4]A word of caution should be said at this point: despite the strong similarity between this first map and the first map of figure 2.1c, no conclusion can be drawn on the precise nature of the SP mode. Indeed, as previously underlined, both nanoprisms have radically different dimensions. In particular, the quasistatic nature, or either the symmetric or antisymmetric character of the SP mode cannot be simply inferred from this energy filtered map.

[5]Once again, nothing can be simply inferred about this apparent Edge mode, as it may result from the superpo-

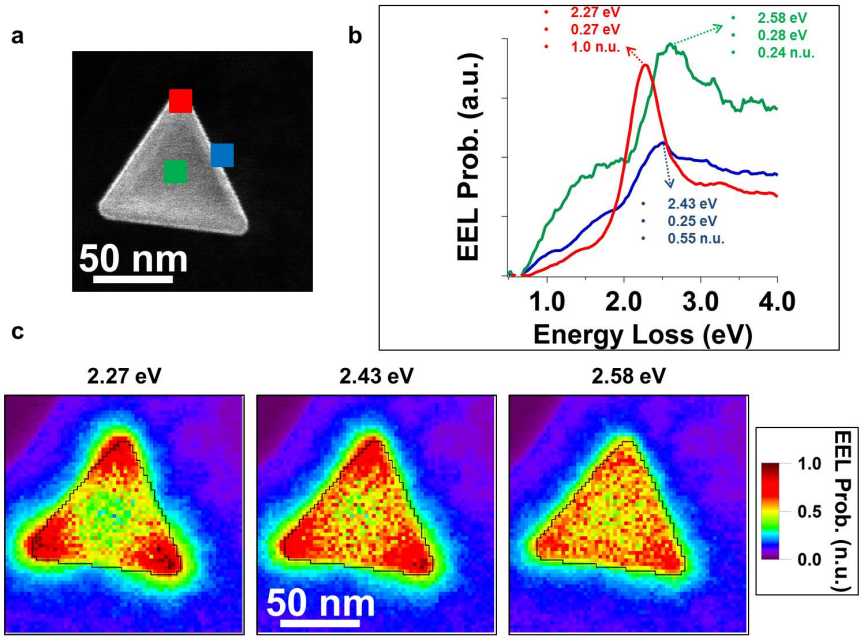


Figure 4.4: STEM EELS measurements on the gold nanoprism. a) HAADF image of the nanoprism acquired before the measurement. b) EEL probability spectra corresponding to electron probe positions located at the tip (red), at the edge (blue) and at the centre (green) of the nanoprism. c) Energy filtered maps of the EEL probability for the energy loss values of 2.27 eV, 2.43 eV and 2.58 eV.

futureless pattern in which the signal spreads all over the nanoprism. It most probably results from the additive contribution of a large number of SP modes with very similar resonance frequencies, as expected from the asymptotic behaviour of the dispersion curves of figure 2.3. The third resonance, in fact, is very close to the value of the loss peak which has been previously measured in gold films [159], different from the bulk plasmon resonance, and which corresponds to the frequency of the asymptote of a single interface SP mode.

To clearly reveal the modes, multipeak fitting was performed in each spectrum of the dataset following the method described in subsection 3.3.2. Extending the quasistatic theory of chapter 2, we may interpret the central energy, FWHM and amplitude of each peak as some resonance energy, broadened spectral width and local value of the projected electric field intensity, all these three parameters being characteristic of the SP mode locally excited at the corresponding probe position. Figure 4.5 shows maps of the central energy, FWHM and amplitude of the peaks of the EEL spectra whose central energy and FWHM match the resonances appearing in the Tip EEL spectrum (up) and in the Edge EEL spectrum (down)[6]. Following the theory of chapter 2, these maps thus respectively show some resonance energy, broadened spectral width and spatial variations

sition of some degenerate quadrupolar [38, 40] or higher order [51] modes.

[6]Obtaining such maps requires filtering the complete fitted dataset as exposed in subsection 3.3.2. In the present case, the retained peaks have center energies corresponding to the resonance energies indicated in the spectra +/- 0.10 eV and FWHM higher than the spectral resolution of the experiment.

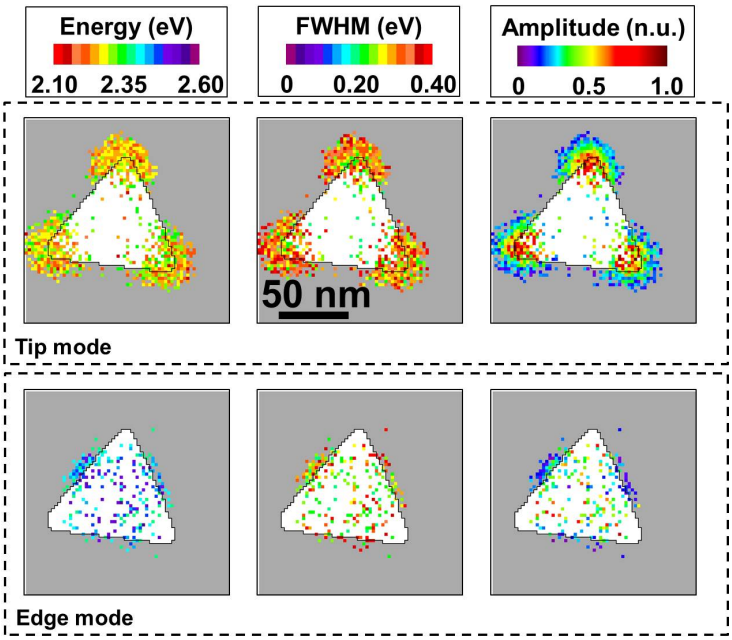


Figure 4.5: EELS multipeak fitting. Maps of the energy, FWHM and amplitude of the peaks whose central energy and FWHM match the resonances appearing in the Tip EEL spectrum (Tip mode) and in the Edge EEL spectrum (Edge mode).

of projected electric field intensity inherent to two SP modes: the Tip mode and the Edge mode. As clear from these maps, the resonance appearing in the Tip spectrum is found for all electron probe locations located around the three tips of the nanoprism, and the amplitude of the resonance increases at close proximity to the tips. This means that the electric field of the Tip mode increases locally around the three tips of the nanoprism[7]. From a similar argument, the electric field of the Edge mode is found to increase around the three edges of the nanoprism.

### 4.3.3 CL measurements

Figure 4.6a shows an HAADF image of the nanoprism acquired just before the STEM CL measurement[8]. CL local spectra corresponding to probe positions located at the tip (red, tip CL spectrum), at the edge (blue, edge CL spectrum) and at the centre (green, centre CL spectrum) of the nanoprism are shown on figure 4.6b. Similarly to the STEM EELS results, a probe position located at the tip induces a single peak. Nevertheless, each of the edge and centre spectra show at least two clear resonances. The spectral characteristics of the peaks, as obtained from multipeak

[7]Notice that the proper access to the mode requires fitting the dataset, as the energy filtered map at the EELS resonance energy of the Tip mode shown on figure 4.4c shows a blurred mix of modes.

[8]The unclear contours of the object are attributable to the high incident angles adopted during the measurement, resulting in a poor spatial resolution.

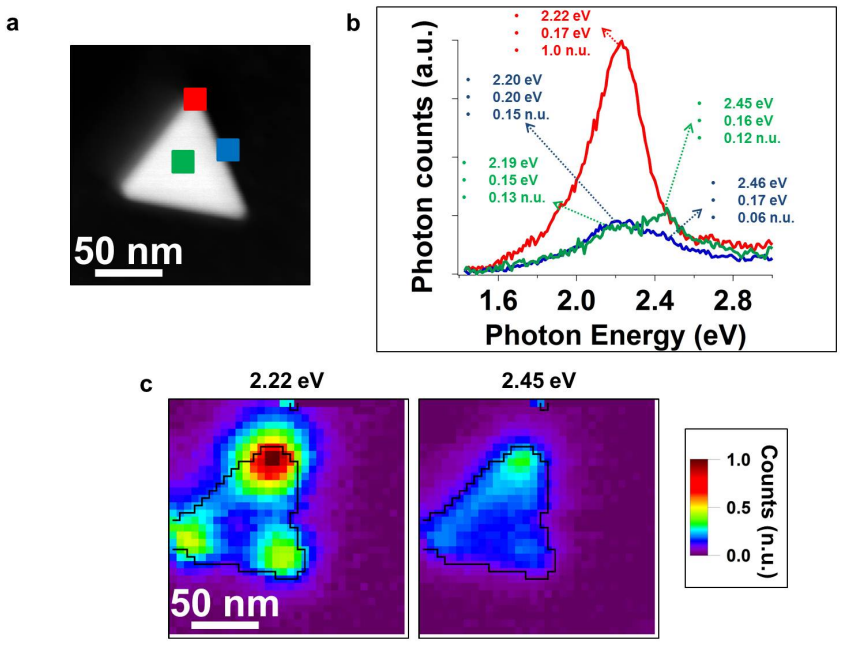


Figure 4.6: STEM CL measurements on the gold nanoprism. a) HAADF image of the nanoprism acquired before the measurement. b) CL spectra corresponding to electron probe positions located at the tip (red), at the edge (blue) and at the centre (green) of the nanoprism. c) Energy filtered maps of the CL Intensity for the photon energy values of 2.22 eV and 2.45 eV.

fitting, are indicated on the spectra. One clearly sees that the peaks measured in STEM CL are globally redshifted and much narrower than the peaks measured in STEM EELS. The large difference in the spectral resolutions of the experiment prevents from ascribing these changes in spectral width to physical phenomena. However, such difference cannot explain the spectral shift between both sets of results, on which we will come again later. Contrary to EELS, only two resonances are perceptible in the overall three spectra. The lowest energy peak is the peak apparent in the tip spectrum, that is observed as a shoulder of variable intensity when the electron probe is focussed at the edge and at the centre of the nanoprism. The highest energy peak is the dominant peak when the electron probe is focussed at the centre of the nanoprism, minority when the electron probe is focussed at the edge and apparently absent when the electron probe is focussed at the tip of the nanoprism.

The energy filtered maps of figure 4.6c display the spatial variations of the EEL probability when filtered at the two resonance energies[9]. The first map still clearly shows spots located at the tip, which decrease in intensity in the second map, yet they still dominate the contrast[10].

Very naturally, we can extend the analysis we made on the EELS dataset to the case of the CL

[9]The distortion in the sample profile obtained from the HAADF image acquired simultaneously is due to the long acquisition time during which the sample is subject to drift.

[10]Notice that the spectra are not normalized with respect to the incoming electron probe current, which strongly decreased during the acquisition. This may explain the high intensity observed at the upper tip as compared to the bottom tips.

dataset. Figure 4.7 shows maps of the energy, FWHM and amplitude of the peaks whose central energy and FWHM match the resonances appearing in the spectra. The amplitude maps exhibit patterns closely ressembling the amplitude maps of figure 4.5. Precisely, strong local maxima are located at the three tips of the nanoprism in the amplitude map of the first resonance. Contrary to EELS, peaks have also been fitted inside the nanoprism, yet they also have a much lower amplitude than the peaks fitted around the tips. Similar observations can be made about the amplitude map of the second resonance, which exhibits some signal inside as well as around the edges of the nanoprism. It thus seems reasonable to state that these CL amplitude maps are related to the same Tip and Edge modes probed in EELS, pretty much in the same way as the EELS amplitude maps. Precisely, these amplitude maps should display some spatial variations of the projected electric field intensities of the Tip and Edge modes. Furthermore, the energy and FWHM maps should show some resonance energies and spectral widths inherent to the Tip and Edge mode. As a consequence, both techniques seem to probe the same modes but through different resonances related to the technique[11,12], that we will refer to as EELS and CL resonances of the mode.

Once again, the much smaller spectral width of the CL resonance with respect to the spectral width of the EELS resonance for the same mode (compare the FWHM maps for EELS and CL) may be explained by the large difference in the spectral resolutions. However, the redshift in the center energy of the CL resonance as compared to the center energy of the EELS resonance for the same mode (compare the energy maps for EELS and CL) is quite puzzling. Indeed, one may think that the EELS as well as CL resonance of a mode should give the spectral characteristics of the mode. Such a spectral shift is, however, in accordance with the calculations of [154], and will be confirmed in the next section.

### 4.3.4 EELS and CL: numerical simulations

These findings were verified with numerical simulations, which allow comparing quantitatively the EIRE probability and the EEL probability. The top view of the simulated nanoprism is shown on figure 4.8a. Figure 4.8b shows the EEL probability spectra (left) and EIRE probability spectra (right) obtained for an electron impact parameter located at the tip (red spectrum), at the edge (blue spectrum) and at the centre (green spectrum) of the nanoprism. The characteristics of the peaks are indicated. Although the resonances are slighlty redshifted when compared to the resonances appearing in the measured spectra, these spectra agree qualitatively well with the experiment. In particular, the slight shift between the EELS and CL resonances corresponding to a given electron probe position is recovered. The small shift between measurements and simulations for a given resonance remains very reasonable, equally applies to each dataset (EELS as well as CL) and should be attributable to either the deviations from the real geometry of the nanoprism and/or the account being not taken of the carbon foil. In the case of the EELS spectra, these theoretical spectra are narrower than the experimental spectra, which is in qualitative agreement with the spectral resolution of the experiment. The FWHM agree much better for the CL spectra, due to the largely

[11] Such a statement is not completely sure. A proper evidence that the modes probed by EELS and CL are the same would require, for instance, simulating the surface charges and currents located at the boundaries of the particle at resonance. This can be achieved using BEM simulations. Unfortunately, we do not possess such simulation results.

[12] The reason why the modes seem to spread inside the nanoprism in the CL dataset while they exclusively confine around the nanoprism in the EELS dataset much probably has to do with the poor signal to noise ratio inside the nanoprism in the STEM EELS experiment.

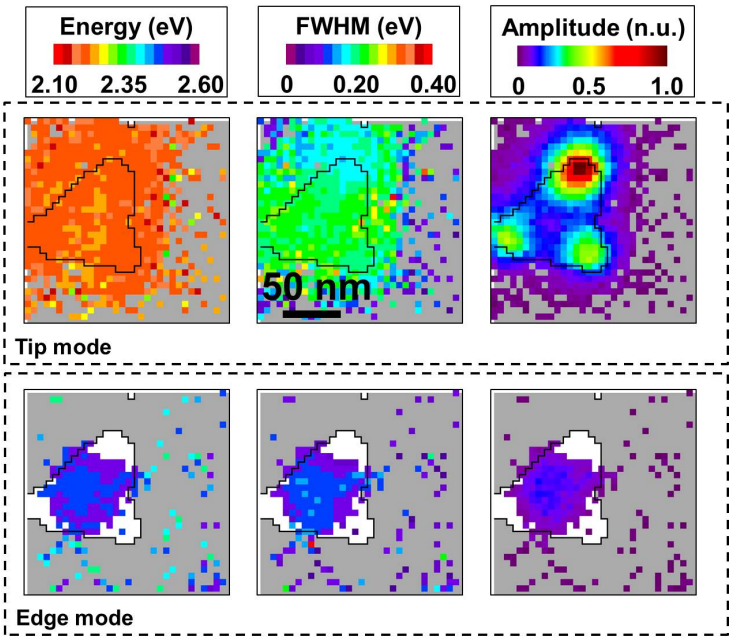


Figure 4.7: CL multipeak fitting. Maps of the energy, FWHM and amplitude of the peaks whose central energy and FWHM match the resonances appearing in the Tip CL spectrum (Tip mode) and in the Edge CL spectrum (Edge mode).

enhanced spectral resolution of STEM CL when compared to STEM EELS[13]. Quantitatively, the amplitude of the peaks apparing in the CL spectra are three times lower than the amplitude of the peaks of the EELS spectra, and the ratio of the peak amplitude from a tip spectrum to an edge spectrum is 0.16 in EELS, 0.10 in CL.

The energy filtered maps of 4.8c display the spatial variations of the EEL probability and EIRE probability when calculated at the resonances of the peaks appearing in the tip and edge spectra. These maps are normalized with respect to the maximum value found in the ensemble of these four maps. They also agree well with the measurements, despite some slight discrepancies that we can attribute to the theoretically infinite spectral resolution of the numerical simulations. Nevertheless, some spots of high intensity located at the tips, thus related to the Tip mode, still dominate each of these maps.

Finally, figure 4.8d shows maps of the energy, FWHM and amplitudes of the peaks corresponding to the resonances appearing in the spectra. These maps confirm all our previous statements: the patterns in the amplitude maps are very similar in EELS and CL, and are thus attributable to the Tip and Edge modes evidenced experimentally. These simulations also confirm that the CL resonance energy of a mode is slightly redshifted with respect to its EELS resonance energy, which is well recovered for both modes.

[13]A calculated FWHM corresponding to a given electron probe position does not differ much from EELS to CL. Although it might seem pertinent based on the broadness of the measured peaks, any discussion about some differences between the spectral width of the EELS and CL resonances is thus irrelevant.

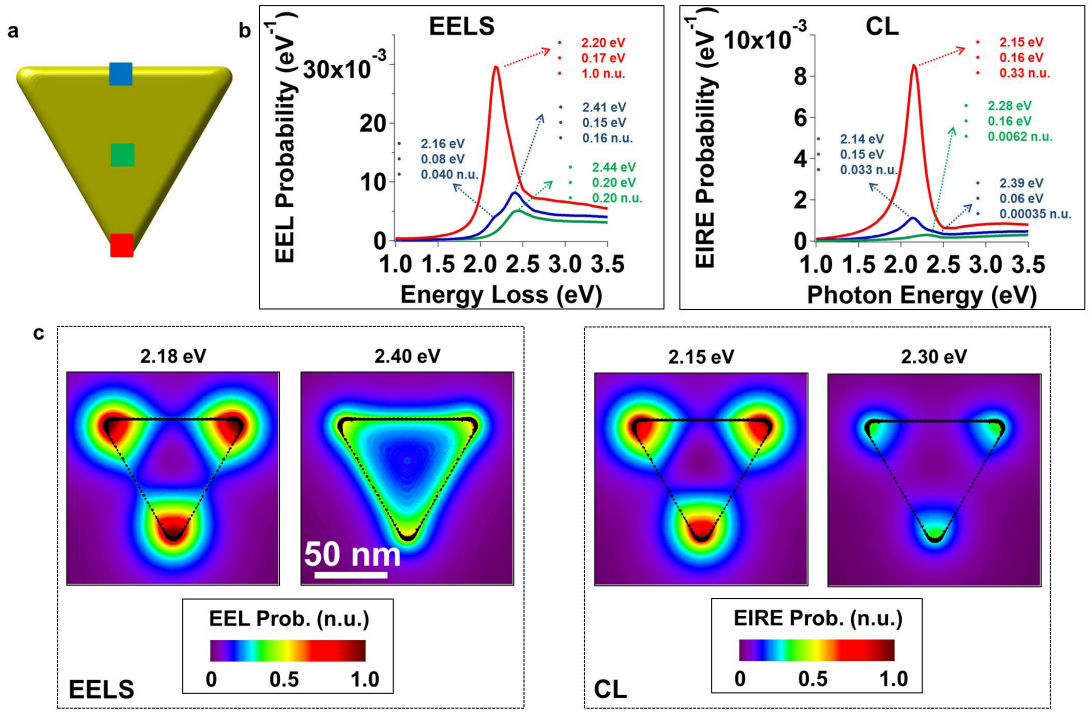


Figure 4.8: EELS and CL numerical simulations. a) Top view of the simulated nanoprism. b) EEL (left) and EIRE (right) probability spectra obtained for an electron parameter located at the tip (red), edge (blue) and centre (green) of the nanoprism. c) Energy filtered maps of the EEL (blue) and EIRE (red) probability corresponding to the resonance energies appearing in the spectra.

### 4.3.5 Optical spectroscopies: numerical simulations

Finally, in order to evidence some similarity between EELS, CL and optical spectroscopies, numerical simulations of the extinction, scattering and absorption cross sections, and of the light induced fields, were performed using the BEM on the simulated nanoprism and compared to the numerical simulations of EELS and CL.

The extinction, scattering and absorption spectra computed for an incoming light propagation direction perpendicular and a polarization parallel to the upper plane of the nanoprism directed along the rblack arrow are shown on figure 4.10a. A single resonant peak, whose characteristics are indicated, is visible in each spectrum. The maximum scattering is found to be slightly redshifted as compared to the maximum extinction, which is in accordance with previously reported combined extinction and scattering measurements and numerical simulations on single gold nanoparticles[14] [160] but contradictory to some simple calculations using harmonic oscillator models [161]. This makes extinction approach EELS and scattering approach CL. Furthermore, an almost quantitative agreement can be found between the features (center energy, FWHM and relative amplitude) of the peak appearing in the extinction cross section and in the calculated Tip EELS spectrum on the one

[14]Notice, however, that contradictory observations have been made in [152].

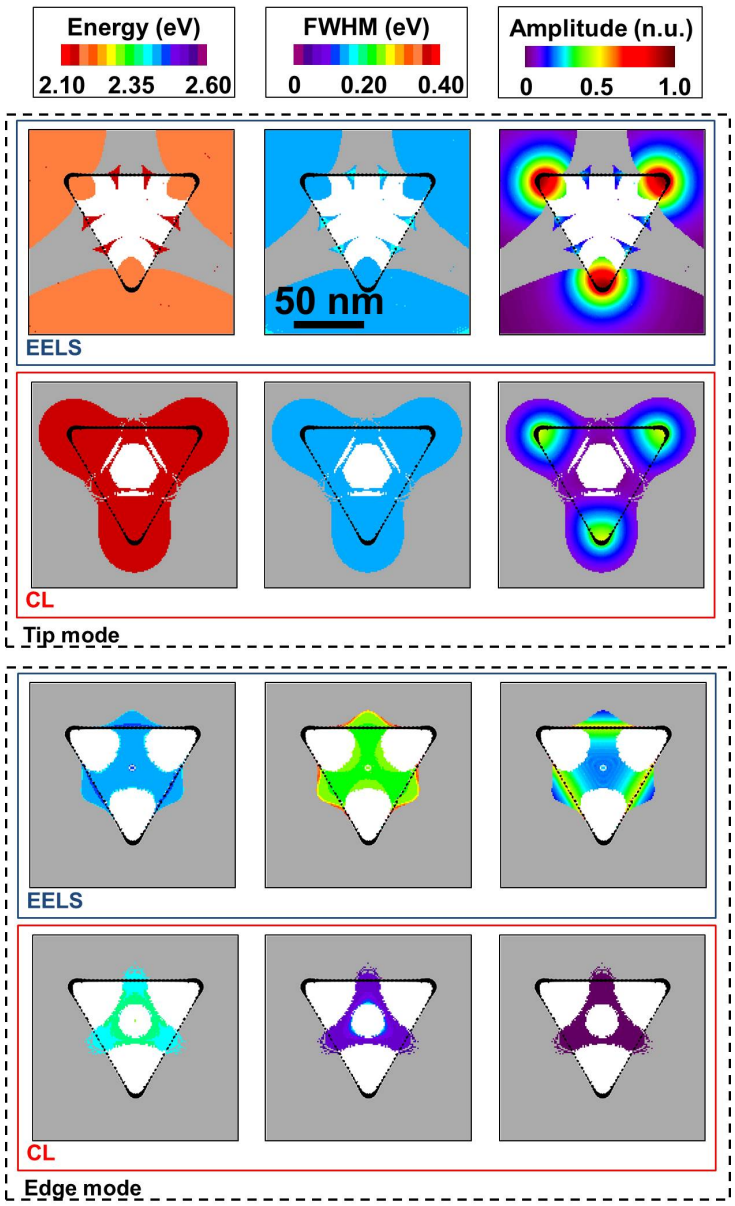


Figure 4.9: Simulated EELS and CL multipeak fitting. Maps of the energy, FWHM and amplitude of the peaks whose central energy and FWHM match the resonance appearing in the Tip spectra (Tip mode) and in the Edge spectra (Edge mode).

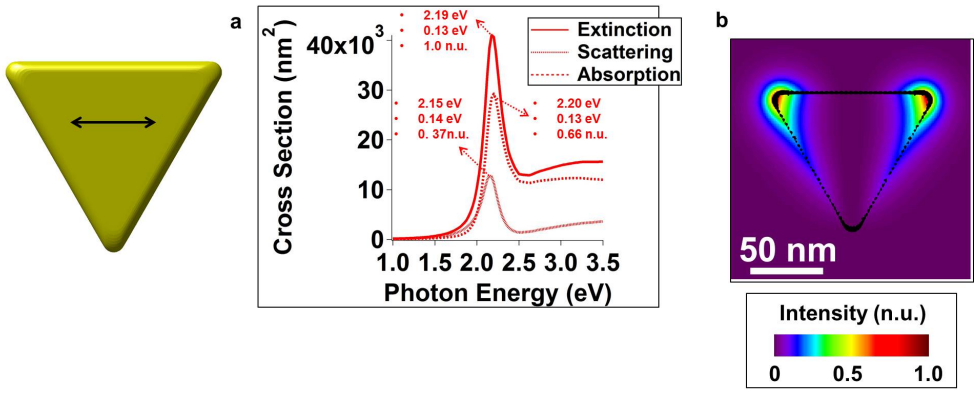


Figure 4.10: Optical numerical simulations on the gold nanoprism. a) Extinction, scattering and absorption spectra calculated for an incident light polarization indicated by the black arrow. c) Near field z-electric field intensity calculated at resonance energy 2.20 eV.

hand, and in the scattering cross section and in the calculated Tip CL spectrum on the other hand (compare figures 4.10 and 4.8). This suggests that these resonances in the optical properties result from the excitation of the Tip mode, whose spectral response is similar in EELS and extinction on the one hand, and in CL and scattering on the other hand.

A map of the z-projected electric field intensity, calculated in a plane located at close proximity to the upper face of the nanoprism for a light excitation at resonance, is shown on figure 4.10b for the same polarization. Some local spots of high intensity are located around two tips of the nanoprism, due to some local strengthening of the electric field[15]. Because the polarization of light brings a symmetry breaking that is not found when exciting the nanoprism with an electron, and because the light induced electromagnetic local fields are not, yet they are mediated by, the SP modes, the resulting pattern is not exactly similar to the spatial variations of the z electric field intensity of the Tip mode as determined by EELS and CL. Nevertheless, the locations of the high intensity spots at the tips indicate that the resonances in the optical spectra are due to the excitation of one of the dipolar modes that constitute the apparent Tip mode.

These numerical simulations tend to show that EELS and CL are nanometric equivalents of extinction and scattering, with the difference that light, for a given propagation direction and polarization, cannot couple to all the modes that are accessible to the electron. In our case, the dipolar mode is a bright mode, because it induces a resonance in the optical spectra. However, the modes responsible for the apparent Edge mode in EELS and CL appear to be dark, at least for this polarization.

### 4.3.6 Conclusions

The conclusions of this section are summed up in figure 4.11, which compares EELS and CL measurements and EELS, CL and optical numerical simulations in the case of the Tip mode.

[15]In the litterature, these local field strenghtenings induced by some light excitation of a metallic nanoobject are often called Hot Spots (HS). As for us, we keep such designation only to qualify the highest local field strenghtenings occuring when illuminating a percolating metal film with a plane wave (see chapter 5).

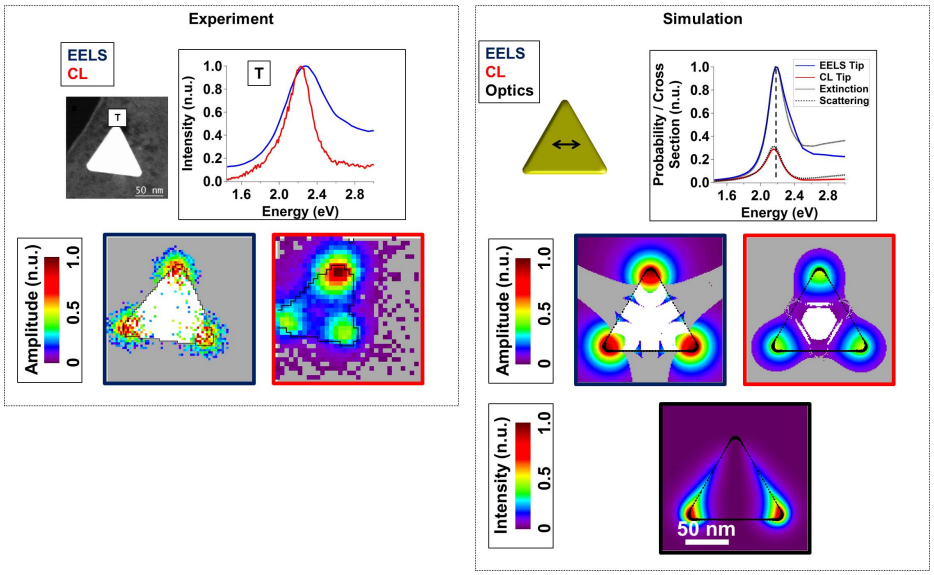


Figure 4.11: Tip mode probed by fast electron based an optical spectroscopies: experiments and simulations. Left (experimental): CL and EELS spectra corresponding to an electron probe located at the tip of the nanoprism. Amplitude maps associated to the resonances. Right (simulated): CL and EELS spectra corresponding to an electron probe located at the tip of the nanoprism, extinction and scattering cross section spectra for an incident light polarization indicated by the black arrow. Amplitude maps associated to the resonances appearing for EELS and CL. Near field z-electric field intensity calculated at the resonance of the optical spectra.

Figure 4.11 (left) shows experimental EELS and CL spectra corresponding to an electron probe located at the tip of the nanoprism. A clear resonance appears in each spectrum, CL being slightly redshifted with respect to EELS. These resonances are associated to the excitation of the same Tip mode, whose spatial variations are shown by the amplitude maps at the bottom.

At the right of figure 4.11, calculated EELS and CL spectra corresponding to an electron probe located at the tip of the nanoprism are displayed, as well as extinction and scattering spectra for a light polarization indicated by the black arrow. As clear from such superposition, EELS and CL clearly respectively match extinction and scattering. In particular, the resonance appearing in the scattering/CL spectrum is redshifted with respect to the resonance appearing in the extinction/EELS spectrum, in accordance with the experiments. In the case of EELS and CL, these resonances are associated to the excitation of three degenerate dipolar modes (a Tip mode), whose spatial variations are shown by the amplitude maps. In the case of extinction and scattering, these resonances are associated to the excitation of one of these three dipolar modes, whose spatial variations are indirectly shown by the intensity map at the bottom.

We are going to justify these findings in the next section by proposing modal decompositions of CL, extinction and scattering in the quasistatic approximation.

## 4.4 Theoretical interpretation

### 4.4.1 Introduction

This section aims at deriving theory elements to explain the results of the last section.

Before considering back again our generic 3D system introduced in section 2 to give a general range to this interpretation, it is worth mentionning that the link between EELS and extinction on the one hand, CL and scattering on the other hand, is obvious in the case of a sphere, for which analytical expressions for the EEL and EIRE probabilities and scattering and extinction cross sections have been derived previously either in the quasistatic approximation or in a full relativistic approach. In particular, in the case of a small gold sphere, these theories predict that the absorption/extinction and scattering resonances occur at slightly the same energies as the EELS and CL resonances and are clearly shifted with respect to each other. Further details can be found in appendix B.

The aim of the following subsections is to derive modal decompositions of the form:

$$\Gamma_{EIRE}(\vec{R},\omega) \sim \sum_{i=rad} \frac{1}{\omega^2}\mathcal{F}_{i,EIRE}(\omega)\left|E_i^z(\vec{R},\frac{\omega}{v})\right|^2 = \mathcal{F}_{i,EIRE}(\omega)\left|\phi_i(\vec{R},\frac{\omega}{v})\right|^2 \quad (4.4.1)$$

$$C_{ext}(\omega) \sim \sum_{i=rad} \mathcal{F}_{i,ext}(\omega) \quad (4.4.2)$$

$$C_{sca}(\omega) \sim \sum_{i=rad} \mathcal{F}_{i,sca}(\omega) \quad (4.4.3)$$

where $\Gamma_{EIRE}(\vec{R},\omega)$ is the EIRE probability, $C_{ext}(\omega)$ and $C_{sca}(\omega)$ are the extinction and scattering cross sections, and $E_i^z(\vec{R},\frac{\omega}{v})$ and $\phi_i(\vec{R},\frac{\omega}{v})$ are the Fourier transform along the direction of the electron of the projection along the direction of the electron of the electric field of a mode and of the potential of a mode at $\frac{\omega}{v}$ (see section 2.5). In these expressions, the sums include only the radiative modes $i = rad$ of the system. All the energy dependent functions $\mathcal{F}_{i,EIRE}(\omega)$, $\mathcal{F}_{i,ext}(\omega)$ and $\mathcal{F}_{i,sca}(\omega)$ should be resonant spectral functions characteristic of the mode $i$. For a given mode, the resonance of $\mathcal{F}_{i,EIRE}(\omega)$ should match the resonance of $\mathcal{F}_{i,sca}(\omega)$ while being slightly redshifted with respect to the resonance of $\Im\{f_i(\omega)\}$, which should itself match the resonance of $\mathcal{F}_{i,sca}(\omega)$, when adapted to our particular system.

### 4.4.2 CL: a modal decomposition

In the quasistatic approximation, the interaction between a fast electron and a generic system is all contained within the Poisson equation in which we introduce the source term given by equation 2.5.1, namely:

$$\vec{\nabla}.\left[\tilde{\varepsilon}(\vec{r},\omega)\vec{\nabla}\phi_{el}(\vec{r},\omega)\right] = -4\pi\rho_{el}(\vec{r},\omega) \quad (4.4.4)$$

As a first step, we are going to demonstrate that the electron interacting with the system is equivalent from the far-field as a dipole of dipole moment that we are going to determine. The solution of the above equation can be shown to write[16] in the a BEM framework [162]:

[16] To easily find this expression back, one can think of using the modal decomposition of the scalar Green function in terms of eigenpotentials derived in [37] to express the electric potential [20].

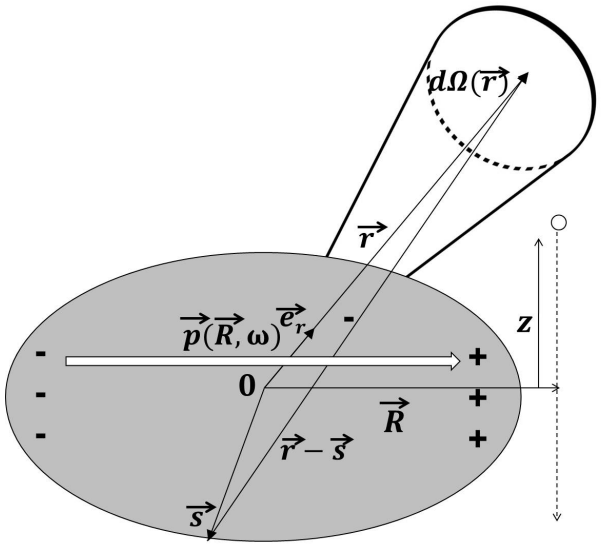


Figure 4.12: Emission of light into the far field. For a given electron parameter $\vec{R}$, each frequency component of the electron polarizes the particle, which is equivalent to a small dipole of dipole moment $\vec{p}(\vec{R},\omega)$. This dipole radiates electromagnetic energy into the far field. The CL emission is known from integrating the corresponding Poynting vector over all solid angles $d\Omega(\vec{r})$ pointing along the direction given by the unit vector $\vec{e}_r$ of a sphere of infinitely large radius $|\vec{r}|$. All the other notations are kept the same as in chapter 2.

$$\phi_{el}(\vec{r},\omega) = \phi_{el}^{ext}(\vec{r},\omega) + \phi_{el}^{ind}(\vec{r},\omega) \tag{4.4.5}$$

where, in the general case:

$$\phi_{el}^{ext}(\vec{r},\omega) = -\frac{e}{v}\int_{\mathbb{R}} \frac{1}{\varepsilon(\vec{R}+z'\vec{e}_z,\omega)\left|\vec{r}-\vec{R}-z'\vec{e}_z\right|} e^{i\omega z'/v} dz' \tag{4.4.6}$$

and:

$$\phi_{el}^{ind}(\vec{r},\omega) = -\frac{e}{v}\int_{\mathbb{R}} \sum_i \left[ g_i(\omega) - \frac{1}{\varepsilon(\vec{R}+z'\vec{e}_z,\omega)} \right] \phi_i(\vec{r})\phi_i^*(\vec{R}+z'\vec{e}_z) e^{i\omega z'/v} dz' \tag{4.4.7}$$

where $\phi_i(\vec{r})$ is the potential of the geometric eigenmode $i$ given by equation 2.3.19. The first term is the Coulomb electric potential while the second term is the induced electric potential, resulting from the scattering of the field accompanying the electron by the object. Let us consider the simpler case where the electron has a non-penetrating trajectory. In this case, the two above formulas write:

$$\phi_{el}^{ext}(\vec{r},\omega) = -\frac{e}{v\varepsilon_2(\omega)}\int_{\mathbb{R}} \frac{1}{\left|\vec{r}-\vec{R}-z'\vec{e}_z\right|} e^{i\omega z'/v} dz' \tag{4.4.8}$$

and:

$$\phi_{el}^{ind}(\vec{r},\omega) = -\frac{e}{v}\sum_i f_i(\omega)\phi_i^*(\vec{R},\frac{\omega}{v})\phi_i(\vec{r}) \tag{4.4.9}$$

where $\phi_i(\vec{R},k_z) = \int \phi_i(\vec{R}+z\vec{e}_z,\omega)e^{ik_z z}dz$ is the Fourier transform along z of $\phi_i(\vec{r})$ and the expression for $f_i(\omega)$ has been given in equation 2.4.15. Assuming $|\vec{r}|$ large enough, we can then expand each $\phi_i(\vec{r})$ in the dipolar approximation (valid if $|\vec{r}| \gg |\vec{s}|$). To the second order, the potential associated with the mode $i$ writes:

$$\phi_i(\vec{r}) = \frac{1}{|\vec{r}|}\left[\oint_{\Omega_1\cap\Omega_2}\sigma_i(\vec{s})\,d\vec{s} + \frac{1}{|\vec{r}|}\oint_{\Omega_1\cap\Omega_2}[\sigma_i(\vec{s})\,\vec{s}.\vec{e}_r d\vec{s}]\right] + o\left(\frac{1}{|\vec{r}|^3}\right)_i \tag{4.4.10}$$

The first term is zero due to charge neutrality. However, the second term either can or cannot be non zero, depending on the mode we consider. In particular, we can define dipolar modes $i = d$ as some modes $i$ with non zero dipole moment, where the dipole moment of the mode $i$ writes:

$$\vec{p}_i = \oint_{\Omega_1\cap\Omega_2}\sigma_i(\vec{s})\,\vec{s}d\vec{s} \tag{4.4.11}$$

Introducing this expression into equation 4.4.10, the potential associated with the mode $i$ writes, in the dipolar approximation:

$$\phi_i(\vec{r}) = \frac{1}{|\vec{r}|^2}\vec{p}_i.\vec{e}_r + o\left(\frac{1}{|\vec{r}|^3}\right)_i \tag{4.4.12}$$

As a consequence, the potential induced by the fast electron writes, introducing equation 4.4.12 into equation 4.4.9:

$$\phi_{el}^{ind}(\vec{r},\omega) = -\frac{e}{v}\sum_i f_i(\omega)\phi_i^*(\vec{R},\frac{\omega}{v})\left[\frac{1}{|\vec{r}|^2}\vec{p}_i.\vec{e}_r + o\left(\frac{1}{|\vec{r}|^3}\right)_i\right] \tag{4.4.13}$$

For $|\vec{r}|$ sufficiently large, this expression reads:

$$\phi_{el}^{ind}(\vec{r},\omega) \sim_{|\vec{r}|\to\infty} \frac{1}{|\vec{r}|^2}\vec{p}(\vec{R},\omega).\vec{e}_r = \phi_{el}^{ind,FF}(\vec{r},\omega) \tag{4.4.14}$$

where $\phi_{el}^{ind,FF}(\vec{r},\omega)$ is the far-field electric potential induced by the electron and:

$$\vec{p}(\vec{R},\omega) = -\frac{e}{v}\sum_{i=d} f_i(\omega)\phi_i^*(\vec{R},\frac{\omega}{v})\vec{p}_i \tag{4.4.15}$$

or, introducing the Fourier transform along z of the projection along z of the electric field of the mode $i$ through $E_i^z(\vec{R},k_z) = -ik_z\phi_i(\vec{R},k_z)$ :

$$\vec{p}(\vec{R},\omega) = -i\frac{e}{\omega}\sum_{i=d} f_i(\omega)E_i^{z*}(\vec{R},\frac{\omega}{v})\vec{p}_i \tag{4.4.16}$$

Notice that only the dipolar modes have non-zero weights within the summation, because all the other modes have potentials on the order of $\frac{1}{|\vec{r}|^n}$, where $n > 2$. We have thus changed the summation

over the modes $i$ as a summation over the dipolar modes $i = d$. We recognize in equation 4.4.14 the quasistatic expression of the electric potential of a dipole with dipole moment $\vec{p}(\vec{R},\omega)$ [10]. Otherwise speaking, we have shown that the electron interacting with the system is equivalent from the far-field as a dipole of dipole moment $\vec{p}(\vec{R},\omega)$ whose expression is given by equation 4.4.16[17].

In a retarded approach, the EIRE probability is related to the electromagnetic energy radiated into the far field, which can be calculated by integrating the Poynting vector normal to an infinitely large sphere centered around the nanoparticle. This radiated energy reads [20, 67, 92]:

$$\Delta W^{rad}(\vec{R}) = \frac{c}{4\pi} lim_{|\vec{r}|\to\infty} \int_{4\pi} \int |\vec{r}|^2 \, \vec{e}_r . \left[\vec{E}_{el}(\vec{r},t) \times \vec{H}_{el}(\vec{r},t)\right] d\Omega_{\vec{e}_r} dt \tag{4.4.17}$$

where $\vec{e}_r$ is a unit vector pointing towards the direction of $\vec{r}$ and $d\Omega_{\vec{e}_r} = sin\theta d\theta d\Phi$ is the solid angle of a sphere of radius $|\vec{r}|$ in the direction of $\vec{e}_r$ (see figure 4.12). The radiative energy can then be decomposed in spectral components by introducing the EIRE probability $\Gamma_{EIRE}(\vec{R},\omega)$ such as:

$$\Delta W^{rad}(\vec{R}) = \int_0^{+\infty} \hbar\omega \Gamma_{EIRE}(\vec{R},\omega) d\omega \tag{4.4.18}$$

The EIRE probability can thus be calculated from [67]:

$$\Gamma_{EIRE}(\vec{R},\omega) = \frac{c}{4\pi^2\hbar\omega} lim_{|\vec{r}|\to\infty} \int_{4\pi} |\vec{r}|^2 \, \Re\left\{\vec{e}_r . \left[\vec{E}_{el}(\vec{r},\omega) \times \vec{H}_{el}(\vec{r},\omega)\right]\right\} d\Omega_{\vec{e}_r} \tag{4.4.19}$$

Introducing the far-field amplitude of the electric field $\vec{E}^{FF}_{0,el}(\vec{e}_r,\omega)$ through:

$$\vec{E}^{FF}_{el}(\vec{r},\omega) = \frac{e^{ikr}}{r} \vec{E}^{FF}_{0,el}(\vec{e}_r,\omega) \tag{4.4.20}$$

where $k = \dfrac{\omega}{c}$ and $\vec{E}^{FF}_{el}(\vec{r},\omega)$ is the far-field limit of $\vec{E}_{el}(\vec{r},\omega)$, the EIRE probabiliy can also be expressed as [20]:

$$\Gamma_{EIRE}(\vec{R},\omega) = \frac{c}{4\pi^2\hbar\omega} \int_{4\pi} \left|\vec{E}^{FF}_{0,el}(\vec{e}_r,\omega)\right|^2 d\Omega_{\vec{e}_r} \tag{4.4.21}$$

Unfortunately, there is no radiation of electromagnetic energy in the quasistatic approximation. In the following, we will thus assume that, in a retarded approach, the electron interacting with the system is still equivalent from the far-field as a dipole of dipole moment $\vec{p}(\vec{R},\omega)$ given by equation 4.4.16 [10]. Therefore, the far-field amplitude fulfills the well-known expression [163]:

$$\vec{E}^{FF}_{0,el}(\vec{e}_r,\omega) = -\frac{k^2}{4\pi} \vec{e}_r \times \vec{e}_r \times \vec{p}(\vec{R},\omega) \tag{4.4.22}$$

Introducing equation 4.4.22 into equation 4.4.21, the EIRE probability can be expressed as a function of the dipole moment $\vec{p}(\vec{R},\omega)$ through:

$$\Gamma_{EIRE}(\vec{R},\omega) = \frac{\omega^3}{64\pi^4\hbar c^3} \int_{4\pi} \left|\vec{p}_\perp(\vec{R},\omega)\right|^2 d\Omega_{\vec{e}_r} \tag{4.4.23}$$

[17] We here neglect any contribution to radiation from the bare field of the electron, otherwise speaking, Cherenkov emission, which would appear in a complete retarded approach but is not found in the quasistatic approximation [20].

where $\vec{p}_\perp(\vec{R},\omega) = \vec{p}(\vec{R},\omega) - \vec{e}_r.\vec{p}(\vec{R},\omega)\vec{e}_r$ is the transverse component of the electron induced dipole moment. The CL thus reads, inserting into equation 4.4.23 the expression for $\vec{p}(\vec{R},\omega)$:

$$\Gamma_{EIRE}(\vec{R},\omega) = \frac{e^2\omega}{64v^2\pi^4\hbar c^3}\int_{4\pi}\left|\sum_{i=d} f_i(\omega)E_i^{z*}(\vec{R},\frac{\omega}{v})\vec{p}_{i\perp}\right|^2 d\Omega_{\vec{e}_r} \tag{4.4.24}$$

where $\vec{p}_{i\perp}$=$\vec{p}_i$-$\vec{e}_r.\vec{p}_i\vec{e}_r$ is the transverse component of $\vec{p}_i$. Developping the square of the sum appearing in the expression, equation 4.4.24 becomes:

$$\begin{aligned}\Gamma_{EIRE}(\vec{R},\omega) = {} & \frac{e^2\omega}{64v^2\pi^4\hbar c^3}\Big(\sum_{i=d}|f_i(\omega)|^2\left|E_i^z(\vec{R},\frac{\omega}{v})\right|^2\left|\int_{4\pi}\vec{p}_{i\perp}d\Omega_{\vec{e}_r}\right|^2 \\ & + \sum_{i=d}\sum_{\{j\neq i\}=d} f_i(\omega)f_j(\omega)^*E_i^{z*}(\vec{R},\frac{\omega}{v})E_j^z(\vec{R},\frac{\omega}{v})\int_{4\pi}\vec{p}_{i\perp}.\vec{p}_{j\perp}d\Omega_{\vec{e}_r}\Big)\end{aligned} \tag{4.4.25}$$

If the spectral responses $f_i(\omega)$ of the modes are well separated , the crossterm $f_i(\omega)f_j(\omega)^*$ appearing in the second expression becomes negligible. The expression thus becomes:

$$\boxed{\Gamma_{EIRE}(\vec{R},\omega)\approx \frac{e^2\omega}{64\pi^4\hbar c^3}\sum_{i=d}|f_i(\omega)|^2\left|\int_{4\pi}\vec{p}_{i\perp}d\Omega_{\vec{e}_r}\right|^2\left|E_i^z(\vec{R},\frac{\omega}{v})\right|^2} \tag{4.4.26}$$

or, alternatively:

$$\boxed{\Gamma_{EIRE}(\vec{R},\omega)\approx \frac{e^2\omega^3}{64\pi^4\hbar c^3}\sum_{i=d}|f_i(\omega)|^2\left|\int_{4\pi}\vec{p}_{i\perp}d\Omega_{\vec{e}_r}\right|^2\left|\phi_i(\vec{R},\frac{\omega}{v})\right|^2} \tag{4.4.27}$$

This expression is fully consistent with the generic expression of the EIRE probability proposed in the introduction if one defines a radiative mode as a dipolar mode and the energy dependent function $\mathcal{F}_{i,EIRE}(\omega)$ as $\omega^3|f_i(\omega)|^2$.

### 4.4.3 Extinction and scattering of light: a modal decomposition

We are now going to derive some modal decompositions of the extinction and scattering cross sections based on a quasistatic BEM theory framework in order to highlight the close resemblance between EELS and extinction, and CL and scattering. In the quasistatic approximation, the optical properties of the system can be derived by cancelling the external souce term within the Poisson equation [29, 34], namely:

$$\vec{\nabla}.\left[\tilde{\varepsilon}(\vec{r},\omega)\vec{\nabla}\phi(\vec{r},\omega)\right] = 0 \tag{4.4.28}$$

The solution of the above equation writes:

$$\phi(\vec{r},\omega) = \phi^{ext}(\vec{r},\omega) + \phi^{sca}(\vec{r},\omega) \tag{4.4.29}$$

where $-\vec{\nabla}\phi^{ext}(\vec{r},\omega) = \vec{E}^{ext}(\omega)$ is the external field and $\phi^{sca}(\vec{r},\omega)$ is the scattered electric potential. This scattered electric potential can be shown, in a similar way the electric potential induced by a fast electron was derived in [162], to express as:

$$\phi^{sca}(\vec{r},\omega) = \frac{1}{2\pi}\sum_i \frac{1}{\lambda(\omega)-\lambda_i}\left\{\oint_{\Omega_1\cap\Omega_2} \vec{e}_{N(\vec{s})}.\vec{E}^{ext}(\omega)\phi_i(\vec{s})^* d\vec{s}\right\}\phi_i(\vec{r}) \tag{4.4.30}$$

where $\phi_i(\vec{r})$ is, again, the potential of the geometric eigenmode $i$ given by equation 2.3.19, $\vec{e}_{N(\vec{s})}$ is the normal unit vector located at position $\vec{s}$ on the boundary pointing from medium 1 to medium 2 (see subsection 2.3.3) and $\lambda(\omega)$ is given by equation 2.3.13. Expending each eigenpotential $\phi_i(\vec{r})$ within the dipolar approximation, we find that, for large $|\vec{r}|$, the scattered potential writes:

$$\phi^{sca}(\vec{r},\omega) = \frac{1}{|\vec{r}|^2}\vec{p}(\omega).\vec{e}_r + o\left(\frac{1}{|\vec{r}|^2}\right) \tag{4.4.31}$$

where:

$$\vec{p}(\omega) = \frac{1}{2\pi}\sum_{i=d} \frac{1}{\lambda(\omega)-\lambda_i}\left\{\oint \vec{e}_{N(\vec{s})}.\vec{E}^{ext}(\omega)\phi_i(\vec{s})^* d\vec{s}\right\}\vec{p}_i$$

where$\vec{p}_i$ is the dipole moment of the mode $i$, that we defined in the previous subsection. As seen from the far field, the illuminated particle is thus equivalent to a dipole with dipole moment $\vec{p}(\omega)$. In a similar way we have derived the modal decomposition of CL, we here assume that this last statement holds in a relativistic approach. The illuminated particle thus radiates an electric field [163]:

$$\vec{E}^{sca}_{FF}(\vec{r},\omega) = \frac{e^{ikr}}{r}\vec{E}^{sca}_{FF0}(\vec{e}_r,\omega) \tag{4.4.32}$$

where $k = \dfrac{\omega}{c}$ and

$$\vec{E}^{sca}_{FF0}(\vec{e}_r,\omega) = -\frac{k^2}{4\pi}\vec{e}_r\times\vec{e}_r\times\vec{p}(\omega) \tag{4.4.33}$$

is the scattering amplitude. The extinction and scattering cross sections can be found from the scattering amplitude using [10]:

$$C_{ext}(\omega) = \frac{4\pi}{k\left|\vec{E}^{ext}(\omega)\right|^2}\Im\left\{\vec{E}^{sca}_{FF0}(\vec{e}_{r_{ext}},\omega).\vec{E}^{ext}(\omega)\right\} \tag{4.4.34}$$

$$C_{sca}(\omega) = \frac{1}{\left|\vec{E}^{ext}(\omega)\right|^2}\int_{4\pi}\left|\vec{E}^{sca}_{FF0}(\vec{e}_r,\omega)\right|^2 d\Omega_{\vec{e}_r} \tag{4.4.35}$$

where $\vec{e}_{r_{ext}}$ defines the propagation direction of the excitation plane wave and $d\Omega_{\vec{e}_r}$ is the solid angle of a sphere of radius $|\vec{r}|$ in the direction of $\vec{e}_r$. These expressions become, in terms of the dipole moment $\vec{p}(\omega)$:

$$C_{ext}(\omega) = -\frac{1}{\left|\vec{E}^{ext}(\omega)\right|^2}\frac{\omega}{c}\Im\left\{\vec{e}_{r_{ext}}\times\vec{e}_{r_{ext}}\times\vec{p}(\omega).\vec{E}^{ext}(\omega)\right\} \tag{4.4.36}$$

$$C_{sca}(\omega) = \frac{1}{\left|\vec{E}^{ext}(\omega)\right|^2}\frac{\omega^4}{16\pi^2c^4}\int_{4\pi}\left|\vec{p}_\perp(\omega)\right|^2 d\Omega_{\vec{e}_r} \tag{4.4.37}$$

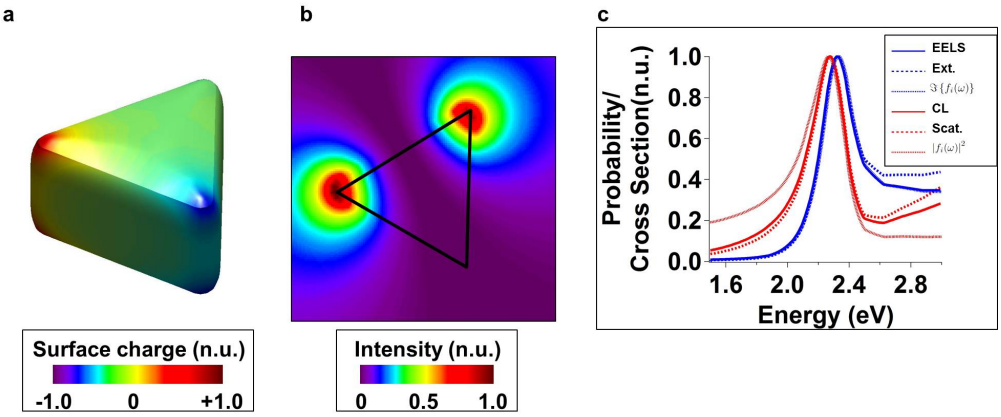


Figure 4.13: Interpretation of the modal decompositions in the case a thick gold triangular nanoprism. a) Eigenvector of the geometric mode of a thick nanoprism of eigenvalue -0.64. b) $\left|\phi_i(\vec{R},\frac{\omega}{v})\right|^2$ as a function of $\vec{R}$ for $\omega$=2.3 eV and $v$=c/2. c)$\Im\{f_i(\omega)\}\left|\phi_i(\vec{R},\frac{\omega}{v})\right|^2$ (EELS), $\omega\Im\{f_i(\omega)\}$ (extinction), $\Im\{f_i(\omega)\}$, $\omega^3\left|f_i(\omega)\right|^2\left|\phi_i(\vec{R},\frac{\omega}{v})\right|^2$ (CL), $\omega^4\left|f_i(\omega)\right|^2$ (scattering) and $\left|f_i(\omega)\right|^2$ as a function of $\omega$ for a gold nanoprism surrounded by vacuum. In the case of EELS and CL, the electron impact parameter was chosen to be located at the tip of the nanoprism.

where $\vec{p}_\perp(\omega)=\vec{p}(\omega)-\vec{e}_r.\vec{p}(\omega)\vec{e}_r$. Introducing the expression for $\vec{p}(\omega)$ given by equation 4.4.16, one obtains for the extinction and scattering cross sections:

$$C_{ext}(\omega)=\frac{1}{\left|\vec{E}^{ext}(\omega)\right|^2}\frac{\omega}{c}\sum_{i=d}\frac{1}{\lambda_i+1}\left\{\oint_{\Omega_1\cap\Omega_2}\vec{e}_{N(\vec{s})}.\vec{E}^{ext}(\omega)\phi_i(\vec{s})^*d\vec{s}\right\}\left\{\vec{e}_{r_{ext}}\times\vec{e}_{r_{ext}}\times\vec{p}_i.\vec{E}^{ext}(\omega)\right\}\Im\{f_i(\omega)\} \tag{4.4.38}$$

and:

$$C_{sca}(\omega)\approx\frac{1}{\left|\vec{E}^{ext}(\omega)\right|^2}\frac{\omega^4}{64\pi^4c^3}\sum_{i=d}\frac{1}{(\lambda_i+1)^2}\left|\oint_{\Omega_1\cap\Omega_2}\vec{e}_{N(\vec{s})}.\vec{E}^{ext}(\omega)\phi_i(\vec{s})^*d\vec{s}\right|^2\left|\int_{4\pi}\vec{p}_{i\perp}d\Omega_{\vec{e}_r}\right|^2\left|f_i(\omega)\right|^2 \tag{4.4.39}$$

where $\vec{p}_{i\perp}=\vec{p}_i-\vec{e}_r.\vec{p}_i\vec{e}_r$ and $f_i(\omega)$ has been given in equation 2.4.15. In the expression for the scattering cross section, we have neglected the crossterms appearing in $\left|\vec{p}_\perp(\omega)\right|^2$ knowing that, in most situations, the spectral responses $f_i(\omega)$ are well separated, thus the crossproduct $f_i(\omega)f_j(\omega)^*$ is negligible.

These expressions are again fully consistent with the generic expression of the extinction and scattering cross sections proposed in the introduction if one defines the energy dependent functions $\mathcal{F}_{i,ext}(\omega)$ and $\mathcal{F}_{i,sca}(\omega)$ as $\omega\Im\{f_i(\omega\}$ and $\omega^4\left|f_i(\omega)\right|^2$.

### 4.4.4 Comparison between the modal decompositions

We are now going to confront the modal decompositions derived in the last subsections with the modal decomposition of EELS recalled in chapter 2 to explain the experimental and numerical results of section 4.3. These modal decompositions read:

$$\Gamma_{EEL}(\vec{R},\omega) \sim \frac{1}{\omega^2}\sum_i \Im\left\{f_i(\omega)\right\}\left|E_i^z(\vec{R},\frac{\omega}{v})\right|^2 \tag{4.4.40}$$

$$\sim \sum_i \Im\left\{f_i(\omega)\right\}\left|\phi_i(\vec{R},\frac{\omega}{v})\right|^2 \tag{4.4.41}$$

$$\sim \sum_i \Im\left\{f_i(\omega)\right\}\left|\oint_{\Omega_1\cap\Omega_2}\sigma_i\left(\vec{s}\right)e^{-i\frac{\omega}{v}s_z}K_0\left(\frac{\omega}{v}\left|\vec{R}-s_\perp\vec{e}_\perp\right|\right)d\vec{s}\right|^2 \tag{4.4.42}$$

$$\Gamma_{EIRE}(\vec{R},\omega) \sim \sum_{i=d}\omega\left|f_i(\omega)\right|^2\left|E_i^z(\vec{R},\frac{\omega}{v})\right|^2 \tag{4.4.43}$$

$$\sim \sum_{i=d}\omega^3\left|f_i(\omega)\right|^2\left|\phi_i(\vec{R},\frac{\omega}{v})\right|^2 \tag{4.4.44}$$

$$\sim \sum_i \omega^3\left|f_i(\omega)\right|^2\left|\oint_{\Omega_1\cap\Omega_2}\sigma_i\left(\vec{s}\right)e^{-i\frac{\omega}{v}s_z}K_0\left(\frac{\omega}{v}\left|\vec{R}-s_\perp\vec{e}_\perp\right|\right)d\vec{s}\right|^2 \tag{4.4.45}$$

$$C_{ext}(\omega) \sim \sum_{i=d}\omega\Im\left\{f_i(\omega)\right\} \tag{4.4.46}$$

$$C_{sca}(\omega) \sim \sum_{i=d}\omega^4\left|f_i(\omega)\right|^2 \tag{4.4.47}$$

In these two expressions, the sums involve the geometric eigenmodes of the system. However, the sum appearing in the modal decomposition of EELS encompasses all the modes while the sum appearing in the modal decomposition of CL, extinction and scattering encompasses the dipolar modes only. The spectral variations of EELS and extinction on the one hand, CL and scattering on the other hand, are respectively dictated by the imaginary part and the square modulus of the same energy dependent function $f_i(\omega)$, yet with different energy dependent prefactors. Furthermore, the spatial variations of EELS and CL are dictated by the same quantities $\left|E_i^z(\vec{R},\frac{\omega}{v})\right|^2$ or $\left|\phi_i(\vec{R},\frac{\omega}{v})\right|^2$ that we defined in chapter 2.

Let us analyze these terms in the special case of a gold triangular nanoprism with dimensions corresponding to the nanoprism studied in section 4.3 surrounded by vacuum. The geometric modes of the nanoprism can be known by solving numerically equation 2.3.15. Figure 4.13a shows the eigenvector of the geometric mode of eigenvalue $\lambda_i = -0.64$, and figure 4.13b shows the spatial variations of this mode as measured by EELS and CL. This geometric mode corresponds to a dipolar mode. Furthermore, the spectral contribution from this mode to EELS and CL for an impact parameter at the tip is compared to its spectral contribution to extinction and scattering in figure 4.13c, for a gold-vacuum system, by inserting into the above expressions the gold dielectric function [74] as $\varepsilon_1(\omega)$, $\varepsilon_2(\omega) = 1$ and $\lambda_i = -0.64$. The spectral dependences of $\Im\left\{f_i(\omega)\right\}$ to $\left|f_i(\omega)\right|^2$, which dictate the spectral variations of these four quantities, are superimposed. In this

graph, EELS corresponds to extinction, and CL to scattering, with the resonance of CL/scattering being slightly redshifted as compared to EELS/extinction.

It is thus clear that the above modal decompositions well account for the results of section 4.3. The slight redshift from EELS to CL for the Tip mode or from extinction to scattering observed either experimentally or numerically is explained by the slight redshift from $\Im\{f_i(\omega)\}$ to $|f_i(\omega)|^2$. Furthermore, the local spots of high intensity located at the three tips observed on the EELS or CL amplitude maps corresponding to the Tip mode are explained by the local increases of the square of the Fourier transform along z of the z-projection of the electric field of the geometric mode.

As previously noticed, EELS and extinction, and CL and scattering, are respectively dictated by the imaginary part and the square modulus of the same energy dependent function $f_i(\omega)$. This draws a clear parallel between extinction and EELS on the one hand, if we exclude the fact that the modal decomposition of the extinction cross section only sums the dipolar modes of the system, and scattering and CL on the other hand. Precisely, we have shown that, for a given dipolar mode, the EEL and EIRE probabilities are respectively proportional to the extinction and scattering cross sections spatially modulated by the square of the Fourier transform of the z Electric field of the mode. However, the extra $\omega$ contribution from fast electron based spectroscopies to optical spectroscopies would induce a slight redshift of CL with respect to scattering and of EELS with respect to extinction. Such redshift is unnoticeable in our calculations (see figure 4.13c). Nevertheless, it has been previously underlined in numerical simulations of EELS and extinction [152], and heads to the spreaded idea that fast electron based spectroscopy resonances, supposed to reflect some near field properties of the system, should be slightly redshifted as compared to light spectroscopy resonances, which would reflect some far field properties of the system[18].

Finally, it should be noticed that the resonances calculated for the dipolar mode do not perfectly match the resonances evidenced experimentally as well as numerically. This may be due to either a change in the nanoprism dimensions, the absence of substrate in our model or the fact that we rely on the quasistatic approximation. Furthermore, let us stress that, following our theory, the geometric mode corresponding to the Edge mode has a vanishing dipole moment, and should thus not be seen in CL, which is contrary to what we observed in the experiments and numerical simulations. A relativistic extension of such theory would most probably include such a non-dipolar mode within the EIRE probability. Nevertheless, notice also that the FWHM of the resonances match almost quantitatively the results of the last section, suggesting that the quasistatic approximation is actually rather appropriate for modelling the situation.

### 4.4.5 Conclusion

In this section, we have theoretically justified the experimental and numerical results presented in section 4.3. Modal decompositions of the EIRE probability, extinction and scattering have been proposed in the quasistatic approximation and compared to the well-known modal decomposition of the EEL probability. These modal decompositions well explain the results of section 4.3.

These expressions justify that a parallel can be drawn between STEM EELS and extinction spectroscopy on the one hand, STEM CL and scattering spectroscopy on the other hand. Indeed, we have found that, for a given dipolar mode, the EEL and EIRE probabilities are respectively

[18] A few counter examples can be found in the literature. For instance, let us quote the blueshifted calculated EELS with respect to calculated extinction of prolate gold spheroids reported in [164], or the blueshifted simulated zEMLDOS with respect to simulated extinction of gold nanocrosses [42]. Globally speaking, the situation is thus unclear at the moment, as also noted in [152].

proportional to the extinction and scattering cross sections spatially modulated by the square of the Fourier transform of the z Electric field of the mode. Otherwise speaking, we have properly demonstrated that EELS and CL are nanometric equivalent of optical spectroscopies. This link may be intuitively extended to a fully retarded regime by stating that EELS should be related to extinction and CL should be related to scattering, at the nanometer scale.

It should be noticed, however, that a great difference happens between fast electron based spectroscopies and optical spectroscopies due to their different excitation source. In particular, some dark modes that cannot couple to light for a given polarization may be excited by an electron. Within the bright modes, we can also intuitively define, similarly to the radiative modes which appear both in EELS and CL, radiative bright modes appearing both in extinction and scattering spectroscopy. Such qualifying is not superfluous as some bright modes might not induce resonances in scattering spectra, contrary to extinction spectra [165]. Generally speaking, any equivalence between excitation and detection is not straightforward. In particular, some radiative dark modes, visible in CL while being invisible in scattering might exist (see the comparison between calculated scattering and CL spectra reported in [138]).

Furthermore, and as importantly, the modal decompositions allow interpreting fast electron based spectroscopies in general as well as optical spectroscopies in terms of SP modes. Indeed, as explained in section 2.3, the square of the Fourier transform along z of the z-projection of the electric field of a geometric mode corresponds to the square of the Fourier transform along z of the z-projection of the electric field of some surface eigenmode, in particular, in the case of a metal-dielectric system, of some SP mode. Therefore, the closely similar spatial variations observed when fitting the peaks at the resonance energies appearing in the EELS and CL spectra are the spatial variations of the z electric field intensities of some SP mode. The EELS and CL resonances are obviously related to the spectral characteristics of this SP mode, because the spectral contribution from a mode to EELS and CL is given by the imaginary part and square modulus of the function $f_i(\omega)$, whose pole gives the SP mode condition (equation 2.3.17) which defines the spectral characteristics of the mode. The same holds for extinction and scattering. However, these relationships are non-trivial, as demonstrated by the spectral shifts discussed before for the same mode. It can be simply shown using a Drude model that such shift should be related to the virtual character of the mode (in the quasistatic approximation, to the dissipative character of the metal) and may not exist for true eigenmodes (see appendix B). For virtual modes, the resonance conditions of the imaginary part and squared modulus of $f_i(\omega)$, as well as all their related expressions, can slightly differ. However, our model predicts shifts that do depend on the dielectric properties of the media through the expression of $f_i(\omega)$. As a consequence, these shifts are not a general feature for a SP mode.

As an example, let us consider the observed as well as interpreted spectral redshift from EELS to CL. Such shift may remind the slight systematic redshift from the maximum absorption to the maximum oscillation amplitude of a damped harmonic oscillator [166], which is usually evoked to explain some spectral shift between the near field and far field optical responses of metal nanoparticles [167], and to which EELS and CL may be intuitively thought of as respectively. However, following our model, such shift between EELS and CL would be due to the behaviour of the dielectric function of gold in this spectral range[19] only.

Interestingly, our model also predicts, when using a Drude model for the dielectric function of the metal, that CL/scattering should be always slightly blueshifted with respect to EELS/extinction,

[19]Gold is known to have an interband transition at 2.6 eV [168], which may already affect the metallic optical properties of the medium around 2.2 eV.

which is contrary to what we have found. Keeping in mind that the above theory well accounts for the experimental and numerical results, these last points demonstrate the failure of the Drude model for modeling the optical properties of gold in the visible and the departure of SP modes from naive oscillator models. We leave all the details to appendix B.

## 4.5 Conclusion

In this chapter, we have shown that fast electron based spectroscopies can be viewed as nanometric equivalent of optical spectroscopies. With a distinction made between EELS, CL, extinction and scattering, we have shown that EELS corresponds to extinction and that CL corresponds to scattering, both at the nanometer scale.

To do so, we have performed combined STEM EELS and STEM CL measurements on a single gold triangular nanoprim, which constitutes the first experimental comparison of EELS and CL on a single metallic nanoparticle. We have evidenced slightly shifted resonances from EELS to CL associated to similar SP modes. Otherwise speaking, we have shown that the modes accessed in CL are the same as the modes accessed with EELS, yet they appear as sligthly shifted resonances in the spectra. These findings were conformed by BEM simulations. Further simulations of the optical properties of the same object have shown that a similar shift occurs between extinction and scattering. Modal decompositions of CL, extinction and scattering have been proposed based on a BEM framework in the quasistatic approximation. These modal decompositions constitute the first general theoretical framework within which CL, extinction and scattering can be readily understood as reflecting the spatial and/or spectral properties of its SP modes. Precisely, the space dependences of both EELS and CL reflect the spatial variations of the electron axis (z) projected electric field intensities of the modes, while the energy dependence of EELS, CL, extinction and scattering are dictated by the imaginary part and square modulus of some function whose pole defines the spectral characteristics of a mode. In parallel, the comparison of these modal decompositions reproduce most of the observations. In particular, it predicts spectral redshifts from EELS to CL and from extinction to scattering , due to slightly different spectral dependences of the imaginary part and square modulus. Finally, the modal decompositions set fast electron based spectroscopies as nanometric equivalent of optical spectroscopies. Precisely, for a given dipolar mode, EELS and CL are respectively found to be proportional to the extinction and scattering cross sections spatially modulated by the square of the Fourier transform of the z Electric field of the mode. However, the interplay between electrons and light may be rather complex, deserving further careful investigation.

The close link between EELS and CL underlined in this chapter makes fast electron based spectroscopies in general as great valuable tools for studying SP modes. As an advantage when compared to EELS, CL offers a much enhanced spectral resolution, allowing the acquisition of peaks with physical widths. However, combined EELS and CL measurements can be very useful in some situations. Indeed, in the same way we have defined a radiative mode from our calculation, we can predict non-radiative modes as non dipolar modes. Such a mode would be detectable only in EELS as it appears only in the EELS modal decomposition. The evidence of radiative and non-radiative modes by comparing EELS and CL should thus be feasible, and of great interest for some complicated systems (see next chapters).

Finally, the close relationship that exist between the expression of the EIRE and EEL probabilities may be intuitively extended to a close relationship between the EIRE probability and the EMLDOS. Indeed, following the relationship that exists between the EEL probability and the

EMLDOS (equation 2.5.12), we can intuitively define a rEMLDOS and a n-projected rEMLDOS in the quasistatic approximation as:

$$\rho^{rad}(\vec{r},\omega) \sim \sum_{i=d} \left| -g_i(\omega) + \frac{1}{\tilde{\varepsilon}(\vec{r},\omega)} \right|^2 \left| \vec{E}_i(\vec{r}) \right|^2 \tag{4.5.1}$$

$$\rho_n^{rad}(\vec{r},\omega) \sim \sum_{i=d} \left| -g_i(\omega) + \frac{1}{\tilde{\varepsilon}(\vec{r},\omega)} \right|^2 |E_i^n(\vec{r})|^2 \tag{4.5.2}$$

so that the EIRE probability expresses as:

$$\Gamma_{EIRE}(\vec{R},\omega) \sim \tilde{\rho}_z^{rad}(\vec{R},\frac{\omega}{v},\omega) \tag{4.5.3}$$

where $\tilde{\rho}_z^{rad}(\vec{R},k_z,\omega) = \int\int \rho_z^{rad}(\vec{R}+z\vec{e}_z,\vec{R}\,'+z'\vec{e}_z,\omega)e^{i(k_z z+k_z' z')}dzdz'$ is the Fourier transform of the radiative EMLDOS with respect to z and z' . At first sight, we might anticipate that a radiative EMLDOS would be defined in a full relativistic treatement as:

$$\rho^{rad}(\vec{r},\omega) \sim \mathcal{T}\left[ \left| \overleftrightarrow{G}(\vec{r},\vec{r},\omega) \right|^2 \right] \tag{4.5.4}$$

$$\rho_n^{rad}(\vec{r},\omega) \sim \vec{e}_n . \left| \overleftrightarrow{G}(\vec{r},\vec{r},\omega) \right|^2 . \vec{e}_n \tag{4.5.5}$$

so that the relation between the EIRE probability and the radiative EMLDOS given by equation 4.5.3 would hold in general. However, it turns out that the above quantities diverge. At this time, any proper definition of a radiative EMLDOS is still an open question.

# Chapter 5

# SP modes of disordered media

## 5.1 Introduction

### 5.1.1 Positioning of this study

The SP modes of single nanoparticles have spatial and spectral features which depend on the shape of the nanoparticle. Moreover, for simple shapes, the eigenfrequencies follow trends with the size, consitutive material and dielectric environment of the nanoparticle which are now well known (see, for instance, section 2.3). Therefore, the nanoscale light induced electric fields, mediated by the SP modes, and, by extension, the optical properties of simple single nanoobjects are quite well understood. However, the situation is far more complex in disordered, or random metal-dielectric systems, like, for instance, an assembly of nanoparticles with non-predictible shapes and locations. Such a system is obtained naturally by depositing some metal onto a dielectric substrate. The sample obtained is often called "semicontinuous metal film", and is usually modelled theoretically by randomly generating a square lattice of metal and dielectric bonds. Very broadband strong absorption features have been reported in semicontinuous metal films around the percolation threshold [169, 170]. Simple models related them to some light induced randomly dispersed very intense electric fields, confined on a few nanometers and arising over a broad spectral range. These strongly confined fields were called "Hot Spots" (HS) [29]. To explain their anomalous feature, these HS were interpreted as being the expression of a rich and complex set of SP modes [33, 34]. These modes have been predicted to have very close eigenfrequencies and electric fields strongly confined locally. Their supposed coexistence in a same system would make a semicontinuous film around the percolation threshold a spectrally and spatially dense system.

Soon after the HS were theoretically predicted, maps acquired with SNOM suggested localized intensity maxima on percolating metal films [171]. However, the fine nanometric spatial structure, broadband character and exact location of these localized spots could not be retrieved. This was due to a limited spatial resolution[1], a restricted spectral range of excitation and a non-simultaneous access to the sample morphology. In fact, such drawbacks are reminiscent of many near-field optical techniques in general. Furthermore, the probe of a SNOM is known to be invasive, inducing distortions in the measured signal [124, 125]. As a consequence, despite numerous experimental studies based on various near-field techniques [172–178], a full and reliable characterization of the

[1] Let us remind that the predicted size of a HS was predicted to be less than 10 nm [29].

local fields, at the relevant length scale, is still missing at this time in percolating systems. By extension, it is unclear how close these electric fields are to the predicted HS [29].

Moreover, fundamental questions have been raised concerning the SP modes of a percolating system themselves. In particular, their either localized or coherent character over large distances has been questionned [33, 34], together with their radiative or non-radiative nature [34]. Furthermore, as the electric fields induced by light excitation of a percolating film have been predicted to be highly different from those of a random ensemble of small nanoparticles [29], the modes they ensue from should also differ. The SP modes of percolating metal films have been adressed in the past by Bosman et al. through STEM EELS measurements [39]. Nevertheless, such study has not been extended to semicontinuous films in general so far. Moreover, the SP modes of semicontinuous films (as opposed to their associated electric fields as visualized at a single wavelength) have never been directly identified in all the other works based on near-field optical techniques, mainly because these techniques do not combine a high spatial resolution and a broadband excitation[2]. Any proper demonstration of some extraordinary character of the SP modes of semicontinuous films around the percolation threshold is thus missing at this time.

As previously stressed in the last chapter, spatially resolved fast electron based spectroscopies can not only map the electric field intensities associated to the SP modes at the nanoscale, over a broad spectral range and with a direct access to the sample morphology. Such techniques can also allow identifying directly, spatially and spectrally, the SP modes. We have thus used STEM EELS on various semicontinuous films to extract and discuss the modes of such systems themselve in order to demonstrate that the modes of a percolating system differ from the modes of a random ensemble of small nanoparticles from some extraordinary properties. The results of such a study are exposed in this chapter. We have relied on EELS rather than on CL to answer this question because it appeared that the light induced by the interaction with fast electrons with such samples is very weak. However, preliminary results of comparative measurements of STEM EELS and STEM CL on semicontinuous films have been obtained but still require further attempts. They are thus not reproduced here, but are exposed briefly in chapter 6.

### 5.1.2 Semicontinuous films, broadband optical properties, HS and SP modes

Semicontinous metal films are usually grown by thermal evaporation or sputtering of metal onto a dielectric substrate. The shape of the obtained sample is largely dependent on the metallic effective thickness deposited. Bright Field (BF) images[3] of semicontinuous gold films of increasing (from the left to the right) metal quantity deposited on glass are shown on figure 5.1a. At low metal coverage, the substrate sustains a large number of small, disconnected and spherical metallic clusters. At high metal coverage, a continuous flat metal film is obtained, with possibly a few voids if the effective thickness is not large enough. Between these two regimes, the metallic clusters progressively grow, coalesce and aquire very tortuous geometries. At the percolation threshold, a continuous conductive channel is formed, allowing some current to flow from one end to the other. Such a percolating film is one of the most famous examples of a natural fractal shaped system [179], which can be opposed to Euclidian shapes. For instance, a small cluster found at low metal coverage is a typical Euclidian object.

[2]Indeed, as we have demonstrated in the previous chapters, a mode cannot be accessed from a simple energy-filtered map.

[3]In such images, gold appear dark over a bright background.

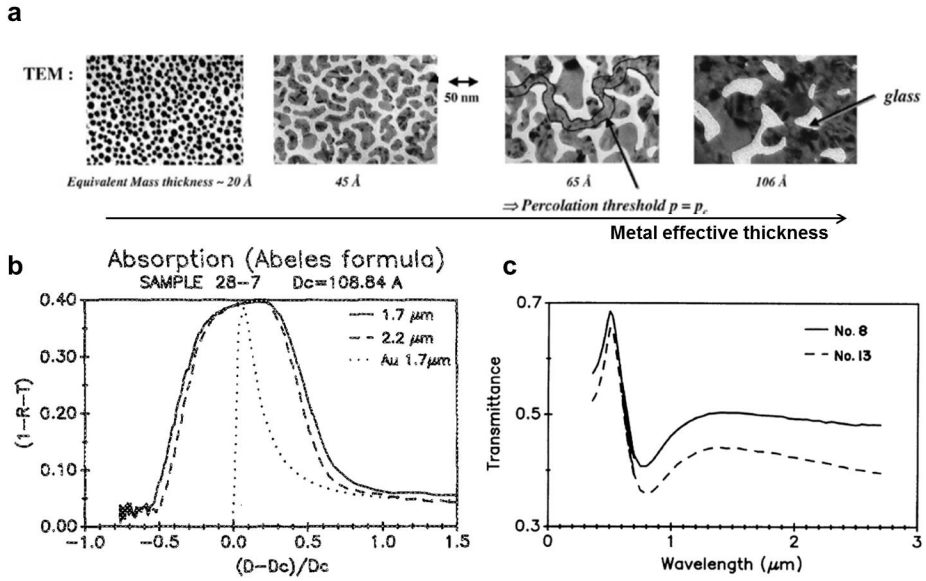


Figure 5.1: Semicontinuous metal films. a) Bright Field (BF) images of semicontinuous gold films of increasing metal quantity deposited on glass. At the percolation threshold, a continuous conductive channel is formed, allowing some current to flow from one end to the other. b) Absorption cross section of semicontinuous gold films, measured in situ, at excitation wavelengths of 1.7 µm and 2.2 µm, as a function of the metal concentration. The percolation occurs at zero abcissa. Extracted from [169]. c) Transmittance spectra of two percolating gold samples. Extracted from [170].

A semicontinuous film is well known for its electrical or optical properties, which strongly depend on the metallic concentration and may acquire fascinating characters [180]. Figure 5.1b shows the absorption cross section of semicontinuous gold films, measured in situ, at excitation wavelengths of 1.7 µm and 2.2 µm, as a function of the metal concentration, which was reported in [169]. Clearly, the absorption, being zero at both low and high metallic concentrations, strongly increases around the percolation threshold. The authors thus attributed these strong absorption features to the fractal character of such film. They later refined this statement by proposing a scaling law relying on the percolation theory to interpret these results [181]. Furthermore, these strong IR absorption cross sections of percolating films were later shown to extend up to 500 µm, as shown from figure c, which displays the transmittance spectra of two percolating gold samples [170].

These extraordinary optical properties have been predicted to be related to a very singular electromagnetic phenomenon at the nanoscale. The electromagnetic properties of a semicontinuous film can be modelled by numerous means [182]. In particular, models based on the percolation theory well render the random or disordered character of such a semicontinuous film. Beyond them, a random resistor-inductor-capacitor (RIC) model consists in randomly generating a square lattice of metal and dielectric bonds with corresponding dielectric functions, with a certain probability for a bond to be metallic. This probability thus accounts directly for the metal coverage of the semicontinuous film. In particular, the generated square is at percolation if this probability is equal to some critical probability. Shalaev and Sarychev used the RIC model to perform numerical

simulations of the local light induced electromagnetic fields, in the quasistatic approximation, and for different metallic coverages [29]. Among their findings, they have shown that illuminating a semicontinuous film at the percolation threshold with a monochromatic plane wave induces very strong spatial and spectral variations of the electromagnetic fields at the nanoscale. Precisely, they calculated nanometer resolved maps of the electric field intensities at different excitation wavelengths, which are reproduced on figure 5.2a. Very clearly, numerous local intensity maxima can be resolved in each map. A parallel between these spots and the local field strengthenings found by exciting a nanoobject with light and mediated by the SP modes (see, eg., figure 4.10), may be easily drawn. However, as compared to the case of a single nanoobject, these spots show very unusual features. Indeed, the spatial pattern they form is much more complicated. The number of spots is very large, and their spatial density very high. The spots appear to be randomly distributed in space. Their intensity is strongly varying, from one to another. These spots are strongly confined, their size being less than 10 nm. Their spatial distribution highly depends on the excitation wavelength. Finally, these spots are still present very far in the IR, the last map being calculated at 20 µm. To express the fact that their intensity exceeds the applied field by several orders of magnitude, the authors gave to the strongest of these spots the name of HS. Such HS would be responsible for the previously measured broadband optical properties, and other giant linear Rayleigh [183], Raman scattering [184], and non-linear optical effects [29].

Recently, such a simple theoretical modelling has been refined on the basis of electromagnetic simulations of systems whose morphologies are reproduced from real semicontinuous films. FDTD simulations have been reported on a simulated percolating system [185, 186], and reproduced the existence of HS. Highly confined local spots of high intensity were also evidenced in calculated energy filtered maps of the EMLDOS [112, 142, 187], shortly after strong spatial variations of the EMLDOS were experimentally evidenced on a percolating sample [177].

After the theoretical predictions proposed by Shalaev and Sarychev [29], Grésillon et al. used SNOM to acquire maps of the field intensities induced by laser excitation of a semicontinuous film around the percolation threshold at a given wavelength [171]. They could distinguish highly localized intensity maxima that form a pattern which changes with the excitation wavelength. They thus interpreted these local spots as the HS proposed by Shalaev and Sarychev. Following this pioneering work, semicontinuous films have been studied using many near-field optical setups, from Photon Scanning Tunneling Microscopes (PSTM) [173, 174] to aperture [175, 176] or scattering-type (apertureless) SNOM [172]. Each ot these works confirmed the existence of confined intensity maxima, which were observed at various excitation wavelengths, from the near UV [172] to the visible [173], or closer to the IR [175, 176]. The excitation wavelength and polarization was demonstrated to affect the pattern of the spots in the image [171–173, 175, 176]. The study of these local spots was also widened to various sample morphologies, from small individual nanoparticles to an almost continuous film [173, 174]. It was noticed that the observed pattern also depends on the sample, which can be characterized from its metallic quantity. Recently, PEEM was also shown to resolve local intensity maxima in the IR in semicontinuous films [178]. These local maxima were interpreted as HS, whose pattern has been studied at different excitation wavelengths and for different metallic coverages. These observations were found to be satisfyingly explained by the scaling theory proposed early by Shalaev and Sarychev to describe the wavelength and metal quantity dependence on the HS [29]. Finally, the EMLDOS was directly accessed on semicontinuous films by measuring the decay rates of fluorescent emitters randomly dispersed over semicontinuous films using a fluorescence confocal microscopy setup [177]. It was evidenced that the strongest spatial variations of the EMLDOS on a semicontinuous film are found around the percolation threshold.

The authors related this observation to the fractal character of such a system. It is thus well admitted that the fractal geometry of a semicontinuous film around the percolation threshold is directly responsible for the extremely strong spatial fluctuations of the electric fields at a given excitation wavelength. This was early noticed by Shalaev and Sarychev when they predicted the HS [29], as similar features were previously encountered in other fractal systems. For instance, similar broadband optical properties and nanoscale HS were also predicted for fractal aggregates of small particles [188], before being confirmed by SNOM experiments [189]. Moreover, similar observations of confined intensity maxima were also made on self-affine metal films [190] or rough metal films [191].

As previously mentioned, a semicontinuous film is a typical example of a disordered, or random system. Fundamentally, very interesting questions are raised when considering the eigenmodes of a disordered system. In particular, closely related to this topic of disordered media is the spatial localization of their eigenmodes, which can be confined into extremely small scales when induced by large degrees of disorder [192]. A famous example is, for instance, the Anderson localization of light or electron states [193]. However, lower disorder degrees tend to favor weak localization rather than Anderson localization. Moreover, the eigenmodes may also display long-range coherence properties.

For SP modes, these fundamental problems emerged with the understanding that the local fields induced by light excitation on a a random metal dielectric composite would be strongly confined at the nanoscale. Indeed, a HS, as induced from a plane wave excitation, is obviously related to some SP mode of a system. Therefore, the small size of the HS would suggest some underlying localized SP modes. The localized character of the SP modes of disordered metal dielectric systems was first discussed for fractal aggregates of small particles, independently by Shalaev et al. [31] and Stockman et al. [32], with contradictory conclusions. The debate was later extended to semicontinuous films around the percolation threshold [33, 34], after it was realized that there is no trivial correlation between a light-induced HS and a mode [29]. This issue of SP mode localization of semicontinuous films was tackled experimentally by Seal et al. [194] and Krachmalnicoff et al. [177], who extracted a characteristic size of the modes from either high order moments of intensity enhancements measured in SNOM or variations in the decay rate of dispersed fluorescence emitters measured in fluorescence confocal microscopy. Today, it seems well established that the global spatial extension of the modes of a semicontinuous film decreases around the percolation threshold. This was confirmed theoretically by Cazé et al., who introduced the concept of cross EMLDOS to quantify this spatial extension of a SP mode [112]. Finally, Bosman et al. paved the way for studying the SP modes of semicontinuous films through STEM EELS measurements by studying percolating silver films [39], by evidencing multiple modes responsible for a large number of resonances in the EEL spectra.

On the theoretical side, Stockman et al. simulated the SP modes of a semicontinuous film slightly before the percolation threshold, modelled by randomly positioning some metal elements with a one half probability, in the quasistatic approximation [34]. The authors showed that the set of SP modes is extremely complex, consisting in a very large number of modes with very close eigenfrequencies. The electric fields of these modes featurelessly consist either in a single strongly confined local spot or an ensemble of several strongly confined local spots separated by large distances. The corresponding modes were respectively called localized and delocalized. The electric field intensities of some examples of localized and delocalized modes can be seen in figure 5.2b. Stockman et al. thus contradicted similar simulations performed earlier by Shalaev et al., who interpreted the pattern of the HS as resulting from the light excitation of some modes assumed to be Anderson localized [33]. Indeed, Stockman et al. showed that not all the modes are Anderson localized, which was attested later by Genov et al. [194]. This coexistence of so-called localized and

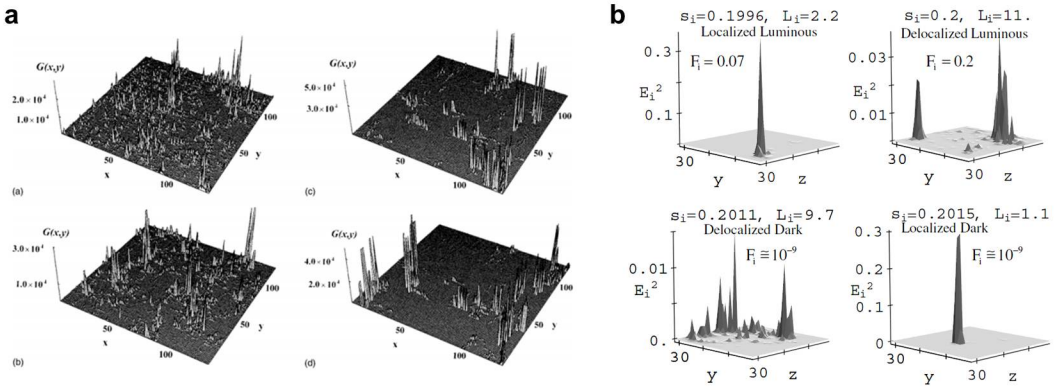


Figure 5.2: Quasistatic numerical simulations of random metal-dielectric composites. a) Maps of the electric field intensities induced by the monochromatic plane wave excitation of a percolating-like system. The maps correspond to excitation wavelengths of 0.5 µm, 1.5 µm, 10 µm and 20 µm and show strongly localized HS located at some positions. Extracted from [29]. b) Electric field intensities of the SP modes of a percolating-like system. A distinction is made between localized, delocalized, luminous and dark modes. Extracted from [34].

delocalized modes is often referred to as an "inhomogeneous localization" of the modes [195], and has not been directly experimentally evidenced so far. Furthermore, it is important to stress that both a set of Anderson localized modes and such an inhomogeneous localization would induce HS equally well when the medium is excited by light.

For all the above listed difficulties they raise, which are typical to disordered media, the SP modes of semicontinuous films have attracted and still attract much attention as model cases of eigenmodes of disordered systems. To that, we can add the fact that Stockman et al. raised an interesting question dealing with the coupling of these modes to light [34]. They defined "luminous" and "dark" modes, depending on their coupling efficiency to light. Examples can again be seen in figure 5.2b. These modes have not been verified experimentally so far. The topic was later tackled by Cazé et al., who compared calculated EMLDOS and rEMLDOS for such systems [142]. The SP modes of semicontinuous films, which drive the HS, are thus a very rich topic, which deserves much consideration.

This chapter is devoted to the works we have performed in this direction in collaboration with Sophie Camelio, David Babonneau and Frédéric Pailloux from the Institut P Prime of the Université de Poitiers, David Rossouw and Gianluigi Botton from the Department of Materials Science and Engineering of Hamilton Mc Master University, and Mondher Besbes and Jean-Jacques Greffet from the Laboratoire Charles Fabry of the Institut d'Optique Graduate School. The samples were synthesized by our collaborators from Poitiers, and are made of ion beam sputtered silver sandwiched between two amorphous silicon nitride ($Si_3N_4$). Details on the preparation can be found in appendix C. Each sample contains many semicontinuous areas with their own morphology, allowing the study of multiple systems on the same sample. Most of the STEM EELS experiments were performed in Orsay using the VG STEM. However, a few additional experiments were performed by our collaborators from Mc Master University. Numerical simulations of the EMLDOS were performed by our collaborators from the Laboratoire Charles Fabry using a Finite Element Method (FEM) (details are also kept to appendix C).

This chapter is divided into two sections. In section 5.3, a typical semicontinuous system around the percolation threshold is studied. Typical local EEL probability spatial maxima, related to a strong point to point spectral complexity EEL probability and sharing many character traits with the HS, are evidenced at constant energy in the low energy spectral range. These singular spectral and spatial variations of the EEL probability are linked to a complex set of modes that we evidence and fully characterize. Section 5.4 then evidences that these modes are the result of the fractal geometry of the medium.

## 5.2 Methods

### 5.2.1 STEM EELS measurements

Most of the experiments which brought the following results have been performed at Université Paris Sud using the VG STEM. Additional minoritory experiments were also achieved at Mc Master University using the FEI TEM. The main difference between these two instruments is their spectral resolution (see section 3.2), which is on the order of 200 to 250 meV for the VG STEM and less than 100 meV for the FEI TEM after deconvolution. The reason why these extra experiments were performed was to ensure that the observations obtained on the VG STEM were reliable (see appendix C).

On section 5.3 (subsections 5.3.2 and 5.3.3), a typical semicontinuous region of a sample around the percolation will be studied locally with the high spectral resolution STEM EELS measurements allowed by the FEI TEM. The results presented here were obtained by scanning a small, 77 x 77 nm large, area, belonging to this region and whose HAADF image can also be seen on figure 5.5a, with an equivalent spatial sampling of 2.4 nm. Additional similar measurements were also obtained in two other areas, whose HAADF images are shown on figure 5.3. The spectral resolution of the experiment is 60 meV.

Then, on subsection 5.3.4, a large similar area will be examined based on some measurements performed with the VG STEM. To avoid very pronounced ring effects in the deconvolution (see section 3.3), the number of iterations has been limited to a few iterations, so that the spectral resolution of these measurements is estimated as only 250 meV. To avoid the spatial sampling to be too different from the spatial resolution, the measurements have been restricted to small regions of the area, such as the one delimited by the blue dashed square visible on figure 5.4a. However, several (21 in total) small regions adjacent to each other were probed further in order to completely cover a large area, delimited by the white dashed square in figure 5.4a. The total dataset thus corresponds to a 888x1030 nm large area, scanned with a sampling step of 3.9 nm. The HAADF image of the region covered by the measurements shown on figure 5.8a was reconstructed by cross-correlating each of the HAADF images obtained during the STEM EELS measurements with a large field of view of the area (the HAADF shown on the bottom left of figure 5.4a) recorded separately. Each dataset was processed independently by performing multipeak fitting. The amplitude, FWHM and energy maps of figure 5.8b were then also obtained from cross-correlation.

Finally, section 5.4 compares STEM EELS measurements performed using the VG STEM in three different areas of a sample. This time, the measurements were performed at once. The total size of each scanned area is 485x485 nm, and the spatial sampling was set to 3.9 nm. For fair comparison, each dataset was obtained with similar acquisition conditions, and display an equal spectral resolution of 200 meV. Furthermore, the normalization condition of each dataset allows quantitatively comparing the EEL probability of each dataset. Finally, the conditions imposed

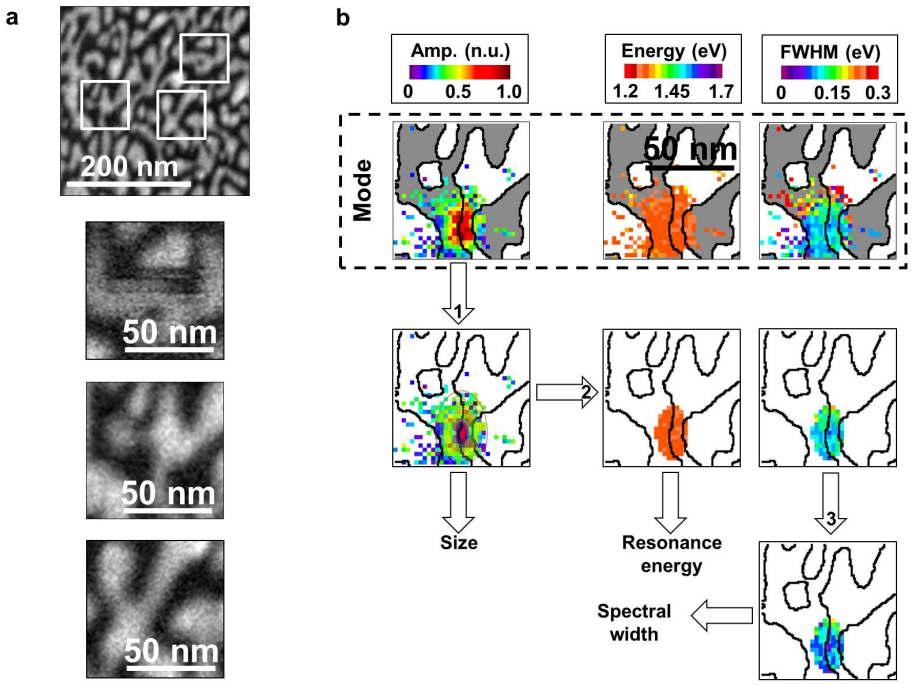


Figure 5.3: Fully characterizing the SP modes. a) HAADF image of the semicontinuous region inside which the STEM EELS measurements have been performed. The HAADF images of three small areas which have been scanned independently are added. b) Evaluation procedure for the features (size, resonance energy, spectral width) of a single mode, from the maps of the amplitude, central energy and FWHM of the corresponding peaks. Step 1: a 2D Gaussian function is fitted on the amplitude map. Step 2: only the pixels of the FWHM and energy maps that correspond to pixels of the amplitude map whose value is larger than the half maximum of the Gaussian function are kept. Step 3: the values of the remaing pixels of the FWHM map are deconvolved to remove the effect of the finite spectral resolution (see section 3.4).

when fitting the spectra (see subsection 3.3.2) were also set similar for each dataset.

### 5.2.2 Extracting the features of a SP mode

In subsection 5.3.3, we propose to extract quantitively the complete spatial and spectral features (location, intensity, "size"[4], resonance energy and spectral width) of a mode offered by the technique. In order to do so, the peaks whose central energies are found within very narrow energy windows are selected to provide maps of the amplitude, central energy and FWHM of the peaks corresponding to a single mode, as was done in chapter 4. The amplitude map shows the z-electric field intensity local variations of the mode in the scanned area. Such a map, in combination with the superimposed sample profile, thus allows visualizing directly the position over the substrate, size and intensity of the mode. The energy map shows the resonance energy inherent to the mode as measured by the

[4]Such a size is defined as the area covered locally by a mode. It is thus not, strictly speaking, the complete size of the mode.

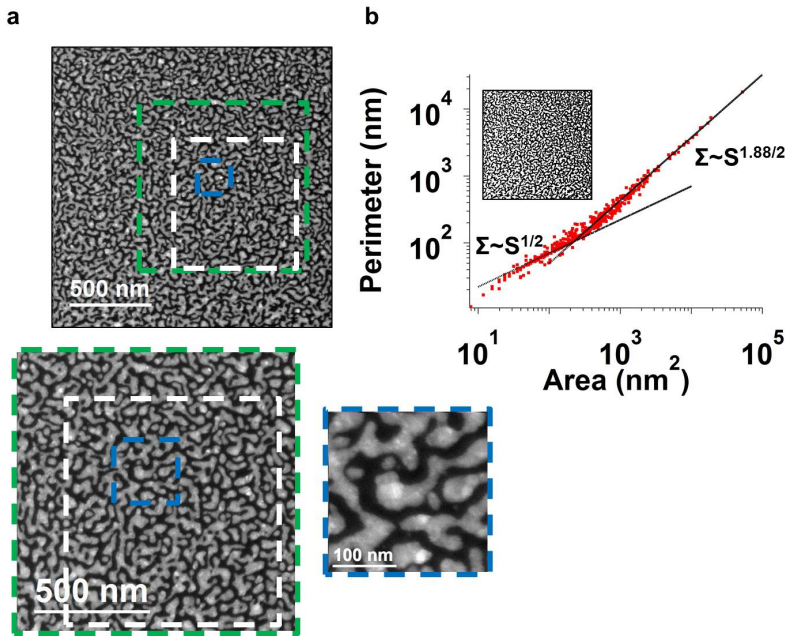


Figure 5.4: A typical semicontinuous area around the percolation threshold. a) HAADF images of a typical disordered area, displayed at different magnifications. The colored dashed squares delimit the zoomed-in areas. b) log-log plot of the perimeters of the metal clusters found in the binary HAADF image shown in inset, as a function of their areas. For small clusters, the perimeter roughly scales with the square root of the surface. The slope increases for large clusters.

technique. Finally, the FWHM map shows the spectral width inherent to the mode broadened by the spectral resolution of the technique. The combination of the three maps thus completely defines, spatially (yet locally) as well as spectrally, the mode. The scheme to extract the size, resonance energy and spectral width of the mode is shown on figure 5.3b. A 2D Gaussian function was fitted on the amplitude map (step 1), allowing to define a size of the mode as the FWHM of this Gaussian function. Then, to evaluate its spectral width and resonance energy, only the pixels of the FWHM and energy maps that correspond to pixels of the amplitude map whose value is larger than the half maximum of the Gaussian function are kept to remove noise effects and contributions from aberrant fits (step 2). The resonance energy of the mode is thus directly defined as the mean value of the new energy map. For the spectral width, the values of the remaing pixels of the FWHM map are deconvolved to remove the effect of the finite spectral resolution (step 3, see section 3.4). The spectral width of the mode is then defined as the mean value of the resulting FWHM map.

## 5.3 STEM EELS on a semicontinous area around the percolation threshold

### 5.3.1 Introduction

This section aims at studying a typical disordered system, similar to the region that the HAADF images of figure 5.4a show at different magnifications. The colored dashed squares on the HAADF images demarcate the zoomed-in areas. To relate the morphology of this region with the semicontinuous films which have been previously studied in the litterature, a geometrical analysis has been performed by thresholding and binarizing the HAADF image with large field of view and performing a contour detection of the silver clusters. Figure 5.4b shows the plot in log log scale of the perimeters of the metal clusters found in the binarized HAADF image, shown in inset, as a function of their areas. The perimeter is found to roughly scale with the area following two power laws which depend on the sizes of the clusters. The two regimes are separated by a well pronounced change of slope. In the first regime, the perimeter roughly scales with the square root of the surface as evidenced by the reference slope line: $\Sigma \sim S^{1/2}$ (if $\Sigma$ is the perimeter and $S$ is the area of a cluster). Such geometrical relationship is typical to objects with Euclidian shapes. However, the power exponent increases in the second regime, translating the fact that the larger clusters acquire a very tortuous geometry. Such an increased slope is characteristic of fractal objects, for which it can be shown that the perimeter scales with the surface as: $\Sigma \sim S^{1.88/2}$ [177]. This relationship is a universal scaling law typifying the fractal geometry, which is quite well reproduced here. As a consequence, in such an area, the smallest clusters are found to display an Euclidian geometry while the biggest ones show a fractal character. This is characteristic of metal dielectric composites, or semicontinuous films, near the percolation threshold [196]. The results presented below can thus be safely compared to the abundant litterature dealing with semicontinuous films.

Because they approach at best the real properties of the system due to the high spectral resolution offered by the FEI TEM, we choose to present first some representative results based on the experiments performed in Mc Master University. However, the findings are not significantly changed when based on the VG STEM experiments. In particular, VG STEM experiments were the first to suggest that some anomalously strong spatial and spectral variations of the EEL probability at a very local scale would be related to some modes which could be evidenced through a resonance energy and spectral width. The qualitative agreement between non-monochromated and monomochromated measurements can be examined further in appendix C.

We will first examine in subsection 5.3.2 the spatial and spectral variations of the EEL probability that exist in such system at a very local scale. We will then locally characterize in subsection 5.3.3 the SP modes they are due to. These modes will finally be observed at a much larger scale in subsection 5.3.4.

### 5.3.2 High spectral resolution STEM EELS measurements

Figure 5.5a shows the HAADF image of the scanned area recorded during the STEM EELS acquisition, together with the HAADF image of the sample region it belongs to. Local EEL probability spectra are shown on figure 5.5b. The spectra correspond to probe positions separated one from another by 25 nm. Despite these close distances, each spectrum has its own structure, showing multiple peaks from 0.5 eV[5] up to 4 eV. These peaks have their own spectral characteristics (central

[5]This value is most probably an experimental limitation resulting from the FWHM of the ZLP.

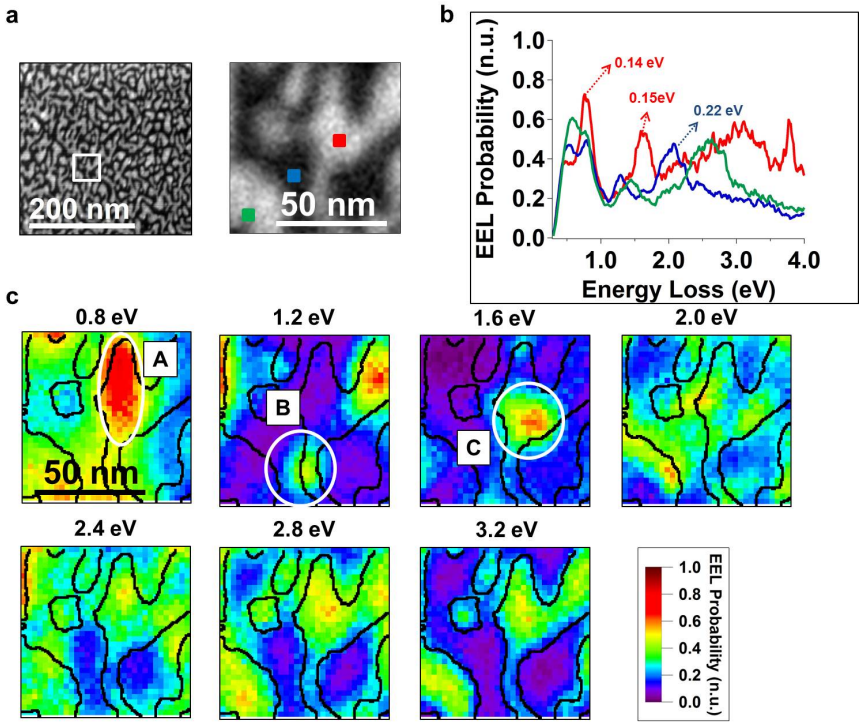


Figure 5.5: STEM EELS measurements in a local semicontinuous area. a) HAADF image of the scanned area recorded during the STEM EELS acquisition. b) Local EEL probability spectra corresponding to the electron probe positions indicated in the HAADF image and separated by 25 nm. c) Energy filtered maps of the EEL probability for some energy loss values spanning the whole spectral range of interest. The white circles delimit small regions where the EEL probability overcomes the surrounding. The corresponding spots as referred to as spots A to C.

energy, FWHM and amplitude), suggesting a particularly rich set of SP modes spatially coexisting at small spatial scales. The FWHM of some peaks, as obtained from multipeak fitting, are added to the spectra. It should be noticed that the FWHM of these peaks are not less than 100 meV. Taking into account the 60 meV spectral resolution, a measured FWHM of 100 meV would correspond to an intrinsic FWHM of 80 meV. Knowing that the gap between such a measured FWHM and an intrinsic FWHM reduces as the measured FWHM increases, we can thus conclude that the dataset is very slightly affected by the finite spectral resolution.

These strong point to point spectral variations lead to strong spatial variations of the EEL probability all over the spectrum, that are illustrated in the energy filtered maps of figure 5.5c. The energy loss values were chosen to span the whole spectrum. In each map, small regions where the EEL probability overcomes the surrounding can be seen, down to 0.5 eV[6]. Three of these spots, denoted as spots A to C, are evidenced by the white circles. At the lowest energies (upper pannel), the location of the spots is strongly affected by changes in energy, and seem randomly distributed

[6]We deliberately do not use the term "HS" since we reserve it to qualify the light induced electromagnetic fields mediated by the SP modes predicted by Shalaev and Sarychev [29].

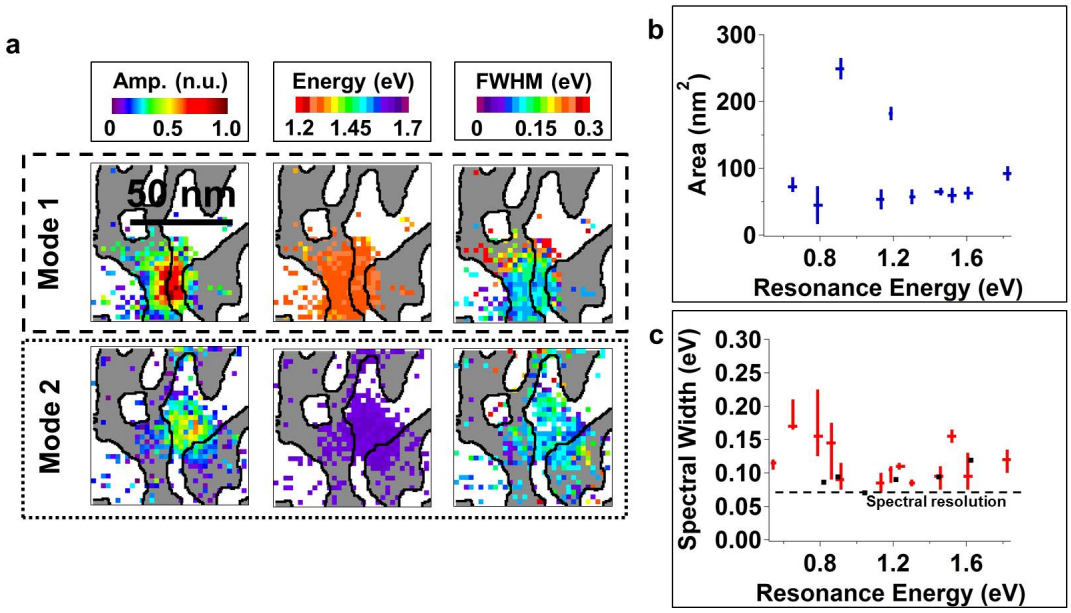


Figure 5.6: Local characterization of the low energy SP modes of a semicontinuous film around the percolation threshold. a) Maps of the amplitude, energy and FWHM of the peaks whose energy is 1.30 +/- 0.025 eV (mode 1) and 1.61 +/- 0.025 eV (mode 2). b) Area locally covered by the modes as a function of their resonance energy. c) Spectral widths of the modes as a function of their resonance energy (red dots) and FWHM of some simulated peaks as a function of their central energy (black dots). The black dashed line indicates the spectral resolution of the measurement.

over the substrate, independently on the metallic or dielectric character of the local material. They are strongly confined down to very small sizes. For instance, the area covered by the spots A to C are respectively estimated, from the spatial FWHM of the Gaussian functions used to fit them locally, as (7.8 +/- 0.3) x (22.5 +/- 0.4) nm, (5.8 +/- 0.2) x (8.9 +/- 0.3) nm and (9.9 +/- 0.3) x (9.0 +/- 0.2) nm. Their intensity is inhomogeneous, and some of them reach very high intensities. On the other hand, after 2.0 eV, the pattern does not significantly change with energy, and the spots are now, irrespective of the energy, exclusively located on the metal (compare the maps and the HAADF image)[7].

Before moving forward, let us stress the point that these findings are related to the electric field intensities of the modes when observed at a single energy rather than the SP modes themselves. We will thus concentrate on the modes in the following.

### 5.3.3 Random SP modes

In the aim of revealing the SP modes responsible for the atypical spatial and spectral variations of the EEL probability evidenced in the previous section, multipeak fitting has been performed in the experimental dataset. As the strongest and most unusual variations were found only at

[7]Notice that the values of the energy losses were chosen to be sufficiently far away from the bulk plasmon resonance of silver to exclude the possibility for this observation to be due to the bulk plasmon mode of silver.

low energies, we thus focus on the modes of low resonance energy (ie less than 2.0 eV). At this point, it is important to stress that our measurements only concentrate on a very small part of a system which has basically no boundaries. As a consequence, the results shown below can only be interpreted at a local scale. This is most particularly true when considering modes whose coherent length may exceed the dimensions of the scanned area [34, 177]. The features of the SP modes have been obtained following subsection 5.2.2. For illustration, we restrict to the same small area studied in the last subsection. However, in the interest of statistics, acquisition and subsequent data processing were performed in two additional areas belonging to the sample region. Their HAADF images are shown on figure 5.3a.

The maps of the amplitude, central energy and FWHM of the peaks whose central energies are part of two narrow spectral ranges (1.275-1.325 eV and 1.585-1.635 eV) are shown on figure 5.6a. These spectral ranges were chosen to select two single modes, referred to in the figure as modes 1 and 2.

As explained in the last chapters of this manuscript, these sets of three maps offer precious insight about the properties of the SP modes by revealing some resonance energy, spectral width and spatial variations of the projected electric field intensities inherent to the modes. The z-projected electric field intensities of these modes visible in the amplitude maps show local strengthening which form spots at very small scales. Precisely, the sizes of these two modes are evaluated, following the procedure exposed in subsection 5.2.2, as 8.3 x 5.2 nm and 8.1 x 8.4 nm. The modes show no obvious correlation with the substrate local geometry, as they can spread featurelessly over metal and dielectric. The intensities of these modes are not equal, mode 1 being more intense than mode 2. They coexist as very close neighboors, as the areas these modes occupy overlap. The resonance energies of the modes as deduced from the energy maps are 1.31 and 1.61 eV, which are very close values. Finally, the spectral widths of the modes as deduced from the FWHM maps are 86 and 96 meV.

The very small size of the modes, together with the fact that they do not show any obvious correlation with the substrate geometry, is strongly unsusual when compared to classical SP modes of nanoparticles (for instance the Tip and Edge modes of the nanoprism of chapter 4). We will thus qualify them as random modes. Despite their extraordinary character, the quite high spectral widths of the random modes are similar to the spectral widths of usual SP modes of nanoparticles[8]. To verify these findings, we have performed further measurements and characterized other modes in the same way. Considering the rather limited covered area, a large number of modes with very close resonance energies, has been evidenced. These numerous, strongly confined and randomly located neighboring random modes well explain the strong spatial and spectral variations of the EEL probability evidenced in section 5.3. Figure 5.6b shows the size of these modes as a function of their resonance energy[9]. Figure 5.6b confirms that many of the modes have nanometric dimensions, while a few of them are spreading over space more than the others. Furthermore, figure 5.6c (red dots) shows the spectral width of the modes as a function of their resonance energy[10]. Figure 5.6c thus attests that the modes have rather spectral widths, synonymous with high relaxation rates. These values can be well trusted because they correspond to FWHM larger than the spectral resolution of

[8]For instance, in [42], Bosman et al. evidenced half spectral widths between 45 and 31 meV, corresponding to some dephasing times between 10 and 15 fs, in this spectral range for gold nanorods and nanocrosses of various sizes.

[9]The error bars are obtained from the left and right FWHM of the asymmetrical distribution of the pixel values of the energy maps (uncertainty on the resonance energy), and from the error evaluated in fitting a 2D Gaussian function on the amplitude map (uncertainty on the size).

[10]The uncertainty on the relaxation rate is deduced from the left and right FWHM of the asymmetrical distribution of the pixel values of the FWHM maps.

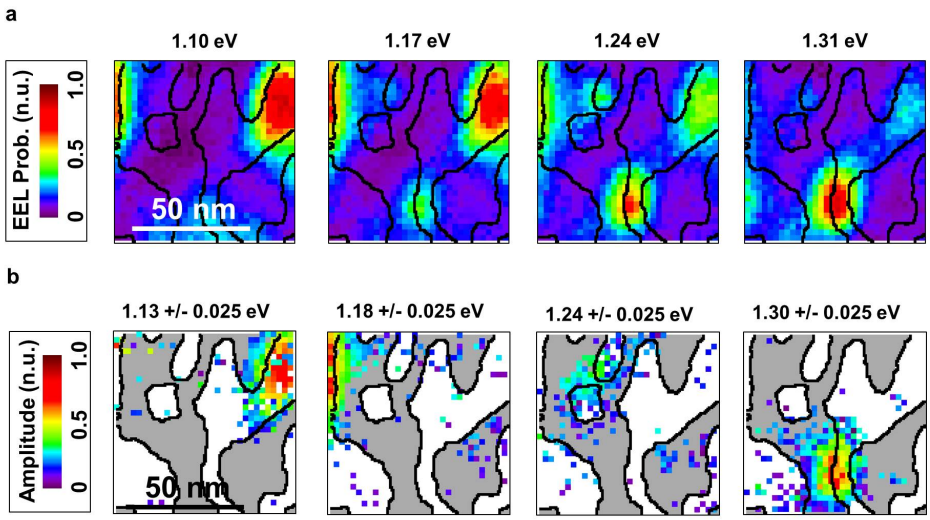


Figure 5.7: Disentangling the modes. a) Energy filtered map of the EEL probability at 1.10, 1.17, 1.24 and 1.31 eV. b) Maps of the amplitude of the peaks whose energy is 1.13 +/- 0.025 eV, 1.18 +/- 0.025 eV, 1.24 +/- 0.025 eV and 1.30 +/- 0.025 eV.

the measurement [42], which is here symbolized by the black doted line. The spectral characteristics of some simulated zEMLDOS peaks (resonance energy and FWHM), obtained as described in appendix C, are superimposed by the black dots. They agree well with the measurements in the whole spectral range.

Reasoning in terms of modes is particularly relevant in such a system, as the complexity of the modes evidenced previously is responsible for a strong mixing of their electric field intensities within the energy filtered maps of the EEL probability. Figures 5.7a and 5.7b compares energy filtered maps of the EEL probability at close energies (figure 5.7a) and maps of the amplitude of the peaks which have been found in four narrow spectral windows retained to select four single modes of close resonance energies (figure 5.7b). By comparing these amplitude maps with the energy filtered maps, it is clear that each of the modes leads to a local spot in each energy filtered map, located at the same place and whose intensity depends on the energy. The resulting pattern is an entanglement of mixed modes that cannot be distinguished from each other. This work thus constitutes, to the best of our knowledge, the first proper and complete access to the modes of a semicontinuous metal film around the percolation.

### 5.3.4 A spatially and spectrally dense system

After having characterized these modes locally, we can now think of investigating a complete set of modes of low resonance energies sustained by a large semicontinuous area around the percolation threshold. Figure 5.8a shows the HAADF image of such area, in which STEM EELS measurements have been performed (see subsection 5.2.1 for details). Figure 5.8b displays maps of the energy, FWHM and amplitude of the peaks which have been found in each pixel between 1.0 and 1.8

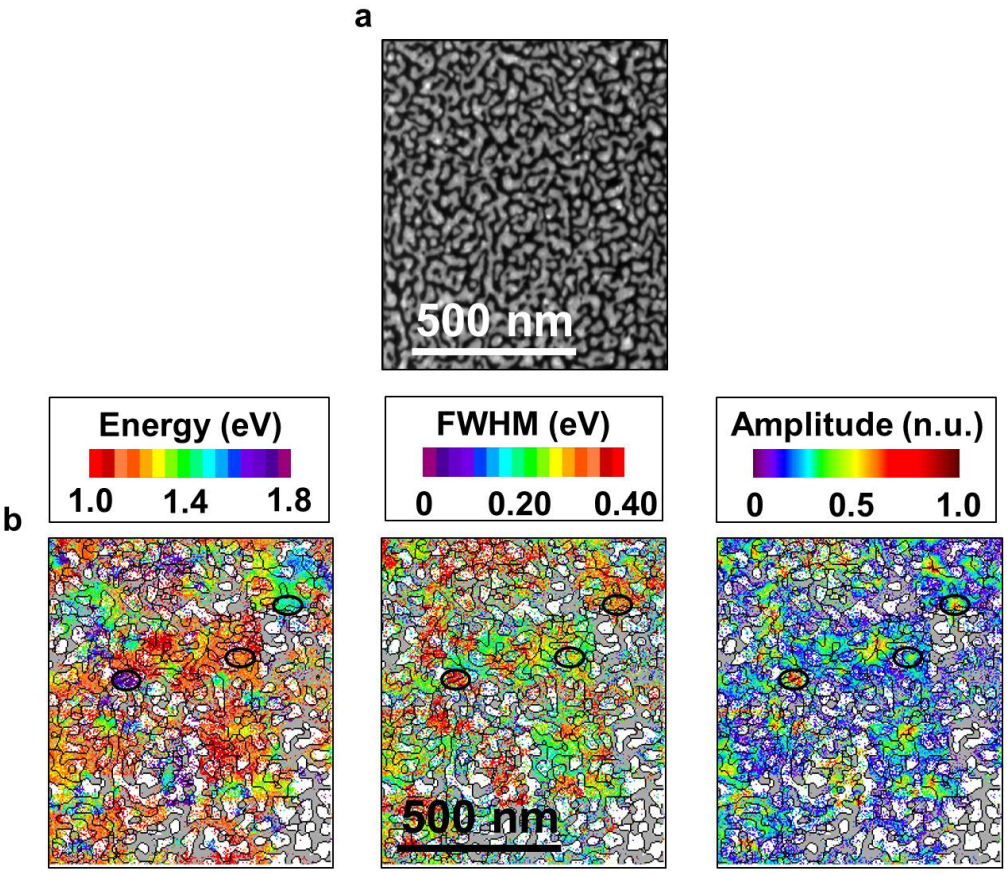


Figure 5.8: Low energy SP modes of a disordered system. a) HAADF image of the total scanned area. b) Maps of the energy, FWHM and amplitude of the peaks which have been fitted between 1.0 and 1.8 eV. The black circles evidence three SP modes.

eV[11, 12]. As obvious from these maps, in which local spots in the amplitude map can be associated to a constant peak energy in the energy map and a constant peak FWHM in the FWHM map, our reduced spectral resolution does not prevent us from interpreting the dataset in terms of modes. The resonance energy, spectral width and electric field local strenghtening of a mode can be obtained from this constant peak energy, constant peak FWHM and local spot in the amplitude map. Three different modes, distinguishable one from each other through their spectral features, are evidenced by the black circles. Notice that the typical values of FWHM are in qualitative agreement with the FWHM measured using the FEI TEM, when broadened by the spectral resolution of the VG STEM. As a consequence, the modes evidenced by these three maps are the same modes as the random modes studied in the last subsection. Otherwise speaking, VG STEM experiments can be well trusted. As evidenced by the complexity of the maps, a very large number of random modes

[11] No peak was fitted before 1.0 eV because of the experimental limitation inherent to the VG STEM.
[12] We still only retain the low energy modes. The complete results can be found in appendix C.

appears to coexist over very large scales, in accordance with [39].

### 5.3.5 Conclusions

In this section, we have evidenced experimentally strong and very local spatial and spectral variations of the EEL probability in a typical semicontinuous area around the percolation threshold. EEL probability spectra were shown to be highly complex and to suffer radical changes at nanometric scales. Small areas, some of which being strongly localized (around 10 nm in size), in which the EEL probability overcomes the surroundings, are observed in energy filtered maps of the EEL probability down to 0.5 eV. At the lowest energies, the position of these spots is strongly affected by changes in energy and shows no obvious correlation with the substrate local geometry. As a consequence, these spots share many similarities with Shalaev and Sarychev's HS [29], as well as with the localized intensity maxima previously acquired using various near-field techniques [171–173,175,176,178], yet with a very significant increase of the spatial resolution. Moreover, these strong spatial variations of the EEL probability also remind the strong spatial variations of the EMLDOS, measured indirectly by Krachmalnicoff et al. [177], or calculated by Cazé et al. [112, 142] and Castanié et al. [187]. It is interesting to notice that, despite the numerous differences between EELS experiments with regards to all the previous listed works, the findings are not much changed in this spectral range: the energy filtered maps show clear HS-like patterns. However, at higher energies, these spots are exclusively located on metal clusters and are not much energy dependent.

The SP modes responsible for the singular spatial and spectral variations of the EEL probability at low energies have then been unveiled. Their electric field intensities were shown to be strongly confined locally down to very small scales (on the order of 10 nm) at apparently random locations. These extremely small spatial extensions agree with the pioneering predictions of Shalaev and Stockman [29, 34]. The modes were shown to have different yet very close resonance energies and to coexist at a very local scale. These features make these random modes differ from classical SP modes of single nanoparticles, contrary to their relatively high spectral widths, synonymous with high relaxation rates. Further measurements have shown that these random modes are sustained at very large scales. In addition to rationalizing the large field variations usually measured at a constant excitation wavelength, these modes also well explain the anomalous optical response when illuminating the medium with a white light diffraction limited spot. In this case, all the coexisting modes are simultaneously excited, leading to broadband absorption spectra. The medium is thus demonstrated to be spatially as well as spectrally dense.

The spectral widths of the modes, as determined from our technique, seem to disagree with previous studies reported in the litterature. Indeed, SNOM and PEEM have measured resonant peaks FWHM of 20 to 40 meV both in the visible [171] and near IR [178]. The relaxation rate of a mode, which dictates its spectral width, may be affected by the sample preparation technique or the dielectric matrix. However, such a strong gap cannot be entirely explained by these two arguments. We thus attribute these discrepancies to some differences in the measured physical quantities. EELS does only probe the z projection of the fields, but it should not affect the peak widths. EELS might also be blind to some modes close to the light line in $(\omega, \vec{k})$ space (see subsection 2.5.2). If they exist, these modes may be excited by light (otherwise speaking, they should be bright modes). However, because they can couple to light, they should also have larger relaxation rates than the modes probed in EELS, through some additional radiative decay channels. We can thus dismiss the possibility for these lower peak FWHM measured with near-field optical techniques to be due to the only excitation of bright modes. These measurements might thus simply not probe the real

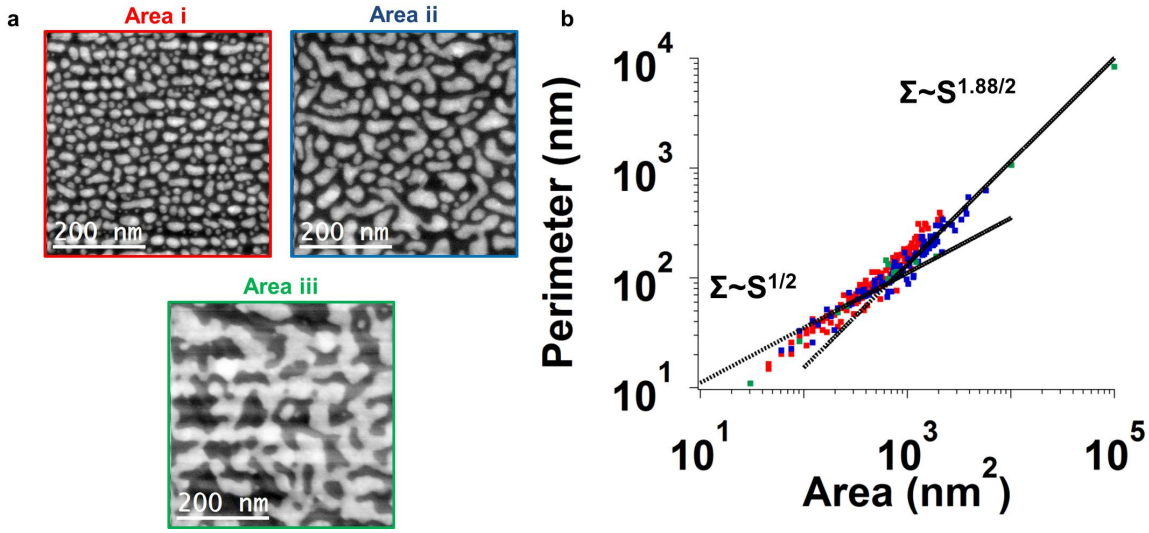


Figure 5.9: Three semicontinuous areas towards the percolation threshold. a) HAADF images of three areas (area i to iii) showing radically different morphologies. b) Log-log plot of the perimeters of the metal clusters found in the digitalized HAADF images as a function of their areas. The fractal cluster-Euclidian cluster ratio increases from area i to iii, as expected from semicontinuous films towards the percolation threshold.

characteristics of the modes, either due to the fact that PEEM is blind to the fields at the surface of the dielectrics or relies on non-linear photon emission processes, or that the SNOM signal might be distorted by the probe. In the absence of any clear answer, all we can do is make assumptions.

Moreover, the fixed pattern in an energy filtered map at various energies suggests, despite a higher dissipation in this spectral range, an increased density of states[13] with respect to the modes of low energies. Such an increased density of states is commonly found in simple metal dielectric systems[14]. But the parallel with simple nanoobjects does not stop here. For a flat nanoparticle or a nanowire, the electric fields of the modes at high frequencies are mostly located within the metal. The superposition of the electric fields of all these modes in an energy filtered map, resulting from their close eigenfrequencies, thus encompasses the whole nanoparticle. This is exactly what we see. However, the most likely existence of some high energy modes having very close resonance frequencies is difficult to evidence directly in the dataset (see the complete set of modes of the large area in appendix C). It is nevertheless very reasonable to suppose that the modes lose their singularities at high energies.

## 5.4 Random SP modes and the system geometry

### 5.4.1 Introduction

Up to now, we have shown that a typical semicontinuous area around the percolation threshold sustains an extremely complex set of random modes at low energies. However, the way the morphology of the system would have an influence on the modes remains unclear. This section aims at clarifying this point by examining three different areas, chosen for their radically different morphologies. Their HAADF images acquired before the STEM EELS measurements are shown on figure 5.9a. These areas will be referred to, from the left to the right, as areas i to iii. Area i is an ensemble of aligned and disconnected small nanoparticles, while area iii corresponds to a percolating-like, large and tortuous cluster. A geometrical analysis of these three HAADF images has, again, been performed. Figure 5.9b shows the plot in log log scale of the perimeters of the metal clusters found in areas i to iii as a function of their areas. Once again, in each area, the Euclidian character of the smallest clusters as well as the fractal geometry of the largest clusters is recovered. However, the three areas differ from their fractal cluster-Euclidian cluster ratio, which increases from area i to iii. Such finding is expected for metal-dielectric composite samples, for which increasing the metal fraction increases the proportion of fractal clusters with regards to the number of euclidian clusters before the percolation threshold [177]. At the percolation threshold, an infinite fractal cluster is formed and the fractal cluster-Euclidian cluster ratio diverges. Area i thus corresponds to a low metal coverage regime, where all the clusters are basically small and Euclidian, while area iii is clearly close to the percolation threshold, where the fractal geometry of the percolating cluster dominates the geometry of the system. Area ii is in an intermediate regime, where some of the disconnected clusters acquire a fractal character. In relation to these three regimes, the area which was studied in the last section corresponds to a metallic coverage between areas ii and iii. The fractal geometry is known to be responsible for the unusual optical properties of semicontinuous films around the percolation threshold, most particularly in the IR, where no optical absorption is found either in pure dielectric or metallic states. The set of SP modes is thus expected to change depending on the investigated area, which we are now going to demonstrate properly.

### 5.4.2 STEM EELS measurements

The HAADF images of the three areas recorded during the STEM-EELS measurements are shown on figure 5.10a. Local EEL probability spectra recorded at probe positions separated by 40 nm are shown on figure 5.10b. (in color). A mean spectrum, obtained by averaging all the EEL probability spectra, is also shown in grey. As clearly apparent from the datasets, the growing metallic coverage from area i to iii is accompanied by a progressive spectral complexity. In area i, each spectrum is dominated by a single resonance at around 1.9 eV, which is the spectral signature of a Mie-type mode. However, in area iii, each spectrum exhibits its own set of multiple resonances, indicating a complex set of modes. Slightly displacing the probe goes with dramatic changes in the shapes of the spectra, even more than in the region studied in the previous section. Moreover, leaving area i to iii seems to be accompanied by a growing appearance of peaks at low energies, in the IR. In area iii, these peaks become very high and affect the shape of the mean spectrum.

[13] By density of states, we simply mean the number of modes of the system whose frequency is between $\omega$ and $\omega + d\omega$. Contrary to the EMLDOS, we do not refer to any local features of the modes.

[14] Remember the asymptotic behaviour at high frequencies of the dispersion curves of the SP modes (section 2.3).

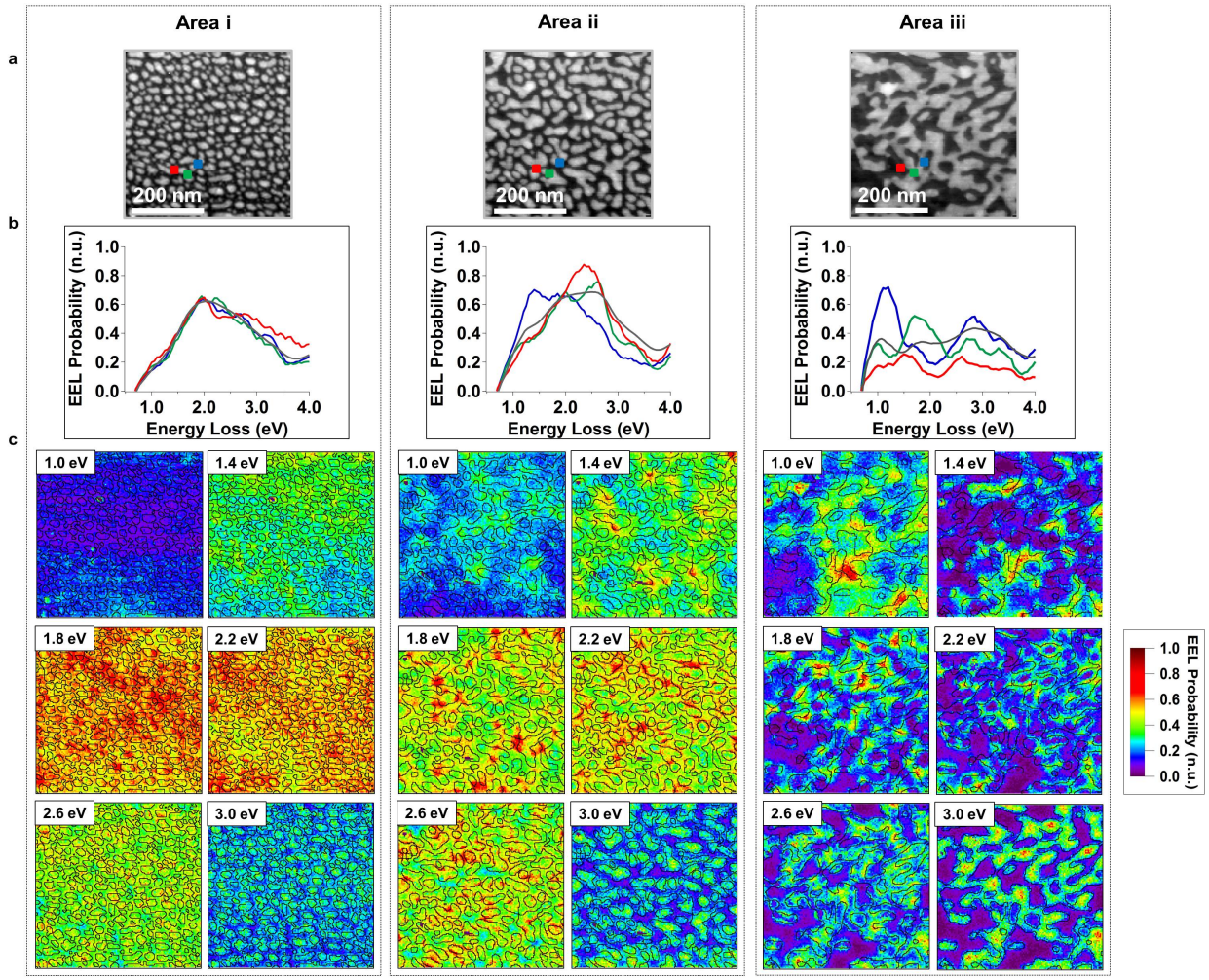


Figure 5.10: STEM EELS measurements in areas i to iii. a) HAADF images of the scanned areas recorded during the STEM EELS acquisition. b) Colored: local EEL probability spectra corresponding to the electron probe positions indicated in the HAADF images and separated by 40 nm. Grey: mean spectrum obtained by averaging all the EEL probability spectra of the dataset. c) Energy filtered maps of the EEL probability for some energy loss values spanning the whole spectral range of interest.

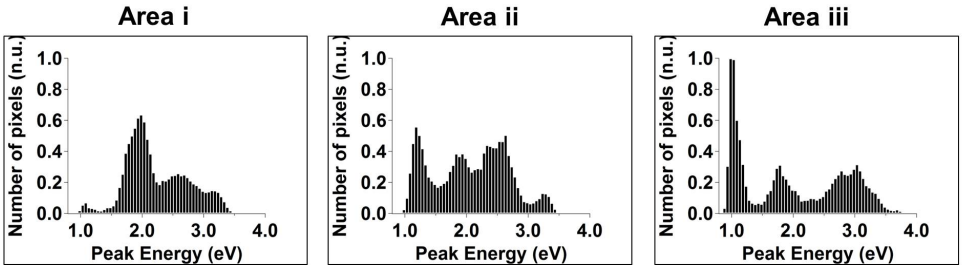


Figure 5.11: Histograms of the number of probe positions for which a peak with a given central energy was found in the corresponding spectrum, weighted by the amplitude of the peaks, for areas i to iii .

The resulting spectral complexity of the dataset is found in the energy filtered maps of the EEL probability, which are compared for the three areas on figure 5.10c. As clear in these maps, the EEL probability spatial varations increase, at a given energy, when going from area i to iii, in accordance with [35, 175, 178, 194]. The patterns are thus the most inhomogeneous in area iii, where very strong EEL probabilities are spatially confined at some locations. At the lowest energies (upper pannels), the EEL probability reaches very high values in some spots in area iii. Changing the energy as little as 400 meV has a strong effect on the shape and spatial arrangement of these spots. In comparison, the EEL probability strongly decreases in areas ii then i, whose patterns seem less affected. At intermediate energies (middle pannel), the EEL probability increases from area iii to i, due to the fact that the number of metal clusters supporting Mie-type SP modes also increases. In area iii, strong small spots are still visible but appear to be located more and more around the metal clusters, as was already observed in the area studied in section 5.3. Finally, at the highest energies (bottom pannel), the maxima of EEL probability are irrespective of the area, weakly energy dependent and exclusively located on the metal clusters.

### 5.4.3 Mode analysis

To directly evidence any difference between the SP modes sustained by these three areas, multipeak fitting has been performed in each spectrum of each dataset. The histograms of figure 5.11 show the number of probe positions for which a peak with a given central energy was found in the corresponding spectrum, weighted by the peak amplitudes. Clearly, while all the areas have similar spectral features at high energies, they also differ from an increasing contribution from some modes with resonance energies lower than around 1.5 eV, when going from area i to area iii. The complete results of the fitting procedure are given in appendix C. We here focus on the low energy modes by showing on figure 5.12 maps of the energy, FWHM and amplitude of the peaks whose energy is found between 0.8 and 1.6 eV. In area i, only a few (if not no) modes are detected in this spectral range. In area ii, smooth field intensities spatial variations are associated to some modes that do not spread much in the spectral range and do not have resonance energies before 1.1 eV. In comparison, area iii shows a rich multiplicity of modes of close resonance energies, detected down to 0.95 eV, whose electric fields are strongly varying and reach very high intensities. There is thus a clear progressive appearance of strong modes at low energies when going from area i to iii.

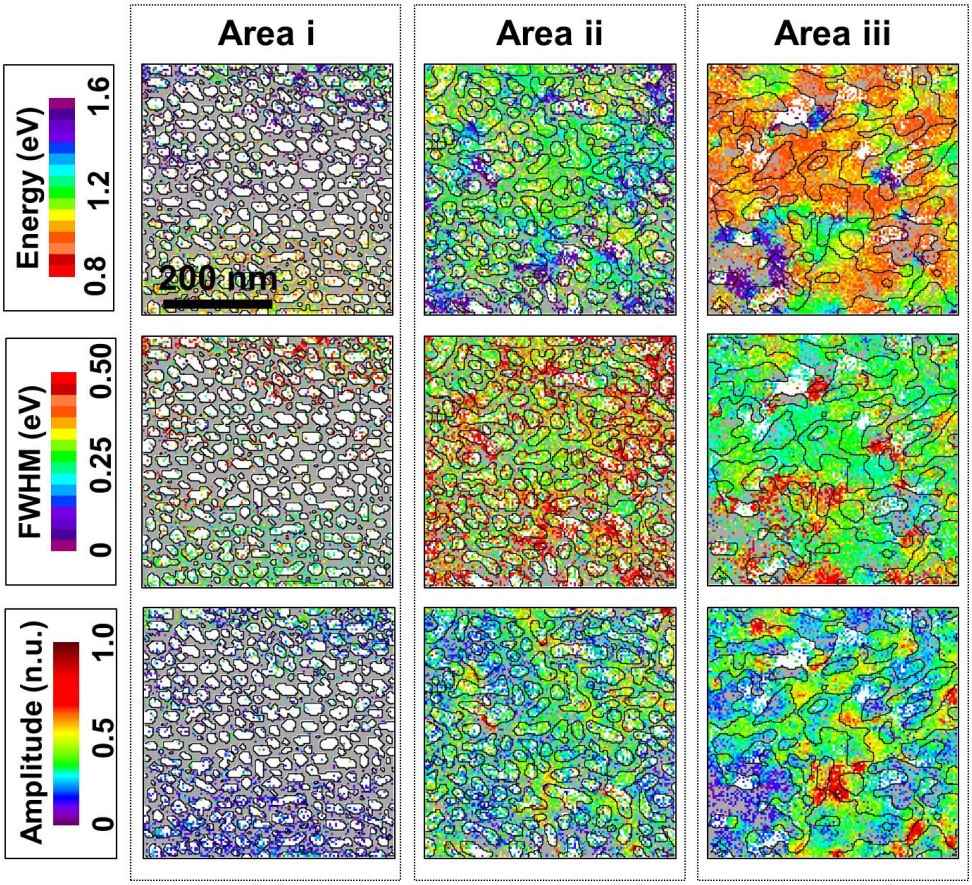


Figure 5.12: Maps of the energy, FWHM and amplitude of the peaks found between 0.8 and 1.6 eV.

### 5.4.4 Conclusion

In this section, we have investigated the effect of the morphology of the system on the SP modes. We have first shown that the spatial and spectral variations of the EEL probability actually increase when going from a random collection of individual small nanoparticles to a percolating cluster. The observation of highly energy dependent patterns consisting of randomly distributed sharp spots, already observed in the semicontinuous area around the percolation threshold studied in the last section, is most particularly recovered in the percolating cluster at low energies. However, each area looks similar at higher energies, exhibiting again fixed patterns of spots located in the metal clusters. This is further confirmation that the SP modes of semicontinuous films around the percolation threshold are singular only at low energies.

Each dataset in the IR was related to a set of modes. In particular, the increasing spatial and spectral variations of the EEL probability were explained by the progressive appearance of SP modes of low resonance energies, which are not sustained by the random collection of individual small nanoparticles. This is in accordance with [29], which attributed the existence of HS in the

IR in a percolating system to the SP resonance of fractal clusters. These low resonance energy SP modes induced by the fractal geometry of the system are the random modes which were studied in a typical semicontinuous area around the percolation threshold in section 5.3. The strengths of the electric field intensities, spatial variations and spectral densities of the random modes are found to increase when getting close to the percolation threshold, due to the increased domination of fractal clusters.

## 5.5 Conclusion

We have observed typical strong spatial and spectral variations of the EEL probability when studying semicontinuous metal films around the percolation threshold. Very local spots where the EEL probability increases spatially have been observed in the energy filtered maps. We have found that the position of these spots over the substrate appears to be random and highly energy dependent at low energies, in strong contrast to the high energies. We have related this singular behaviour to a very complex set of strongly confined random SP modes of close resonance energies. These modes are typified by their very small size (around 10 nm) and apparent absence of correlation with the substrate geometry, contrary to their relatively high spectral widths, synonymous with high relaxation rates. They were shown to coexist both at the very local and large scales, which makes such a system spatially and spectrally dense. Further investigation has shown that these random modes are induced by the fractal character of the metallic clusters. They have indeed proven to be absent from a system consisting in a random collection of Euclidian nanoparticles. By comparing three different semicontinuous systems with increasing metallic fraction towards the percolation theshold, the strengths of the electric field intensities, spatial variations and spectral densities of the random modes have been found to increase when getting close to the percolation threshold, due to the increased domination of fractal clusters.

It should be noticed that, despite the unclear link between the EEL probability and some light induced field intensities, our findings are in agreement with the properties of the HS proposed by Shalaev and Sarychev only at low energy around the percolation threshold [29]. These results also explain the strong as well as broadband absorption of semicontinuous films around the percolation threshold [169, 170]. They finally confirm the modal structure of the SP modes that was predicted theoretically for disordered media [31–34]. Finally, these findings let open interesting questions concerning the physics of these modes. Indeed, it is clear that we cannot claim we are able to evidence a single mode from its resonance energy, based on the extreme complexity of the system. Therefore, the spatial coherence of the modes, which has been debated in the previously quoted papers, cannot be accessed in this way. Regarding the apparent absence of correlation of the modes with the substrate local geometry, some complete three dimensional access to the sample morphology, for instance using Atomic Force Microscopy or electron tomography, would also be useful to properly check whether or not the modes would be sensitive to some substrate roughness. Finally, the radiative or non-radiative nature of these fractal modes is unclear, and should thus be studied thoroughly. Some results of a preliminary work are shown on the next chapter.

Finally, let us stess that we only focussed the discussion on the low energy range, because this is where the situation is the clearest. However, multiple modes can also be evidenced at higher energies. Further data can be found in appendix C.

# Chapter 6

# Perspectives

Within the STEM group, the works achieved with STEM EELS presented in this thesis are the outcome of numerous previous instrumental and methodology advances, comprehensive experimental studies of the SP modes of metal nanoparticles and theoretical interpretations. STEM CL, on the other hand, is relatively new, because performed with a light detection system which has been built only recently. Chapter 4 has shown that STEM CL could be equally valuable than STEM EELS for studying SP modes, with some advantages. Moreover, CL measurements may offer some complementary information to EELS measurements, mostly related to the coupling of the modes to light. In the following, we will show three different examples related to the study of SP modes, which would benefit from either STEM CL measurements directly or its light detection system. These works have been tackled but could not be completed for a question of time. They may lead to complete studies in a more or less close future.

## 6.1 A fine spectral resolution

With respect to STEM EELS, STEM CL offers a much enhanced spectral resolution, allowing access to very fine spectral behaviours. For illustration, figure 6.1a shows the HAADF image of a gold triangular nanoprism, similar to the nanoprism studied in chapter 4, yet of different dimensions. As seen in the HAADF image, the nanoprism does not entirely hold on the carbon foil but has its upper tip standing above vacuum. It is well known that the dielectric environment affects the eigenfrequency of the SP modes of a nanoparticle [155, 197, 198], which is here translated into some changes in the CL local measurements. Figure 6.1b shows CL local spectra extracted from STEM CL measurements performed on the nanoprism, corresponding to some electron positions located at the three tips of the object. Contrary to the nanoprism, standing completely on the carbon foil, studied in chapter 4, the spectra at the three tips do not show a single resonance, but three resonances slightly shifted with respect to each other, appearing as either frank peaks or shoulders depending on the tip the electron beam is focussed onto. The resonance energies, as estimated by eye, are added to the spectra. Such a phenomenon is most probably due to a lift of degeneracy of the dipolar modes of the nanoprism induced by the different dielectric environment at the three tips, but is difficult to evidence in the energy filtered maps of figure 6.1c, due to the very close resonance energies of the modes. It is interesting to notice that the modes seem to keep their spatial coherence, as the three resonances appear in each spectrum or, equivalently, each energy

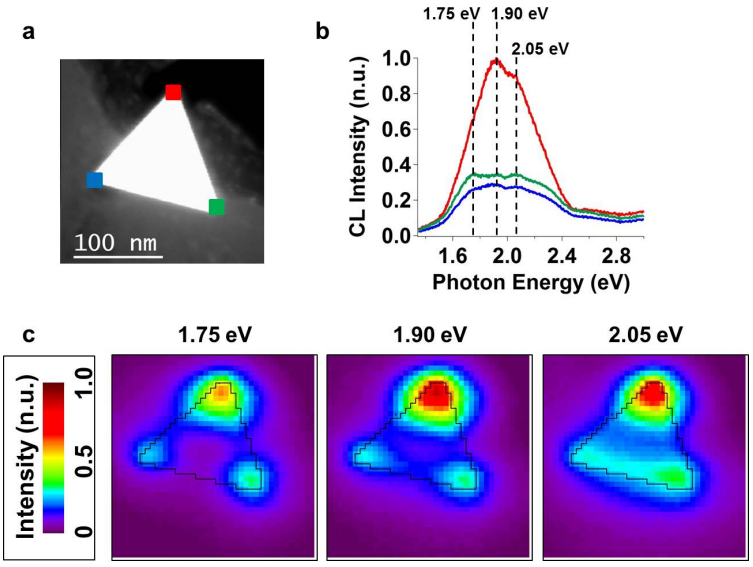


Figure 6.1: STEM CL measurements on a gold triangular nanoprism with broken symmetry. a) HAADF image of a gold nanoprism. The nanoprism does not entirely hold on the carbon foil but has its upper tip standing above vacuum. b) Local CL spectra extracted from STEM CL measurements performed on the nanoprism, corresponding to some electron positions located at the three tips of the object. Three resonances slightly shifted with respect to each other appear in the three spectra. c) Energy filtered maps of the CL intensity, at the three resonance energies.

filtered map show spots of high intensity at each of the three tips. Disentangling the modes, yet difficult, should be feasible and is currently considered. To confirm these findings, some numerical simulations should be of great value and are also thought of.

## 6.2 SP modes of disordered systems

Obviously, the results of chapter 5 only scratch the surface of the physics of the SP modes of disordered systems. In the following, we focus on some other problems which might be solved using fast electron based spectroscopies. To these points, we can also add, for instance, the phase of the modes[1], which has not be examined so far, but may be determined by apertureless SNOM with heterodyne detection [85, 199].

### 6.2.1 Radiative character of the modes

Chapter 5 already exposed the reasons motivating a combined EELS/CL study of a semicontinuous film around the percolation threshold, namely, the evidence of the either radiative or non-radiative character of the SP modes. Figure 6.2 presents the quite promising preliminary results obtained on a gold film embedded in $Si_3N_4$, prepared by our collaborators from Poitiers similarly to the silver films

[1] As early notice in chapter 2, fast electron based spectroscopies only detect the square of the electric fields.

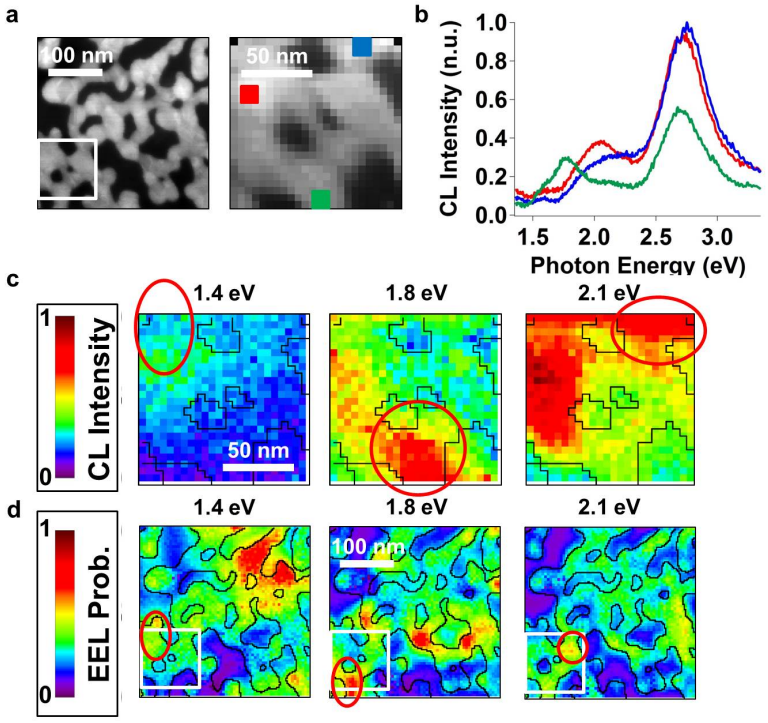


Figure 6.2: Combined EELS and CL measurements on a gold semicontinuous film around the percolation threshold. a) HAADF image of a large region of a gold semicontinuous film around the percolation threshold, recorded during the STEM EELS measurement (left image) and HAADF image of a small area belonging to this region, scanned during the STEM CL measurement (right image). b) Local CL spectra corresponding to some electron probe positions separated by around 100 nm. The dominant peak located at around 2.8 eV may be due to photon emission from the $Si_3N_4$ matrix. c) Energy filtered maps of the CL intensity at three low energies. d) Energy filtered maps of the EEL probability at the same energies.

studied in the previous chapter[2]. Figure 6.2a shows the HAADF image of a large sample region, recorded during a STEM EELS measurement (left image), and the HAADF image of a small area belonging to this region, scanned during a STEM CL measurement (right image). The location of the small area in the large region is indicated by the white square on the left HAADF image. Figure 6.2b shows CL local spectra corresponding to some electron probe positions separated by around 100 nm. The spectra display several peaks in the whole spectral range, the dominant one being located at around 2.8 eV. This peak is not affected by a change in the electron probe position[3], and is most probably due to some luminescence of the $Si_3N_4$ layer [201]. On the contrary, the peaks at lower energies (between 1.5 and 2.5 eV) greatly change with the electron probe position,

[2]The reason why we use gold instead of silver is that the SP modes of gold nanoparticles have been shown to have high photon emission rates, when submitted to photoluminescence experiments, due to some non-radiative decay channels within the band structure of gold [200].

[3]The change in the amplitude is only due to the decrease in the incoming current.

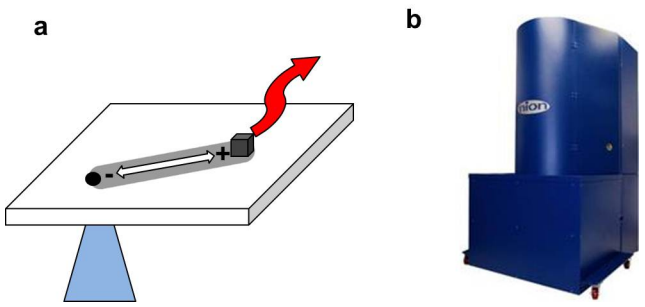


Figure 6.3: Spatial coherence of the modes probed by fast electron based spectroscopies. a) Coupling between a SP mode and a quantum emitter. b) Photo of the Nion UltraSTEM set up in Orsay.

and remind the strong point to point spectral variations of the EEL probability evidenced in the silver semicontinuous films. Figure 6.2c show energy filtered maps of the CL intensity at three energies taken in this spectral range. Yet the contrast is strongly affected by the dominant peak at 2.8 eV, some local spots where the intensity is higher than the surroundings can be seen in each map, as evidenced by the red circles. Finally, figure 6.2d show energy filtered maps of the EEL probability, obtained from the STEM EELS measurements performed in the large area, at the very same energies. In each map, a local spot of high EEL probability can be seen at the same position as the spot appearing in the corresponding energy filtered map of the CL intensity. These spots of high EEL probability have been related to the SP modes of the system in chapter 5. The local variations of the light emission observed in this spectral range can thus be attributed to the SP modes as well. In our case, the three related modes would be radiative. However, this might not be the case for all the modes. A careful and exhaustive examination of the modes in each dataset, with, as usual, multipeak fitting, should bring some conclusions on the radiative or non-radiative character of the modes of semicontinuous films around the percolation threshold. Notice that a spot absent from the third EELS energy filtered maps is visible in the third CL energy filtered map, which is not logical at first sight. Further measurements are thus necessary, ideally in samples free from substrate light emission, in order to confirm these first observations. Moreover, it should be noticed that these results are in stark contrast with the energy filtered maps of the EMLDOS and radiative EMLDOS calculated by Cazé et al. [142], which show completely different spatial distributions at a very same frequency. A careful investigation is thus most essential.

At the moment, additionnal samples have been prepared by our collaborators from Poitiers with no $Si_3N_4$ matrix in order to remove the dominant light emission at high energies, whose spectral characteristics vary with the location on the sample. Contrary to the process detailed on appendix C, the gold deposition was performed directly onto thin silicon grids perfectly suitable for being observed in a STEM. Further measurements are expected very soon.

### 6.2.2 Coherence of the modes

The (spatially) coherent character of the SP modes around the percolation threshold could not be resolved in our STEM EELS measurements. The most straightforward evidence of such a spatial coherence would require separating the excitation position, located at point A, from the detection position, located at point B. This would allow measuring the cross density of states defined by Cazé

et al. [112]. In the domain of fast electron based spectroscopies, a combination of STEM EELS and electron holography, being developped nowadays [202], may ultimately achieve such a scheme.

However, a "simple" STEM CL experiment, sketched on figure 6.3a, can also be considered. A quantum emitter is deposited over the sample at a given point and the electron probe is focussed onto the sample at another point. The electron beam excites some modes, which might couple locally to the quantum emitter if their electric fields are not zero at the position of the emitter. In this case, this would induce light emission from the emitter, detectable with the STEM CL system. Because the emission rate may be strongly enhanced [203], the light emission coming from the emitter should be easily distinguished from the light emission induced by the SP modes themselves.

Moreover, an alternative can also be envisioned, consisting in damaging the sample at point A to affect the signal detected at point B. If we consider a STEM EELS experiment, we can think of recording a full dataset in a given area, then damaging the medium very locally at a point of this area using the electron beam, and finally recording another dataset in the same area. The mode whose electric field is non zero at the point where the medium was damaged would be affected as a whole, which would thus be detected at some other point in the EELS dataset. Damaging a sample such as a semicontinuous film around the percolation threshold with an electron beam would require an extremely high brightness, which may be reached by using the Nion UltraSTEM [204] (see figure 6.3b) set up in Orsay. At the moment, the second alternative is seriously considered.

## 6.3 Light injection inside a STEM: towards new fast electron based spectroscopies

### 6.3.1 Motivation

An exciting new trend for the near-future of nanooptics with fast electron based spectroscopies is coupling electrons and photons [208, 209]. Such an orientation relies on the ability to inject light within an electron microscope, which has been developped over the last few years [210]. Although many interesting studies can be performed when irradiating a sample inside an electron microscope, including observations of thermal effects [137] or phase transformations [211], time-resolved measurements [212, 213] or imaging of light induced SP mediated electric fields on metal nanoparticles [207], to which we can add the perspective of out-of-equilibrium and non-linear phenomena probed by STEM EELS and STEM CL, we focus in the following on a very specific application, which is Electron Energy Gain Spectroscopy (EEGS) [205].

The principle of EEGS is depicted on figure 6.4a, and is directly related to the process of energy gain of an electron interacting with a medium. Such phenomenon can be easily described in a pure classical picture in the following way[4]. If a metal nanoparticle is illuminated by an optical beam, the medium scatters the light throught its SP modes. The fast electron can then be accelerated by interacting with the scattered electric field, rather than being slowed down. The electron thus gains an amount of energy corresponding to the frequency of the scattered field, with a certain probability being related to the magnitude of the field. In a real-life experiment, a resonant peak appears at the left of the ZLP in an EEL spectrum. The area of this peak is proportional to the probability for an electron of gaining a certain amount of energy, that we can call EEG probability. Very low energy

[4] According to [205], such a classical approach leads to incorrect conclusions, so that EEGS has to be treated quantum mechanically. We however stick to this classical picture, which is similar to the classical electrodynamics approach of EELS we took, for simplicity.

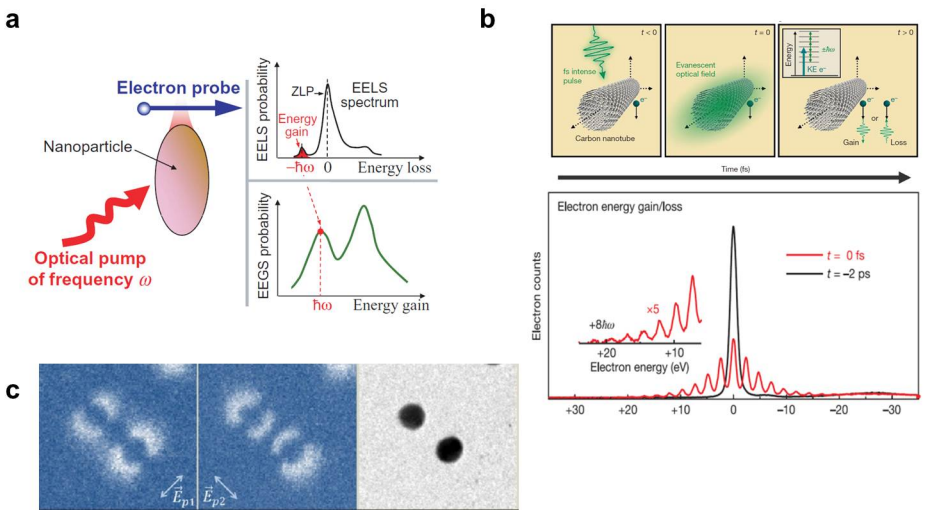


Figure 6.4: Motivation for light injection inside a STEM. a) Principle of EEGS. Extracted from [205]. b) Proof of principle of energy transfers from light to electrons mediated by the surface eigenmodes of a nanoparticle. Extracted from [206]. c) Imaging of light induced SP mediated electric fields on metal nanoparticles (PINEM). Extracted from [207].

gain of fast electrons mediated by vibrational excitations thermally excited was already evidenced back to 1966 by Boersch et al. [214]. However, energy gain in the visible range mediated by the SP modes of illuminated metallic nanoparticles has only be observed very recently [206].

EEGS, in itself, is a new type of fast electron based spectroscopy proposed by García de Abajo and Kociak to study the SP modes, which supposes the use of a tunable laser source. Suppose that STEM EELS is performed in a regular way, except that the sample is illuminated. The electron probe is located at a position where it can excite and gain energy from a given mode. An EEL spectrum is thus recorded and shows a peak at the left of the ZLP corresponding to a gain event mediated by this mode. Tuning the frequency of the laser allows tuning the spectral mismatch between the excitation and the mode. In the same time, the area of the energy gain peak varies, being maximum at the resonance frequency of the mode. Plotting the area of this peak as a function of energy allows accessing an EEG probability spectrum, which should in theory be, to simplify[5], equivalent to an EEL probability spectrum. However, experimentally, the EEG probability spectrum obtained as such has a spectral resolution which is not limited by the energy spread of the incoming electrons, but rather by the bandwidth of the laser source. With respect to STEM EELS, STEM EEGS would thus offer a spectacular spectral resolution while keeping the same spatial resolution[6]. Moreover, calculations have suggested that, at moderate laser intensity and at resonance of a mode, the EEG probability should be 40 times higher than the EEL probability [205].

[5]There is no need to stress that the electron-light interplay actually brings significant complexity [215]. If one only considers that the interaction of the electron with the nanoparticle is negligible with regards to the light excitation, one can already suppose that an EEG probability spectrum will only see the "bright" modes of the nanoparticle.

[6]An additional, yet minoritory advantage, results from the assymetric shape of the ZLP when the electrons are extracted from a FEG. The left tail of the ZLP spreads less than its right tail, thus allowing the detection of peaks at slightly lower energies.

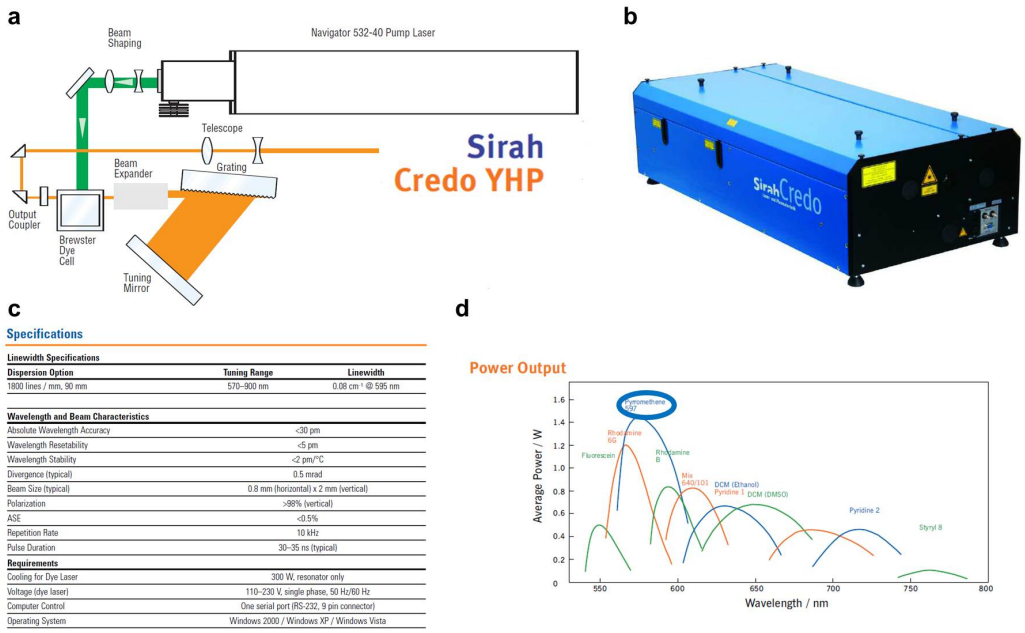


Figure 6.5: Syrah Credo laser. Scheme (a), photograph (b), technical specifications (c) and power output (d).

STEM EEGS would thus offer a much increased signal to noise ratio as compared to STEM EELS, and even more as compared to CL. Furthermore, STEM EEGS would benefit from the well-known degrees of freedom of the optical techniques (notably polarization control). More fundamentally, it would finally bring new insight about the coupling between light and SP modes.

Figure 6.4b shows the proof of principle of energy transfers from light to electrons mediated by the surface eigenmodes of a nanoparticle brought by Barwick et al. [206], who sent single fast electron packets in temporal coincidence with a femtosecond laser pulse on a carbon nanotube using the ultrafast electron microscope built by Zewail's team [216]. Such a setup relies on the use of a photocathode as an electron source, which is excited by a laser pulse whose temporal delay can be varied with respect to the laser pulse exciting the sample. As seen in the spectra, the energy gain peaks appear only when electrons and photons are in coincidence, and show up as multiple quanta, similar to the symmetric energy loss peaks[7]. It should be noticed that, because it uses a very high power monochromatic laser interacting highly non-linearly with the sample, the ultrafast electron microscope is not suitable for performing EEGS as such. In the context of plasmonics, it is currently used to map the electric fields induced by some SP modes off-resonantly excited by light, a technique called Photon Induced Near-field Electron Microscopy (PINEM) [206, 207] (see figure 6.4c).

[7]These multiple quanta are the result of multiple energy exchanges occuring between electrons and photons [217]. The energies only reflect the wavelength of the laser, and not the intrinsic features of the sample, which only acts as a passive mediator.

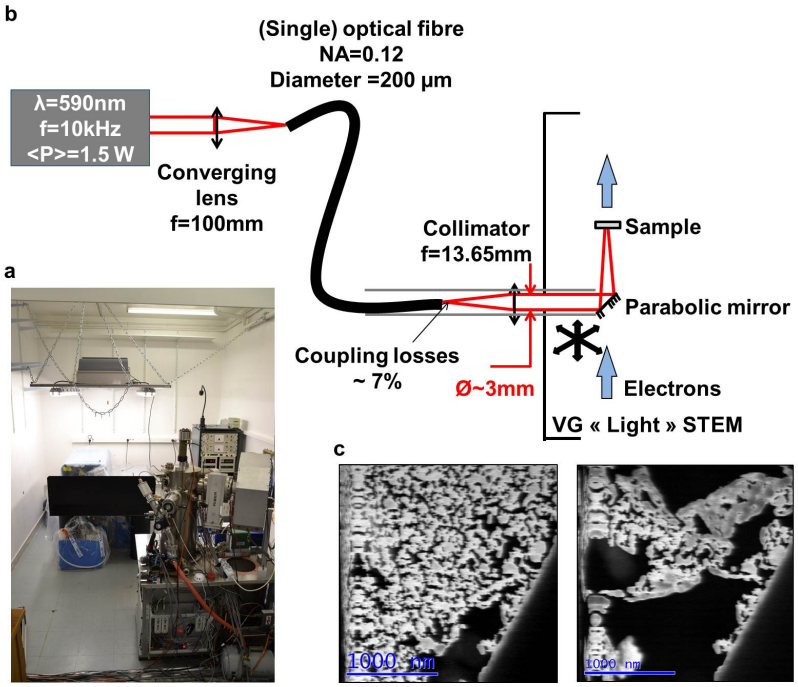


Figure 6.6: Preliminary tests of light injection within a VG STEM. a) Sketch of the experiment. b) Photograph of the installation. c) HAADF images of a thin silver film before (left) and after (right) high power laser irradiation.

The light detector fitted to the CL system of the VG STEM would be perfectly suitable for injecting light onto a sample. A laser was thus bought in the aim of illuminating the sample through the CL detector system. The Sirah Credo is a tunable Q-switched pulsed dye laser pumped by a frequency doubled Nd-YAG laser. The scheme and photograph of the laser can be seen on figures 6.5a and b. Figure 6.5c shows the complete technical characteristics of the Credo, and figure 6.5d the average output power as a function of the dye. The spectral range of excitation is at this time limited to the single dye that has been bought, namely, pyrromethene. However, several dyes can be used in a single experiment, allowing, by switching from one dye to another, to cover a large spectral window. The laser was chosen to allow performing linear "continuous" spectroscopies in the visible range. Precisely, the wavelength can be tuned from 570 nm (2.4 eV) to 900 nm (1.5 eV). Typical pulse duration, repetition rate and average power are respectively on the order of a few tens of ns, 10 kHz and 1 W, which corresponds to moderate peak powers despite the rather high average power[8].

### 6.3.2 Preliminary results

The laser has been installed in close proximity to a VG STEM dedicated to instrumental developments, the aptly named "VG light" (see the installation on the photograph of figure6.6b). Very preliminary tests of light injection within a STEM through the CL detection system have been performed with the precious help of Jean-Denis Blazit in Orsay. The configuration is shown on figure 6.6a. A converging lens focusses the laser beam into a single optical fibre[9], which guides the beam towards the light detection system. An industrial collimator is directly screwed onto the end slit of the optical fibre to obtain a collimated beam[10] of diameter 3 nm[11]. A thin silver film has been illuminated at high power (around 1.5 W). The HAADF image of the sample with the mirror out of focus (left image) and in focus (right image) are shown on figure 6.6c[12]. The film is destroyed locally when the laser is in focus. Moreover, displacing the mirror in the plane of the sample leads to the progressive destruction of the sample. During this experiment, the light spot within the sample has been roughly determined to be less than 100 µm x 100 µm. Further characterization and experiments are obviously necessary, but such a proof that light can be injected within the STEM using the CL detection system is already encouraging.

[8] If we take the average power as 1.5 W for a repetition rate of 10 kHz and a pulse duration of 30 ns, the peak power is 5 kW. This value can be compared to the peak power of the femtosecond laser used in the ultrafast electron microscope setup, which is around 50 GW [216].

[9] No fibre bundle, commonly used for STEM CL measurements, is used in this experiment in order to avoid interference effects between the light beams.

[10] A well collimated beam requires the use of an optical fibre of small diameter, which in turn requires a focussing lens of low focal length. However, the focal length cannot be too low to ensure that the focussing angle is less than the NA of the fibre. In our case, a fibre diameter of 200 µm and a focal length of 100 mm have appeared to constitute a good tradeoff, leading to 7% of power losses. The NA of the optical fibre is 0.12 in order to be able to perform both detection and injection of light in a same fibre.

[11] This value has been considered to match the diameter of the light beam coming out from the STEM in a CL experiment when the light detection system is perfectly aligned (see figure 3.2)

[12] The alignement was not optimized because the mirror was simply moved by eye. To properly irradiate the sample, the mirror should be aligned in order to maximize the light emission coming from some source point on the sample before injecting light with the same fibre.

# Conclusion

The power of fast electron based spectrosopies for studying optical excitations of nanostructures relies on their combined nanometric resolution, broad spectral range of excitation and simultaneous imaging of the sample. This allows achieving spectroscopies at the nanometric scale with precise knowledge of the local morphology of the sample and without any inhomogeneous broadening. Furthermore, perhaps just as importantly, fast electron based spectroscopies probe directly the fundamental excitations of a sample, with no distortion which would be induced by the measurement. Indeed, Electron Energy Loss Spectroscopy (EELS), and, in non-dissipative systems, Cathodoluminescence (CL), measure some quantities which are very close to the Electromagnetic Local Density of States (EMLDOS). In particular, in metal-dielectric systems, EELS is sensitive to some intrinsic spatial and spectral features of the Surface Plasmon (SP) modes of the system, namely, their eigenfrequency, relaxation rate and projected electric field intensity. This has been known for years for simple systems like metallic spheres, but such an extension to a generic system provided by the key concept of EMLDOS has been allowed only recently. Nevertheless, although some experimental and theoretical works tend to suggest a similar situation, any transposition of this statement to STEM CL is a priori not straightforward.

Fast electron based spectroscopies are now routinely performed in a Scanning Transmission Electron Microscope (STEM) to achieve hyperspectral imaging of a sample. If we consider STEM EELS, which can now be safely interpreted, such hyperspectral imaging observes, when studying a metal-dielectric sample, the spatial variations at the nanometric scale of the electric field intensities of the SP modes excited by a given amount of energy, in a broad spectral range. However, due to the finite lifetime of the SP modes, these electric field intensities are not the electric field intensities of a mode whose eigenfrequency would correspond to this amount of energy. On the contrary, they are the results of the (possibly numerous) modes with same or close resonance energies. This prevents from characterizing a single mode in a simple way. Nevertheless, because a complete spectrum is recorded at each point of space, the SP modes can be disentangled from each other, and be fully characterized from a resonance energy, spectral width and intensity of its projected electric field. This makes STEM EELS a very valuable technique for obtaining fundamental insight about the modes themselves. We have taken profit from such a capability in two systems: a gold triangular nanoprism, and a random silver film.

The gold nanoprism has been considered as a simple, model system whose SP modes are now rather well-known, because extensively studied in the litterature. A combination of experimental results and numerical simulations allowed us to compare STEM EELS, STEM CL and optical spectroscopies in this system. We have evidenced strong similarities but also some dissimilarities between fast electron based spectroscopies. On the contrary, we have underlined a close resemblance between EELS and extinction on the one hand, CL and scattering on the other hand. We have

derived modal decompositions of CL, extinction and scattering that we have compared with the well-known modal decomposition of EELS. Such modal decompositions explain most of the experimental results and numerical simulations. They also offer an efficient framework to set fast electron based spectroscopies on their whole as a precious tool for studying SP modes as well as some nanometer scale counterparts of extinction and scattering of light.

Contrary to the nanoprism, random metal dielectric systems are well-known problematic systems which have been studied with many near-field techniques, but whose SP modes remain elusive as much as complex. An experimental STEM EELS study has evidenced the SP modes of a semicontinuous film around the percolation threshold, which encompasses a disordered collection of Euclidian and fractal clusters. In the IR, the SP modes have been shown be numerous, each one having its own resonance frequency and coexisting locally with the others. The electric fields of these modes have been shown to be confined within very small areas (around 10 nm in size), located at apparent random positions with respect to the sample morphology covering the whole system. A comparison of different systems allowed us to attibute these extraordinary random-type SP modes to the fractal character of a semicontinuous film around the percolation threshold.

Obviously, such results only scratch the surface of the physics of the modes of random systems, whose complexity deserves further studies. Preliminary results of comparative measurements of STEM EELS and STEM CL have proved to be encouraging for revealing the radiative character of such modes. Moreover, any experimental evidence of their coherent character is currently at study. Furthermore, we focussed only on the fundamental aspect of the problem, but SP modes of random system may be interesting for various applications, including quantum emitters coupling [218], non-linear optics [219] or random lasing [220].

Laser light injection inside a STEM has finally be demonstrated within this thesis, opening exciting new perspectives for spatially resolved spectroscopies of SP modes at the nanoscale combining fast electrons and photons. Most particularly, Electron Energy Gain Spectroscopy (EEGS) or non-equilibrium EELS are targetted.

We have only adressed a restricted domain of nanooptics all along this thesis. However, spatially resolved fast electron based spectroscopies have proved to be useful for multiple problems related to this topic, notably quantum confined excitations [135]. Multiple experiments are today borrowed from optics to be adapted to fast electrons, including uses of fast electrons carrying angular momentum [121] or time resolved measurements [213]. Quantum nanooptics is also nowadays adressed [134]. Nanooptics with fast electrons is thus a rapidly growing field. Finally, thanks to the continuous technical advances in the development of electron monochromators and CCD cameras with high quantum efficiency in the IR, any access to the low energy, down to vibrational, excitations, currently one of the few weak points of such techniques, is not far away from being reached. With this, a brand new field of condensed matter will be made possible to adress.

# Appendix A

# Supplementary information to Chapter 2

## A.1 Numerical simulations

The numerical simulations were performed using the MNPBEM toolbox in the quasistatic approximation [79]. The nanoprism geometry has been obtained easily, because it is already implemented in the toolbox. The Poisson equation was solved for an arbitrary piecewise inhomogeneous system, similar to the system depicted in figure 2.2a[1], submitted to some external perturbation. The electric is known from the scalar potential as:

$$\vec{E}(\vec{r},\omega) \quad = \quad -\vec{\nabla}\phi(\vec{r},\omega) \tag{A.1.1}$$

On the other hand, the scalar potential is expressed in each region $\Omega_j$ ($j \in \{1,2\}$) through some boundary charges $\sigma(\vec{s},\omega)$ distributed at the surface of the object as:

$$\phi_j(\vec{r},\omega) \quad = \quad \phi_{ext,j}(\vec{r},\omega) + \oint_{\partial\Omega_1\cap\Omega_2} \frac{\sigma(\vec{s},\omega)}{|\vec{r}-\vec{s}|} d\vec{s} \tag{A.1.2}$$

where $\phi_{ext}(\vec{r},\omega)$ is the external potential. The discontinuity of the normal component of the electric field and the continuity of the normal component of the electric displacement at the boundaries sets the equation [72]:

$$2\pi\lambda(\omega)\sigma(\vec{s},\omega) = \vec{e}_{N(\vec{s})}.\vec{\nabla}\phi_{ext}(\vec{s},\omega) + PP\left\{\oint_{\Omega_1\cap\Omega_2} F(\vec{s},\vec{s}\,')\sigma(\vec{s}\,',\omega)d\vec{s}\,'\right\} \tag{A.1.3}$$

The above equation is solved numerically by discretizing the integrals of the equations through a number of meshing points distributed over the boundary of the object to obtain the surface charge $\sigma(\vec{s},\omega)$. Once the surface charge is known, the potential, and, in turn, the electric field can be

[1] We stick to this system made of some object embedded in a matrix, but any extension to an arbitrary number of media is straightforward.

determined in all space. The latter can be done for any external perturbation. For instance, the geometric modes are determined by cancelling the excitation term in the above equation, which gives the eigenvalue equation 2.3.12. The electric field induced by an electron can also be obtained by expressing the external potential through its charge density term (equation 2.5.1) with equation 4.4.4. The EEL probability is then obtained from equation 2.5.8. Finally, the zEMLDOS can be obtained as indicated in appendix C.

## A.2 "Model" SP modes

Occasionally, the dielectric function of "ideal" noble metals might be modelled through a classical free electron model, mathematically expressed by a Drude dielectric function:

$$\varepsilon_D(\omega) = 1 - \frac{\omega_p^2}{\omega^2 + i\Gamma\omega} \tag{A.2.1}$$

where $\omega_p$ is the bulk plasmon frequency and $\Gamma$ is a phenomenological damping rate[2]. The non-zero imaginary part describes absorption of electromagnetic radiation, ie, dissipation of energy associated with the motion of electrons. In terms of realism, the Drude dielectric function proves to be rather suitable for describing silver or gold in the IR, where the optical properties are dominated by intraband transitions. However, the accordance with measured optical properties decreases when approaching the UV regime, most particularly in the case of gold [168]. The reason for this is is that the Drude model can only account for the optical properties related to the electrons of the conduction band, and fails at describing other absorption channels such as interband transitions. Nevertheless, the Drude model can be a comprehensive simple model to capture the essence of the phenomena in play. In particular, a "model" SP mode can be viewed as a mode of the 3D generic system defined in chapter 2 by taking $\varepsilon_1(\omega) = \varepsilon_D(\omega)$ and $\varepsilon_2(\omega) = 1$.

For instance, we can express the spectral characteristics of a mode, whose existence condition is given by equation 2.3.17. The eigenfrequency and relaxation rate are respectively given by equations 2.3.20 and 2.3.21. By only retaining the solution with positive non zero real part, we find:

$$\omega_{i_0}^{SP} = \sqrt{\tilde{\omega}_i^2 - \frac{\Gamma^2}{4}} \tag{A.2.2}$$

$$\Gamma_i^{SP} = \frac{\Gamma}{2} \tag{A.2.3}$$

where:

$$\tilde{\omega}_i = \sqrt{1+\lambda_i}\frac{\omega_p}{\sqrt{2}} \tag{A.2.4}$$

is the eigenfrequency of the mode when there is no dissipation and is obtained by cancelling the loss term in the Drude model. From the above equation, the lifetime of a SP mode is essentially due to the dissipation of energy within the metal, which is modelled by the $\Gamma$ factor of the Drude model[3,4].

[2]For a better agreement, the relaxation rate should be $\omega$ dependent to account for the electron scattering processes occuring in a given spectral range [97].

[3]Such a statement fails in a complete relativistic treatment. In this case, radiative losses, ie, decays into photons, add to these non radiative losses, which are decays into electron-hole pairs.

[4]Because the intraband electron scattering processes and the either presence or absence of interband transitions

Let us transpose this model to the EMLDOS, whose expression is given by equation 2.4.18 if $\vec{r}$ is outside the nanoparticle. The expression for $f_i(\omega)$ reads :

$$f_i(\omega) = \frac{\tilde{\omega}_i^2}{\omega^2 - \tilde{\omega}_i^2 + i\Gamma\omega} \tag{A.2.5}$$

We then find:

$$\Im\{f_i(\omega)\} = \frac{\Gamma\tilde{\omega}_i^2\omega}{\Gamma^2\omega^2 + (\omega^2 - \tilde{\omega}_i^2)^2} \tag{A.2.6}$$

The EMLDOS thus reads:

$$\rho(\vec{r},\omega) = \frac{1}{2\pi^2}\sum_i \frac{\Gamma\tilde{\omega}_i^2}{\Gamma^2\omega^2 + (\omega^2 - \tilde{\omega}_i^2)^2}\left|\vec{E}_i(\vec{r})\right|^2 \tag{A.2.7}$$

Before discussing this result, let us consider the particular, ideal case of $\Gamma \to 0$. Using the identity $lim_{\eta\to 0}\frac{1}{x - x_0 - i\eta} = PP\left\{\frac{1}{x - x_0}\right\} + i\pi\delta(x - x_0)$ [112], we find:

$$lim_{\Gamma\to 0}\Im\{f_i(\omega)\} = \frac{\pi}{2}\omega\delta(\omega - \tilde{\omega}_i) \tag{A.2.8}$$

In this case, the EMLDOS reads:

$$lim_{\Gamma\to 0}\rho(\vec{r},\omega) = \frac{1}{4\pi}\sum_i \delta(\omega - \tilde{\omega}_i)\left|\vec{E}_i(\vec{r})\right|^2 \tag{A.2.9}$$

We thus recover a modal decomposition of type equation 2.4.10. However, in the most general case, the dissipative character of the metal induces a broadening of $\frac{1}{\omega}\Im\{f_i(\omega)\}$, which becomes Lorrentzian. The central frequency of this Lorrentzian function is the frequency $\omega_{i_0}^{Res}$ verifying:

$$\omega_{i_0}^{Res} = \sqrt{\tilde{\omega}_i^2 - \frac{\Gamma^2}{2}} \tag{A.2.10}$$

The spectral contribution from the mode $i$ to the EMLDOS is thus resonant very close to the eigenfrequency of the SP mode $\omega_{i_0}^{SP}$ given in equation A.2.2. On the other hand, the FWHM of the Lorrentzian function $\Gamma_i^{Res}$ is, if $\frac{\Gamma}{\sqrt{2}} \ll \tilde{\omega}_i$ :

$$\Gamma_i^{Res} \approx \Gamma \tag{A.2.11}$$

Therefore, the FWHM of the resonance associated to the mode $i$ is equal to twice its relaxation rate $\Gamma_i^{SP}$ given in equation A.2.3.

depend on the spectral range considered, the damping rate should also vary with the resonance frequency of the mode.

# Appendix B

# Supplementary information to Chapter 4

## B.1 Experimental conditions

| | STEM EELS (subsection 4.3.2) | STEM CL (subsection 4.3.3) |
|---|---|---|
| Acceleration voltage | 7.5 mrad | 15 mrad |
| Incidence angle | 7.5 mrad | 15 mrad |
| Collection angle | 11 mrad | 1.2 Pi srd |
| Dwell time | 5 ms | 500 ms |
| Field size | 150x150 nm | 180x180 nm |
| ChronoSI | Yes (4 spectra per pixel) | No |
| Spatial binning | Yes (x2) | No |
| Equivalent sampling step | 2.4 nm | 5.6 nm |
| CCD dispersion | 20 meV per channel | 10 meV per channel (centered at 600 nm) |
| Spectral resolution | 180 meV | 30 meV |

## B.2 Numerical simulations

The numerical simulations rely on a full relativistic 3D BEM [158]. Such a method is similar to the quasistatic BEM used in chapter 2, except that the full set of Maxwell equations is solved. In this approach, the electric and magnetic fields are related to the scalar and vector potentials as:

$$\vec{E}(\vec{r},\omega) = i\frac{\omega}{c}\vec{A}(\vec{r},\omega) - \vec{\nabla}\phi(\vec{r},\omega) \quad \text{(B.2.1)}$$

$$\vec{B}(\vec{r},\omega) = \vec{\nabla}\times\vec{A}(\vec{r},\omega) \quad \text{(B.2.2)}$$

Moreover, the potentials are related one to each other through the Lorentz gauge, which reads:

$$\vec{\nabla}.\vec{A}(\vec{r},\omega) = i\frac{\omega}{c}\varepsilon(\omega)\phi(\vec{r},\omega) \quad \text{(B.2.3)}$$

In analogy with the quasistatic case, the potentials are expressed in each region $\Omega_j$ through some boundary charges and currents $\sigma_j(\vec{s},\omega)$ and $\vec{h_j}(\vec{s},\omega)$ as:

$$\phi_j(\vec{r},\omega) = \phi_{ext,j}(\vec{r},\omega) + \oint_{\partial\Omega} \tilde{G}_j(\vec{r}-\vec{s})\sigma_j(\vec{s},\omega)d\vec{s} \quad \text{(B.2.4)}$$

$$\vec{A}_j(\vec{r},\omega) = \vec{A}_{ext,j}(\vec{r},\omega) + \oint_{\partial\Omega} \tilde{G}_j(\vec{r}-\vec{s})\vec{h_j}(\vec{s},\omega)d\vec{s} \quad \text{(B.2.5)}$$

where:

$$\tilde{G}_j(\vec{r}-\vec{r}') = \frac{e^{i\sqrt{\varepsilon_j(\vec{r},\omega)}\frac{\omega}{c}|\vec{r}-\vec{r}'|}}{|\vec{r}-\vec{r}'|} \quad \text{(B.2.6)}$$

Expressing the continuity of the potentials at the boundary leads to a set of surface integral equations, from which $\sigma_j(\vec{s},\omega)$ and $\vec{h_j}(\vec{s},\omega)$ (for $j \in \{1,2\}$) can be known [92].

STEM EELS and CL experiments have been modelled by introducing a source term corresponding to a fast electron, which is equivalent to setting:

$$\phi_{ext,j}(\vec{r},\omega) = \frac{1}{\varepsilon_j(\vec{r},\omega)} \int \tilde{G}_j(\vec{r}-\vec{r}')\rho_{el}(\vec{r}',\omega)d\vec{r}' \quad \text{(B.2.7)}$$

$$\vec{A}_{ext,j}(\vec{r},\omega) = \frac{1}{c} \int \tilde{G}_j(\vec{r}-\vec{r}')\vec{J}_{el}(\vec{r}',\omega)d\vec{r}' \quad \text{(B.2.8)}$$

where $\rho_{el}(\vec{r}',\omega)$ and $\vec{J}_{el}(\vec{r}',\omega)$ are given by equations 2.5.1 or 2.5.2. The electromagnetic field induced by the fast electron can then be determined from the boundary source terms, and injected into equations 2.5.8 and 4.4.19 to compute the EEL and EIRE probabilities.

Furthermore, the optical properties can be computed by plane wave excitation at a given frequency, that is, by taking:

$$i\frac{\omega}{c}\vec{A}_{ext,j}(\vec{r},\omega) - \vec{\nabla}\phi_{ext,j}(\vec{r},\omega) = \vec{E}_0 e^{i(\vec{k}_{,j}.\vec{r}-\omega t)} \quad \text{(B.2.9)}$$

$$\vec{\nabla} \times \vec{A}_{ext,j}(\vec{r},\omega) = \vec{B}_0 e^{i(\vec{k}_{,j}.\vec{r}-\omega t)} \quad \text{(B.2.10)}$$

where $\vec{k}_{,j}$ is the wave vector of the plane wave. By decomposing the total electromagnetic field as: $\vec{E}(\vec{r},\omega) = \vec{E}_{ext}(\vec{r},\omega) + \vec{E}_{sca}(\vec{r},\omega)$ and $\vec{H}(\vec{r},\omega) = \vec{H}_{ext}(\vec{r},\omega) + \vec{H}_{sca}(\vec{r},\omega)$ and introducing the far field amplitude $\vec{E}^{sca}_{FF0}(\vec{e}_r,\omega)$ such that the far field limit of $\vec{E}_{sca}(\vec{r},\omega)$ writes: $\vec{E}^{sca}_{FF}(\vec{r},\omega) = \frac{e^{ik_0 r}}{r}\vec{E}^{sca}_{FF0}(\vec{e}_r,\omega)$, where $k_0 = \frac{\omega}{c}$, the scattering, extinction and scattering cross section can be obtained from equations 4.4.34 and 4.4.35.

## B.3 Additional measurements

In this section, we show some results of further combined EELS and CL experiments on single gold triangular nanoprisms relying completely on a carbon foil. Figure B.1 displays HAADF images of nanoprisms of various dimensions, as well as EELS and CL spectra corresponding to electron probe

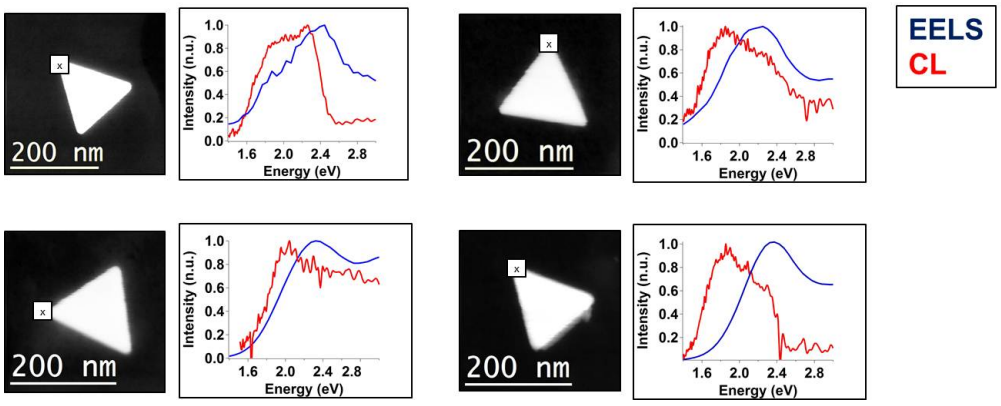


Figure B.1: HAADF images of gold triangular nanoprisms of various dimensions and EELS and CL spectra corresponding to electron probe positions located at one tip.

positions located at one tip. Each spectrum shows a clear resonance associated to a dipolar mode. In each case, the CL resonance is redshifted as compared to the EELS resonance, in accordance with chapter 4.

Furthermore, figure B.2 shows an HAADF image of a fifth gold nanoprims, EELS and CL spectra corresponding to electron probe positions located at the tip (T spectrum) and at the side (S spectrum) of the nanoprism, and maps of the amplitude of the peaks corresponding to the dominant resonances appearing in the spectra at around 1.8 and 2.4 eV[1]. We well recover a Tip mode and an Edge mode similar to the modes discussed in chapter 4. As clear from the spectra, the CL resonance energy of the Edge mode is slightly redshifted as compared to its EELS resonance energy, still in accordance with chapter 4. However, the CL resonance energy of the Tip mode is slightly blushifted as compared to its EELS resonance energy. The modal decomposition derived in chapter 4 may explain this seeming discrepancy. Indeed, the explicit dependence of the resonance energies as a function of the dielectric functions of the media predicts an apparent cancelling of the shift before 2.0 eV in the case of gold, due to some disappearance of the interband transitions (see section B.6 in this appendix). More precisely, because the optical properties of gold approach a Drude model in this spectral range, the CL resonance of a mode should be very slightly blushifted with respect to the EELS resonance (see section B.5). The resonance energies of the Tip mode being located before 1.8 eV, contrary to the resonance energies of the Edge mode as well as the resonances visible in figure B.1, such blueshift of CL with respect to EELS for the Tip mode only is thus not so surprising. The higher magnitude of the shift as compared to the theoretical predictions might be explained by some effect of the carbon foil.

## B.4 The sphere case

In this section, we examine the only system for which analytical expressions of the EEL probability, the EIRE probability, extinction/absorption and scattering cross sections can be found in the lit-

[1]The second resonance at around 2.2 eV visible in the EELS T spectrum is likely to be due to an additional mode which is not discussed here.

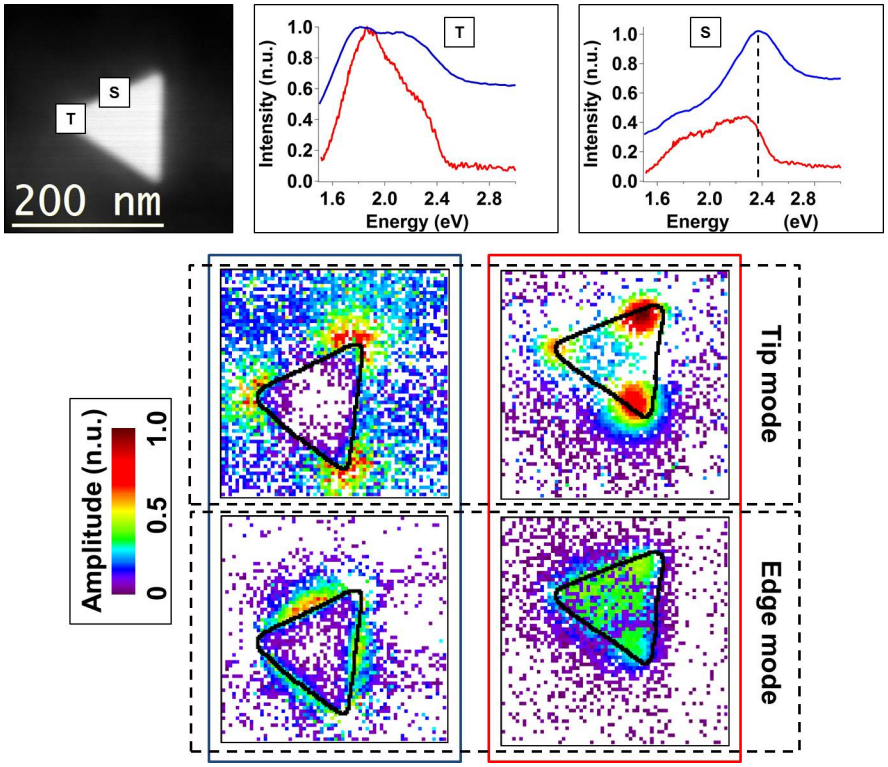


Figure B.2: HAADF image of a gold triangular nanoprism. EELS and CL spectra corresponding to electron probe positions located at the tip (T spectrum) and at the side (S spectrum) of the nanoprism. Maps of the amplitude of the peaks corresponding to the dominant resonances.

terature. We thus consider here a dielectric sphere dielectric function $\varepsilon(\omega)$ and radius $a$ surrounded by vacuum. In the following, we take the centre of the sphere as the origin and $\vec{R}$ outside the sphere (see figure B.3a).

## Quasistatic approximation

In the quasistatic approximation, the EEL probability can be expressed as [67]:

$$\Gamma^{qs}_{EEL}(\vec{R},\omega) = \frac{1}{\pi^2 v^2 a^2} \sum_{l=1}^{\infty} \left(\frac{\omega a}{v}\right)^{2l} \Im\left\{\alpha_l(\omega)\right\} \sum_{m=-l}^{l} \frac{l}{(l+m)!(l-m)!} K_m^2 \left(\frac{\omega}{v}\left|\vec{R}\right|\right) \tag{B.4.1}$$

where:

$$\alpha_l(\omega) = 4\pi a^3 \frac{\varepsilon(\omega)-1}{l\varepsilon(\omega)+l+1} \tag{B.4.2}$$

are the multipolar polarisabilities of the sphere, whose poles give the electric electromagnetic surface modes of the sphere ($\alpha_1(\omega)$ is the dipolar polarisability, whose pole gives the dipolar mode of the

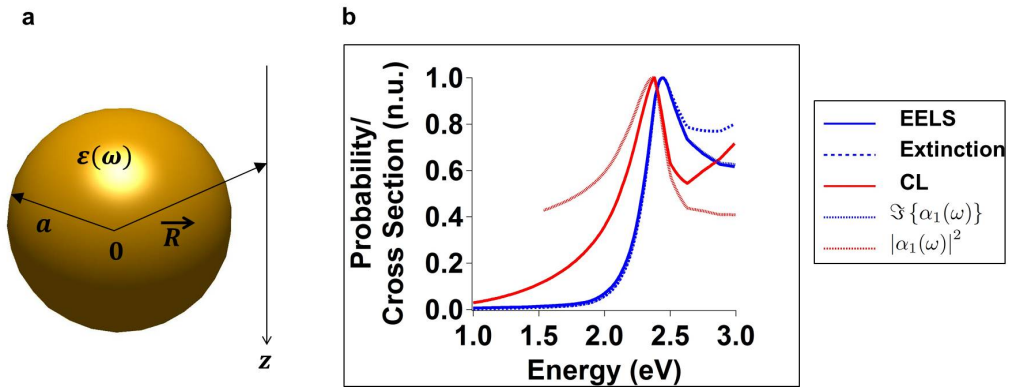


Figure B.3: EELS, CL and extinction of a gold sphere surrounded by vacuum. a) Scheme of the interaction between the fast electron and the sphere. The centre of the sphere of dielectric function $\varepsilon(\omega)$ is taken as the origin. The electron moves outside the sphere of radius $a$ in vacuum. The other notations are kept the same as in section 1.2. b) EELS, CL and extinction of a gold (left plot) and silver (right plot) sphere of diameter 20 nm. For EELS and CL, the electron is directed 5 nm away from the surface of the sphere.

sphere), and $K_m$ is the modified Bessel function of order $m$. Furthermore, the scattering and extinction cross section are given by [10]:

$$C_{ext}^{qs}(\omega) = \frac{\omega}{c}\Im\{\alpha_1(\omega)\} \tag{B.4.3}$$

$$C_{sca}^{qs}(\omega) = \frac{8\pi}{3}\frac{\omega^4}{c^4}\left|\alpha_1(\omega)\right|^2 \tag{B.4.4}$$

In the quasistatic approximation, the extinction and scattering cross section are respectively proportional to the imaginary part and square modulus of the dipolar polarisability of the sphere. Moreover, the spectral variations of EELS, for a given mode, are dictated by the imaginary part of the multipolar polarisability. We here well see the close resemblance between EELS and extinction, and the slight difference between EELS and scattering.

## Retarded regime

In a fully relativistic approach, the EEL and EIRE probabilities can be expressed as [67]:

$$\Gamma_{EEL}^{ret}(\vec{R},\omega) = \frac{1}{c\omega}\sum_{l=1}^{\infty}\sum_{m=-l}^{l}\left[C_{lm}^{E}\Re\{a_l(\omega)\} + C_{lm}^{M}\Re\{b_l(\omega)\}\right]K_m^2\left(\frac{\omega}{v\gamma}\left|\vec{R}\right|\right) \tag{B.4.5}$$

$$\Gamma_{EIRE}^{ret}(\vec{R},\omega) = \frac{1}{c\omega}\sum_{l=1}^{\infty}\sum_{m=-l}^{l}\left[C_{lm}^{E}\left|a_l(\omega)\right|^2 + C_{lm}^{M}\left|b_l(\omega)\right|^2\right]K_m^2\left(\frac{\omega}{v\gamma}\left|\vec{R}\right|\right) \tag{B.4.6}$$

where $a_l(\omega)$ and $b_l(\omega)$ are the electric and magnetic Mie coefficients, whose expressions can be found in reference textbooks [10], $C_{lm}^{E}$ and $C_{lm}^{M}$ are positive coefficients that exclusively depend on the

ratio $v/c$ and $\gamma = \dfrac{1}{\sqrt{1-(v/c)^2}}$. The poles of the Mie coefficients give the electric (for $a_l(\omega)$) and magnetic (for $b_l(\omega)$) electromagnetic surface modes of the sphere. On the other hand, the extinction and scattering cross sections are given by the Mie theory and write [10]:

$$C_{ext}^{ret}(\omega) = \frac{2c^2}{\omega^2}\sum_{l=1}^{\infty}(2l+1)\left[\Re\left\{a_l(\omega)\right\}+\Re\left\{b_l(\omega)\right\}\right] \tag{B.4.7}$$

$$C_{sca}^{ret}(\omega) = \frac{2c^2}{\omega^2}\sum_{l=1}^{\infty}(2l+1)\left[\left|a_l(\omega)\right|^2+\left|b_l(\omega)\right|^2\right] \tag{B.4.8}$$

For a given mode, the spectral variations of EELS and extinction on the one hand, CL and scattering on the other hand, are thus respectively dictated by either $\Re\left\{a_l(\omega)\right\}$ or $\Re\left\{b_l(\omega)\right\}$ and $\left|a_l(\omega)\right|^2$ or $\left|b_l(\omega)\right|^2$. We here well see the close resemblance between EELS and extinction on the one hand, CL and scattering on the other hand .

We can consider the small sphere limit by taking in these expressions $\dfrac{\omega}{c}a \ll 1$. We obtain [10,67]:

$$\Gamma_{EEL}^{ret,a\to 0}(\vec{R},\omega) = \frac{1}{\pi^2}\frac{\omega^2}{v^4\gamma^2}\Im\left\{\alpha_1(\omega)\right\}\left[K_1^2\left(\frac{\omega}{v\gamma}\left|\vec{R}\right|\right)+\frac{1}{\gamma^2}K_0^2\left(\frac{\omega}{v\gamma}\left|\vec{R}\right|\right)\right] \tag{B.4.9}$$

$$\Gamma_{EIRE}^{ret,a\to 0}(\vec{R},\omega) = \frac{4\pi}{\pi^2c^3}\frac{\omega^5}{v^4\gamma^2}\left|\alpha_1(\omega)\right|^2\left[K_1^2\left(\frac{\omega}{v\gamma}\left|\vec{R}\right|\right)+\frac{1}{\gamma^2}K_0^2\left(\frac{\omega}{v\gamma}\left|\vec{R}\right|\right)\right] \tag{B.4.10}$$

$$C_{ext}^{ret,a\to 0}(\omega) = C_{abs}^{ret,a\to 0}(\omega)+\frac{1}{6\pi}\frac{\omega^4}{c^4}\left|\alpha_1(\omega)\right|^2 \tag{B.4.11}$$

$$C_{sca}^{ret,a\to 0}(\omega) = \frac{1}{6\pi}\frac{\omega^4}{c^4}\left|\alpha_1(\omega)\right|^2 \tag{B.4.12}$$

where $\alpha_1(\omega)$ has the same expression than in the quasistatic approximation and:

$$C_{abs}^{ret,a\to 0}(\omega) = \frac{\omega}{c}\Im\left\{\alpha_1(\omega)\right\}$$

is the absorption cross section of the sphere[2]. In these expressions, EELS and, if scattering is negligible compared to absorption, extinction are proportional to the imaginary part of the dipolar polarisability, while CL and scattering are proportional to the square modulus of the dipolar polarisability.

Let us now consider the spectral dependence of EELS, CL and extinction in a particular case. Figure B.3b plots EELS, CL and extinction spectra obtained from the retarded expressions[3], as well as the energy dependence of the imaginary part and square modulus of the dipolar polarisability,

[2]Notice the non-equivalence of the small sphere limit and the quasistatic approximation. For EELS, the only mode appearing in the above expression is the dipolar mode, contrary to the quasistatic approximation which involves multipolar modes. For EELS, the small sphere limit is thus equivalent to the quasistatic approximation only if the higher order modes are negligible as compared to the dipolar mode. Furthermore, extinction includes a contribution from scattering that was not present in the quasistatic approximation. For extinction, the small sphere limit is thus equivalent to the quasistatic approximation only if scattering is negligible as compared to absorption. Finally, note that in the small sphere limit, the dipolar mode is involved in all the quantities, in particular in CL, and is thus radiative.

[3]The calculation was performed with Javier Garcia de Abajo's widgets, which can be found at the following website adress: http://nanophotonics.csic.es/static/widgets/.

of a gold sphere of diameter 20 nm. The dielectric function was taken from [74] and the electron is taken to travel 5 nm away from the surface of the sphere. EELS and extinction, as well as CL and scattering, are clearly resonant at the same energy. However, CL/scattering is slightly redshifted with respect to EELS/extinction, which is due to the slight redshift from the imaginary part to the square modulus of the dipolar polarisability.

## B.5 EELS, CL, extinction and scattering for model SP modes

As developped in chapters 2 and 4, the EEL and EIRE probabilities read, for the arbitrary system defined in chapter 2 and a non-penetrating trajectory:

$$\Gamma_{EEL}(\vec{R},\omega) \sim \frac{1}{\omega^2}\sum_i \Im\left\{f_i(\omega)\right\}\left|E_i^z(\vec{R},\frac{\omega}{v})\right|^2 \tag{B.5.1}$$

$$\Gamma_{EIRE}(\vec{R},\omega) \sim \omega\sum_{i=d} |f_i(\omega)|^2\left|E_i^z(\vec{R},\frac{\omega}{v})\right|^2 \tag{B.5.2}$$

We here examine what happens for model SP modes described by taking $\varepsilon_1(\omega)$ as a Drude model and $\varepsilon_2(\omega) = 1$ . In this case:

$$f_i(\omega) = \frac{\tilde{\omega}_i^2}{\omega^2 - \tilde{\omega}_i^2 + i\Gamma\omega} \tag{B.5.3}$$

Therefore, the EEL and EIRE probabilities read:

$$\Gamma_{EEL}(\vec{R},\omega) \sim \frac{1}{\omega}\sum_i \frac{\Gamma\tilde{\omega}_i^2}{\Gamma^2\omega^2 + (\omega^2 - \tilde{\omega}_i^2)^2}\left|E_i^z(\vec{R},\frac{\omega}{v})\right|^2 \tag{B.5.4}$$

$$\Gamma_{EIRE}(\vec{R},\omega) \sim \omega\sum_{i=d} \frac{\tilde{\omega}_i^4}{\Gamma^2\omega^2 + (\omega^2 - \tilde{\omega}_i^2)^2}\left|E_i^z(\vec{R},\frac{\omega}{v})\right|^2 \tag{B.5.5}$$

If we now consider the case of $\Gamma \to 0$, we find, using the identity $lim_{\eta\to 0}\frac{\eta}{\eta^2 + x^2} = \pi\delta(x)$, that these expressions become:

$$\Gamma_{EEL}(\vec{R},\omega) \sim \sum_i \delta(\omega - \tilde{\omega}_i)\left|E_i^z(\vec{R},\frac{\omega}{v})\right|^2 \tag{B.5.6}$$

$$\Gamma_{EIRE}(\vec{R},\omega) \sim \sum_{i=d} \delta(\omega - \tilde{\omega}_i)\left|E_i^z(\vec{R},\frac{\omega}{v})\right|^2 \tag{B.5.7}$$

Therefore, in the non-dissipative limit, resonance energy shifts between EELS and CL are forbidden. Such spectral shifts may however appear at non-zero dissipation, due to different energy dependences in the EEL and EIRE probabilities. However, we note that, using this model, $\Gamma_{EEL}(\vec{R},\omega) \sim \frac{1}{\omega^2}\Gamma_{EIRE}(\vec{R},\omega)$ for a given dipolar mode. This implies that the CL resonance energy of a given mode should be automatically blue-shifted relative to its EELS resonance energy.

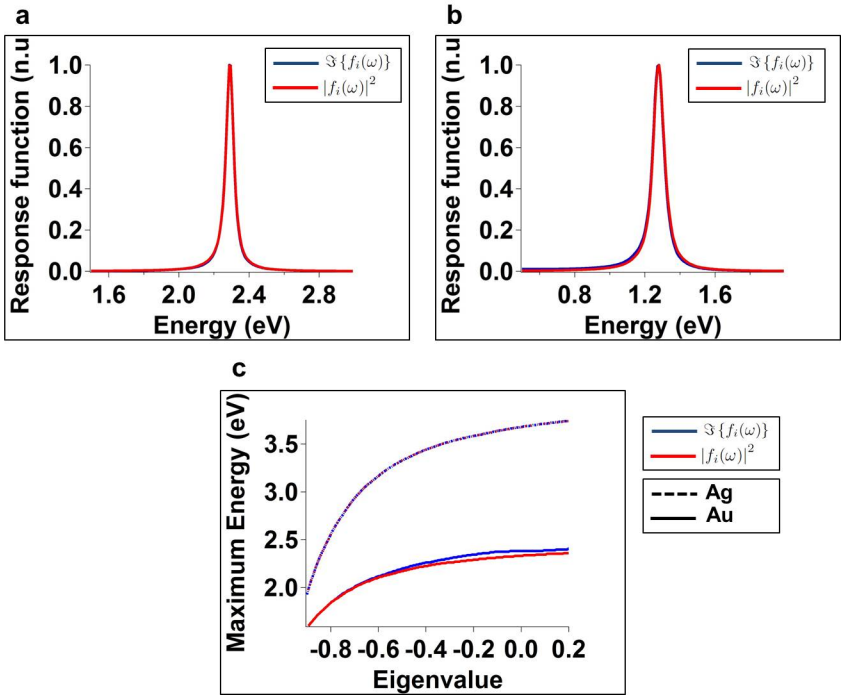


Figure B.4: $\Im\{f_i(\omega)\}$ and $|f_i(\omega)|^2$ for different parameters. a) $\varepsilon_1(\omega) = \varepsilon_{Ag}(\omega)$, $\varepsilon_2(\omega) = 1$ and $\lambda_i = -0.85$. b) $\varepsilon_1(\omega) = \varepsilon_{Au}(\omega)$, $\varepsilon_2(\omega) = 1$ and $\lambda_i = -0.95$. c) Maximum of $\Im\{f_i(\omega)\}$ and $|f_i(\omega)|^2$ as a function of the eigenvalue of the mode $\lambda_i$.

We can also argue similarly with the extinction and scattering cross sections, whose expressions read:

$$C_{ext}(\omega) \sim \omega^2 \sum_{i=d} \frac{\Gamma\tilde{\omega}_i^2}{\Gamma^2\omega^2 + (\omega^2 - \tilde{\omega}_i^2)^2} \tag{B.5.8}$$

$$C_{sca}(\omega) \sim \omega^4 \sum_{i=d} \frac{\tilde{\omega}_i^4}{\Gamma^2\omega^2 + (\omega^2 - \tilde{\omega}_i^2)^2} \tag{B.5.9}$$

A scattering resonance is thus blue-shifted relative to an extinction resonance, in accordance with [161].

Therefore, a Drude model leads to predictions contradictory to what we have observed in chapter 4. Our work thus constitutes a proof of the departure of SP modes in gold from classical oscillator models [161, 166].

## B.6 A particular feature

It has been shown in chapter 4 that the spectral shift from EELS to CL or from extinction to scattering is due to the spectral shift from $\Im\{f_i(\omega)\}$ to $|f_i(\omega)|^2$, for a given mode of a gold object in the visible range.

Figure B.4 shows $\Im\{f_i(\omega)\}$ and $|f_i(\omega)|^2$ by taking $\varepsilon_1(\omega)$ as the dielectric function of silver [74], $\varepsilon_2(\omega) = 1$ , and $\lambda_i = -0.85$ (figure B.4a), and $\varepsilon_1(\omega)$ as the dielectric function of gold [74], $\varepsilon_2(\omega) = 1$ , and $\lambda_i = -0.95$ (figure B.4b). In the first case, $\lambda_i$ was chosen so that the resonances fall in the same spectral range as in the experimental dataset with silver instead of gold, while in the second case, $\lambda_i$ was chosen so that the resonances fall in a much lower spectral range with gold. In both cases, both $\Im\{f_i(\omega)\}$ and $|f_i(\omega)|^2$ are resonant at the very same energy, which would lead to similar resonances and EELS and in CL, contrary to what was found in the experiments and in the simulations. Therefore, the observed spectral shift is not a feature universal to SP modes. Furthermore, figure B.4c shows the energy where $\Im\{f_i(\omega)\}$ and $|f_i(\omega)|^2$ are maximum when taking $\varepsilon_1(\omega)$ as the dielectric function of either silver (dotted lines) or gold (solid lines) and $\varepsilon_2(\omega) = 1$ as a function of $\lambda_i$. At low energies, the maxima of $\Im\{f_i(\omega)\}$ and $|f_i(\omega)|^2$ occur at the same resonance energy for both silver and gold. However, beyond 2.0 eV, the maximum of $\Im\{f_i(\omega)\}$ splits of from the maximum of $|f_i(\omega)|^2$ in the case of gold only. Such splitting is due to the behaviour of the dielectric function of gold in the visible range.

# Appendix C

# Supplementary information to Chapter 5

## C.1 Sample preparation

The sample consists of silver sandwiched between two amorphous $Si_3N_4$ films and its preparation was carried out by alternate ion beam sputtering (IBS) in a Nordiko$^{TM}$ 3000 vacuum chamber and has been depicted in detail in [221, 222]. A thick $Si_3N_4$ film was first deposited at 200°C onto a faceted NaCl single crystal and was then sputtered at room temperature with 1 keV $Xe^+$ ions at a sputtering angle of 55° with respect to the normal of the mean (001) surface and with a total fluence of 5.4x10$^{16}$ions/cm$^2$. It is well known that IBS under off-normal incidence may result in the generation of unidirectional ripples [223]. The phenomenon, which is related to the interplay between surface roughening (due to the curvature dependence of the sputtering yield) and the smoothing of the surface by different relaxation mechanisms, strongly depends on the sputtering conditions (angle of incidence, temperature, ion energy and mass, total fluence, etc.). Therefore, only the (001) facets of the NaCl surface exposed to the defocused $Xe^+$ flux at an incidence of 55° develop nanoripples (oriented perpendicular to the ion beam and with a period around 25 nm), while other areas with different orientations remain flat. The inhomogeneously pre-patterned surface of the $Si_3N_4$ buffer-layer was then used as template for the subsequent growth of silver occurring by Volmer-Weber mechanism. Silver deposition was accomplished at room temperature with a glancing angle of 5° from the mean surface and with the metallic flux being oriented perpendicular to the periodic ripples. Shadowing effects associated with a preferential diffusion of silver atoms along the ripples resulted in the production of aligned ellipsoidal nanoparticles in the rippled areas [221, 222], while tortuous or percolating-like structures were formed in the flat areas where the deposition rate was higher. Finally, after deposition of an additional $Si_3N_4$ capping-layer at 200°C, the sample was floated in purified water and the resulting freestanding thin film was collected on microscope copper grids.

## C.2 Experimental conditions

| | FEI TEM data (subsections 5.3.2 and 5.3.3) | VG STEM data (subsection 5.3.4) |
|---|---|---|
| Acceleration voltage | 80 kV | 100 kV |
| Incidence angle | 7 mrad | 7 mrad |
| Collection angle | 14 mrad | 11 mrad |
| Dwell time | 5 ms | 1 ms |
| Field size | 77x77 nm (3 areas studied) | 888x1030 nm (divided into 21 small regions) |
| ChronoSI | No | Yes (15 spectra per pixel) |
| Spatial binning | Yes (x4) | No |
| Equivalent sampling step | 2.4 nm | 3.9 nm |
| CCD dispersion | 10 meV per channel | 50 meV per channel |
| Spectral resolution | 60 meV | 250 meV |

| | VG STEM data (section 5.4S) |
|---|---|
| Acceleration voltage | 100 kV |
| Incidence angle | 7 mrad |
| Collection angle | 11 mrad |
| Dwell time | 5 ms |
| Field size | 485x485 nm |
| ChronoSI | Yes (15 spectra per pixel) |
| Spatial binning | No |
| Equivalent sampling step | 3.9 nm |
| CCD dispersion | 50 meV per channel |
| Spectral resolution | 200 meV |

## C.3 Additional data

### Subsections 5.3.2 and 5.3.3

Subsections 5.3.2 and 5.3.3 base on experiments performed with the FEI TEM. However, as mentioned in the text, the findings are not significantly changed when based on the VG STEM experiments, which were the first to suggest our mode analysis. The results presented here are obtained from some measurements performed with the VG STEM in a small semicontinuous sample region around the percolation threshold. Figure C.1a shows the HAADF image of this region recorded during the STEM EELS acquisition[1], together with some local EEL probability spectra shown on figure C.1b. The spectra correspond to probe positions separated by around 100 nm, and dramatically change from one position to the other. Figure C.1c displays energy filtered maps of the EEL probability. In each map, spots very similar to the spots evidenced in the energy filtered maps of subsection 5.3.2 are visible (see the white squares). Figure C.1d shows the maps of the energy and amplitude of the peaks which have been fitted between 0.8 and 1.6 eV. As evidenced by the black

[1]Such a region is one of the 21 regions investigated during the measurements of subsection 5.3.4. The experimental conditions can thus be found in the corresponding table of the last section.

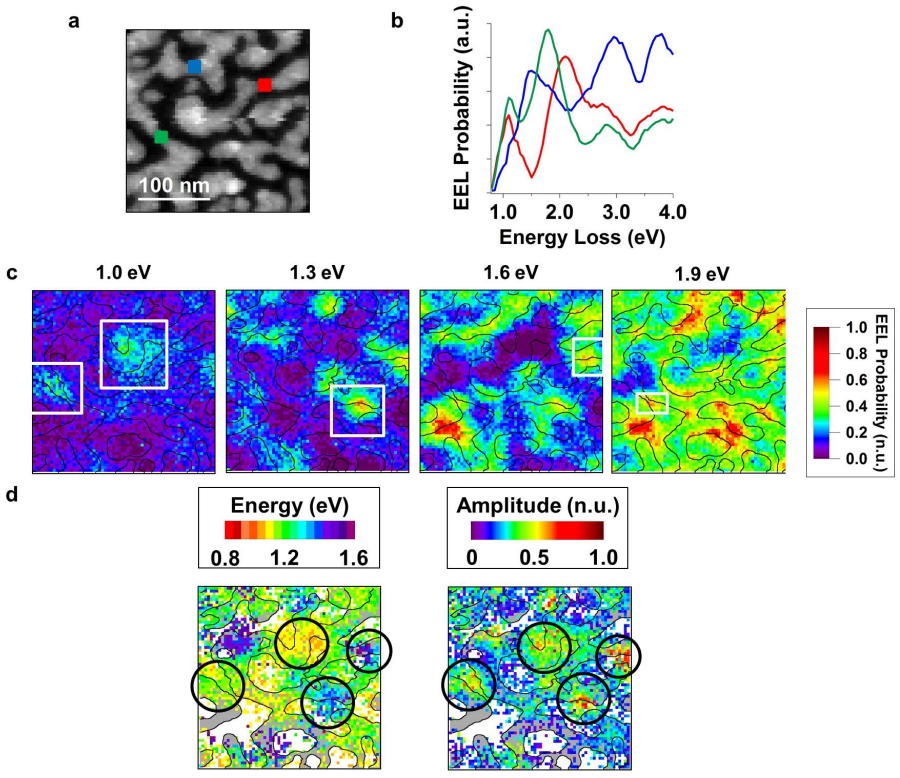


Figure C.1: a) HAADF image of the scanned area recorded during the STEM EELS acquisition. b) Local EEL probability spectra corresponding to the electron probe positions indicated on the HAADF image and separated by 100 nm. c) Energy filtered maps of the EEL probability for some energy loss values taken at low energies. The white squares delimit small regions where the EEL probability overcomes the surrounding. d) Maps of the energy and amplitude of the peaks which have been fitted between 0.8 and 1.6 eV. The black circles delimit some modes with different resonance energies.

circles, local amplitude maxima in the amplitude maps can be associated to a constant peak energy, as well as a spot in the energy filtered maps. Therefore, we are well able to interpret the dataset in terms of modes.

## Subsection 5.3.4

The HAADF image of the area studied in subsection 5.3.4 is displayed on figure 5.8a. Figure C.2b shows histograms counting the number of probe positions for which a given number of peaks has been fitted in the corresponding spectrum (left histogram) and for which a peak with a given central energy has been fitted, weighted by the peak amplitudes (right histogram). These histograms do not include the probe positions for which the fitting procedure failed. Very strikingly, despite the large size of the covered area, at least 1 peak has been found for each probe position (maximum 6), and the mean number of peaks in a single spectrum is 3.3. Moreover, all the modes of the area

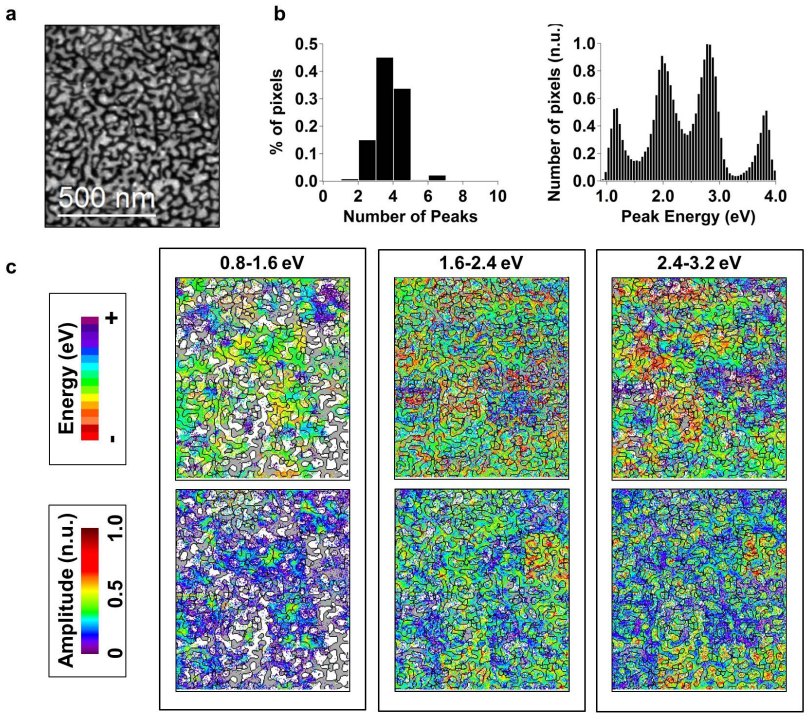


Figure C.2: a) HAADF image of the total scanned area. b) Histograms counting the number of probe positions for which a given number of peaks has been fitted in the corresponding spectrum (left histogram) and for which a peak with a given central energy has been fitted (right histogram). The latter is weighted by the peak amplitudes. c) Maps of the energy and amplitude of the peaks which have been fitted between 0.8 and 1.6 eV (left pannel), 1.6 and 2.4 eV (middle pannel) and 2.4 and 3.2 eV (right pannel).

spread all over the spectrum, despite the repeated apparent domination of some modes at some resonance energies. Figure 5.8c displays maps of the energy and amplitude of the peaks which have been found in each pixel between 0.8 and 1.6 eV, 1.6 and 2.4 eV and 2.4 and 3.2 eV. These maps show that the modes are not only numerous at low energies, but also spread over the complete spectral range.

## Section 5.4

Figure C.3b shows maps of the energy and amplitude of the peaks whose energy is found between 0.8 and 1.6, 1.6 and 2.4, and 2.4 and 3.2 eV. At low energies (upper maps), both the mean intensities and the variations in the intensity of the electric fields associated to the modes clearly increase from area i to iii. In area i, only a few (if not no) modes are detected in this spectral range. In area ii, smooth field intensities spatial variations are associated to some modes that do not spread much in

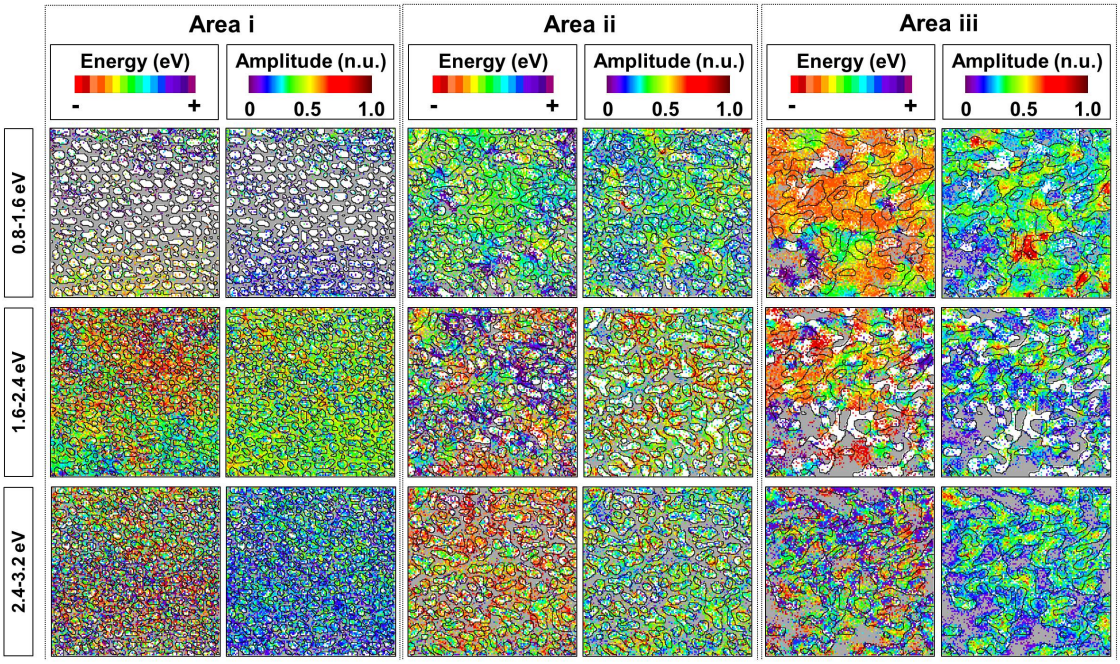


Figure C.3: Maps of the energy (left) and amplitude (right) of the peaks, found in each spectrum of area i to iii, and whose central energy is between 0.8 and 1.6, 1.6 and 2.4 and 2.4 and 3.2 eV.

the spectral range and do not have resonance energies before 1.1 eV. In comparison, area iii shows a rich multiplicity of modes with close resonance energies, detected down to 0.95 eV, and whose electric fields are strongly varying and reach very high intensities at some locations. At intermediate energies (middle maps), the largest area covered by the modes is found in area i, for which any distinction of modes is difficult. Indeed, the amplitude map shows a rather uniform pattern, and no clear areas of constant peak energy can be delimited in the energy map. The modes which are in play in this energy range are most probably the Mie-type modes of individual particles, with possible coupling effects. The area covered by the modes decreases progressively when heading to areas ii then iii. In area iii, very small spots in the amplitude maps, whose intensity is lower than those at the low energies, are clearly associated to different modes. Finally, no clear distinction between the modes of the three areas, whose field intensities encompass the metal clusters, can be drawn at the highest energies (lower maps).

## C.4 Numerical simulations

### Methods

The numerical simulations have been achieved by our collaborators from the Laboratoire Charles Fabry with a FEM. Similarly to the BEM, such a method allows solving numerically the Maxwell equations in an inhomogeneous system consisting of homogeneous piecewise media described by local

dielectric functions and separated by abrupt interfaces (see section 2.3) [224]. However, contrary to the BEM, the whole volume of the system has to be meshed. The modelization procedure of a semicontinuous film around the percolation threshold is illustrated on figure C.4. A 400 x 400 nm large HAADF image of a semicontinuous area around the percolation threshold [2] was thresholded and binarized. A particle analysis was then performed, and the coordinates of a number of points equally distributed over the contour of the clusters were extracted. The minimum distance between two of these points was set to 2.5 nm, in order to obtain an acceptable yet realistic in-plane meshing precision. The shape was then extruded up to a thickness of 10 nm, and the volume of the obtained objects meshed. Finally, these objects were included in a box filled by $Si_3N_4$ and closed by Perfectly Matched Layers (PML, i.e. artificial totally absorbing layers) to model boundary conditions [225]. The empty volume of the box was finally meshed. The dielectric function of silver was adapted from [74], and the dielectric function of $Si_3N_4$ was set constant to 2.03 [221]. In the FEM, the electromagnetic fields have to be calculated in all space of the system, which is discretized with edge elements [226]. To account for our experiments, the EEL probability was approximated as the projection of the EMLDOS along the direction perpendicular to the plane of the film evaluated at a distance of 10 nm above the upper side of the film. To calculate the EMLDOS, a vertically polarized electric point-like dipole oscillating at a given frequency is placed at a certain position in a plane located 10 nm above the film. This dipole thus enters the Maxwell equations through a current source writing as [91]:

$$\vec{J}_{dip}(\vec{r},t) = -ip_0\omega_0 e^{-i\omega_0 t}\delta(\vec{r}-\vec{r}_0)\vec{e}_z \tag{C.4.1}$$

where $\omega_0$ is the frequency and $p_0$ is the amplitude of the dipole. The power emitted by the dipole can be expressed as a function of the induced electric field $\vec{E}_{dip}(\vec{r},t)$ as [163]:

$$\begin{aligned} P_{dip} &= \frac{1}{2}\left\langle \Re\left\{ \int \vec{J}^*_{dip}(\vec{r},t).\vec{E}_{dip}(\vec{r},t)d^3\vec{r} \right\} \right\rangle \\ &= \frac{1}{2}\left\langle \Re\left\{ ip_0\omega_0 e^{-i\omega_0 t} E^z_{dip}(\vec{r}_0,t) \right\} \right\rangle \end{aligned} \tag{C.4.2}$$

The spontaneous decay rate of the dipole $\Gamma$ can in turn be calculated from this dipole radiation power as [227]:

$$\Gamma = \frac{P_{dip}}{P^0_{dip}}\Gamma^0 \tag{C.4.3}$$

where $P^0_{dip}$ and $\Gamma^0$ are the dipole emission power and spontaneous decay rate in the absence of metallic environment. The Purcell enhancement factor can be defined as the ratio between the spontaneous decay rates with and without metallic environment, namely [228]:

$$F_p = \frac{\Gamma}{\Gamma^0} \tag{C.4.4}$$

Therefore, the Purcell factor can also be defined from the power emitted by the dipole with and without environment as:

$$F_p = \frac{P_{dip}}{P^0_{dip}} \tag{C.4.5}$$

[2] This area corresponds to area iii of section 5.4.

On the other hand, the spontaneous decay rate can also be expressed as a function of the EMLDOS as [36, 177, 187]:

$$\Gamma = \frac{4\pi^2\omega_0}{\hbar} p_0^2 \rho(\vec{r}_0, \omega_0) \tag{C.4.6}$$

Therefore, the EMLDOS at the position and frequency of the dipole writes:

$$\begin{aligned} \rho(\vec{r}_0, \omega_0) &= \frac{\hbar}{4\pi^2\omega_0 p_0^2}\Gamma^0 F_p \\ &= \frac{\hbar}{8\pi^2 P_{dip}^0 \omega_0 p_0^2} \left\langle \Re\left\{ i p_0 \omega_0 e^{-i\omega_0 t} E_{dip}^z(\vec{r}_0, t)\right\}\right\rangle \end{aligned} \tag{C.4.7}$$

To sum up, in order to calculate the Purcell factor, or, equivalently, the EMLDOS at a given point location and frequency, the electric field induced by an electric dipole located at this point location and oscillating at this frequency is calculated in all space. The map on the right of figure C.4b shows, for illustration, the calculated electric field in a plane located 5 nm above the upper side of the film for a dipole oscillating at a frequency of 1.57 eV located at an in-plane position indicated by the red square on the left image. The EMLDOS is then deduced from the value of the electric field located at the position of the dipole using equation C.4.7. EMLDOS spectra are thus calculated by tuning the frequency of the dipole at a fixed point location. Alternatively, EMLDOS frequency filtered maps are computed by displacing a dipole of given frequency all over the plane.

## Results

Figure C.5b shows the Purcell factor local spectra calculated for dipole positions separated by 35 nm. The corresponding dipole positions are shown explicitely on figure C.5a. The very strong spectral variations at nanometric scale evidenced experimentally are well reproduced. However, the multiple resonant peaks appearing within these spectra are far narrower than the peaks evidenced within the measured EEL probability spectra. It is known that for thin metal films, the absorption of light increases around the visible range, due to some structural imperfections and impurities within the metal crystalline structure [78]. This increased absorption as compared to the reference measurements of [74] can be accounted for by multiplying the imaginary part of the dielectric function by a certain constant factor. The spectra calculated with a factor of 3 and corresponding to the same dipole positions are shown on figure C.5c. These spectra are more in qualitative agreement with the experimental spectra. Such an adjustement using a factor of 3 is consistent with the data reported in [78].

Energy filtered maps of the zEMLDOS have been tried to be calculated in order to reproduce some HS-like patterns, but with no success, apparently due to some meshing issues around the dipole.

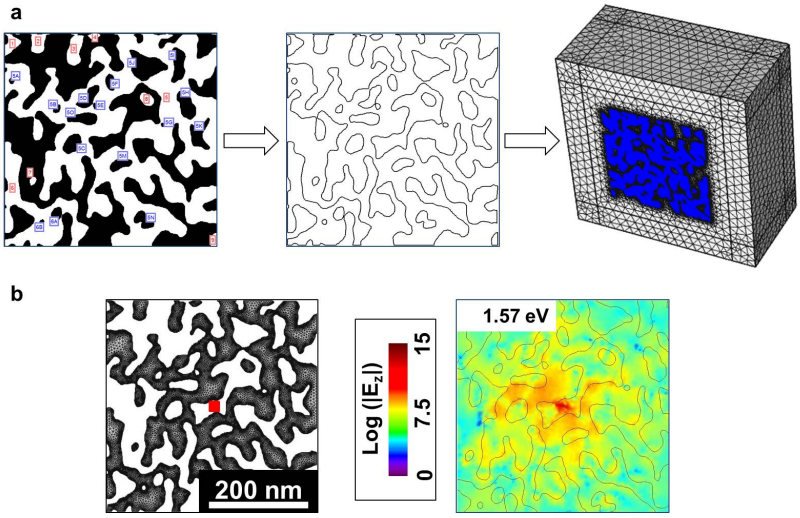


Figure C.4: Calculating the EMLDOS of a semicontinuous area around the percolation threshold. a) Modelization procedure of the system. An HAADF image of a semicontinuous area around the percolation threshold is thresholded and binarized. A particle analysis is performed, and the coordinates of a number of points equally distributed over the contour of the clusters are extracted. The shape is then extruded, and the meshed objects are included in a volume meshed box. b) Calculated electric field in a plane located 5 nm above the upper side of the film for a dipole oscillating at a frequency of 1.57 eV located at an in-plane position indicated by the red square on the left image.

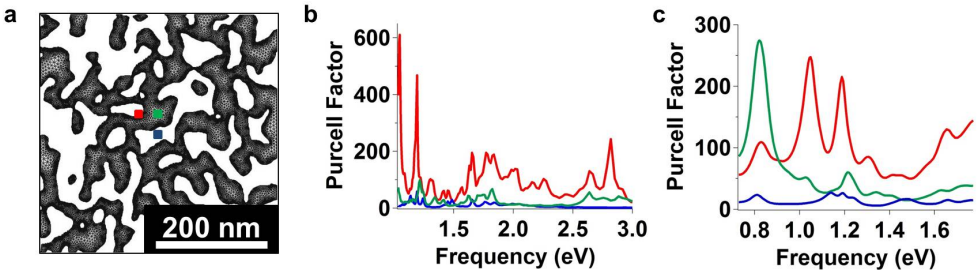


Figure C.5: Numerical calculations of the EMLDOS. a) Meshed semicontinuous film. b and c) Purcell factor local spectra calculated at the dipole positions indicated on image C.5a and separated by 35 nm. b): the dielectric function of silver is taken from [74]. c): the imaginary part of the dielectric function of silver is multiplied by a constant factor of 3.

# Appendix D

# List of acronyms

BEM: Boundary Element Method

BF: Bright Field

CCD: Charge Coupled Device

CDOS: Cross Density Of States

cFEG: cold Field Emission Gun

CL: CathodoLuminescence

DDA: Discrete Dipole Approximation

DGTD: Discontinuous Galerkin Time-Domain

EDS: Energy Dispersive x-ray spectroscopy

EIRE: Electron Induced Radiation Emission

EEGS: Electron Energy Gain Spectroscopy

EEL: Electron Energy Loss

EELS: Electron Energy Loss Spectroscopy

eLDOS: Electric Local Density Of States

EMLDOS: ElectroMagnetic Local Density Of States

FDTD: Finite Difference Time Domain

FEG: Field Emission Gun

FEM: Finite Element Method

FWHM: Full Width at Half Maximum

HAADF: High Angle Annular Dark Field

HS: Hot Spot

IR: InfraRed

LDOS: Local Density Of States

mLDOS: Magnetic Local Density of States

NA: Numerical Aperture

nEMLDOS: n-projected ElectroMagnetic Local Density Of States

PCA: Principal Component Analysis

PEEM: Photon Emission Electron Microscopy

PML: Perfectly Matched Layers

PSF: Point Spread Function

rEMLDOS: radiative ElectroMagnetic Local Density Of States

RIC: Resistor-Inductor-Capacitor

SEE: Secondary Electron Emission

SEM: Scanning Electron Microscope

SI: Spectrum Image

SNOM: Scanning Near-Field Optical Microscopy

SP: Surface Plasmon

SPP: Surface Plasmon Polariton

STEM: Scanning Transmission Electron Microscope

STEM CL: spatially resolved CathodoLuminescence

STEM EEGS: spatially resolved Electron Energy Gain Spectroscopy

STEM EELS: spatially resolved Electron Energy Loss Spectroscopy

TEM: Transmission Electron Microcope

TPL: Two Photon Luminescence

UV: UltraViolet

VG: Vacuum Generators

zEMLDOS: z-projected ElectroMagnetic Local Density Of States

ZLP: Zero Loss Peak

# Bibliography


[1] L. Novotny and B. Hecht. *Principles of Nano-Optics*. Cambridge University Press, 2011.

[2] S. A. Maier. *Plasmonics: fundamentals and applications*. Springer, New York, 2007.

[3] S. Enoch and N. Bonod. *Plasmonics from basics to advanced topics*. Springer, Berlin; New York, 2012.

[4] J.-J. Greffet. Introduction to surface plasmon theory. In S. Enoch and N. Bonod, editors, *Plasmonics*, volume 167 of *Springer Series in Optical Sciences*, page 105. Springer Berlin Heidelberg, 2012.

[5] J. M. Pitarke, V. M. Silkin, E. V. Chulkov, and P. M. Echenique. Theory of surface plasmons and surface-plasmon polaritons. *Rep. Prog. Phys.*, 70:1, 2007.

[6] J. Aizpurua and R. Hillenbrand. Localized surface plasmons: Basics and applications in field-enhanced spectroscopy. In S. Enoch and N. Bonod, editors, *Plasmonics*, volume 167, page 151. Springer Berlin Heidelberg, Berlin, Heidelberg, 2012.

[7] K. L. Kelly, E. Coronado, L. L. Zhao, and G. C. Schatz. The optical properties of metal nanoparticles: The influence of size, shape, and dielectric environment. *J. Phys. Chem. B*, 107:668, 2003.

[8] M. Hu, C. Novo, A. Funston, H. Wang, H. Staleva, S. Zou, P. Mulvaney, Y. Xia, and G. V. Hartland. Dark-field microscopy studies of single metal nanoparticles: understanding the factors that influence the linewidth of the localized surface plasmon resonance. *J. Mater. Chem.*, 18:1949, 2008.

[9] G. Mie. Beitraege zur optik trueber medien, speziell kolloidaler metalloesungen. *Annalen der Physik*, 25:377, 1908.

[10] C. F. Bohren and D. R. Huffman. *Absorption and scattering of light by small particles*. Wiley, New York, 1983.

[11] G. Schider, J. Krenn, A. Hohenau, H. Ditlbacher, A. Leitner, F. Aussenegg, W. Schaich, I. Puscasu, B. Monacelli, and G. Boreman. Plasmon dispersion relation of au and ag nanowires. *Phy. Rev. B*, 68:155427, 2003.

[12] C. Sönnichsen, T. Franzl, T. Wilk, G. von Plessen, J. Feldmann, O. Wilson, and P. Mulvaney. Drastic reduction of plasmon damping in gold nanorods. *Phys. Rev. Lett.*, 88:077402, 2002.

[13] A. Tcherniak, J. W. Ha, S. Dominguez-Medina, L. S. Slaughter, and S. Link. Probing a century old prediction one plasmonic particle at a time. *Nano Lett.*, 10:1398, 2010.

[14] P. Bharadwaj, B. Deutsch, and L. Novotny. Optical antennas. *Adv. Opt. Photon.*, 1:438, 2009.

[15] V. Giannini, A. I. Fernández-Domínguez, S. C. Heck, and S. A. Maier. Plasmonic nanoantennas: Fundamentals and their use in controlling the radiative properties of nanoemitters. *Chem. Rev.*, 111:3888, 2011.

[16] A. Bouhelier, G. Colas des Francs, and J. Grandidier. Imaging surface plasmons. In S. Enoch and N. Bonod, editors, *Plasmonics*, volume 167, page 225. Springer Berlin Heidelberg, Berlin, Heidelberg, 2012.

[17] G. P. Wiederrecht. Near-field optical imaging of noble metal nanoparticles. *Eur. Phys. J. Applied Physics*, 28:3, 2004.

[18] T. Klar, M. Perner, S. Grosse, G. von Plessen, W. Spirkl, and J. Feldmann. Surface-plasmon resonances in single metallic nanoparticles. *Phys. Rev. Lett.*, 80:4249, 1998.

[19] J. R. Krenn, A. Dereux, J. C. Weeber, E. Bourillot, Y. Lacroute, J. P. Goudonnet, G. Schider, W. Gotschy, A. Leitner, F. R. Aussenegg, and C. Girard. Squeezing the optical near-field zone by plasmon coupling of metallic nanoparticles. *Phys. Rev. Lett.*, 82:2590, 1999.

[20] F. J. García de Abajo. Optical excitations in electron microscopy. *Rev. Mod. Phys.*, 82:209, 2010.

[21] S. J. Pennycook and P. D. Nellist. *Scanning transmission electron microscopy: imaging and analysis*. Springer, New York, 2011.

[22] M. Kociak and J. García de Abajo. Nanoscale mapping of plasmons, photons, and excitons. *MRS Bulletin*, 37:39, 2012.

[23] K. L. Kliewer and R. Fuchs. Theory of dynamical properties of dielectric surfaces. *Advances in Chemical Physics: Aspects of the Study of Surfaces, Volume 27*, page 355, 2007.

[24] Coherent control of nanoscale localization of ultrafast optical excitation in nanosystems. *Phys. Rev. B*, 69:054202.

[25] I. Mayergoyz, D. Fredkin, and Z. Zhang. Electrostatic (plasmon) resonances in nanoparticles. *Phys. Rev. B*, 72:155412, 2005.

[26] U. Hohenester and J. Krenn. Surface plasmon resonances of single and coupled metallic nanoparticles: A boundary integral method approach. *Phys. Rev. B*, 72:195429.

[27] T. J. Davis, K. C. Vernon, and D. E. Gomez. Effect of retardation on localized surface plasmon resonances in a metallic nanorod. *Opt. Express*, 17:23655, 2009.

[28] S. Wuestner, A. Pusch, K. L. Tsakmakidis, J. M. Hamm, and O. Hess. Comment on "spaser action, loss compensation, and stability in plasmonic systems with gain". *Phys. Rev. Lett.*, 107:259701, 2011.

[29] V. Shalaev and A. K. Sarychev. Nonlinear optics of random metal-dielectric films. *Phys. Rev. B*, 57:13265, 1998.

[30] L. Novotny. Effective wavelength scaling for optical antennas. *Phys. Rev. Lett.*, 98:266802, 2007.

[31] V. Shalaev, R. Botet, and A. Butenko. Localization of collective dipole excitations on fractals. *Phys. Rev. B*, 48:6662, 1993.

[32] M. I. Stockman, L. Pandey, and T. George. Inhomogeneous localization of polar eigenmodes in fractals. *Phys. Rev. B*, 53:2183, 1996.

[33] A. Sarychev, V. Shubin, and V. Shalaev. Anderson localization of surface plasmons and nonlinear optics of metal-dielectric composites. *Phys. Rev. B*, 60:16389, 1999.

[34] M. Stockman, S. Faleev, and D. Bergman. Localization versus delocalization of surface plasmons in nanosystems: Can one state have both characteristics? *Phys. Rev. Lett.*, 87:167401, 2001.

[35] K. Joulain, R. Carminati, J.-P. Mulet, and J;-J. Greffet. Definition and measurement of the local density of electromagnetic states close to an interface. *Phys. Rev. B*, 68:245405, 2003.

[36] F. J. García de Abajo and M. Kociak. Probing the photonic local density of states with electron energy loss spectroscopy. *Phys. Rev. Lett.*, 100:106804, 2008.

[37] G. Boudarham and M. Kociak. Modal decompositions of the local electromagnetic density of states and spatially resolved electron energy loss probability in terms of geometric modes. *Phys. Rev. B*, 85:245447, 2012.

[38] J. Nelayah, M. Kociak, O. Stéphan, F. J. García de Abajo, M. Tencé, L. Henrard, D. Taverna, I. Pastoriza-Santos, L. M. Liz-Marzán, and C. Colliex. Mapping surface plasmons on a single metallic nanoparticle. *Nat. Phys.*, 3:348, 2007.

[39] M. Bosman, G. R. Anstis, V. J. Keast, J. D. Clarke, and M. B. Cortie. Light splitting in nanoporous gold and silver. *ACS Nano*, 6:319, 2012.

[40] J. Nelayah, M. Kociak, O. Stéphan, N. Geuquet, L. Henrard, F. J. García de Abajo, I. Pastoriza-Santos, L. M. Liz-Marzán, and C. Colliex. Two-dimensional quasistatic stationary short range surface plasmons in flat nanoprisms. *Nano Lett.*, 10:902, 2010.

[41] S. Mazzucco, O. Stéphan, C. Colliex, I. Pastoriza-Santos, L. M. Liz-Marzan, J. García de Abajo, and M. Kociak. Spatially resolved measurements of plasmonic eigenstates in complex-shaped, asymmetric nanoparticles: gold nanostars. *Eur. Phys. Journ. Applied Physics*, 54:33512, 2011.

[42] M. Bosman, E. Ye, S. F. Tan, C. A. Nijhuis, J. K. W. Yang, R. Marty, A. Mlayah, A. Arbouet, C. Girard, and M.-Y. Han. Surface plasmon damping quantified with an electron nanoprobe. *Sci. Rep.*, 3:1312, 2013.

[43] E. J. R. Vesseur, R. de Waele, M. Kuttge, and A. Polman. Direct observation of plasmonic modes in au nanowires using high-resolution cathodoluminescence spectroscopy. *Nano Lett.*, 7:2843, 2007.

[44] M. Kuttge, E. J. R. Vesseur, A. F. Koenderink, H. J. Lezec, H. A. Atwater, F. J. García de Abajo, and A. Polman. Local density of states, spectrum, and far-field interference of surface plasmon polaritons probed by cathodoluminescence. *Phys. Rev. B*, 79:113405, 2009.

[45] J. Nelayah, L. Gu, W. Sigle, C. T. Koch, I. Pastoriza-Santos, L. M. Liz-Marzán, and P. A. van Aken. Direct imaging of surface plasmon resonances on single triangular silver nanoprisms at optical wavelength using low-loss EFTEM imaging. *Opt. Lett.*, 34:1003, 2009.

[46] P. Chaturvedi, K. H. Hsu, A.l Kumar, K. H. Fung, J. C. Mabon, and N. X. Fang. Imaging of plasmonic modes of silver nanoparticles using high-resolution cathodoluminescence spectroscopy. *ACS Nano*, 3:2965, 2009.

[47] A. Kumar, K.-H. Fung, J. C. Mabon, E. Chow, and N. X. Fang. Excitation and imaging of resonant optical modes of au triangular nanoantennas using cathodoluminescence spectroscopy. *J.V.S.T. B*, 28:C6C21, 2010.

[48] B. Schaffer, W. Grogger, and F. Kothleitner, G.and Hofer. Comparison of EFTEM and STEM EELS plasmon imaging of gold nanoparticles in a monochromated TEM. *Ultramicroscopy*, 110:1087, 2010.

[49] L. Gu, W. Sigle, C. T. Koch, B. Ögüt, P. A. van Aken, N. Talebi, R. Vogelgesang, J. Mu, X. Wen, and J. Mao. Resonant wedge-plasmon modes in single-crystalline gold nanoplatelets. *Phys. Rev. B*, 83:195433, 2011.

[50] N. Talebi, W. Sigle, R. Vogelgesang, C. T. Koch, Cristina Fernández-López, L. M. Liz-Marzán, B. Ögüt, M. Rohm, and P. A. van Aken. Breaking the mode degeneracy of surface plasmon resonances in a triangular system. *Langmuir*, 28:8867, 2012.

[51] P. Das, T. K. Chini, and J. Pond. Probing higher order surface plasmon modes on individual truncated tetrahedral gold nanoparticle using cathodoluminescence imaging and spectroscopy combined with FDTD simulations. *J. Phys. Chem. C*, 116:15610, 2012.

[52] H. Duan, A. I. Fernández-Domínguez, M. Bosman, S. A. Maier, and J. K. W. Yang. Nanoplasmonics: Classical down to the nanometer scale. *Nano Lett.*, 12:1683, 2012.

[53] R. F. Egerton. *Electron energy-loss spectroscopy in the electron microscope*. The language of science. Springer, New York, third edition edition, 2011.

[54] B. G. Yacobi and D. B. Holt. *Cathodoluminescence microscopy of inorganic solids*. Plenum Press, New York, 1990.

[55] J. Goldstein. *Scanning electron microscopy and x-ray microanalysis*. Kluwer Academic/Plenum Publishers, New York, 3rd ed edition, 2003.

[56] M. Kociak, O. Stéphan, M. G. Walls, and C. Tencé, M.and Colliex. Spatially resolved EELS: the spectrum-imaging technique and its applications. In S. J. Pennycook and P. D. Nellist, editors, *Scanning Transmission Electron Microscopy*, page 163. Springer New York, New York, NY, 2011.

[57] C. Jeanguillaume and C. Colliex. Spectrum-image: The next step in EELS digital acquisition and processing. *Ultramicroscopy*, 28:252, 1989.

[58] H. Raether. *Excitation of Plasmons and Interband Transitions by Electrons*. Springer-Verlag : Springer e-books, Berlin, Heidelberg, 1980.

[59] V. Iberi, N. Mirsaleh-Kohan, and J. P. Camden. Understanding plasmonic properties in metallic nanostructures by correlating photonic and electronic excitations. *J. Phys. Chem. Lett.*, 4:1070, 2013.

[60] R. H. Ritchie. Plasma losses by fast electrons in thin films. *Phys. Rev.*, 106:874, 1957.

[61] C. J. Powell and J. B. Swan. Origin of the characteristic electron energy losses in aluminum. *Phys. Rev.*, 115:869, 1959.

[62] E. A. Stern and R. A. Ferrell. Surface plasma oscillations of a degenerate electron gas. *Phys. Rev.*, 120:130, 1960.

[63] M. Achèche, C. Colliex, H. Kohl, A. Nourtier, and P. Trebbia. Theoretical and experimental study of plasmon excitations in small metallic spheres. *Ultramicroscopy*, 20:99, 1986.

[64] P. Batson. Surface plasmon coupling in clusters of small spheres. *Phys. Rev. Lett.*, 49:936, 1982.

[65] D. Ugarte, C. Colliex, and P. Trebbia. Surface- and interface-plasmon modes on small semiconducting spheres. *Phys. Rev. B*, 45:4332, 1992.

[66] T. L. Ferrell and P. M. Echenique. Generation of surface excitations on dielectric spheres by an external electron beam. *Phys. Rev. Lett.*, 55:1526, 1985.

[67] F. García de Abajo. Relativistic energy loss and induced photon emission in the interaction of a dielectric sphere with an external electron beam. *Phys. Rev. B*, 59:3095.

[68] R. Fuchs and K. L. Kliewer. Optical modes of vibration in an ionic crystal sphere. *J. Opt. Soc. Am.*, 58:319, 1968.

[69] I. Khan, D. Cunningham, S. Lazar, D. Graham, W. Ewen Smith, and D. W. McComb. A TEM and electron energy loss spectroscopy (EELS) investigation of active and inactive silver particles for surface enhanced resonance raman spectroscopy (SERRS). *Faraday Discuss.*, 132:171, 2006.

[70] M. Bosman, V. J. Keast, M.i Watanabe, A. I. Maaroof, and M.l B. Cortie. Mapping surface plasmons at the nanometre scale with an electron beam. *Nanotechnology*, 18:165505, 2007.

[71] E. Fermi. The ionization loss of energy in gases and in condensed materials. *Phys. Rev.*, 57:485, 1940.

[72] F. J. García de Abajo and J. Aizpurua. Numerical simulation of electron energy loss near inhomogeneous dielectrics. *Phys. Rev. B*, 56:15873, 1997.

[73] F. Ouyang and M. Isaacson. Surface plasmon excitation of objects with arbitrary shape and dielectric constant. *Philos. Mag. Part B*, 60:481, 1989.

[74] P. B. Johnson and R. W. Christy. Optical constants of the noble metals. *Phys. Rev. B*, 6:4370, 1972.

[75] J. Lindhard. *On the Properties of a Gas of Charged Particles.* Mathematisk-fysiske meddelelser. I kommission hos Munksgaard, 1954.

[76] C. David and F. J. García de Abajo. Spatial nonlocality in the optical response of metal nanoparticles. *J. Phys. Chem. C*, 115:19470, 2011.

[77] *Handbook of optical constants of solids II.* Academic Press, Boston, 1991.

[78] M.-L. Theye. Investigation of the optical properties of au by means of thin semitransparent films. *Phys. Rev. B*, 2:3060, 1970.

[79] U. Hohenester and A. Trugler. MNPBEM a matlab toolbox for the simulation of plasmonic nanoparticles. *Comput. Phys. Commun.*, 183:370, 2012.

[80] K. L. Shuford, M. A. Ratner, and G. C. Schatz. Multipolar excitation in triangular nanoprisms. *J. Chem. Phys.*, 123:114713, 2005.

[81] Y. He and G. Shi. Surface plasmon resonances of silver triangle nanoplates: Graphic assignments of resonance modes and linear fittings of resonance peaks. *J. Phys. Chem. B*, 109:17503, 2005.

[82] L. J. Sherry, R. Jin, C. A. Mirkin, G. C. Schatz, and R. P. Van Duyne. Localized surface plasmon resonance spectroscopy of single silver triangular nanoprisms. *Nano Lett.*, 6:2060, 2006.

[83] N. Félidj, J. Grand, G. Laurent, J. Aubard, G. Lévi, A. Hohenau, N. Galler, F. R. Aussenegg, and J. R. Krenn. Multipolar surface plasmon peaks on gold nanotriangles. *J. Chem. Phys.*, 128:094702, 2008.

[84] J. Kottmann, O. Martin, D. Smith, and S. Schultz. Spectral response of plasmon resonant nanoparticles with a non-regular shape. *Opt. Express*, 6:213, 2000.

[85] M. Rang, A. C. Jones, F. Zhou, Z.-Y. Li, B. J. Wiley, Y. Xia, and M. B. Raschke. Optical near-field mapping of plasmonic nanoprisms. *Nano Lett.*, 8:3357, 2008.

[86] F.-P. Schmidt, H. Ditlbacher, U. Hohenester, A. Hohenau, F. Hofer, and J. R. Krenn. Dark plasmonic breathing modes in silver nanodisks. *Nano Lett.*, 12:5780, 2012.

[87] D. Rossouw, M. Couillard, J. Vickery, E. Kumacheva, and G. A. Botton. Multipolar plasmonic resonances in silver nanowire antennas imaged with a subnanometer electron probe. *Nano Lett.*, 11:149, 2011.

[88] O. Nicoletti, M. Wubs, N. A. Mortensen, W. Sigle, P. A. van Aken, and P. A. Midgley. Surface plasmon modes of a single silver nanorod: an electron energy loss study. *Opt. Express*, 19:15371, 2011.

[89] J. K. Lim, K. Imura, T. Nagahara, S. K. Kim, and H. Okamoto. Imaging and dispersion relations of surface plasmon modes in silver nanorods by near-field spectroscopy. *Chem. Phys. Lett.*, 412:41, 2005.

[90] L. Douillard, F. Charra, Z. Korczak, R. Bachelot, S. Kostcheev, G. Lerondel, P.-M. Adam, and P. Royer. Short range plasmon resonators probed by photoemission electron microscopy. *Nano Lett.*, 8:935, 2008.

[91] A. Archambault, T. Teperik, F. Marquier, and J.-J. Greffet. Surface plasmon fourier optics. *Phys. Rev. B*, 79:195414, 2009.

[92] F. García de Abajo and A. Howie. Retarded field calculation of electron energy loss in inhomogeneous dielectrics. *Phys. Rev. B*, 65:115418, 2002.

[93] D. J. Bergman and M. I. Stockman. Surface plasmon amplification by stimulated emission of radiation: Quantum generation of coherent surface plasmons in nanosystems. *Phys. Rev. Lett.*, 90:027402, 2003.

[94] M. Aeschlimann, T. Brixner, A. Fischer, C. Kramer, P. Melchior, W. Pfeiffer, C. Schneider, C. Struber, P. Tuchscherer, and D. V. Voronine. Coherent two-dimensional nanoscopy. *Science*, 333:1723, 2011.

[95] K. Kolwas and A. Derkachova. Damping rates of surface plasmons for particles of size from nano- to micrometers; reduction of the nonradiative decay. *J. Quant. Spectrosc. Radiat. Transf.*, 114:45, 2013.

[96] F. Wang and Y. R. Shen. General properties of local plasmons in metal nanostructures. *Phys. Rev. Lett.*, 97:206806, 2006.

[97] R. T. Beach and R. W. Christy. Electron-electron scattering in the intraband optical conductivity of cu, ag, and au. *Phys. Rev. B*, 16:5277, 1977.

[98] I. Zorić, M. Zäch, B. Kasemo, and C. Langhammer. Gold, platinum, and aluminum nanodisk plasmons: Material independence, subradiance, and damping mechanisms. *ACS Nano*, 5:2535, 2011.

[99] K. Joulain, J.-P. Mulet, F. Marquier, R. Carminati, and J.-J. Greffet. Surface electromagnetic waves thermally excited: Radiative heat transfer, coherence properties and casimir forces revisited in the near field. *Surf. Sci. Rep.*, 57:59, 2005.

[100] W. L. Barnes. Fluorescence near interfaces: The role of photonic mode density. *J. Mod. Opt.*, 45:661, 1998.

[101] J.-C. Weeber, A. Dereux, C. Girard, J. R. Krenn, and J.-P. Goudonnet. Plasmon polaritons of metallic nanowires for controlling submicron propagation of light. *Phys. Rev. B*, 60:9061, 1999.

[102] A. Dereux, C. Girard, and J.-C. Weeber. Theoretical principles of near-field optical microscopies and spectroscopies. *J. Chem. Phys.*, 112:7775, 2000.

[103] G. Colas des Francs, C. Girard, and A. Dereux. Theory of near-field optical imaging with a single molecule as light source. *J. Chem. Phys.*, 117:4659, 2002.

[104] Y. De Wilde, F. Formanek, R. Carminati, B. Gralak, P.-A. Lemoine, K. Joulain, J.-P. Mulet, Y. Chen, and J.-J. Greffet. Thermal radiation scanning tunnelling microscopy. *Nature*, 444:740, 2006.

[105] S. Viarbitskaya, A. Teulle, R. Marty, J. Sharma, C. Girard, A. Arbouet, and E. Dujardin. Tailoring and imaging the plasmonic local density of states in crystalline nanoprisms. *Nature Mater.*, 12:426, 2013.

[106] G. D'Aguanno, N. Mattiucci, M. Centini, M. Scalora, and M. J. Bloemer. Electromagnetic density of modes for a finite-size three-dimensional structure. *Phys. Rev. E*, 69:057601, 2004.

[107] A. Narayanaswamy and G. Chen. Dyadic green's functions and electromagnetic local density of states. *J. Quant. Spectrosc. Radiat. Transf.*, 111:1877, 2010.

[108] Z. Mohammadi, C. P. Van Vlack, S. Hughes, J. Bornemann, and R. Gordon. Vortex electron energy loss spectroscopy for near-field mapping of magnetic plasmons. *Opt. Express*, 20:15024, 2012.

[109] A. I. Kuznetsov, A. E. Miroshnichenko, Y. H. Fu, J. Zhang, and B. Lukyanchuk. Magnetic light. *Sci. Rep.*, 2:492, 2012.

[110] A. K. Sarychev, G. Shvets, and V. M. Shalaev. Magnetic plasmon resonance. *Phys. Rev. E*, 73:036609, 2006.

[111] V. M. Shalaev. Optical negative-index metamaterials. *Nature Photon.*, 1:41, 2007.

[112] A. Cazé, R. Pierrat, and R. Carminati. Spatial coherence in complex photonic and plasmonic systems. *Phys. Rev. Lett.*, 110:063903, 2013.

[113] U. Hohenester, H. Ditlbacher, and J. R. Krenn. Electron-energy-loss spectra of plasmonic nanoparticles. *Phys. Rev. Lett.*, 103:106801, 2009.

[114] C. Matyssek, J. Niegemann, W. Hergert, and K. Busch. Computing electron energy loss spectra with the discontinuous galerkin time-domain method. *Photonics Nanostruct.*, 9:367, 2011.

[115] N. Geuquet and L. Henrard. Eels and optical response of a noble metal nanoparticle in the frame of a discrete dipole approximation. *Ultramicroscopy*, 110:1075, 2010.

[116] V. Myroshnychenko, J. Rodríguez-Fernández, I. Pastoriza-Santos, A. M. Funston, C. Novo, P. Mulvaney, L. M. Liz-Marzán, and F. J. García de Abajo. Modelling the optical response of gold nanoparticles. *Chem. Soc. Rev.*, 37:1792, 2008.

[117] G. Boudarham, N. Feth, V. Myroshnychenko, S. Linden, J. García de Abajo, M. Wegener, and M. Kociak. Spectral imaging of individual split-ring resonators. *Phys. Rev. Lett.*, 105:255501, 2010.

[118] M.-W. Chu, V. Myroshnychenko, C. H. Chen, J.-P. Deng, C.-Y. Mou, and F. J. García de Abajo. Probing bright and dark surface-plasmon modes in individual and coupled noble metal nanoparticles using an electron beam. *Nano Lett.*, 9:399, 2009.

[119] D. Rossouw and G. A. Botton. Plasmonic response of bent silver nanowires for nanophotonic subwavelength waveguiding. *Phys. Rev. Lett.*, 110:066801, 2013.

[120] F. von Cube, S. Irsen, J. Niegemann, C. Matyssek, W. Hergert, K. Busch, and S. Linden. Spatio-spectral characterization of photonic meta-atoms with electron energy-loss spectroscopy. *Opt. Mater. Express*, 1:1009, 2011.

[121] J. Verbeeck, H. Tian, and P. Schattschneider. Production and application of electron vortex beams. *Nature*, 467:301, 2010.

[122] C. Awada, T. Popescu, L. Douillard, F. Charra, A. Perron, H. Yockell-Lelièvre, A.-L. Baudrion, P.-M. Adam, and R. Bachelot. Selective excitation of plasmon resonances of single au triangles by polarization-dependent light excitation. *J. Phys. Chem. C*, 116:14591, 2012.

[123] J. A. Porto, P. Johansson, S. P. Apell, and T. Lopez-Rios. Resonance shift effects in apertureless scanning near-field optical microscopy. *Phys. Rev. B*, 67:085409, 2003.

[124] A. García-Etxarri, I. Romero, F. J. García de Abajo, R. Hillenbrand, and J. Aizpurua. Influence of the tip in near-field imaging of nanoparticle plasmonic modes: Weak and strong coupling regimes. *Phys. Rev. B*, 79:125439, 2009.

[125] A. Babuty, K. Joulain, P.-O. Chapuis, J.-J. Greffet, and Y. De Wilde. Blackbody spectrum revisited in the near field. *Phys. Rev. Lett.*, 110:146103, 2013.

[126] R.F Egerton. New techniques in electron energy-loss spectroscopy and energy-filtered imaging. *Micron*, 34:127, 2003.

[127] K. Kimoto, G. Kothleitner, W. Grogger, Y. Matsui, and F. Hofer. Advantages of a monochromator for bandgap measurements using electron energy-loss spectroscopy. *Micron*, 36:185, 2005.

[128] A. Gloter, A. Douiri, M. Tencé, and C. Colliex. Improving energy resolution of EELS spectra: an alternative to the monochromator solution. *Ultramicroscopy*, 96:385, 2003.

[129] M. Bosman and V. J. Keast. Optimizing EELS acquisition. *Ultramicroscopy*, 108:837, 2008.

[130] P. R. Edwards, D. Sleith, A. W. Wark, and R. W. Martin. Mapping localized surface plasmons within silver nanocubes using cathodoluminescence hyperspectral imaging. *J. Phys. Chem. C*, 115:14031, 2011.

[131] N. Yamamoto, K. Araya, and F. García de Abajo. Photon emission from silver particles induced by a high-energy electron beam. *Phys. Rev. B*, 64:205419, 2001.

[132] T. Coenen, E. J. R. Vesseur, and A. Polman. Angle-resolved cathodoluminescence spectroscopy. *Appl. Phys. Lett.*, 99:143103, 2011.

[133] T. Coenen and A. Polman. Polarization-sensitive cathodoluminescence fourier microscopy. *Opt. Express*, 20:18679, 2012.

[134] L. H. G. Tizei and M. Kociak. Spatially resolved quantum nano-optics of single photons using an electron microscope. *Phys. Rev. Lett.*, 110:153604, 2013.

[135] L. F. Zagonel, S. Mazzucco, M. Tencé, K. March, R. Bernard, B. Laslier, G. Jacopin, M. Tchernycheva, L. Rigutti, F. H. Julien, R. Songmuang, and M. Kociak. Nanometer scale spectral imaging of quantum emitters in nanowires and its correlation to their atomically resolved structure. *Nano Lett.*, 11:568, 2011.

[136] P. C. Tiemeijer, J. H. A. van Lin, B. H. Freitag, and A. F. de Jong. Monochromized 200kv (S)TEM. *Microscopy and Microanalysis*, 8:70, 2002.

[137] D. Rossouw, M. Bugnet, and G. A. Botton. Structural and electronic distortions in individual carbon nanotubes under laser irradiation in the electron microscope. *Phys. Rev. B*, 87:125403, 2013.

[138] R. Gómez-Medina, N. Yamamoto, M. Nakano, and F J García de Abajo. Mapping plasmons in nanoantennas via cathodoluminescence. *New J. Phys.*, 10:105009, 2008.

[139] A. I. Denisyuk, G. Adamo, K. F. MacDonald, J. Edgar, M. D. Arnold, V. Myroshnychenko, M. J. Ford, F. J. Garciía de Abajo, and N. I. Zheludev. Transmitting hertzian optical nanoantenna with free-electron feed. *Nano Lett.*, 10:3250, 2010.

[140] M. W. Knight, L. Liu, Y. Wang, L. Brown, S. Mukherjee, N. S. King, H. O. Everitt, P. Nordlander, and N. J. Halas. Aluminum plasmonic nanoantennas. *Nano Lett.*, 12:6000, 2012.

[141] P. Das and T. K. Chini. Spectroscopy and imaging of plasmonic modes over a single decahedron gold nanoparticle: A combined experimental and numerical study. *J. Phys. Chem. C*, 116:25969, 2012.

[142] A. Cazé, R. Pierrat, and R. Carminati. Radiative and non-radiative local density of states on disordered plasmonic films. *Photonics Nanostruct.*, 10:339, 2012.

[143] R. X. Bian, R. C. Dunn, X. S. Xie, and P. T. Leung. Single molecule emission characteristics in near-field microscopy. *Phys. Rev. Lett.*, 75:4772, 1995.

[144] R. Carminati, J.-J. Greffet, C. Henkel, and J.M. Vigoureux. Radiative and non-radiative decay of a single molecule close to a metallic nanoparticle. *Opt Commun.*, 261:368, 2006.

[145] G. Colas Des Francs, C. Girard, A. Bruyant, and A. Dereux. SNOM signal near plasmonic nanostructures: an analogy with fluorescence decays channels. *J. Microsc.*, 229:302, 2008.

[146] J. B. Lassiter, H. Sobhani, M. W. Knight, W. S. Mielczarek, P. Nordlander, and N. J. Halas. Designing and deconstructing the fano lineshape in plasmonic nanoclusters. *Nano Lett.*, 12:1058, 2012.

[147] M. Frimmer, T. Coenen, and A. F. Koenderink. Signature of a fano resonance in a plasmonic metamolecule's local density of optical states. *Phys. Rev. Lett.*, 108:077404, 2012.

[148] E. J. R. Vesseur, F. J. García de Abajo, and A. Polman. Modal decomposition of surface plasmon whispering gallery resonators. *Nano Lett.*, 9:3147, 2009.

[149] E. S. Barnard, T. Coenen, E. J. R. Vesseur, A. Polman, and M. L. Brongersma. Imaging the hidden modes of ultrathin plasmonic strip antennas by cathodoluminescence. *Nano Lett.*, 11:4265, 2011.

[150] B. S. Guiton, V. Iberi, S. Li, D. N. Leonard, C. M. Parish, P. G. Kotula, M. Varela, G. C. Schatz, S. J. Pennycook, and J. P. Camden. Correlated optical measurements and plasmon mapping of silver nanorods. *Nano Lett.*, 11:3482, 2011.

[151] E. J. R. Vesseur and A. Polman. Plasmonic whispering gallery cavities as optical nanoantennas. *Nano Lett.*, 11:5524, 2011.

[152] M. Husnik, F. von Cube, S. Irsen, S. Linden, J. Niegemann, K. Busch, and M. Wegener. Comparison of electron energy-loss and quantitative optical spectroscopy on individual optical gold antennas. *Nanophotonics*, 2:241, 2013.

[153] S. M. Collins and P. A. Midgley. Surface plasmon excitations in metal spheres: Direct comparison of light scattering and electron energy-loss spectroscopy by modal decomposition. *Phys. Rev. B*, 87:235432, 2013.

[154] V. Myroshnychenko, J. Nelayah, G. Adamo, N. Geuquet, J. Rodríguez-Fernández, I. Pastoriza-Santos, K. F. MacDonald, L. Henrard, L. M. Liz-Marzán, N. I. Zheludev, M. Kociak, and F. J. García de Abajo. Plasmon spectroscopy and imaging of individual gold nanodecahedra: A combined optical microscopy, cathodoluminescence, and electron energy-loss spectroscopy study. *Nano Lett.*, 12:4172, 2012.

[155] S. Mazzucco, N. Geuquet, J. Ye, O. Stéphan, W. Van Roy, P. Van Dorpe, L. Henrard, and M. Kociak. Ultralocal modification of surface plasmons properties in silver nanocubes. *Nano Lett.*, 12:1288, 2012.

[156] F. García de Abajo, A. Rivacoba, N. Zabala, and N. Yamamoto. Boundary effects in cherenkov radiation. *Phys. Rev. B*, 69:155420, 2004.

[157] F. J. García de Abajo and A. Howie. Relativistic electron energy loss and electron-induced photon emission in inhomogeneous dielectrics. *Phys. Rev. Lett.*, 80:5180, 1998.

[158] V. Myroshnychenko, E. Carbo-Argibay, I. Pastoriza-Santos, J. Pérez-Juste, L. M. Liz-Marzán, and F. J. García de Abajo. Modeling the optical response of highly faceted metal nanoparticles with a fully 3D boundary element method. *Adv. Mater.*, 20:4288, 2008.

[159] A. Pulisciano, S. J. Park, and R. E. Palmer. Surface plasmon excitation of Au and Ag in scanning probe energy loss spectroscopy. *Appl. Phys. Lett.*, 93:213109, 2008.

[160] M. Husnik, S. Linden, R. Diehl, J. Niegemann, K. Busch, and M. Wegener. Quantitative experimental determination of scattering and absorption cross-section spectra of individual optical metallic nanoantennas. *Phys. Rev. Lett.*, 109:233902, 2012.

[161] M. A. Kats, N. Yu, P. Genevet, Z. Gaburro, and F. Capasso. Effect of radiation damping on the spectral response of plasmonic components. *Opt. Express*, 19:21748, 2011.

[162] G. Boudarham. *Nanooptique avec des électrons rapides : métamatériaux, formulation modale de la EMLDOS pour des systèmes plasmoniques.* PhD thesis, 2011.

[163] J. D. Jackson. *Classical electrodynamics.* Wiley, New York, 3rd ed edition, 1999.

[164] M. NGom, J. Ringnalda, J. F. Mansfield, A. Agarwal, N. Kotov, N. J. Zaluzec, and T. B. Norris. Single particle plasmon spectroscopy of silver nanowires and gold nanorods. *Nano Lett.*, 8:3200, 2008.

[165] B. Rolly, B. Stout, and N. Bonod. Metallic dimers: When bonding transverse modes shine light. *Phys. Rev. B*, 84:125420, 2011.

[166] J. Zuloaga and P. Nordlander. On the energy shift between near-field and far-field peak intensities in localized plasmon systems. *Nano Lett.*, 11:1280, 2011.

[167] P. Alonso-González, P. Albella, F. Neubrech, C. Huck, J. Chen, F. Golmar, F. Casanova, L. E. Hueso, A. Pucci, J. Aizpurua, and R. Hillenbrand. Experimental verification of the spectral shift between near- and far-field peak intensities of plasmonic infrared nanoantennas. *Phys. Rev. Lett.*, 110:203902, 2013.

[168] P. G. Etchegoin, E. C. Le Ru, and M. Meyer. An analytic model for the optical properties of gold. *J. Chem. Phys.*, 125:164705, 2006.

[169] P. Gadenne, Y. Yagil, and G. Deutscher. Transmittance and reflectance in situ measurements of semicontinuous gold films during deposition. *J. Appl. Phys.*, 66:3019, 1989.

[170] Y. Yagil, P. Gadenne, C. Julien, and G. Deutscher. Optical properties of thin semicontinuous gold films over a wavelength range of 2.5 to 500 microns. *Phys. Rev. B*, 46:2503, 1992.

[171] S. Grésillon, L. Aigouy, A. Boccara, J. Rivoal, X. Quelin, C. Desmarest, P. Gadenne, V. Shubin, A. Sarychev, and V. Shalaev. Experimental observation of localized optical excitations in random metal-dielectric films. *Phys. Rev. Lett.*, 82:4520, 1999.

[172] S. Ducourtieux, V. Podolskiy, S. Grésillon, S. Buil, B. Berini, P. Gadenne, A. Boccara, J. Rivoal, W. Bragg, K. Banerjee, V. Safonov, V. Drachev, Z. Ying, A. Sarychev, and V. Shalaev. Near-field optical studies of semicontinuous metal films. *Phys. Rev. B*, 64:165403, 2001.

[173] K. Seal, M. Nelson, Z. Ying, D. Genov, A. Sarychev, and V. Shalaev. Growth, morphology, and optical and electrical properties of semicontinuous metallic films. *Phys. Rev. B*, 67:035318, 2003.

[174] K. Seal, D. A. Genov, A. K. Sarychev, H. Noh, V. M. Shalaev, Z. C. Ying, X. Zhang, and H. Cao. Coexistence of localized and delocalized surface plasmon modes in percolating metal films. *Phys. Rev. Lett.*, 97:206103, 2006.

[175] S. Buil, J. Aubineau, J. Laverdant, and X. Quélin. Local field intensity enhancements on gold semicontinuous films investigated with an aperture nearfield optical microscope in collection mode. *J. Appl. Phys*, 100:063530, 2006.

[176] J. Laverdant, S. Buil, and X. Quélin. Local field enhancements on gold and silver nanostructures for aperture near field spectroscopy. *J.O.L.*, 127:176, 2007.

[177] V. Krachmalnicoff, E. Castanié, Y. De Wilde, and R. Carminati. Fluctuations of the local density of states probe localized surface plasmons on disordered metal films. *Phys. Rev. Lett.*, 105:183901, 2010.

[178] C. Awada, G. Barbillon, F. Charra, L. Douillard, and J.-J. Greffet. Experimental study of hot spots in gold/glass nanocomposite films by photoemission electron microscopy. *Phys. Rev. B*, 85:045438, 2012.

[179] J.F. Gouyet. *Physique et structures fractales.* Masson, 1992.

[180] A Sarychev. Electromagnetic field fluctuations and optical nonlinearities in metal-dielectric composites. *Phys. Rep.*, 335:275, 2000.

[181] Y. Yagil, M. Yosefin, D. J. Bergman, G. Deutscher, and P. Gadenne. Scaling theory for the optical properties of semicontinuous metal films. *Phys. Rev. B*, 43:11342, 1991.

[182] D. J. Bergman and D. Stroud. Physical properties of macroscopically inhomogeneous media. In *Solid State Physics*, volume 46, page 147. Elsevier, 1992.

[183] F. Brouers, S. Blacher, and A. K. Sarychev. Giant field fluctuations and anomalous light scattering from semicontinuous metal films. *Phys. Rev. B*, 58:15897, 1998.

[184] F. Brouers, S. Blacher, A. N. Lagarkov, A. K. Sarychev, P. Gadenne, and V. M. Shalaev. Theory of giant raman scattering from semicontinuous metal films. *Phys. Rev. B*, 55:13234, 1997.

[185] U. K. Chettiar, P. Nyga, M. D. Thoreson, A. V. Kildishev, V. P. Drachev, and V. M. Shalaev. FDTD modeling of realistic semicontinuous metal films. *Appl. Phys. B*, 100:159, 2010.

[186] S. Buil, J. Laverdant, B. Berini, P. Maso, J.-P. Hermier, and X. Quélin. FDTD simulations of localization and enhancements on fractal plasmonics nanostructures. *Opt. Express*, 20:11968, 2012.

[187] E. Castanié, V. Krachmalnicoff, A. Cazé, R. Pierrat, Y. De Wilde, and R. Carminati. Distance dependence of the local density of states in the near field of a disordered plasmonic film. *Opt. Lett.*, 37:3006, 2012.

[188] V. M. Shalaev. Electromagnetic properties of small-particle composites. *Phys. Rep.*, 272:61, 1996.

[189] D. P. Tsai, J. Kovacs, Z. Wang, M. Moskovits, V. M. Shalaev, J. S. Suh, and R. Botet. Photon scanning tunneling microscopy images of optical excitations of fractal metal colloid clusters. *Phys. Rev. Lett.*, 72:4149, 1994.

[190] P. Zhang, T. L. Haslett, C. Douketis, and M. Moskovits. Mode localization in self-affine fractal interfaces observed by near-field microscopy. *Phys. Rev. B*, 57:15513, 1998.

[191] S. I. Bozhevolnyi, I. I. Smolyaninov, and A. V. Zayats. Near-field microscopy of surface-plasmon polaritons: Localization and internal interface imaging. *Phys. Rev. B*, 51:17916, 1995.

[192] P. Sheng. *Introduction to wave scattering, localization, and mesoscopic phenomena.* Number 88 in Springer series in materials science. Springer, Berlin ; New York, 2nd ed edition, 2006.

[193] E. Akkermans and G. Montambaux. *Mesoscopic physics of electrons and photons.* Cambridge Univ Press, Cambridge, 2011.

[194] K. Seal, D. Genov, A. Sarychev, H. Noh, V. Shalaev, Z. Ying, X. Zhang, and H. Cao. Coexistence of localized and delocalized surface plasmon modes in percolating metal films. *Phys. Rev. Lett.*, 97:206103, 2006.

[195] M. Stockman. Inhomogeneous eigenmode localization, chaos, and correlations in large disordered clusters. *Phys. Rev. E*, 56:6494, 1997.

[196] R. F. Voss, R. B. Laibowitz, and E. I. Allessandrini. Fractal (scaling) clusters in thin gold films near the percolation threshold. *Phys. Rev. Lett.*, 49:1441, 1982.

[197] M. W. Knight, Y. Wu, J. B. Lassiter, P. Nordlander, and N. J. Halas. Substrates matter: Influence of an adjacent dielectric on an individual plasmonic nanoparticle. *Nano Lett.*, 9:2188, 2009.

[198] K. C. Vernon, A. M. Funston, C. Novo, D. E. Gómez, P. Mulvaney, and T. J. Davis. Influence of particle substrate interaction on localized plasmon resonances. *Nano Lett.*, 10:2080, 2010.

[199] R. Esteban, R. Vogelgesang, J. Dorfmuüller, A. Dmitriev, C. Rockstuhl, C. Etrich, and K. Kern. Direct near-field optical imaging of higher order plasmonic resonances. *Nano Lett.*, 8:3155, 2008.

[200] E. Dulkeith, T. Niedereichholz, T. A. Klar, J. Feldmann, G. von Plessen, D. I. Gittins, K. S. Mayya, and F. Caruso. Plasmon emission in photoexcited gold nanoparticles. *Phys. Rev. B*, 70:205424, 2004.

[201] J. Kistner, X. Chen, Y. Weng, H. P. Strunk, M. B. Schubert, and J. H. Werner. Photoluminescence from silicon nitride - no quantum effect. *J. Appl. Phys.*, 110:023520, 2011.

[202] F. Röder and H. Lichte. Inelastic electron holography, first results with surface plasmons. *Eur. Phys. Journ. Applied Physics*, 54:33504, 2011.

[203] S. Kühn, U. Håkanson, L. Rogobete, and V. Sandoghdar. Enhancement of single-molecule fluorescence using a gold nanoparticle as an optical nanoantenna. *Phys. Rev. Lett.*, 97:017402, 2006.

[204] N. Dellby, N. J. Bacon, P. Hrncirik, M. F. Murfitt, G. S. Skone, Z. S. Szilagyi, and O. L. Krivanek. Dedicated STEM for 200 to 40 keV operation. *Eur. Phys. Journ. Applied Physics*, 54:33505, 2011.

[205] F. J. García de Abajo and M. Kociak. Electron energy-gain spectroscopy. *New J. Phys.*, 10:073035, 2008.

[206] B. Barwick, D. J. Flannigan, and A. H. Zewail. Photon-induced near-field electron microscopy. *Nature*, 462:902, 2009.

[207] A. Yurtsever and A. H. Zewail. Direct visualization of near-fields in nanoplasmonics and nanophotonics. *Nano Lett.*, 12:3334, 2012.

[208] A. Howie. Photon assisted electron energy loss spectroscopy and ultrafast imaging. *Microscopy and Microanalysis*, 15:314, 2009.

[209] A. Howie. Photon interactions for electron microscopy applications. *Eur. Phys. Journ. Applied Physics*, 54:33502, 2011.

[210] H. Dömer and O. Bostanjoglo. High-speed transmission electron microscope. *Rev. Sci. Instrum.*, 74:4369, 2003.

[211] B. Xiang, D. J. Hwang, J. B. In, S.-G. Ryu, J.-H. Yoo, O. Dubon, A. M. Minor, and C. P. Grigoropoulos. *In Situ* TEM near-field optical probing of nanoscale silicon crystallization. *Nano Lett.*, 12:2524, 2012.

[212] T. LaGrange, G. H. Campbell, B. W. Reed, M. Taheri, J. B. Pesavento, J. S. Kim, and N. D. Browning. Nanosecond time-resolved investigations using the in situ of dynamic transmission electron microscope (DTEM). *Ultramicroscopy*, 108:1441, 2008.

[213] F. Carbone. Modern electron microscopy resolved in space, energy and time. *Eur. Phys. Journ. Applied Physics*, 54:33503, 2011.

[214] H. Boersch, J. Geiger, and W. Stickel. Interaction of 25-kev electrons with lattice vibrations in lif. experimental evidence for surface modes of lattice vibration. *Phys. Rev. Lett.*, 17:379, 1966.

[215] N. Talebi, W. Sigle, R. Vogelgesang, and P. van Aken. Numerical simulations of interference effects in photon-assisted electron energy-loss spectroscopy. *New J. Phys.*, 15:053013, 2013.

[216] H. S. Park, J. S. Baskin, O.-H. Kwon, and A. H. Zewail. Atomic-scale imaging in real and energy space developed in ultrafast electron microscopy. *Nano Lett.*, 7:2545, 2007.

[217] F. J. García de Abajo, A. Asenjo-Garcia, and M. Kociak. Multiphoton absorption and emission by interaction of swift electrons with evanescent light fields. *Nano Lett.*, 10:1859, 2010.

[218] D. Canneson, I. Mallek-Zouari, S. Buil, X. Quélin, C. Javaux, B. Mahler, B. Dubertret, and J.-P. Hermier. Strong purcell effect observed in single thick-shell cdse/cds nanocrystals coupled to localized surface plasmons. *Phys. Rev. B*, 84:245423, 2011.

[219] M. Breit, V. A. Podolskiy, S. Grésillon, G. von Plessen, J. Feldmann, J. C. Rivoal, P. Gadenne, A. K. Sarychev, and V. M. Shalaev. Experimental observation of percolation-enhanced nonlinear light scattering from semicontinuous metal films. *Phys. Rev. B*, 64:125106, 2001.

[220] N. M. Lawandy. Disordered media: Coherent random lasing. *Nat. Phys.*, 6:246, 2010.

[221] S. Camelio, D. Babonneau, D. Lantiat, L. Simonot, and F. Pailloux. Anisotropic optical properties of silver nanoparticle arrays on rippled dielectric surfaces produced by low-energy ion erosion. *Phys. Rev. B*, 80:155434, 2009.

[222] D. Babonneau, S. Camelio, E. Vandenhecke, S. Rousselet, M. Garel, F. Pailloux, and P. Boesecke. Quantitative analysis of nanoripple and nanoparticle patterns by grazing incidence small-angle x-ray scattering 3d mapping. *Phys. Rev. B*, 85:235415, 2012.

[223] W. L. Chan and E. Chason. Making waves: Kinetic processes controlling surface evolution during low energy ion sputtering. *J. Appl. Phys.*, 101:121301, 2007.

[224] J.-M. Jin. *The finite element method in electromagnetics*. John Wiley & Sons, New York, 2nd ed edition, 2002.

[225] Jean-Pierre Berenger. A perfectly matched layer for the absorption of electromagnetic waves. *J. Comput. Phys.*, 114:185, 1994.

[226] A. Bossavit. A rationale for 'edge-elements' in 3-d fields computations. *IEEE Transactions on Magnetics*, 24:74, 1988.

[227] Y. Xu, J. S. Vučković, R. K. Lee, O. J. Painter, A. Scherer, and A. Yariv. Finite-difference time-domain calculation of spontaneous emission lifetime in a microcavity. *J. Opt. Soc. Am. B*, 16:465, 1999.

[228] H. Iwase, D. Englund, and J. Vučković. Analysis of the purcell effect in photonic and plasmonic crystals with losses. *Opt. Express*, 18:16546, 2010.